SCUOLA DI DOTTORATO
UNIVERSITÀ DEGLI STUDI DI MILANO-BICOCCA

Department of

Materials Science

PhD program in Materials Science and Nanotechnology Cycle XXXIII

Curriculum in Materials Science

POINT DEFECTS IN QUARTZ: ROLE IN TRAPPING AND LUMINESCENCE

Surname: Monti Name: Andrea Maurizio

Registration number: 736725

Tutor: Prof. Marco Martini

Coordinator: Prof. Marco Bernasconi

ACADEMIC YEAR 2019/2020

Index

1. Introduction 3
2. Quartz structural properties and crystal preparation 6
2.1 Quartz crystal structure 6
2.2 Growth processes 7
2.3 Point defects in quartz 8
2.3.1 Intrinsic point defects 8
2.3.2 Extrinsic point defects (Impurities) 9
2.4 Sweeping process 11
3. Experimental techniques and groundwork 12
3. 1 Thermoluminescence 12
3.1.1 Models of Thermoluminescence 12
3.1.2 Glow Curve Analysis 13
3.1.3 Thermoluminescence in Quartz 14
3.1.4 The pre-dose effect 15
3.2 Electron Paramagnetic Resonance 17
3.3 Germanium Centres in Quartz 19
4. Experimental setup 23
4.1 Thermoluminescence equipment 23
4.2 Wavelength Resolved Thermoluminescence equipment 23
4.3 Radioluminescence equipment 24
4.4 Electron Paramagnetic Resonance equipment 24
4.5 Temperature Control 24
5. Anomalous thermal stability of the $[GeO_4]^-$ and 110 °C TSL peak of quartz 25
5.1 Experiment procedure 25
5.1.2 Samples 25
5.1.3 TSL Measurements 25
5.1.4 EPR Measurements 26
5.2 Results 26
5.2.1 TSL Results 26
5.2.2 EPR Results 35
5.3 Comments 36
6. Study on the $[GeO_4/Li^+]^0$ relation with the 375 °C TSL peak of quartz 40
6.1 Experiment procedure 40
6.1.1 Samples 40
6.1.2 TSL measurements 41
6.1.3 EPR measurements 41
6.2 Results 41

6.3 Comments ... 43
7. Investigation of the Spectrally resolved TSL peaks of quartz in the 70 °C-220 °C temperature region ... 45
7.1 Experiment procedure ... 45
7.1.1 Samples ... 45
7.1.2 PMT measurements ... 46
7.1.3 WR-TSL measurements ... 46
7.2 Results ... 46
7.2.1 PMT results ... 46
7.2.2 Wavelength resolved TSL results ... 49
7.3 Comments ... 54
8. Sensitivity changes of RL of natural and synthetic quartz ... 58
8.1 Experiment procedure ... 58
8.1.1 Samples ... 58
8.1.2 RL measurements ... 58
8.2 Results ... 58
8.3 Comments ... 77
9. EPR characterization of germanium related centres in natural quartz and the discovery of a new hydrogen related centre ... 80
9.1 Experimental procedure ... 80
9.1.1 Samples ... 80
9.1.2 EPR measurements ... 80
9.2 Results ... 81
9.2.1 Dose response ... 81
9.2.2 Thermal Stability ... 83
9.2.3 Q-band measurements ... 87
9.3 Comments ... 89
10. Characterization of Titanium and Aluminium related centres with low temperature EPR measurements ... 93
10.1 Experimental procedure ... 94
10.1.1 Samples ... 94
10.1.2 EPR measurements ... 95
10.2 Results ... 95
10.2.1 Dose response ... 95
10.3 Comments ... 107
11. Conclusions and final remarks ... 111
12. References ... 113
Appendix ... 121
Acknowledgments ... 123

1. Introduction

Quartz is a very common material, being one the most abundant minerals on Earth. Its properties make it interesting from a petrologist point of view, having different coloured varieties depending on the impurities naturally included in the crystal structure during its growth, such as rose quartz or amethyst, and the conditions of the crystal growth itself, such as hydrothermal growth or igneous formations. Quartz varieties also had symbolic meanings in many cultural heritages through history, from ancient Greece mythology to Christianity.

This material possesses also important practical applications, thanks to its piezoelectric properties, originated by its crystal structure and used in oscillators and electronic components, and thanks to its luminescence properties (Preusser et al., 2009). These last ones will be the main focus of this thesis work and they are induced in the material by impurities and intrinsic defects in the crystal structure. Impurities are present in the material either as substitutional ones, such as aluminium or germanium, or interstitial ones, such as small alkali ions, due to the large channels along the c-axis originated by the crystal structure of α-quartz, the stable phase at room temperature (Preusser et al., 2009). Both impurities and intrinsic defects, introduce charge trapping and luminescent recombination properties in the material. Luminescent properties make the material useful also for many practical areas of expertise such us dosimetry. Luminescence in quartz is mainly the result of the interaction of the material with ionizing radiation, such as X-rays, beta-rays, gamma-rays etc. The emissions can be observed through radioluminescence (RL), optically stimulated luminescence (OSL) and thermoluminescence (TL, reported also as thermally stimulated luminescence, TSL), which all rely on the aforementioned defect induced properties, and these properties can be used in dosimetry applications. A few examples of them can be the estimation of the age of ceramics which contain quartz (archaeology), the quantification of the radiation impact after a nuclear accident (accident dosimetry) or the estimation of the age of different sediment strata (geology) (Preusser et al., 2009). The interaction with these kinds of radiation (and others such as neutrons, alpha radiation and energetic ions) has also a heavy impact on the piezoelectric properties, which can be crucial in space applications due to the use of quartz in high-frequency clocks (Bloch et al., 2009).

Quartz also modifies its paramagnetic properties after such kind of irradiation. Even though silicon dioxide is a diamagnetic material by itself, apart from some paramagnetic impurities possibly created in the crystal growth, charge carriers from excitons induced by high energy irradiation may be trapped in impurities and/or in lattice sites, creating paramagnetic centres with a certain thermal stability. The more stable ones can be used in dosimetry through electron paramagnetic resonance (EPR, known also as electron spin resonance, ESR; Abragam and Bleany, 2012).

Even if all these properties have been known and used for many decades, a proper model to describe the luminescence processes in a precise way is still missing. The identity of the centres responsible for these properties is still under debate, and their applications still follow empirical protocols, leading

to a large error in the results obtained due to the huge variance from sample to sample in impurity content and thermal history. Luminescent properties alone are only useful to carry out phenomenological studies, by observing possible correlations between impurity content and emission intensity, which is not enough to obtain strong proofs to assign a certain emission the certain trap and recombination centres. The EPR technique can offer a more direct insight into the correlation between luminescent properties and paramagnetic centres, including structural information on the observed defects. Despite the value brought by EPR, its sensitivity is still rather low when compared with luminescent techniques, therefore, a lot of efforts are still going on in the scientific community to try to understand the luminescent and paramagnetic properties of quartz exposed to ionizing irradiation. Moreover, the response of the material to stimuli is not straightforward, leading to a complex behaviour. In fact, the emission intensity can differ by many orders of magnitude from sample to sample, due to different impurity content, and even from different regions of the same bulk crystal due to the low homogeneity of the impurity distribution in quartz. Furthermore, the luminescent properties of quartz do not behave as one would expect from scintillators (RL) or common dosimeters (TSL). The response to the received dose in many cases is not linear, and it strongly depends on the thermal history of the sample (Martini and Fasoli, 2012). An example of these properties would be the so-called "pre-dose effect" (Zimmermann, 1970), which consists of a change of the emission intensity of the material as a response to subsequent irradiations and annealing. This is not necessarily a downside on the applications of this material, as one can also take advantage of this property that can be exploited for using it for dosimetric purposes (Bailiff, 1991, Itoh, 2000). In fact, even luminescence centres unstable at room temperature, such as the so-called 110 °C TL peak of quartz, is worth to be studied.

Aim of this thesis work is to try to understand, from the fundamental point of view, some of the luminescent and paramagnetic properties of quartz and their relationships to point defects. TSL, RL and EPR measurement have been performed in order to try to correlate the data obtained by each technique to each other and to understand the charge transfer mechanisms responsible for the luminescence properties.

This thesis work will be outlined as follows:

- An overview on the crystal structure of quartz, the growth processes to obtain such material and the possible point defects it can contain (Chapter 2)
- A description of the principles of the measurement techniques that have been used in this thesis work, including brief recaps of past works that set the groundwork for the presented studies (Chapter 3), and the instrumentation used (Chapter 4)
- A study that, while confirming conclusions from previous works about the identity of an electron trap being a germanium related centre, brings the attention to an anomaly observed in the thermal stability of such trap level in some samples (Chapter 5)

- A study that shows the correlation between the bleaching properties of two different signals, one observed with TSL experiments and the other with EPR experiments, which allows to identify the point defect responsible for the observed phenomena as another germanium related centre (Chapter 6)
- A study about the emission wavelengths observed during TSL experiments and how each wavelength is correlated to different TSL peaks, giving some insight on the charge transfer mechanisms that produce the emission (Chapter 7)
- A study about the RL properties of different kinds of quartz samples (Chapter 8)
- A study on the EPR properties of germanium related centres and their thermal stability which also brought to light the existence of previously unreported signals (Chapter 9)
- A study on the EPR properties of titanium and aluminium related centres, their thermal stability and their possible relation to TSL properties (Chapter 10)
- Final comments to overview the work presented in this thesis and possible future studies that can be done to continue this field of research (Chapter 11)
- A list of the scientific publications that inspired the presented works and the papers that have been produced by them (Chapter 12)
- An appendix with further details on experimental conditions (Appendix)

2. Quartz structural properties and crystal preparation

2.1 Quartz crystal structure

Crystalline silicon dioxide, possess many polymorphs, such as alpha quartz, beta quartz, cristobalite, etc. The more common form, due to the large stability at room temperature and at 1 atm, is alpha quartz. Without applied pressure, heating the material brings a phase transition to beta quartz at around 573 °C, a second one towards beta tridymite at around 870 °C, a third one at around 1450 °C towards cristobalite and finally the liquid form at around 1700 °C. In Fig. 2.1 is reported the phase transition diagram of crystalline SiO_2, showing also the pressure dependencies of the phases' stability (Huntley and Krueger, 2015). The temperature of most common luminescent experiments on quartz generally does not exceed 500 °C, so the material will not experience any phase transition during the experiment itself. Because of this, the focus of this section will be on this more stable form. However, it should be noted that in some of the presented experiments, quartz samples are submitted to heating treatments at temperatures up to 1000°C. This indeed leads to two different phase transitions during the annealing, but without particular cooling conditions afterwards (e.g. to speed up the cooling rate), the crystal will revert to the more stable alpha quartz structure.

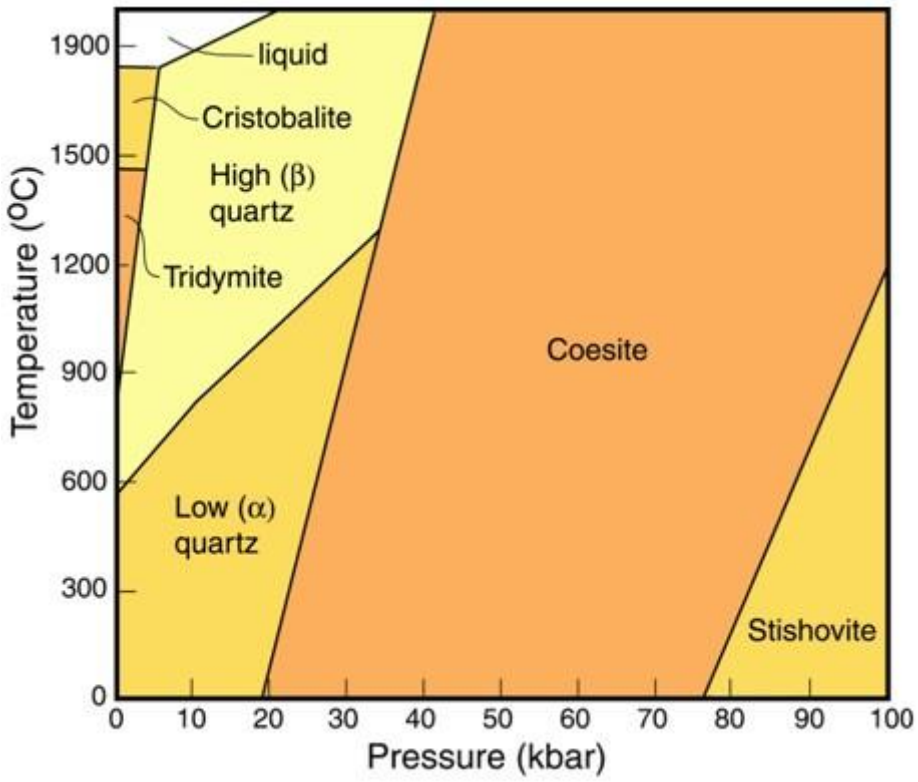

***Fig. 2.1**: Phase diagram of crystalline SiO_2 (Huntley and Krueger, 2015).*

Alpha quartz possesses a trigonal symmetry, with space group $P3_221$. As any other silicon dioxide polymorph, each silicon is surrounded by four oxygens in a tetrahedral arrangement, where a Si atom, in the centre, is surrounded by four O atoms at the tetrahedron's corners. In Fig. 2.2 is reported a scheme of alpha quartz's lattice, projected along the c-axis. It can be seen how such atom arrangement creates channels along this direction, with the neighbouring silicon atoms forming a hexagon when

projected on a plane, large enough to host interstitial impurities such as alkali ions. The mobility of such ions along these channels play an important role in luminescent properties of quartz, as it will be discussed in the next sections, but it also responsible, paired with the crystal structure's anisotropy, for the piezoelectric properties of quartz (Preusser et al., 2009).

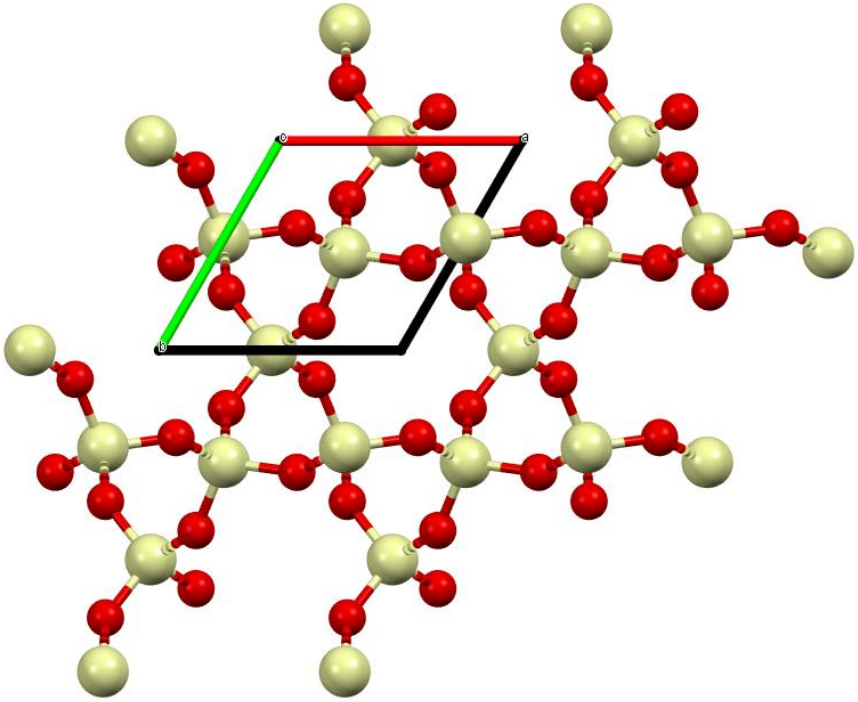

***Fig. 2.2**: Quartz crystal structure projected along the c-axis. Oxygen atoms in red and silicon atoms in white. Note the hexagonal-shaped channels created by the silicon atoms. Image generated with Mercury 2020.2.0.*

2.2 Growth processes

The most common process that produce crystalline quartz is the hydrothermal growth process. This is true for both natural and synthetic quartz. The process consists in silica precursors, orthosilic acid, H_4SiO_4, dissolved in an aqueous solution, being brought at high temperature, usually between 100 °C and 450 °C, and high pressure (around 1000 bar) until they reach the supercritical fluid phase. Then, by accordingly lowering temperature and pressure, the precursors start to deposit and grow as a single crystal on a surface with the following chemical reaction:

$$[Si_nO_m]\text{-}OH + H_4SiO_4 \rightarrow [Si_{n+1}O_{m+2}]\text{-}OH + 2\ H_2O$$

For synthetic quartz, this is done in an autoclave, where some crystalline seeds of known orientation are used to guide the crystal growth. To enhance the solubility of silica precursors, a mineralizer is usually added to the solution: NaOH, Na_2CO_3, KOH or NaF are commonly used as mineralizers (Hosaka and Taki, 1981). In natural conditions, the precursors are dissolved from the surrounding rocks.

Natural quartz is also found as a product of an igneous rock formation, such as pegmatite. These crystals are originated from molten rock, which is a mixture of metal cations, such as K^+ and Mg^{2+}, and anion complexes, such as PO_4^{3-} and of course SiO_4^{4-}. SiO_4^{4-} are usually present in the form of

long branched chains of linked SiO_4 tetrahedra, which are also responsible for the viscosity of the melt. When the molten rock is erupted, it will rapidly cool down to the environment temperature, forming volcanic glass. If the melt stays instead in the Earth's crust, it is possible that it will cool down very slowly, allowing the crystallization of many minerals, depending on the melt composition, including quartz. For this reason, the crystals formed this way are usually polycrystalline, sometimes with an onion-like structure representing different layers of a crystallization occurred in many steps, and richer in impurities from the surrounding growth environment when compared to hydrothermal grown crystals (Akhavan, 2005).

2.3 Point defects in quartz

Quartz crystal growth will always come with defects in the lattice. Some of them are originated from a thermodynamic equilibrium, such as intrinsic vacancies, dislocations and grain boundaries, while others depend on the growth conditions, such as impurities. A few examples are reported in Fig. 2.3 (Götze et al. 2001), and some of them will be described in the following subsections.

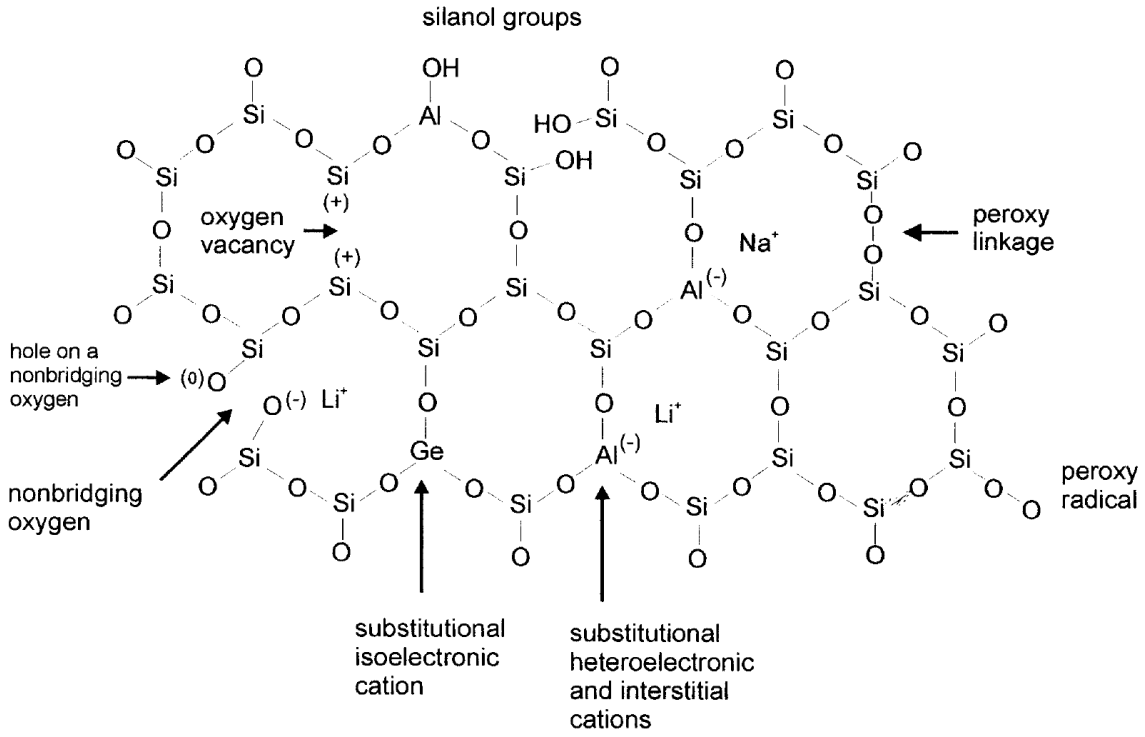

***Fig. 2.3**: Schematic quartz structure showing the most common intrinsic and extrinsic lattice defects (Götze et al., 2001).*

2.3.1 Intrinsic point defects

Both oxygen and silicon vacancies are possible in quartz crystals, although oxygen ones are usually more abundant.

Oxygen vacancies usually result in a Si-Si bond (Feigl et al., 1974), known as "neutral oxygen vacancy", a defect that can also be created with ionizing irradiation. Holes can be trapped at oxygen vacancies, creating a paramagnetic family of defects known as E'. When the hole is trapped at a neutral oxygen vacancy, as a result there will be an unpaired electron on a silicon atom, forming the

E'_1 defect. If there is the presence of hydrogen nearby, E'_2 and E'_4 will be formed. In the occurrence of two different unpaired electrons are present, E'' centres will be produced, where the double prime symbol indicates the number of unpaired electrons. In Fig. 2.4 is reported a graphical representation of E' defects (Rudra et al., 1985).

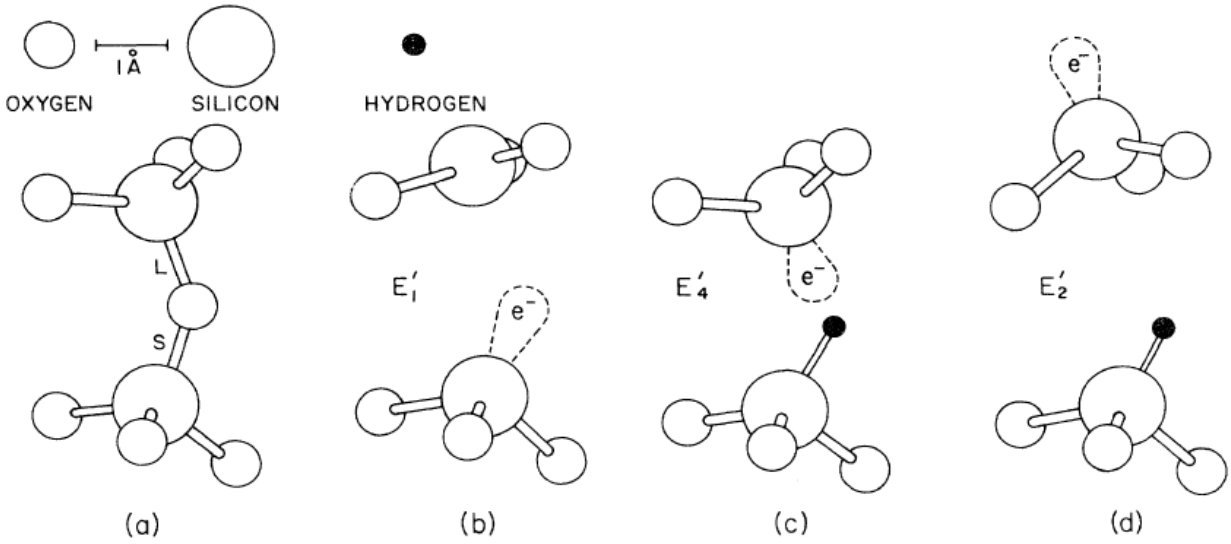

Fig. 2.4*: (a) Fragment of perfect alpha quartz; "L" stands for long bond (1.6122 Å at 298 K) and "S" for short bond (1.6071 Å at 298 K); (b) Model for the E'_1 center; (c) Model for the E'_4 center; (d) Model for the E'_2 center. In (b)-(d), the unpaired electron is shown schematically as e^-. Rudra et al., 1985.*

In the crystal, there may also be an excess abundance in oxygen atoms. This abundance creates a large number of known defects in amorphous silica, but in quartz only two of them have been observed so far. One of them is the Non-Bridging Oxygen Hole Centre (NBOHC, Skuja et al., 2020), which consists in an oxygen atom with an unpaired electron on a dangling bond. The other is the Peroxy Radical (POR, Skuja, 2000), which consists in an oxygen-oxygen bond with a single unpaired electron shared by the two atoms, therefor paramagnetic. These defects are represented in Fig. 2.3.

Silicon vacancies would create dangling bonds from the four oxygen atoms at the tetrahedron corners, which are usually compensated by hydrogen, creating OH terminals. These are usually referred to as $[H_4O_4]^0$, which can act as hole traps after irradiation, by expelling an H atom and becoming $[H_3O_4]^0$. A schematic showing the structure and formation mechanism of such defects is reported in Fig. 2.5, where the authors referred to the precursor $[H_4O_4]^+$ and $[H_3O_4]^0$ as species I and II respectively (Nuttal and Weil, 1980).

2.3.2 Extrinsic point defects (Impurities)

During the growth process, both in natural and synthetic growth, quartz crystals will incorporate impurities in their lattice. They can either be substitutional centres or interstitial centres. A few of them are represented in Fig. 2.3.

Substitutional centres can be found in silicon lattice sites, and some examples of the more common

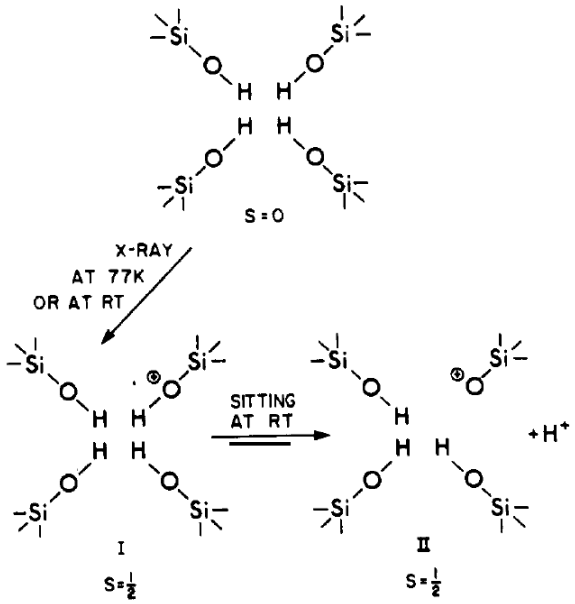

***Fig. 2.5**: Proposed structure and formation mechanism for hydrogenic trapped-hole species I and II (Nuttal and Weil, 1980).*

ones can be germanium, titanium, aluminium, phosphorus and iron, all of them substituting Si ions. Germanium and titanium impurities (Ge^{4+} and Ti^{4+}) are isoelectronic with silicon atoms in the lattice (Si^{4+}). Germanium can act as electron trap, creating paramagnetic $[GeO_4]^-$ centres, which, being no longer locally neutral, can be compensated by alkali ions such as Li^+ and Na^+, creating different $[GeO_4/M^+]^0$ centres (Weil, 1984, Lutoev, 2006). $[GeO_4/H^+]^0$ centres, if they exist, have not been observed yet. Titanium, like germanium, can act as electron trap, forming $[TiO_4]^-$, which can be compensated by alkali ions to give $[TiO_4/M^+]^0$ centres but also by hydrogen, giving $[TiO_4/H^+]^0$ centres (Marfunin, 1979, Weil, 1984).

Aluminium on the other hand, is a trivalent ion (Al^{3+}), bringing a charge imbalance in the lattice. This imbalance is usually compensated by monovalent cations, which can be small alkali ions or hydrogen, but it is possible that other cations such as Ag^+ or Cu^+ can act as compensators although less frequently. Aluminium will then form $[AlO_4/M^+]^0$ or $[AlO_4/H^+]^0$ complexes. Irradiation can push away the compensating cations, transforming the aluminium centre in the paramagnetic hole trap $[AlO_4]^0$ (Malik et al., 1981).

In fact, usually such interstitial impurities that act as charge balancers are located in the hexagonal channels mentioned in section 2.1. Along these channels, such small ions possess a high mobility that can allow them to migrate along the c-axis direction providing energy to the system with irradiation, given the temperature is high enough. Alkali ions can also act as compensators for trapped electrons at silicon sites, which can be observed at low temperatures, like $[SiO_4/M^+]^0$ (Halperin, 1990, Halperin and Sucov, 1993). Hydrogen, as already mentioned while discussing the other defects, plays an important role as compensator for non-isoelectronic impurities and centres with trapped electrons. OH bonds can be studied with infrared absorption experiments (Kats, 1962), showing that they can

also be present in more complex configurations than the ones here discussed (e.g. $GeHLi_2$, Weil, 1971).

2.4 Sweeping process

Part of the quartz samples presented in this thesis work, has been subject to a so called “sweeping process”. This electro-diffusion process consists in a selective ion exchange in the crystal lattice. This is achieved at high temperature (> 500°C) with the application of an electric field along the c-axis. As mentioned in section 2.1, in this direction of the quartz’s crystal lattice, there are hexagonal shaped channels, along which small ions, such as alkali ions, can migrate. By sweeping a crystal, the alkali ions are pulled towards the negative electrode, while they are replaced by other ions pushed from the positive electrode, usually hydrogen from air. Commercially, this technique is used for two main purposes. The first one is to increase the radiation hardness of the crystal, which is crucial for aerospace and defence applications. The second one is to reduce the impurities in the dislocation networks and by consequence to reduce the production of etch channels, which impact the production of quartz devices by deep-etch processing. An extensive review on the procedure of quartz sweeping can be found in Martin (1988). Generally, this electro-diffusion procedure is named “sweeping-out”, because the alkali ions are partly eliminated out of the crystal. On the opposite, “sweeping-in” consists in increasing the concentration of alkali ions, by applying an electro-diffusion from an electrode made by an alkali salt.

3. Experimental techniques and groundwork

3. 1 Thermoluminescence

Irradiating an insulator material with ionizing radiation will generally create, after a cascade excitation process, multiple excitons, that will eventually recombine and possibly emit light if a radiative transition is involved. This process is referred to as radioluminescence (RL). The material though, may possess intragap levels that may trap free charge carriers from the conduction band (electron traps) or the valence band (hole traps), reducing the overall light emission of the material. These trap levels may have a certain stability, defined by their trap depth, i.e. the energy difference between the trap level and the conduction band in the case of electron traps and the valence band in the case of hole traps. If enough energy is provided, the trapped charge will be released. In the case such energy is provided by heat it will be the case of thermoluminescence (TL), referred to also as Thermally Stimulated Luminescence (TSL). The second definition is more precise, because it states explicitly that the light is not produced by the conversion into light of the thermal energy, but the first one has become more popular in scientific literature. For completeness of information, if the energy that releases the charge from the trap levels comes from light, the process is known as Optically Stimulated Luminescence (OSL), referred also as Photostimulated Luminescence (PSL), with the first definition being the most widely used even if the second one is the more precise one.

3.1.1 Models of Thermoluminescence

The main theory that describes the TSL mechanism, starts from considering the charge carrier traffic in the conduction and valence bands. Once trapped, an electron, or hole, has a certain probability of being released that depends on the temperature, which it can be assumed to be described by the Arrhenius law (Bos, 1994, Chen and McKeever, 1997):

[1] $$p = s\ exp\left\{-\frac{E_T}{k_B T}\right\}$$

Where p is the aforementioned probability of being released from the trap level, s is a phenomenological factor, called frequency factor, which represents how often a trapped charge is trying to leave the trap level, E_T is the trap depth, k_B is the Boltzmann constant and T the absolute temperature. If one then considers the rate at which each state changes its population (i.e. charge release and retrapping), and make some assumptions, he can obtain some analytical solutions to describe TSL. One of such assumptions is the so-called quasi equilibrium condition, which requires the concentration of free electrons in the conduction band to be quasi stationary (Chen and McKeever, 1997). A second one can be made to require for the retrapping rate to be negligible. By doing so, one would then obtain the Randall-Wilkins equation, which describes the first-order kinetics of TSL (Randall and Wilkins, 1945). Garlick and Gibson (1948), expanded lately the theory without the second assumption. The Randall-Wilkins equation describes how a so-called glow curve should look like, i.e. the plot of the emitted light intensity as a function of temperature, under the assumption that the released charge recombines without any retrapping. It is reported in eq. [2].

[2] $$I_{TL}(T) = n_0\, s \exp\left(-\frac{E_T}{k_B T}\right) \exp\left\{-\left(\frac{s}{\beta}\right) \int_{T_0}^{T} \exp\left(-\frac{E_T}{k_B \theta}\right) d\theta\right\}$$

Here, β represents a constant heating rate used for the TSL experiment and n_0 is the initial trapped charge population. This model, as already mentioned, is referred to as first order approximation.

If during the process a retrapping probability of the released charges is comparable to the recombination probability, the Garlick-Gibson model must be used, reported in eq. [3].

[3] $$I_{TL}(T) = \frac{{n_0}^2}{N}\, s \exp\left(-\frac{E_T}{k_B T}\right) \exp\left\{1 + \left(\frac{n_0 s}{\beta N}\right) \int_{T_0}^{T} \exp\left(-\frac{E_T}{k_B \theta}\right) d\theta\right\}^{-2}$$

Where N is the total number of both empty and filled trap levels. In this case, it can be seen that the glow curve's shape is much more dependent on the initial population because of the square of n factor, from which the name of second order approximation.

In the more general case, the actual kinetic order of the process will be a constant between 1 and 2, represented by a parameter *b* from the empiric equations of either May and Partrige (1964), eq. [4], or the one by Rasheede (1993), eq. [5].

[4] $$I_{TL}(T) = n_0\, s'' \exp\left(-\frac{E_T}{k_B T}\right) \left[1 + ((b-1)\frac{s''}{\beta} \int_{T_0}^{T} \exp\left(-\frac{E_T}{k_B \theta}\right) d\theta\right]^{-\frac{b}{b-1}}$$

With $s'' = s' n_0^{(b-1)}$.

[5] $$I_{TL}(T) = n_0^b s \exp\left(-\frac{E_T}{k_B T}\right) N^{(1-b)} \left[1 + \frac{s(b-1)\left(\frac{n_0}{N}\right)^{b-1}}{\beta}\right) \int_{T_0}^{T} \exp\left(-\frac{E_T}{k_B \theta}\right) d\theta\Bigg]^{-\frac{b}{b-1}}$$

Both expressions approximate the Randall-Wilkins model for b going to 1, but the first one gives a harder interpretation of the parameter s', whose dimension is dependent on the kinetic order of the process.

As a note, it is worth noting that the positions of the peaks in a glow curve strongly depend on the heating rate β and other experimental conditions, such as the thermal lag between temperature read by the sensor (usually a thermocouple positioned under the heating element) and the actual temperature reached by sample.

3.1.2 Glow Curve Analysis

One can obtain the parameters in these expressions by analysing their experimental data with a fitting program, usually using an approximated form of the Randall-Wilkins equation (Appendix, eq. [A1]). This calculation though is usually done using other methods to obtain them in a more direct way. One of such methods is the Initial Rise method, which can obtain the E_T value from the initial part of the TSL peak (Garlick and Gibson, 1948). In fact, by the approximation that all energy states' occupancy is constant in the initial growth of the peak, eq. [1] can be rewritten as:

[6] $$I_{TL}(T) = C \exp\left(-\frac{E_T}{k_B T}\right)$$

With C a constant that contains the dependence on other trap parameters. If one then plots the natural logarithm of the intensity against the inverse of the temperature, they will obtain a line described by:

[7] $$\ln(I_{TL}) = \ln(C) - \frac{E_T}{k_B T}$$

And so, E_T/k_B will be the slope of the line. This method is valid if one only works with the points of the peak below roughly the 10% of the maximum's intensity, where the approximation's error is negligible. Knowing the E_T value, one can obtain the value of s by either using E_T as a starting value for a fitting process or by further approximations of the Randall-Wilkins model, such as (Hoogenstraaten, 1958):

[8] $$s = \frac{\beta E_T}{k_B T_M^2} \exp(\frac{E_T}{k_B T_M})$$

Where T_M is the temperature of the maximum of the TSL peak. Other methods rely on multiple experiments, such as the Hoogenstraaten method (1958), which studies how the maximum of the peak shifts varying the heating rate of the glow curve's acquisition.

A review on many methods for TSL analysis can be found in McKeever (1985) and in Chen and McKeever (1997).

3.1.3 Thermoluminescence in Quartz

Thermoluminescent materials are used as dosimeters, i.e. as sensors capable to measure the amount of radiation absorbed in a certain span of time. The ionizing radiation's energy is stored in the material in the form of the trapped charge; by their release during a TSL experiment in the form of light one can calculate the amount of radiation to which the sensor was exposed. Such devices can be used to monitor the health safety of medical operators that work with X-ray machines or radiation sources and researchers that work with such radiations involved in their experiments.

Quartz is a singular case, because it is not used in such straightforward applications, but nonetheless it acts as a dosimeter. The main fields of research that take the most from this property are geology, archaeometry and accident dosimetry. The reason of such applications for quartz is due to the natural abundance of this material and because it can act as a natural dosimeter due to its trapping and luminescence properties. In fact, in the case of geology it can be used to estimate the geological age of sediments, which by being underground are not exposed to any consistent optical stimulation from the sun. The stored energy from natural radioactivity of the environment can be measured by TSL and OSL experiments. The same goes for archaeology, because all ceramics (bricks, pottery and such) usually contain a certain amount of crystalline SiO_2, which can be used to estimate the artefact's age. Of course, the material has being absorbing energy from natural radioactivity since its growth, but the production of pottery usually involves the exposure of the artefact to a source of heat, known as "firing", which depletes the trapped levels, "resetting" the quartz's age. Therefore, TSL experiments will evaluate the age since the firing of the studied object. Obviously, this is true assuming that the quartz is extracted from the inner layers of the object, which have not being exposed to natural light, that can detrap electrons in analogy with heat, often through complex processes that may also be multi-episodic or incomplete, and that the artefact itself has not being exposed to any consistent

source of heat after its production, e.g. a fire in the building where the object was stored. OSL principles are very similar, where electron detrapping is due to an intense light exposure and the emitted OSL is obviously optically stimulated, instead of by heat. Lastly, in the case of accident dosimetry quartz can be found in common objects in the accident area and from that extrapolate the absorbed dose following the same aforementioned principles.

Quartz also possesses certain properties that does not allow its use as a dosimeter in a straightforward way as other typical dosimeter materials (e.g. $LiCaAlF_6$, known as LiCAF, usually doped with Ce), which are the point of the still on-going research about it. For example, the emission intensity of quartz depends of both irradiation and thermal history. Under continuous irradiation, the RL sensitivity (the amount of light emitted per unit dose) increases as a function of the amount of cumulative absorbed radiation, especially for the typical blue emissions at around 470 nm Martini et al, 2012a). If the quartz sample is further fired at high temperature (>500 °C), its typical emission at 380 nm increases again as a function of the previously accumulated radiation. In the case of luminescence dosimetry, such changes can be tracked with control measurements on matched materials, while for dating applications the unknown dose must be estimated only after the first laboratory irradiation cycle. Such properties obviously bring some disadvantages that makes less clear how to interpret the data when compared to common dosimeters such as LiCAF, but they also bring some advantages in the dating analysis with procedures that can use unstable trap levels, at room temperature, by exploiting the so called Pre-dose Effect.

3.1.4 The pre-dose effect

The so-called 110 °C TSL (when a heating rate of 10°C/s is applied) peak of quartz is an unstable peak at room temperature, with an average lifetime of less than one hour (Vaccaro et al., 2017). Nonetheless, this peak has a certain importance in dosimetry and can be used for such estimations. This is thanks to the so-called pre-dose effect which affects this peak. This is the property of a TSL peak of being sensitized after irradiations followed by heating, leading to an enhanced intensity of the glow curve using the same TSL experimental conditions multiple times on the same sample.

The application of this property in dosimetry relies on the fact that the geological dose absorbed by the sample is proportional to the enhancements observed with the pre-dose effect. As an example, the experimental procedure proposed by Itoh et al. (2000) id trpotyrf, but also similar ones were proposed in literature (e.g. Bailiff, 1991):

1. Apply a test dose, τ, usually negligible when compared with the geological dose D
2. Heat the sample just above 110 °C at a heating rate around 10°C/s and record the TSL peak intensity as S_0
3. Heat to the activation temperature of the sample (usually between 400 °C and 650 °C)
4. Cool down to room temperature and apply again a test dose τ
5. Heat again to 110 °C and record the TSL intensity as S_n
6. Apply a laboratory dose L

7. Repeat step 3
8. Apply again τ and record S_{n+L} by heating to 110 °C

In this procedure, S_n-S_0 is proportional do D, S_{n+L} Is proportional to D+L and so S_{n+L}-S_n is proportional to L. Translating everything in an equation, and assuming there is not any nonlinearity to consider:

[9] $$D = L\frac{[S_n - S_0]]}{[S_{n+L} - S_n]}$$

With such method, one can use an unstable peak to obtain information on the geological dose absorbed by a sample in much longer periods of time.

On the mechanism that leads to the effect, the first model was proposed by Zimmerman (1971). The main hypothesis was that irradiation followed by heating lead to an activation of a greater number of luminescent centres, by having the trapped holes migrated from non-luminescent centres during the activation process. This would lead to the sensitivity enhancement of the TSL emission. Fig. 3.1 reports a scheme of the levels involved as conceived by Zimmerman.

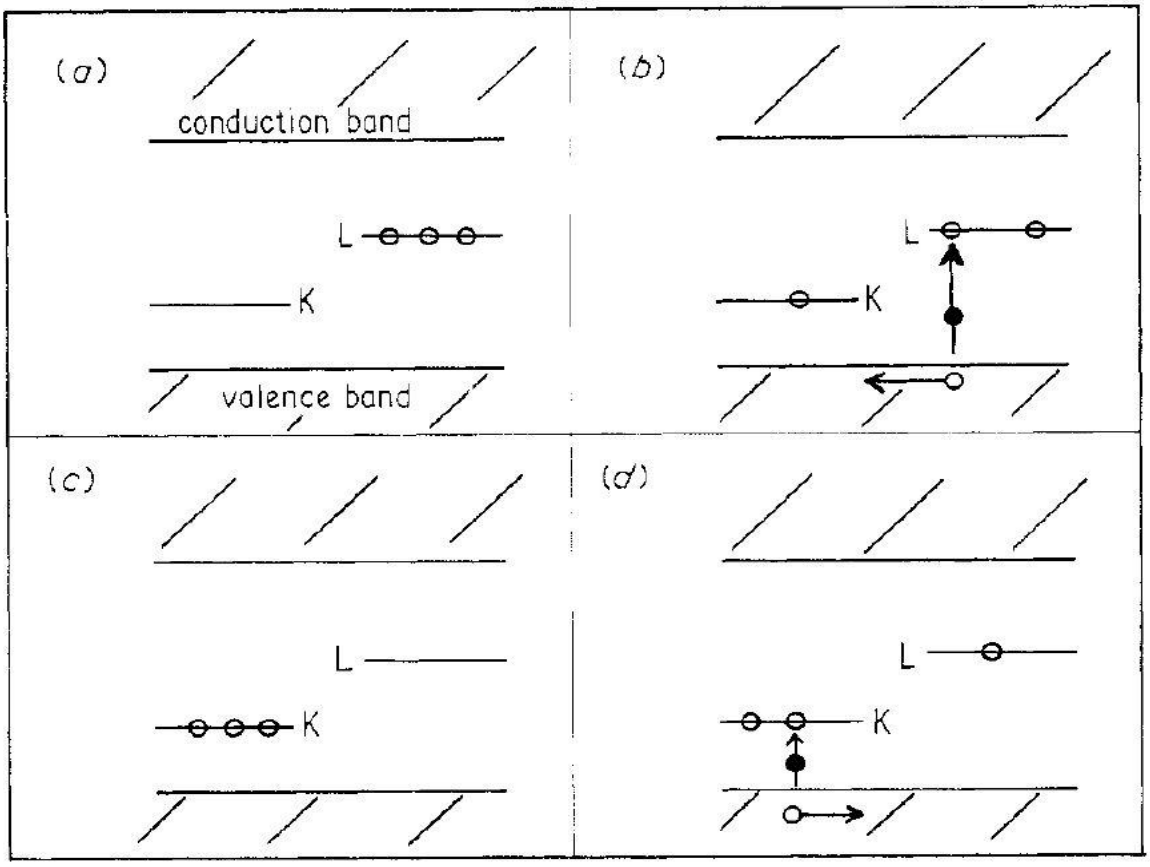

Fig. 3.1: Scheme levels and mechanism to describe pre-dose effect in quartz. Open circles represent holes and closed ones electrons. (a) Initial level population before irradiation at luminescent centres (L) and non-luminescent ones (K). (b) UV Irradiation produces electron and holes that occupy L and K levels, reducing the luminescent sensitivity. (c) Level population after UV irradiation. (d) The firing process moves holes from the K levels to the valence band which then populate L again, enhanching the sensitivity when compared to stage (c).

3.2 Electron Paramagnetic Resonance

Electron Paramagnetic Resonance (EPR), known also as Electron Spin Resonance (ESR), is a spectroscopic technique which studies the electronic transitions between spin states whose degeneracy have been broken by a magnetic field (Zeeman Effect). To do so, the system is required to have a net electron spin angular momentum.

Therefore, this technique is used to study paramagnetic molecules such as organic radicals and paramagnetic metal complexes, obtaining information concerning chemical reaction mechanisms and electronic structure of chemical substances. It is widely used in the fields of biology, chemistry and physics. Of course, this technique can be used also to study paramagnetic centres in the solid state, such in the case of quartz.

The Zeeman effect is originated by the interaction of an electron magnetic moment μ_Z immersed in a magnetic field B with an oscillating field B_1. Such magnetic moment can be expressed in the form of:

[10] $$\mu_Z = \gamma m_l \hbar$$

With the spin component being:

[11] $$\mu_Z = \gamma m_S \hbar$$

Where γ is the electron's gyromagnetic ratio and m_S is the electron spin angular moment. This can also be written as:

[12] $$\mu_Z = -g\beta m_S$$

With the negative sign arising from the negative charge of the electron and beta being the Bohr magneton and g being the so-called "g-factor", which is equal to 2.0023 for a free electron. The quantization of the energy states $E=-\mu_Z B$ then is:

[13] $$E = -g\beta m_S B$$

And therefore the difference in energy between the two possible states, being m_S equal to $\pm\frac{1}{2}$, and resonance condition with an oscillating field, is equal to:

[14] $$\Delta E = g\beta B$$

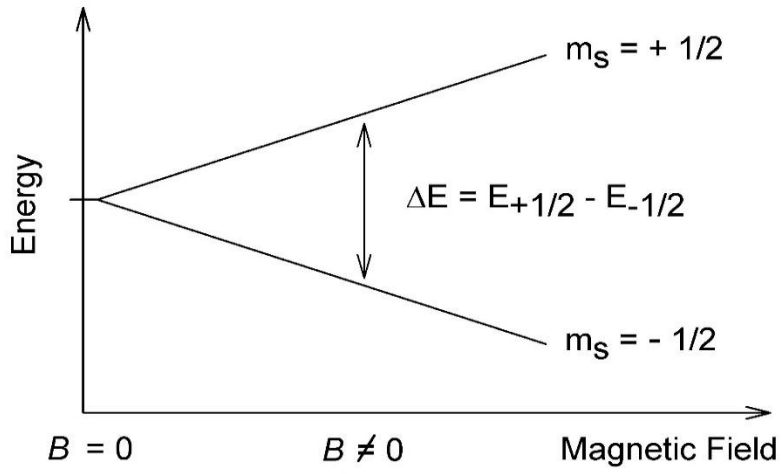

***Fig. 3.2**: Zeeman energy splitting as a function of magnetic field*

An interaction with the nuclear magnetic moment is also present, but so far it will be considered to be negligible. It can be seen from this expression that the transition energy scales with the magnetic field B, as it is schematically shown in Fig. 3.2. Therefore, EPR experiments differ from most spectroscopic techniques by studying the response as a function of the magnetic field instead of the frequency. This approach gives some advantages, because by keeping the frequency of the oscillating field constant, one can build a resonance chamber to enhance the sensitivity of the spectrometer. Additionally, usually the spectra are reported as the first derivative of the absorption spectrum, giving this the advantage of being able to easily detect minor variations on the absorption spectrum itself.
In Fig. 3.3 it is reported how the EPR spectrum of a free electron would look like, reported as first derivative.

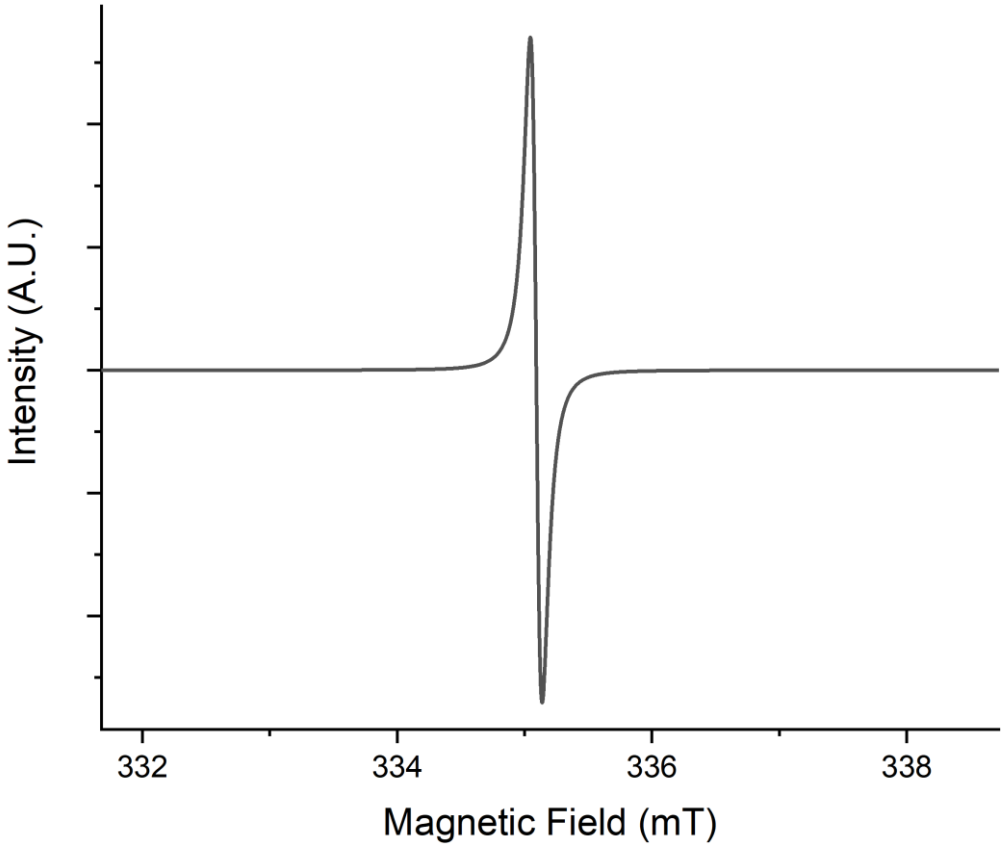

Fig. 3.3*: Free electron EPR spectrum (simulated).*

An important perturbation the unpaired electron can experience is the hyperfine interaction with the magnetic angular moment of nearby nuclei associated with their spin. A nucleus has a magnetic moment μ_N equal to:

[15] $$\mu_N = g_N \beta_N M_i$$

With β_N being the nuclear magneton and M_i the nuclear spin angular moment, whose value depends on the nature of the nucleus (e.g. $\pm\frac{1}{2}$ for a hydrogen nucleus). Therefore, the resonance condition will have a different value from the free electron one. Without going deep into the mathematical calculations, the new condition for an electron perturbed by a nearby atom of hydrogen will be:

[16] $$\Delta E = g\beta B \pm \frac{1}{2} A_0 h$$

Where A_0 is a parameter expressed in Hz called coupling constant. In this case, a nucleus with a magnetic angular moment of $\frac{1}{2}$ will split the EPR line into two different lines, as shown in Fig. 3.3. Generally, the number of lines one can expect from the hyperfine interaction is equal to:

[17] $$\prod_i (2n_i I_i + 1)^{n_i}$$

Where n_i is the number of nuclei with magnetic moment I_i.

In Fig. 3.4 it is shown an example of hyperfine interaction with a single Li nucleus ($I_N = \frac{3}{2}$).

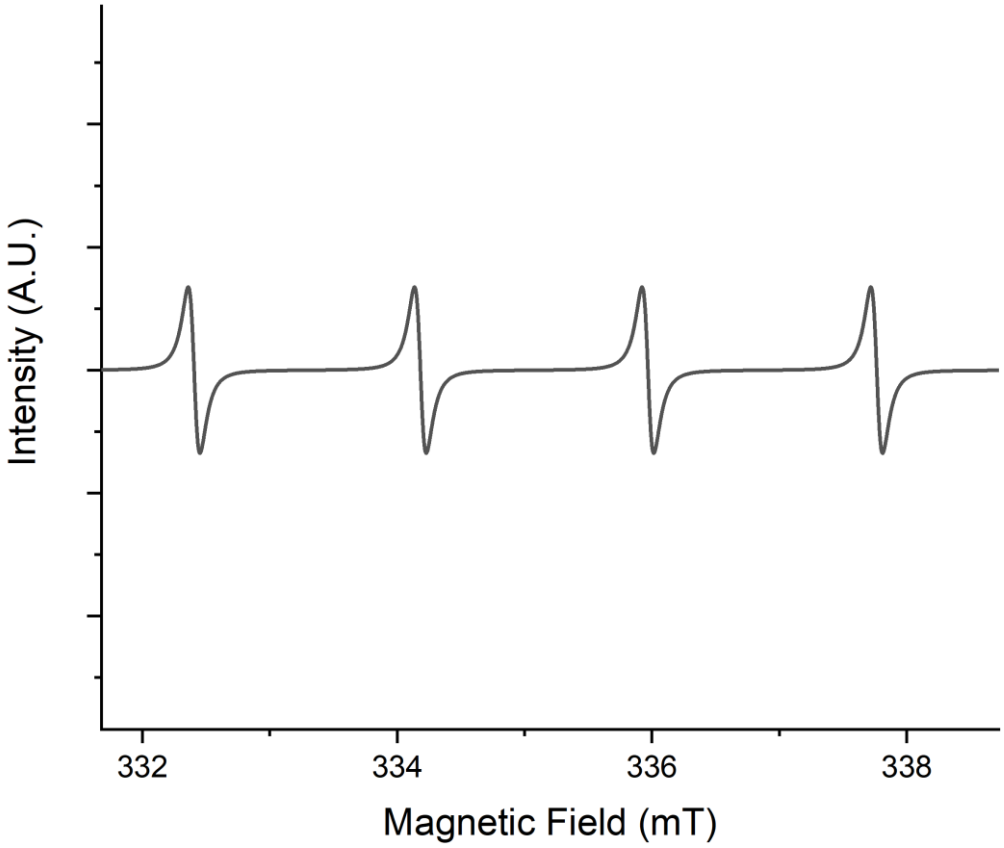

***Fig. 3.4**: Free electron hyperfine interaction with a Li nucleus.*

In a more complex environment, the electron g-factor suffers perturbation from the value of 2.0023, introducing the need of interpreting it as a three-dimensional tensor. An example of this is an unpaired electron in a crystal lattice, which is also the case of interest when studying quartz. In such case, the symmetry of the crystal, i.e. the crystal field, is what most influences the g-factor tensor values, which usually can be approximated as a diagonal matrix with g_x, g_y and g_z values, such as in the case of an orthorhombic symmetry. An example of electron in an orthorhombic environment is reported in Fig. 3.5. As it can be seen, a single electron does not give a single line in the spectrum anymore, but there is a more complex figure even without taking into account hyperfine interaction.

3.3 Germanium Centres in Quartz

Germanium is one of the ubiquitous impurities in crystalline SiO_2, acting as a substitutional defect in the Si lattice sites. Its presence in the lattice brings some distortions that can act as electron traps, which can be more or less stable above room temperature, depending on the surrounding of the

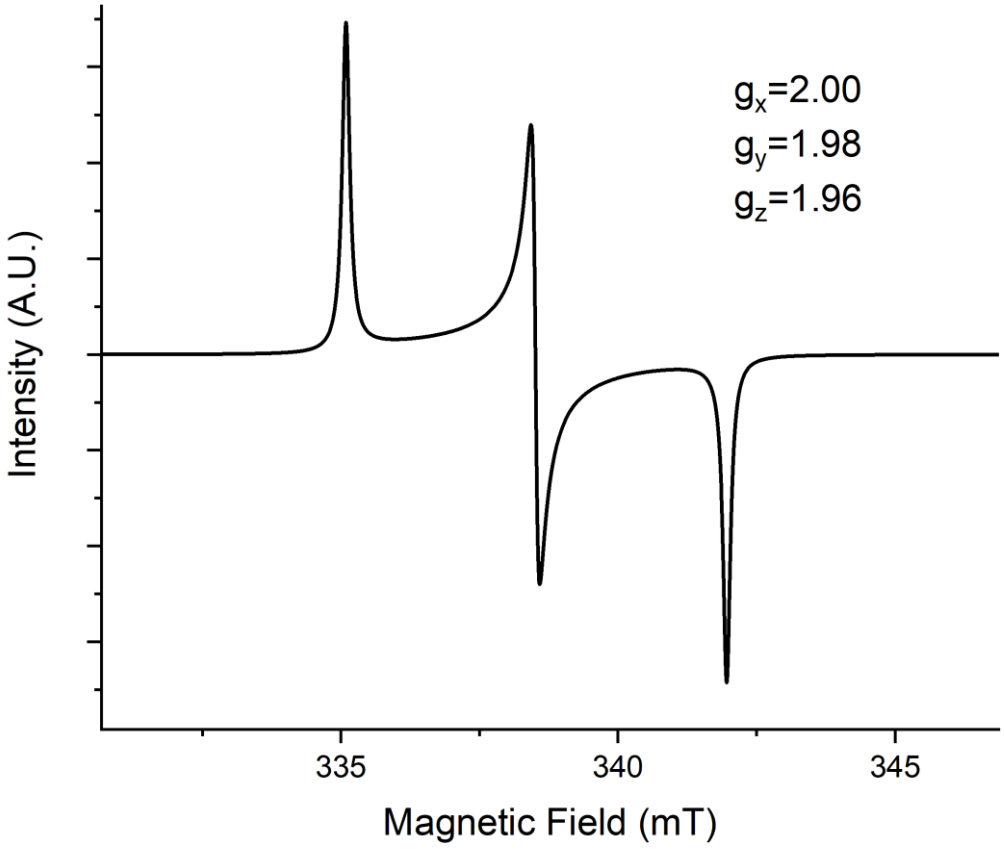

***Fig. 3.5**: EPR spectrum (simulated) of a free electron in an orthorhombic environment.*

defect. EPR has been a key technique in the study of such defects in their paramagnetic form, such as $[GeO_4]^-$ and $[GeO_4/M^+]^0$ (Mackey, 1963, Isoya et al., 1978, Lutoev, 2008). The presence of interstitial monovalent ions enhances the thermal stability of the trapped charge, by local charge compensation in the lattice, making the latter type of centre much more stable than the former. Similar defects are also created around silicon sites, but they are not stable above room temperature and in fact are usually observed at around 10 K, with previous irradiation at around 77 K (Bailey and Weil, 1991).

Thermal stability studies on the germanium family of defects led to the first hypothesis of relation with TSL electron traps, made by McKeever et al. (1985). In that study, the author observed the change of the EPR signal intensity as a function of the annealing temperature, observing that $[GeO_4]^-$ centres decayed at around 100 °C, thus supporting the hypothesis that it could be the same centre responsible for the so-called 110 °C TSL peak of quartz. In the same work, he also reported an increase of $[GeO_4/Li^+]^0$ centres as the formers decreased, accompanied also by an increase of $[AlO_4]^-$ centres and a decrease of $[AlO_4/Li^+]^0$ centres. While there is not a one-to-one correlation, these patterns suggested a migration of lithium between germanium and aluminium centres. This correlation suggests that they are the complimentary centres needed to obtain TSL emissions, the germanium centres acting as electron traps and the aluminium ones as hole traps and recombination centres. The author then proposed a tentative emission model, suggesting that electrons released by $[GeO_4]^-$ recombine with aluminium centres giving an emission at 470 nm and with an unknown centre to give an emission at 380 nm.

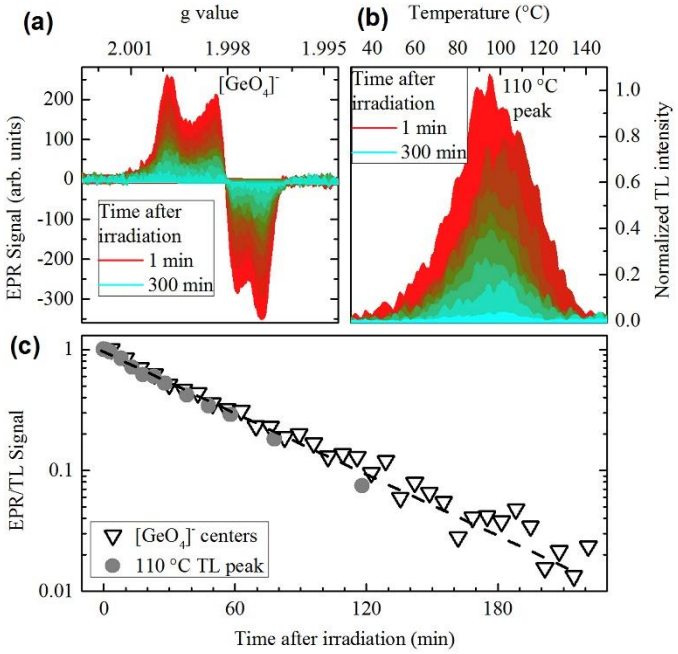

***Fig. 3.6**: (a) Time evolution at room temperature of EPR spectra of $[GeO_4]^-$ centers after irradiation. The minor and stable contribution of $[GeO_4/M^+]^0$ spectrum, observable after 4 h since irradiation, was numerically subtracted from all the EPR spectra so that only the $[GeO_4]^-$ contribution would remain. (b) Time evolution at room temperature of the 110 °C TL peak after irradiation. (c) Comparison of isothermal decay curves at room temperature of $[GeO_4]^-$ center EPR signal and the 110 °C TL peak signal obtained by Fig. 2(a) and (b) [see original publication]. The black dashed-line is the mono-exponential fit curve. The lifetime parameter extracted is 50.4 ± 0.9 min. (Vaccaro et al., 2017)*

Later studies suggested that the unknown emission centres should be originated by a silicon vacancy (Yang and McKeever, 1990), which gives OH groups facing each other, usually reported with the $[H_4O_4]$ notation. When such complex captures a hole, a hydrogen ion is released and thus the complex becomes a $[H_3O_4]$ centre. Later studies (Martini et al., 1995) suggested that the aluminium centre is responsible for the UV emission at 380 nm, and not the one in the blue at 470 nm, but the discussion about this topic is still open.

Giving McKeever work just some tentative models, the idea remained further unexplored until the work by Vaccaro et al. (2017), where more solid proof for such model has been searched. In that work, the authors managed to clearly identify the $[GeO_4]^-$ as the electron trap responsible of the so-called 110 °C TSL peak of quartz. This was done by monitoring the thermal decay of both TSL and EPR signals at a set temperature, comparing the signal intensity as a function of time. In Fig. 3.6 is reported what they observed at room temperature. The experiment was then repeated at different temperatures, calculating the decay time at each measured temperature. This permitted to build curves of the decay time as a function of the reciprocal of the temperature, obtaining a monotone trend which coincided for both signals, TSL and EPR, as reported in Fig. 3.7. This provided a starting point for further analysis that has been explored in this thesis work.

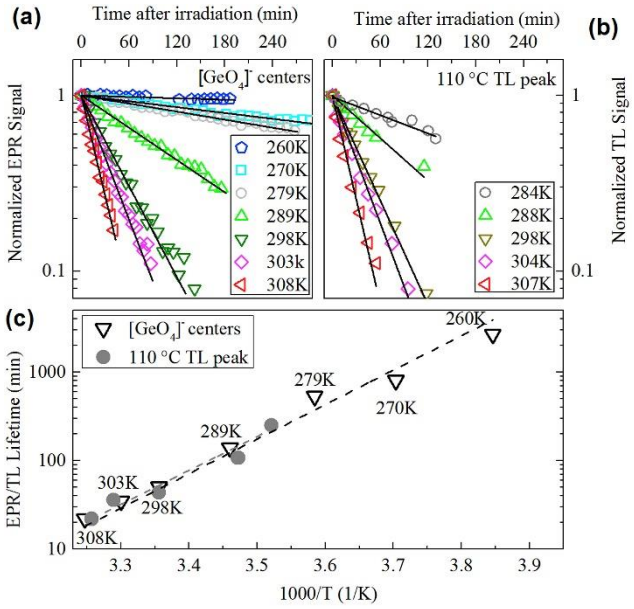

Fig. 3.7*: (a) Isothermal decay curves of $[GeO_4]^-$ center and b) 110 °C TL peak acquired at different temperatures. Black lines indicate the mono-exponential fits. (c) Lifetimes, evaluated from data shown in (a) and (b), plotted as a function of reciprocal temperature. To simplify the interpretation, the temperature in K for the EPR measurements are also reported. Black and grey dashed lines are the fits carried out on $[GeO_4]^-$ center EPR signal and 110 °C TL peak data, respectively, discussed in the text. (Vaccaro et al., 2017)*

4. Experimental setup

The measurements reported in this thesis have been carried out with different instrumentations, depending on the scope of them. Unless stated otherwise, the instrumentation here described is located in the Department of Material Science of the University of Milano-Bicocca.

4.1 Thermoluminescence equipment

Most of the TSL experiments have been run with a Risø TL-OSL DA-20, a commercial TSL reader produced by the Risø laboratory, in Denmark. It is provided with an in-built β-ray source of Sr^{90}-Y^{90} (1.48 GBq, dose rate 0.11 Gy/s on quartz grains between 100 μm and 200 μm, calibrated with coarse-grain quartz provided by the Technical University of Denmark in Risø, batch 91 (Hansen et al., 2015)) permitting sample irradiation just before the TSL measurement. The light sensor is a UV/blue sensitive photomultiplier tube (PMT) Electron Tube PDM 9107-CP-TTL (160-630 nm). It has a rotating wheel which can hold up to 48 samples, allowing to measure multiple samples one after the other, optimizing experimental times. It does not work under vacuum, but under a N_2 flux to avoid oxidation of the heating element at the higher temperatures and to reduce possible spurious TSL. It can also be used for OSL measurements, using blue LEDs as light source. Three optical filters were provided with it (Hoya U-340, Schott BG-39 and Corning 7-59; the absorption spectrum of the Hoya U-340 filter is reported in Appendix), but special parts were homemade to allow fitting also other kinds of filters such us interference ones. The samples, in grain form, were glued on stainless steel plates with silicon oil.

4.2 Wavelength Resolved Thermoluminescence equipment

A special homemade apparatus was used for wavelength resolved TSL (WR-TSL) measurements (Fasoli and Martini, 2016). The light sensor is a charged coupled device (CCD) Horiba Symphony, which which in combination with a diffraction monochromator permits measurements of the intensity of the TSL emission not only as a function of temperature but also as a function of wavelength in real time. The sample is heated by a copper element, under which there is a thermocouple that monitors the temperature. To avoid oxidations at the higher temperatures, the sample holder is set in a vacuum chamber linked to a rotary pump. After low vacuum (about10^{-2} atm) is created, the chamber is filled with N_2 up to roughly 0.5 atm to permit better heat transfer from the heating element to the sample and to keep the chamber sealed by suction. The light is collected by an optical system, which terminates on a Horiba-Jobin Yvon MicroHR monochromator featuring a diffractor grating. After diffraction, the light is finally collected by the CCD. Depending on the resolution needed and the intensity available from the sample, it is possible to use two different diffraction gratings, consisting of either 150 lines/mm or 600 lines/mm. The dispersion of the emitted light implies an obvious reduction of the signal-to-noise ratio, so that the sensitivity of this apparatus in lower than the one of conventional TSL instrumentation using PMTs. The samples, in grain form, were stuck to stainless steel plates with silicon oil and irradiated with the same β-ray source of the Risø TL-OSL DA-20.

4.3 Radioluminescence equipment

An equipment similar to the one used for WR-TSL was used to obtain RL spectra (Martini et al., 2012a and 2012b). The sensor is a CCD Jobin-Yvon Spectrum One 3000, coupled to a Jobin-Yvon Triax 180 spectrograph operating in the 200-1100 nm range. A Philipps 2274 X-ray tube with tungsten target is connected through a beryllium window to the chamber were the sample is placed at around 10 cm distance from it, allowing for irradiation of the sample during acquisition (dose rate adjustable from about 4.8 mGy/s to 360 mGy/s). The program that controls the CCD is able to manage the desired sample rate used to acquire spectral information, while the irradiation source is manually turned on and together with a mechanical shutter connecting it to the sample holding chamber. A vacuum pump is connected to the chamber to create low vacuum, in order to reduce spurious signals originated by the atmosphere interaction with the ionizing radiation. The samples were sticked on stainless steel plates with silicon oil.

4.4 Electron Paramagnetic Resonance equipment

EPR spectra has been acquired with a Bruker EMX plus spectrometer for X-band measurements, while for Q-band measurements the spectrometer was a X/Q-band Bruker ELEXSYS E580. The EMX plus system is provided with a liquid helium cooling system which allows low temperature measurements (down to 10 K). Both instrumentations are located in the laboratories of the Institute of Physics of the Czech Academy of Science, in Prague. For these measurements, the sample were irradiated with ISO56 DEBYEFLEX 3003 highly stabilized X-ray equipment for structure analysis (tungsten target).

The samples were held in quartz tubes around 0.5 mm of thickness. To avoid contaminating signals originated from the sample holder itself, the irradiation process was made using a different tube from the ones used during the spectrum acquisition.

Part of the X-band measurements experiments were made with a Varian spectrometer and equipped with a Bruker cavity ER4102ST (3000 Q-factor).

4.5 Temperature Control

Temperature control, when used, was realised with a Peltier cell connected to a TC2812-RS232 CoolTronic temperature controller and powered by a DC generator (12 V and 3 A max).

5. Anomalous thermal stability of the $[GeO_4]^-$ and 110 °C TSL peak of quartz

In this thesis work, the experiments reported in Vaccaro et al. (2017) and illustrated in the previous sections were repeated on multiple samples of various kind. The thermal stability of both the 110 °C TSL peak and the $[GeO_4]^-$ centre was studied at room temperature.

During the experiment, an anomaly on the decay time in a certain set of samples has been observed. Such samples showed an increased decay time for both the EPR and the TSL signals.

5.1 Experiment procedure

5.1.2 Samples

The sample pool included both natural quartz samples and synthetic ones. The natural ones were hydrothermally grown ones known as colourless or hyaline quartz (labelled as Nat-01 from now on), smoky quartz and rose quartz, and a pegmatitic sample that was labelled K-200. The synthetic quartz was produced by Sawyer Technical Materials through hydrothermal growth.

Part of the synthetic sample was subject to a procedure known as “sweeping”, discussed in section 2.4. Thanks to the application of an electric field and the large channels along the c-axis in the crystal structure, the alkali ions included in the sample were “swept out” of the bulk to be substituted by hydrogen from air.

The samples were then crushed to powder and sieved to collect grains between 100 µm and 200 µm in diameter. The powder of each sample was then divided into three different batches. One batch was annealed at 500 °C in a preheated oven for 10 minutes and then rapidly cooled to room temperature by extracting it from the still hot oven. Another batch was annealed at 1000 °C, following the same procedure and the third one was submitted to no treatments.

5.1.3 TSL Measurements

Each sample was irradiated with 2 Gy of β-rays. After irradiation, the sample was held at 25 °C with the use of a Peltier cell connected to a temperature controller, set to a precision of ±0.1 °C. After a time t from irradiation, the glow curve was acquired, at 5 °C/s with the Risø TSL/OSL reader, using the U-340 optical filter. The experiment was then repeated multiple times on the same aliquot, changing the value of t. Even if the TSL was acquired only up to 220 °C, a weak influence of the pre-dose effect was detected. To compensate this effect, after each acquisition a new glow curve was acquired at t equal to 0 s. The intensity of this glow curve was used as a normalizing factor for the measurement itself. This correction helped keeping track of the sensitivity enhancement of the aliquots as the experiment proceeded. The procedure was performed for every every sample of each batch.

Given that the peak maximum position, in these experimental conditions, was observed at around 80 °C, the intensities were evaluated by integrating the glow curve’s area between 50 °C and 70 °C. This was done to focus on the initial part of the peak, which was the most unaffected by other higher

temperature peaks nearby the 110 °C peak that some samples showed. Such intensity was then plotted as a function of time after irradiation and fitted with the mono-exponential function:

[18] $$\frac{I}{I_0} = A_0 \exp(-t/\tau)$$

Where I is the glow curve intensity, I_0 the normalization intensity, A_0 a pre-exponential factor which in this case should theoretically be about 1, t is the time after irradiation and τ is the decay time of the TSL peak.

5.1.4 EPR Measurements

The EPR signal of $[GeO_4]^-$ was monitored with the EMX plus equipment, by irradiating the samples with roughly 125 Gy of X-rays. Given the simpler nature of the EPR experiment procedure, it was sufficient to irradiate the sample just once and then monitoring the EPR spectrum over time. A temperature control was not possible as for the TSL experiment, but it can be easily assumed that the sample temperature could not fluctuate too much during the experiment thanks to the spectrometer's huge cooled magnets that surrounded the resonator, which acted as thermal reservoir.

The spectrometer was set to acquire 4 scans of the spectrum between 3325 G and 3385 G, 30 s each, and to repeat the procedure each 10 minutes. The intensities have been evaluated with a peak-to-peak approach of the $[GeO_4]^-$ lines, whose g-factor parameters have been compared with Vaccaro et al. (2017 and 2019) and references therein. The time decay has been calculated again with eq. [18], by using the intensity of the first spectrum as I_0. The g-factor evaluation has been made by reconstructing the spectra with Easyspin simulations (Stoll and Schweiger, 2006).

Due to a mere matter of available time in the laboratory in Prague's Institute of Physics of the Czech Academy of Science, this measurement could not be carried out on all the available samples.

5.2 Results

5.2.1 TSL Results

In the following figures, the normalized glow curve obtained during the experiment are reported. These curves were obtained by dividing them by the intensity measured between 50 °C and 70 °C in the normalization curves, that is the interval with actual physical meaning. Side-by-side are presented also the plots of the intensity in such temperature interval as a function of time, accompanied by a fit with equation [18].

As it can be seen, in most of the samples the decay time is found to be around 3000 s, with some fluctuations. There is, however, a limited set of samples which show a significantly longer decay time. The k-200 set for instance shows a decay time longer by a factor of almost 2 when compared to the rest. This happens also for the synthetic swept sample which has been annealed at 1000 °C, showing an estimated decay time longer by at least 50%. This is indeed an anomalous behaviour, unexpected from a TSL peak used for dosimetry applications, because if this anomaly is present in this kind of experiment it is not unreasonable to assume that other anomalies may appear in other dosimetric procedures like the ones taking advantage of the predose (section 3.1.4), for example. One

could argue that the observed peaks could be an overlap of many peaks which result in an apparent single peak. The theoretically possibility of this occurrence has been explored by Chen et al. (2016), and it may not be detected by experiments performed on a routinely schedule. In that paper, the authors show also that by treating an apparently single peak with first order kinetics, one would obtain lower trap depths and/or frequency factor from their analysis. Given the previous work by Vaccaro et al. (2017) on the 110 °C TSL peak and its thermal stability compared with the paramagnetic centre $[GeO_4]^-$, to reproduce this anomalous decay with EPR, a similar experimental approach was tried.

As a side note, one could notice that in some of the figures from 5.1 to 5.16 there is a deviation of the ratio I/I_0 from the value of 1 at time equal to 0. This seems to be related to the presence of a lower temperature peak with low stability, that is not visible anymore after 5 minutes after irradiation. As an example of that, in Fig. 5.17, in a semi-logarithmic scale, the raw glow curves for the synthetic swept sample annealed at 1000 °C are reported, acquired at 1 °C/s, where this effect appears to be more evident. As it can be seen, there is a peak at around 40 °C if the glow curve is recorded right after irradiation, but after just 5 minutes it is not visible anymore, with an almost perfect exponential decrease of the intensity. Pairing this observation with the fact that the intensity monitored well follows a single exponential trend after 5 minutes, it can be concluded that this effect is negligible for the scope of the experiment, i.e. measuring the decay time of the 110 °C TSL peak of quartz.

Additionally, it can be observed in many cases (e.g. Fig. 5.2, 5.5 and 5.7) that the fading of the 110 °C TSL peak is accompanied by an increase of the higher temperature components. This could be interpreted in two ways. The first is a possible retrapping of the charge released from the 110 °C peak electron traps. The second is the possibility that the higher temperature peaks are getting sensitized more than the 110 °C TSL peak. With the current data it is not possible to exclude either of the hypothesis, but some simple experiments on dose response could provide more insights on the subject.

In tab. 5.1 is reported a recap of the decay times measured for the 110 °C TSL peaks in the studied samples, while in Tab. 5.2 is reported a recap of the trap parameters obtained with initial rise calculations (eq. [6] and [7]) and fitting with the Randall-Wilkins equation (eq. [2]).

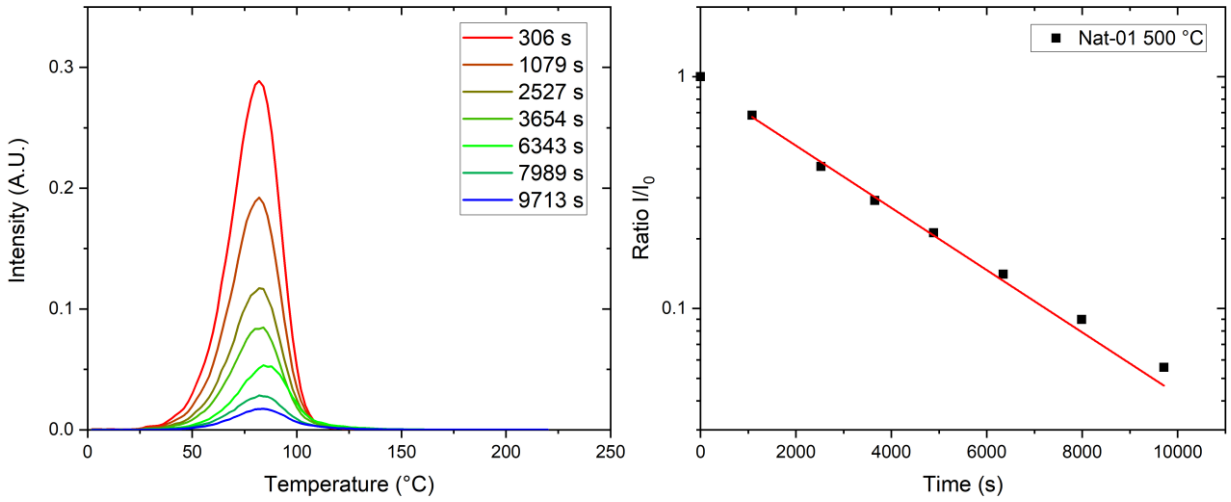

***Fig. 5.1**: Normalized glow curves and intensity evaluation of the Nat-01 quartz sample annealed at 500 °C. The decay time calculated is 3020±150 s.*

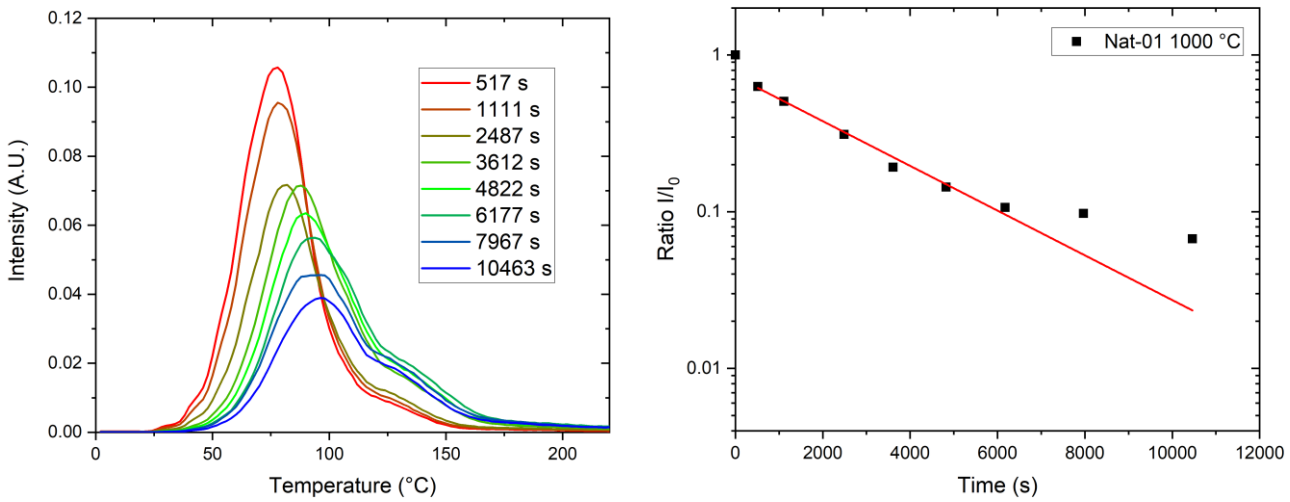

***Fig. 5.2**: Normalized glow curves and intensity evaluation of the Nat-01 quartz sample annealed at 1000 °C. The decay time calculated is 3200±100 s.*

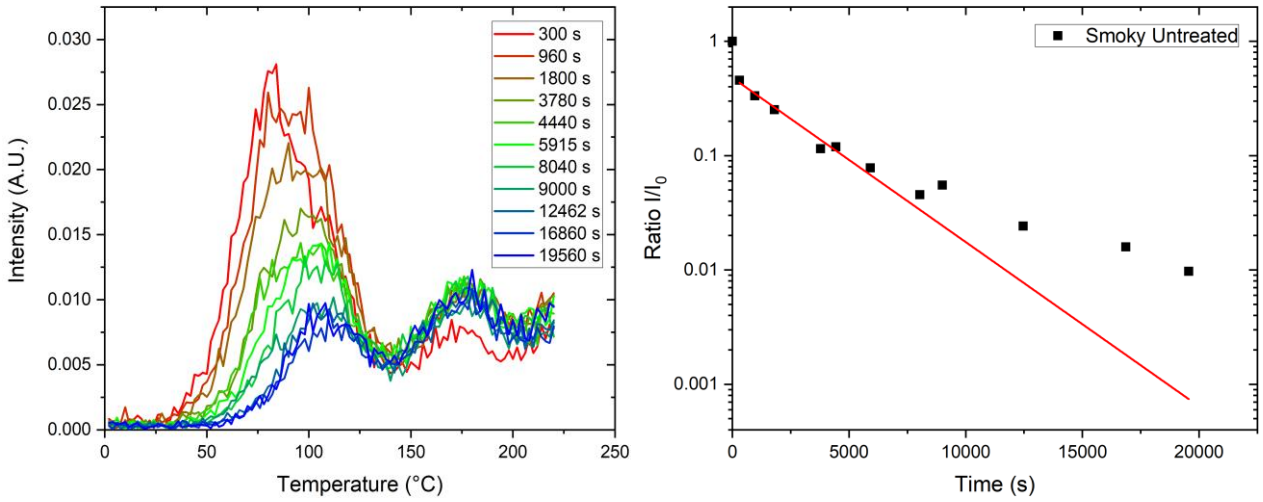

***Fig. 5.3**: Normalized glow curves and intensity evaluation of the smoky quartz sample as received. The decay time calculated is 3000±200 s.*

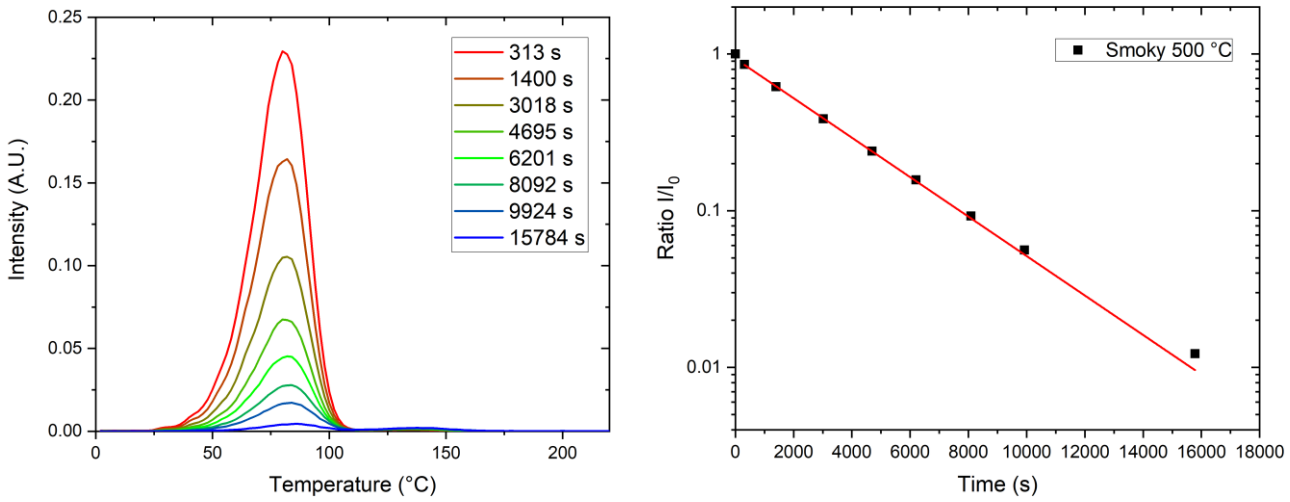

***Fig. 5.4**: Normalized glow curves and intensity evaluation of the smoky quartz sample annealed at 500 °C. The decay time calculated is 3450±30 s.*

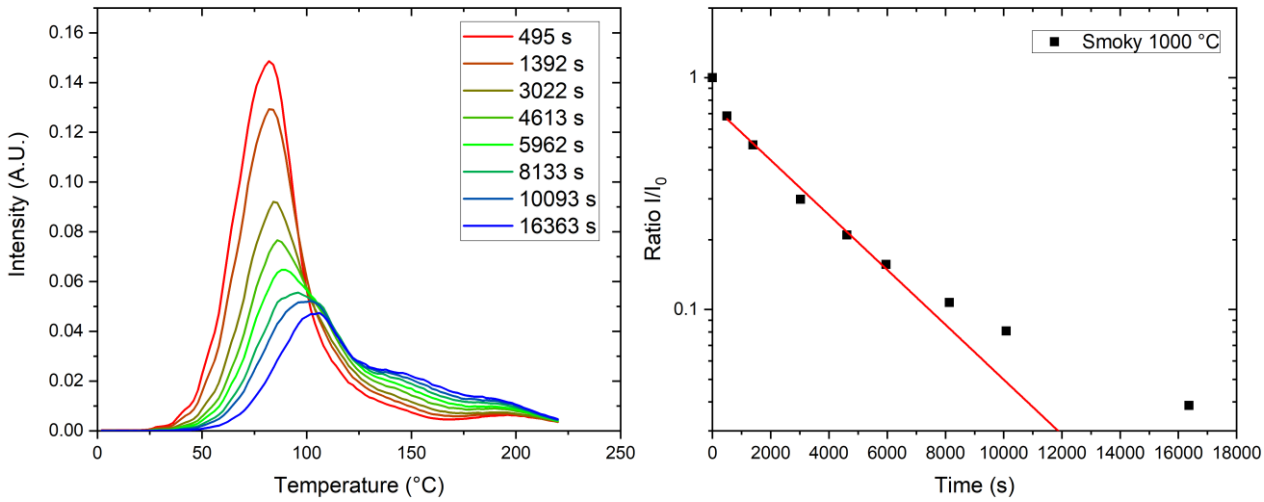

***Fig. 5.5**: Normalized glow curves and intensity evaluation of the smoky quartz sample annealed at 1000 °C. The decay time calculated is 3700±200 s.*

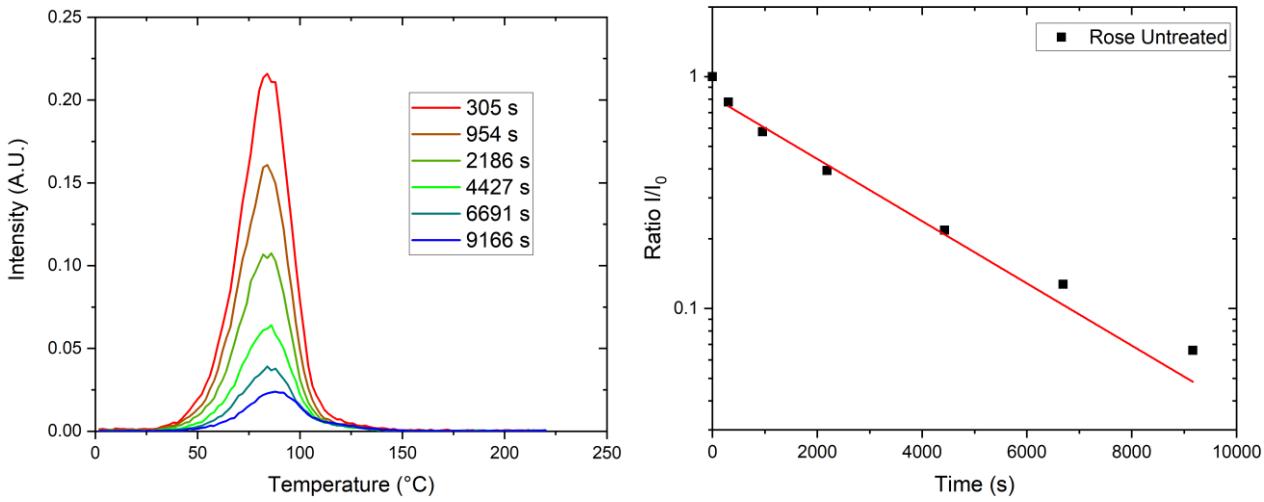

***Fig. 5.6**: Normalized glow curves and intensity evaluation of the rose quartz sample as received. The decay time calculated is 3200±300 s.*

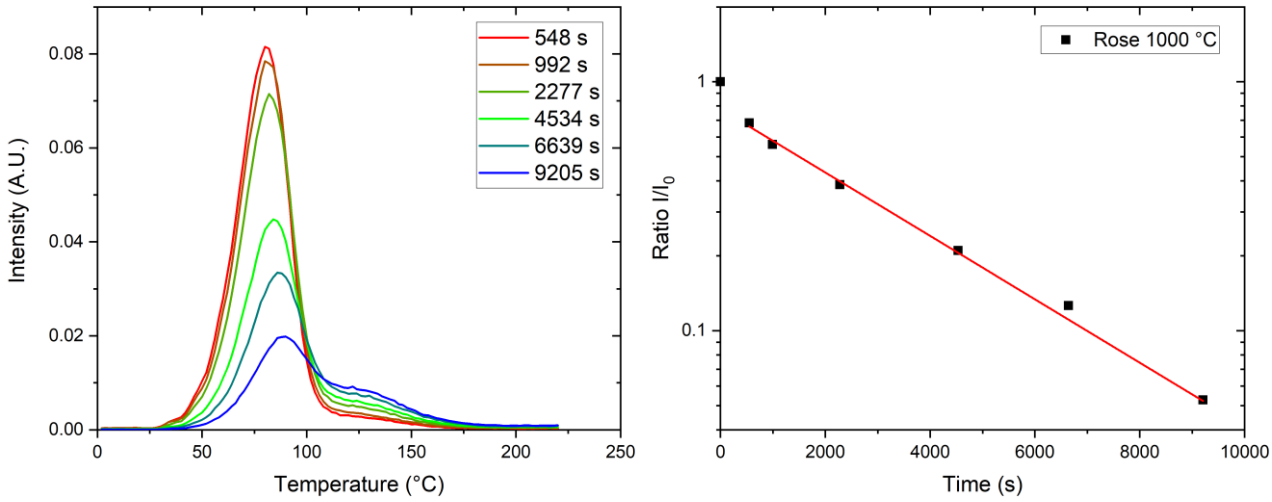

***Fig. 5.7**: Normalized glow curves and intensity evaluation of the rose quartz sample annealed at 1000 °C. The decay time calculated is 3400±200 s.*

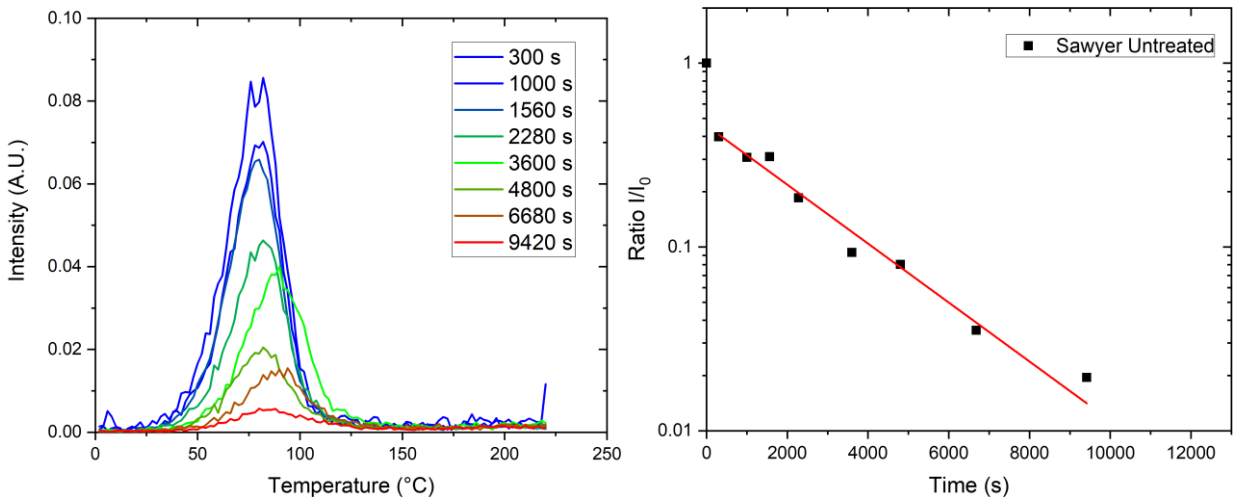

***Fig. 5.8**: Normalized glow curves and intensity evaluation of the sawyer quartz sample as received. The decay time calculated is 3300±160 s.*

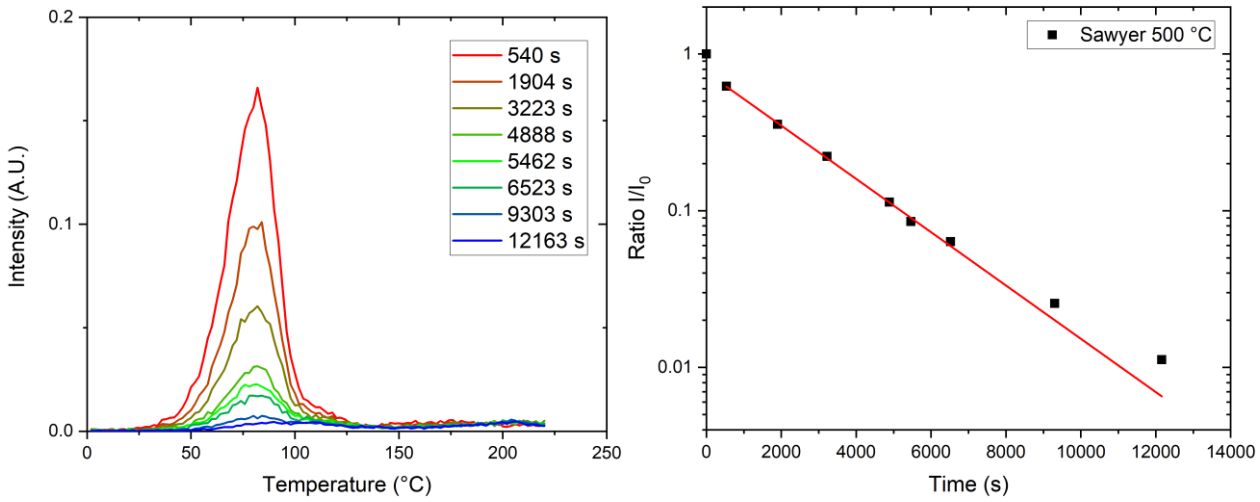

***Fig. 5.9**: Normalized glow curves and intensity evaluation of the sawyer quartz sample annealed at 500 °C. The decay time calculated is 2550±40 s.*

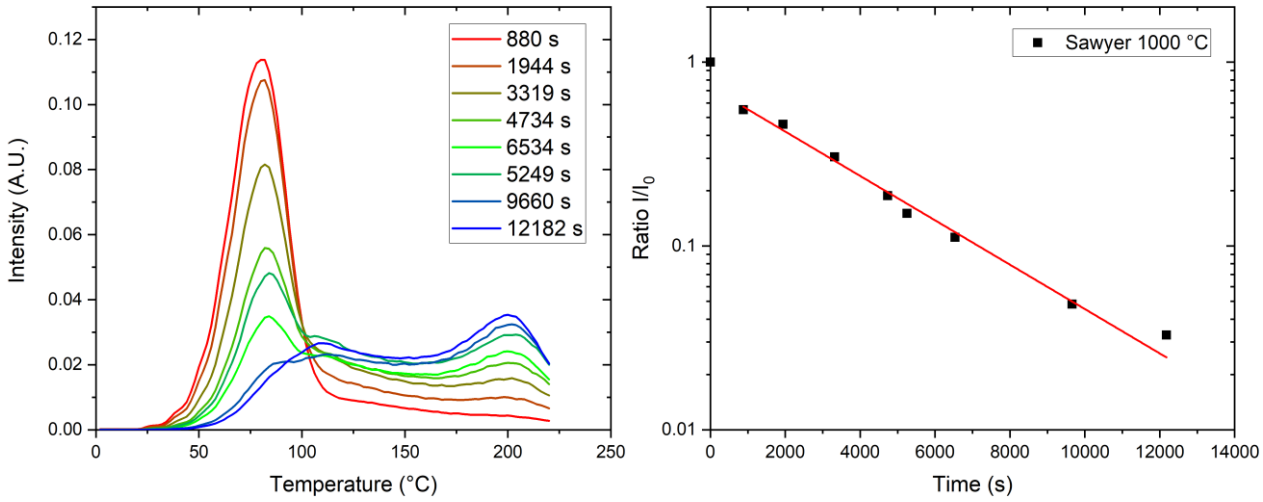

***Fig. 5.10**: Normalized glow curves and intensity evaluation of the sawyer quartz sample annealed at 1000 °C. The decay time calculated is 3600±200 s.*

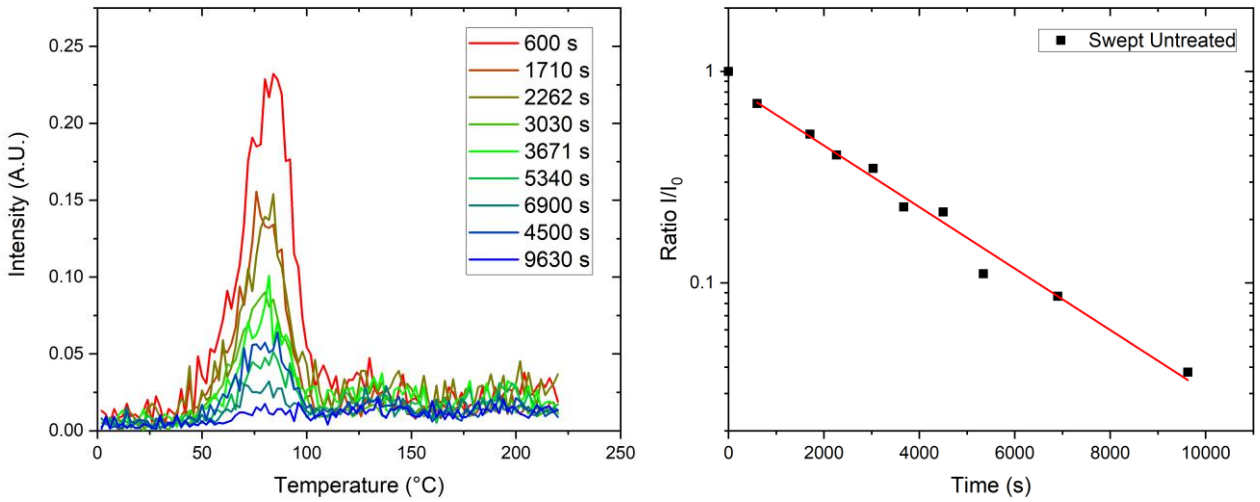

***Fig. 5.11**: Normalized glow curves and intensity evaluation of the swept quartz sample as received. The decay time calculated is 2980±160 s.*

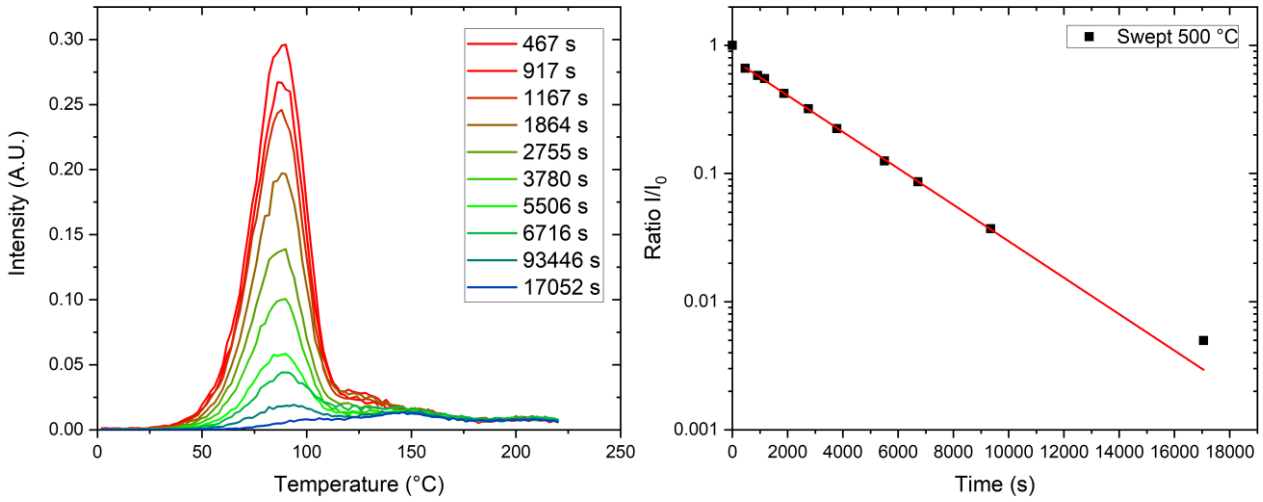

***Fig. 5.12**: Normalized glow curves and intensity evaluation of the swept quartz sample annealed at 500 °C. The decay time calculated is 3050±50 s.*

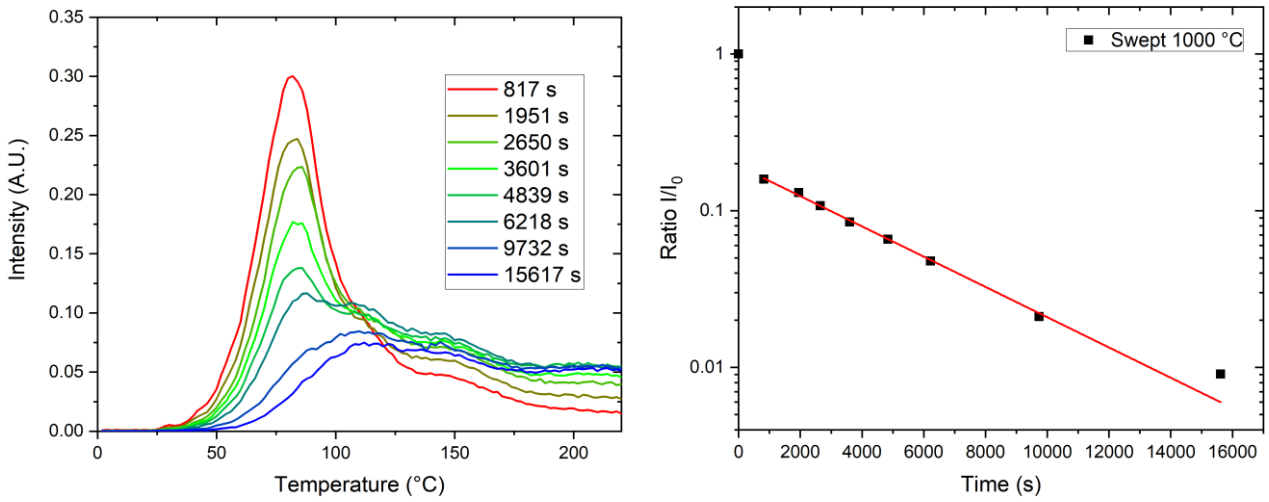

***Fig. 5.13**: Normalized glow curves and intensity evaluation of the swept quartz sample annealed at 1000 °C. The decay time calculated is 4500±140 s.*

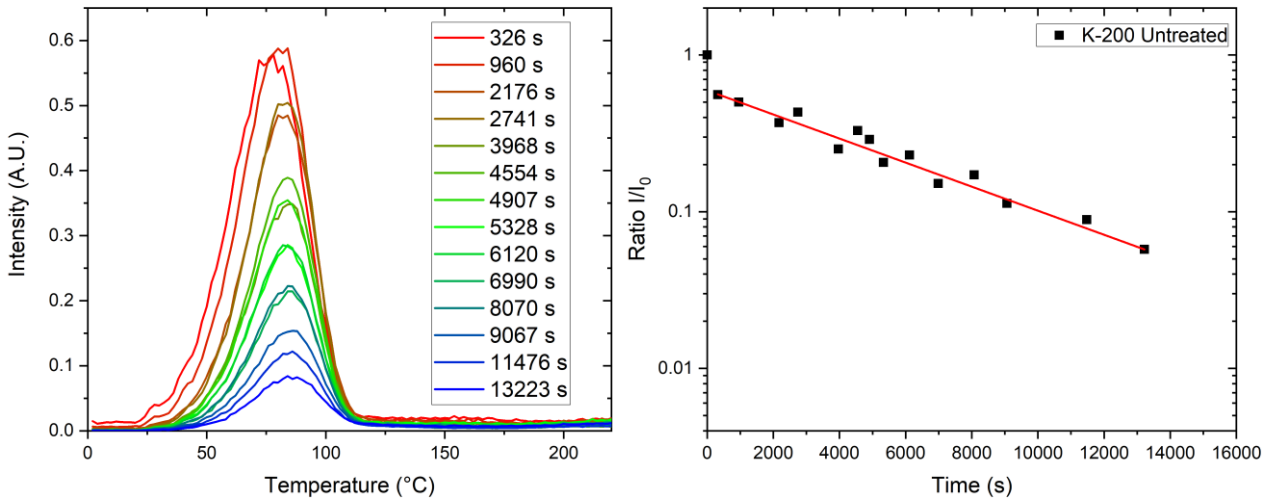

***Fig. 5.14**: Normalized glow curves and intensity evaluation of the K-200 quartz sample annealed as received. The decay time calculated is 2980±160 s.*

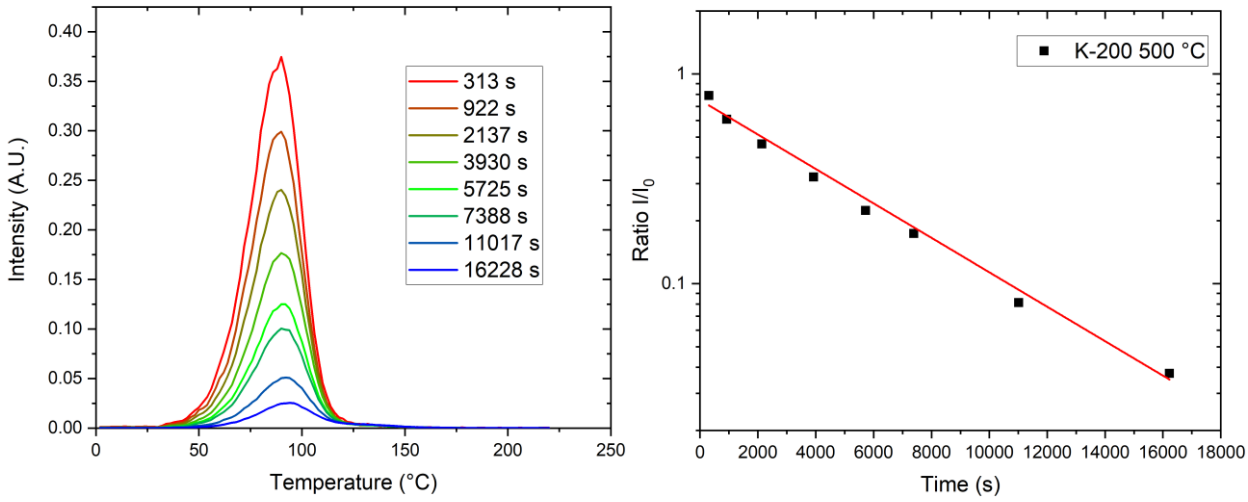

***Fig. 5.15**: Normalized glow curves and intensity evaluation of the K-200 quartz sample annealed at 500 °C. The decay time calculated is 3050±50 s.*

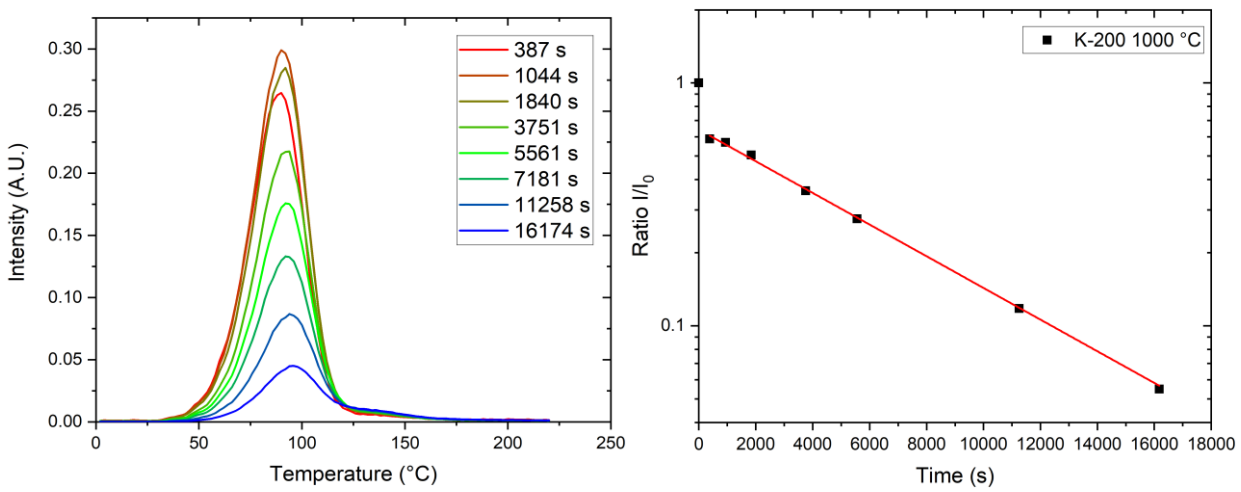

***Fig. 5.16**: Normalized glow curves and intensity evaluation of the K-200 quartz sample annealed at 1000 °C. The decay time calculated is 4500±140 s.*

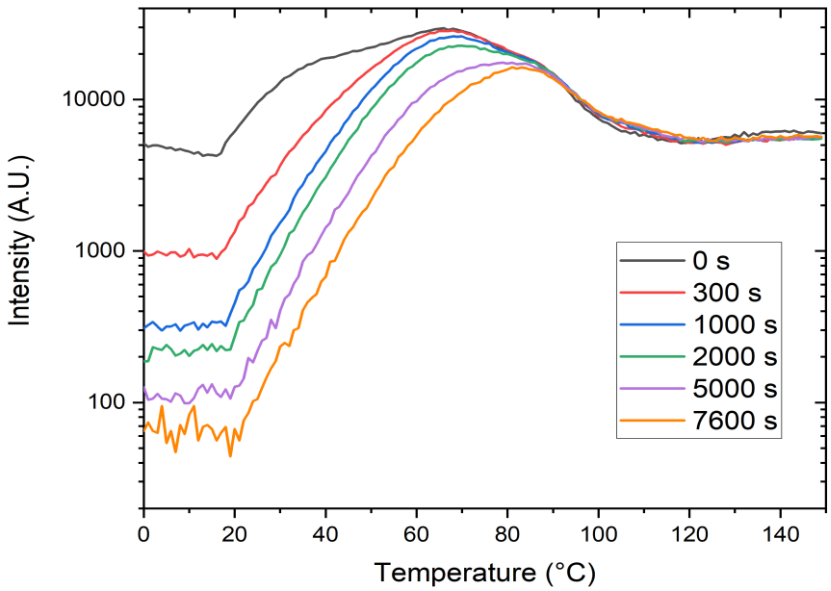

***Fig. 5.17**: Raw glow curves of the synthetic swept sample annealed at 1000 °C in semi-logarithmic scale. Each curve has been acquired after a certain time after the irradiation, as reported in the legend. At 0 s, it appears a low temperature peak at around 40 °C, no longer observable after 300 s from irradiation.*

Sample	Anneal Temperature	Tau (s)	Error (s)
Nat-01	Untreated	3020	150
	500 °C	3200	100
	1000 °C	3000	200
Smoky	Untreated	3000	200
	500 °C	3450	30
	1000 °C	3700	200
Rose	Untreated	3200	300
	1000 °C	3400	200
Sawyer	Untreated	3300	160
	500 °C	2550	40
	1000 °C	3600	200
Swept	Untreated	2980	160
	500 °C	3050	50
	1000 °C	4500	140
K-2-00	Untreated	5700	500
	500 °C	5300	200
	1000 °C	6700	300

Tab. 5.1*: Decay time measured for the 110 °C TSL peak of quartz through isothermal decays at 25 °C.*

		Fit		Initial Rise	
Sample	**Anneal Temperature**	**E_T(eV)**	**s(Hz)**	**E_T(eV)**	**s(Hz)**
Nat-01	Untreated	0.65	6E+08	0.51	3E+06
	500 °C	1	6E+13	1.12	4E+15
	1000 °C	0.75	1E+10	0.96	2E+13
Smoky	Untreated	0.6	5E+07	0.51	2E+06
	500 °C	1	6E+13	1.07	8E+14
	1000 °C	0.82	1E+11	0.96	2E+13
Rose	Untreated	0.62	2E+08	0.62	3E+08
	1000 °C	0.88	9E+11	1.11	3E+15
Sawyer	Untreated	0.76	2E+10	0.37	1E+04
	500 °C	0.75	1E+10	0.51	2E+06
	1000 °C	0.74	7E+09	0.68	8E+08
Swept	Untreated	0.8	6E+10	0.5	1E+06
	500 °C	0.88	1E+12	0.79	4E+10
	1000 °C	0.32	2E+04	0.51	3E+06
K-2-00	Untreated	0.65	7E+08	0.53	8E+06
	500 °C	0.90	1E+12	0.99	5E+12
	1000 °C	0.87	4E+11	0.98	3E+12

Tab. 5.2*: Trap parameters obtained from the TSL measurements for the studied samples. The parameters have been calculated fitting the glow curve with eq. [2] and through initial rise calculations using eq. [6] and [8].*

5.2.2 EPR Results

Seen the TSL results obtained in the previous section, and what has been reported in Vaccaro et al. (2017), the same effect should be observed also in EPR experiments by monitoring the stability at room temperature of the $[GeO_4]^-$ signal. These experiments have been done on the Nat-01 untreated sample, which is the same used in Vaccaro et al. (2017), and the K-200 untreated sample. It was not possible to replicate it on the swept sample annealed at 1000 °C because of the very poor EPR intensity of $[GeO_4]^-$, probably due to the much higher purity of the sample when compared with a natural one (i.e. lower concentration of germanium). The obtained spectra are reported in fig. 5.18 for both samples. The difference in the spectral shape is due to the application of a modulation factor applied on the Nat-01 measurements that enhanced the signal to noise ratio, at the cost of spectral resolution. This was done due to the lower intensity observed when compared with the K-200. Preliminary measurements were done to confirm that the same paramagnetic signal was being observed (i.e. $[GeO_4]^-$). Furthermore, the stable $[GeO_4/Li^+]^0$ signal component, clearly observable after the complete $[GeO_4]^-$ decay, was subtracted from the spectra for the decay time evaluation and

for that reasons the spectra will tend toward a flat line at the longer times. The intensity of each spectrum has been then calculated with a peak-to-peak approach and reported as a function of time from irradiation in Fig. 5.19. By fitting the data with a mono-exponential decay model (eq. [18]), the decay time has been estimated to be 6700±400 s in the case of the K-200 sample and 3700±100 s for the Nat-01 sample.

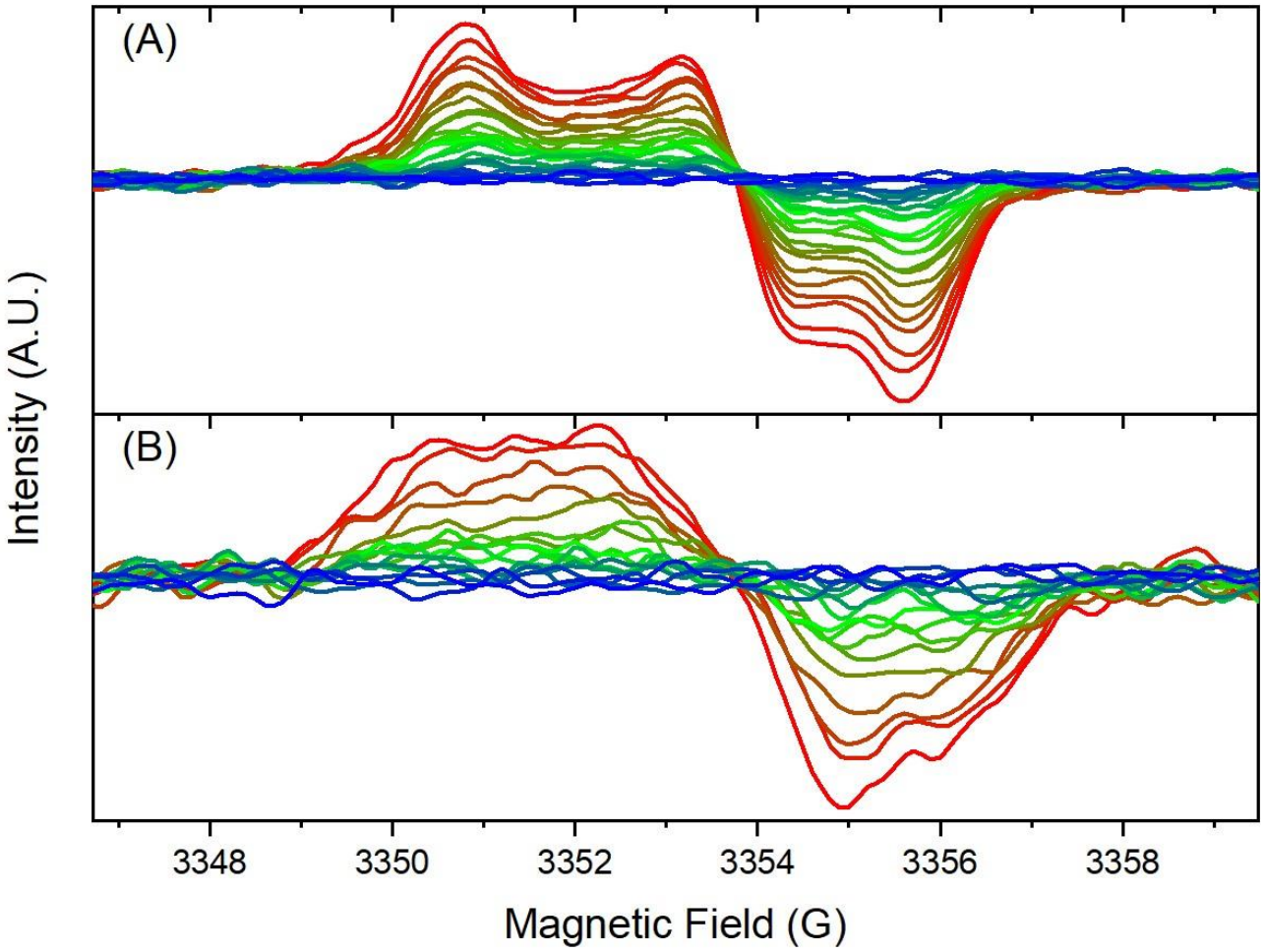

***Fig. 5.18**: Time evolution at room temperature of EPR spectra of (A) K-200 and (B) Nat.01 quartz samples after initial X-ray irradiation. The stable $[GeO_4/Li^+]^0$ component has been removed from the spectra, leaving only the unstable $[GeO_4]^-$. The colour scale red-green-blue indicates the progression of time at 10 min steps.*

5.3 Comments

The data showed in the previous section is confirming again what reported by Vaccaro et al. (2017) and initially suggested by McKeever et al (1985), i.e. that the 110 °C TSL peak of quartz is related to the $[GeO_4]^-$ signal, observable through EPR. In this case though, an anomalous behaviour in a limited set of samples was observed, specifically all the K-200 aliquots, a natural pegmatitic sample, and the sawyer swept sample annealed at 1000 °C. In fact, while the correlation between EPR and TSL signals still holds, the decay time measured in such samples is significantly larger than the rest of the samples in the studied set. In the EPR experiments, the same signal was observed in every sample (i.e. same set of g-factors), so it can be assumed that that is also the same for the trap for the

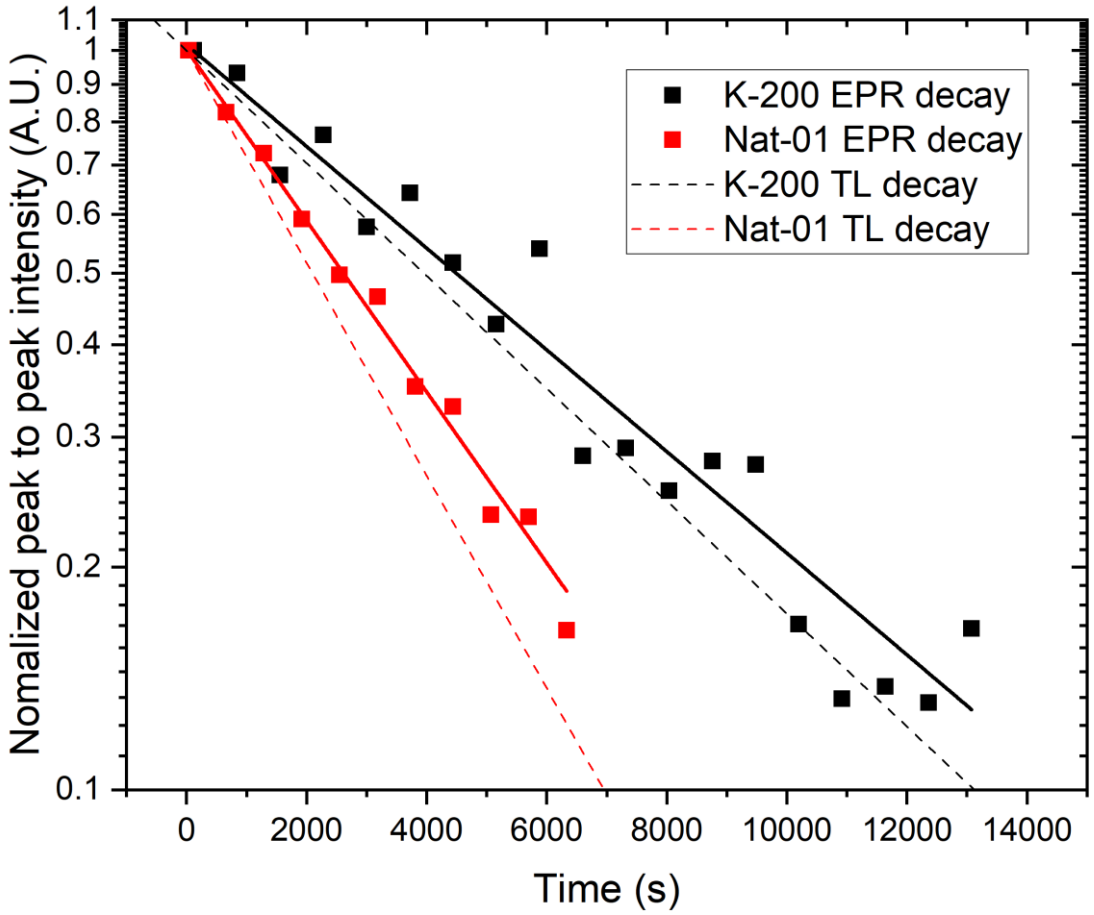

***Fig. 5.19**: [GeO_4]$^-$ EPR intensity as a function of time for untreated K-200 and Nat-01 at room temperature. Full lines represent the fitted exponential decay curve, which estimated the decay times to be 6100±400 s and 3700±100 s for K-200 and Nat-01 respectively. For comparison, the corresponding decay curves with the calculated TSL decay time of the 110 °C TSL peak were plotted (dashed lines).*

110 °C peak of quartz. One could argue that maybe other impurities in the same sample, such as the K-200, could be generating other trap levels with similar characteristics, and as such the glow curve will be a composition of several peaks, apparently prolonging the decay time of the 110 °C peak. This does not seem to be the case, or if it is it does not seem to be a significant effect, because the same kind of deviations are being observed with two different techniques, one which relies on the trapped electron themselves and the other requiring a luminescent process that consumes the released electrons.

Right now, only speculations can be made about the reasons why such effect is observed. The two anomalous samples do not possess a common feature that could be highlighted as a possibility, since their completely different origin (natural and synthetic). The K-200 is a pegmatitic sample, an igneous kind of rock, while the synthetic one has been grown with a hydrothermal procedure, purified from small alkali ions with a sweeping procedure, and it shows such property only after annealing at 1000 °C. Since the higher purity of the synthetic sample, confirmed also by the different EPR intensities observed since in the synthetic sample the [GeO_4]$^-$ is not visible, one would exclude an extrinsic origin of the effect. A possible explanation could be a tunnelling effect of a hole from an unknown

trap next to $[GeO_4]^-$, causing a difference in timing characteristics between samples. Another could be coming from an intrinsic defect, that is abundant for some reason in these two types of samples even though they are from very different origin, and similar to others that do not show this effect. Lastly it could also be that a distorted version of the defect is being observed, whose difference is not evident through the X-band EPR measurements on powders here reported. A hint towards this last possibility could be the dependence of the temperature position of the maximum of the TSL peak to the received dose that can be observed in K-200. Glow curves showing this property are reported in Fig. 5.20. This property is typical for traps that show non-first order kinetics (Garlick and Gibson, 1948), but it is not to be excluded the possibility of having two different overlapping peaks with different dose sensitivity. It must also be considered the possibility that the apparent shift with dose observed in Fig. 5.20 may arise by a charge redistribution during the prolonged irradiation times of the higher doses. The current data is still not enough to favour one hypothesis over the other, but the apparent shift of the 110 °C peak during the fading process slightly favours the overlapping peaks hypothesis.

Following there will be some comments on the analysis of the trap parameters of the 110 °C TSL peak reported in Tab. 5.2. Since many of the not annealed samples showed a very low Signal-To-Noise ratio, unless very high irradiation doses were used, the values obtained from the Initial Rise are not as reliable as the ones obtained by the full curve fit assuming first order kinetics, so the focus will be on these latter ones. Looking at the data obtained, one finds that the energy trap in untreated K-200 is not so different from other natural and untreated samples such as Nat-01. In Nat-01 the trap depth is around 0.65 eV, again around 0.65 eV also in K-200, around 0.62 eV in Rose quartz and around 0.60 eV in Smoky untreated quartz. The frequency factor is very similar as well, with less than one order of magnitude of difference, around 1E8 Hz. The fact that both samples show a significantly different lifetime of the same TSL peak seems in contrast with the parameter calculation, but it is possible that the experimental error in such calculation is much greater than the one concerning the direct lifetime measurement. The annealing has similar effects in every natural sample, with higher trap depth in the ones annealed at 500 °C, than the ones annealed at 1000 °C and untreated, with the last ones showing the lowest values. In the synthetic Sawyer samples, it seems that the annealing does not bring significant changes in trap parameters, for both trap depth and frequency factor, around 0.75 eV and 1E10 Hz respectively. Different case for the swept sample, where the trap depth for the as-received sample and the one annealed at 500 °C are similar, around 0.80 eV and 0.88 eV, while in the one annealed at 1000 °C the trap depth drops drastically to around 0.32 eV. The frequency factor is also at least five orders of magnitude lower than the other swept samples. The shape of the glow curve is also significantly different, with a broader peak that seems to be composite (Fig 5.17). All this seems to be a clue pointing to the fact that the reason of such deviations from the

average of the rest of the samples in K-200 and the swept sample annealed at 1000 °C seems not to be the same despite the similar decay time.

More insight could be possibly achieved through EPR measurements at higher frequency than the X-band. Such spectra could show much more detail on the defect structure, maybe showing the existence of different configurations of it, with different perturbations. Another possibility could be similar studies with oriented samples in single crystal form, which could give more information on the g-tensors of the analysed electron traps.

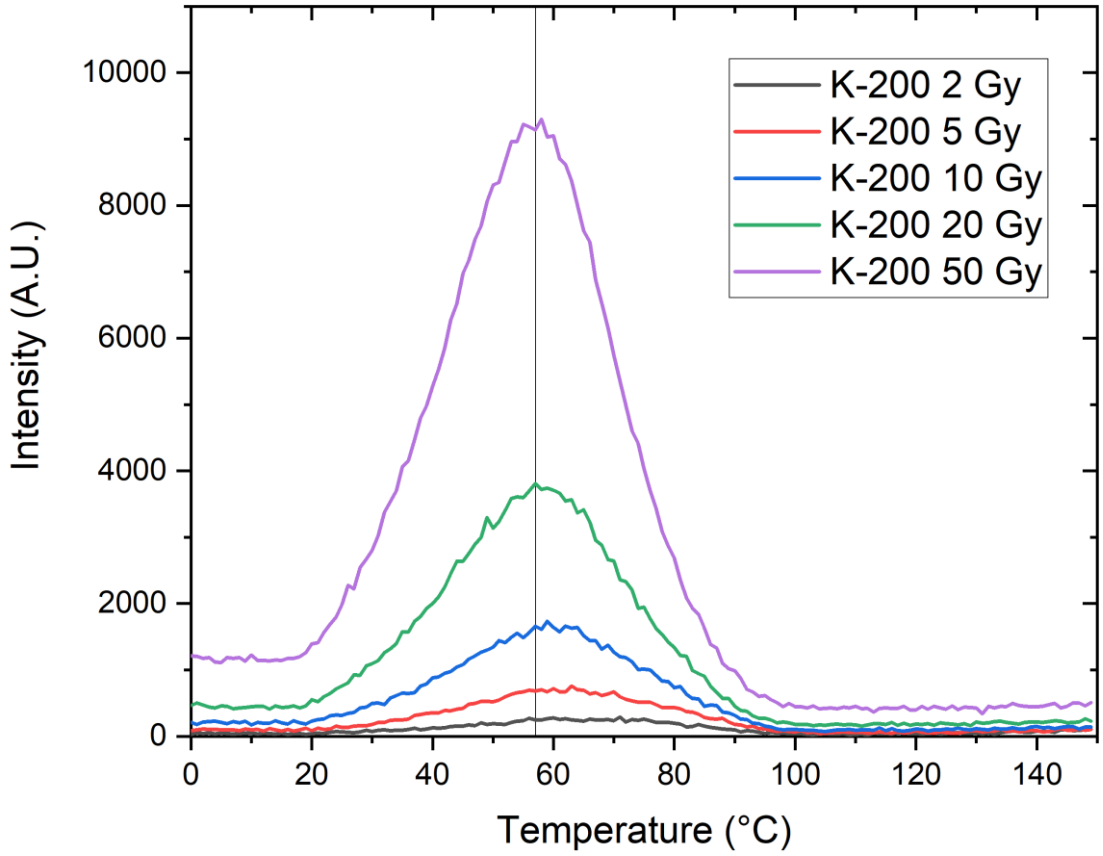

***Fig. 5.20**: Glow curve shape change in K-200 as a function of dose. TSL measured at 5 °C/s. A vertical line at 57 °C is drawn to guide the eye and highlight the peak's maximum shift towards lower temperature with increasing dose.*

To summarize, these experiments have confirmed again what initially proposed by McKeever (1985) and more methodically measured by Vaccaro et al. (2017). The correspondence between the 110 °C TSL peak of quartz and the EPR signal originate from $[GeO_4]^-$, is maintained across different samples without any doubt. The study presented though the possibility of an anomalous behaviour in the thermal stability of such signals. In a set of samples, it has been observed a longer decay time by a factor of almost 2. Due to the possible use of such signals for dating or dosimetry, thanks to the pre-dose effect, it should be studied further if this effect could bring any error in such applications. At the moment, there is not a clear explanation of what originates such effect beside a few suggested speculations.

6. Study on the $[GeO_4/Li^+]^0$ relation with the 375 °C TSL peak of quartz

While studying the $[GeO_4]^-$ centre, it was evident in the EPR spectra a much more stable signal, related to the $[GeO_4/Li^+]^0$ centre. A similar approach was tried to correlate it to another TSL peak of quartz, the one at roughly 200 °C at 5 °C/s. The estimation of its decay time by calculation with TSL models revealed a value compatible with what was observed through EPR for the $[GeO_4/Li^+]^0$ centre and such suggestion was already proposed by Guzzo et al. (2017). The study did not confirm the assignment of the EPR signal to the 200°C TSL peak (Monti, 2017), but it rather suggested that the paramagnetic centre could be related a peak observed around 340 °C. The results presented in this section have been published in Vaccaro et al. (2019).

The peak analysed was the so-called 375 °C TSL peak of quartz, which is reported also as Slowly Bleachable Peak (SBP), referring to the property of being slowly depleted under the illumination of ambient light, in contrast to another peak observed at around 325 °C which is instead rapidly bleached under illumination (Rapidly Bleachable Peak, RBP, Franklin, 1997). In fact, it is known that the SBP is not affected by light with wavelength longer than 400 nm while the RBP it is (Spooner et al., 1988). Preliminary bleaching studies on the studied sample were consistent with this property.

The literature is very contradictory on the correlation between the SBP and $[GeO_4/Li^+]^0$, with some studies apparently suggesting a relation and others not. An example for the first case was brought by McMorris (1971), who observed that a peak at around 300 °C (with heating rate of 0.17 °C/s) possessed characteristics similar to $[GeO_4/M^+]^0$ during thermal annealing up to 400 °C. McMorris did not correlate that peak directly with the SBP, but the bleaching properties he discusses in his works, makes reasonable to assume that it is indeed the SBP. An example of the other side was brought by Woda et al. (2002), who suggested no direct correlation between the $[GeO_4/Li^+]^0$ centre and the SBP after TSL, EPR and RL experiments. Also Guzzo et al. (2017) seemed to exclude such correlation by suggesting a connection with the RBP instead.

For this thesis work, it has been put to test such correlation by comparing TSL and EPR properties of the SBP and the $[GeO_4/Li^+]^0$ centre, but not by monitoring their thermal stabilities like it was done with the 110 °C peak and the $[GeO_4]^-$ centre in the previous section. For this experiment, the bleaching properties under UV radiation has been monitored as a function of illumination time. A thermal approach was initially tried, but the large temperature error of the heating equipment, a simple oven, brought a lot of scattering in the data.

6.1 Experiment procedure

6.1.1 Samples

The sample used for this experiment was Nat-01 in powder form (grain size between 100 µm and 200 µm). To enhance the TSL intensity, the powder was annealed at 800 °C for 10 min before irradiation. Different aliquots were used for TSL and EPR experiments.

6.1.2 TSL measurements

The sample was irradiated with 50 Gy using the Risø TSL/OSL reader beta source. This much larger dose, when compared with the previous section experiment, was needed in order to obtain a good glow curve intensity of the desired TSL peak. The sample was then preheated at 200 °C for 10 s using the Risø TSL/OSL reader. This was done in order to delete the signal of the 110 °C TSL peak and the $[GeO_4]^-$ EPR signal. This was mostly helpful for the EPR characterization, but this step was used also for the TSL procedure to make them equivalent. After the preheating, the glow curve was acquired up to 500 °C with a 5 °C/s heating rate. The sample was then irradiated and preheated again and then put under UV illumination (360 nm) for a certain time t. After illumination the glow curve was again acquired. The whole procedure was then repeated from the start and changing the value of t. The double glow curve acquisition was made with the same principles in mind of the previous section, i.e. keep track of the sensitization of the signal during the experiment on the same aliquot. The intensity of the SBP was evaluated by integrating the glow curve in a 20 °C interval around the peak maximum.

6.1.3 EPR measurements

The EPR measurements were done with the EPR equipment in Milano-Bicocca, and for that reason it was possible to use the same irradiation used for TSL measurements. The sample was irradiated with 50 Gy and preheated to 200 °C for 10 s like for the TSL experiment. The EPR spectrum was then acquired, and after that the sample was illuminated with UV light for a certain time t and then the spectrum was measured again. Given the nature of EPR acquisition, it was necessary only a single irradiation and preheating, and so after each spectrum acquisition the sample was illuminated again with UV light, changing the value of t. The intensity of the $[GeO_4/Li^+]^0$ centre was evaluated from the double integral of the EPR signal. Easyspin (Stoll and Schweiner, 2006) simulations were used in order to obtain the g-factors used to assign the nature of the lines observed.

6.2 Results

In Fig. 6.1 are reported the glow curves and the EPR spectra obtained from the experiment. As it can be seen, the SBP is decreasing in intensity with the increase of the illumination time. It can also be seen that the $[GeO_4/Li^+]^0$ is decreasing in intensity with illumination time. In Fig. 6.2 are reported the same curves, but as a function of illumination of blue LEDs (470 nm), the ones the Risø TL/OSL reader is equipped with. In that case it can be seen that both the SBP and the $[GeO_4/Li^+]^0$ signal are unaffected. Furthermore, the experiment was repeated with no illumination, to confirm that the effects observed were induced by it and not by another effect observable in the studied time scale. In this last case, no significant modifications were observed in both TSL and EPR. Finally, in Fig. 6.3 is reported the intensity evaluation for both experiments and both kinds of illumination as a function of time. A model to describe the trend observed is not available, and the straight lines reported are just a guide

to the eye. Having that said, it seems reasonable to say that the trend for both the SBP and $[GeO_4/Li^+]^0$ is the same.

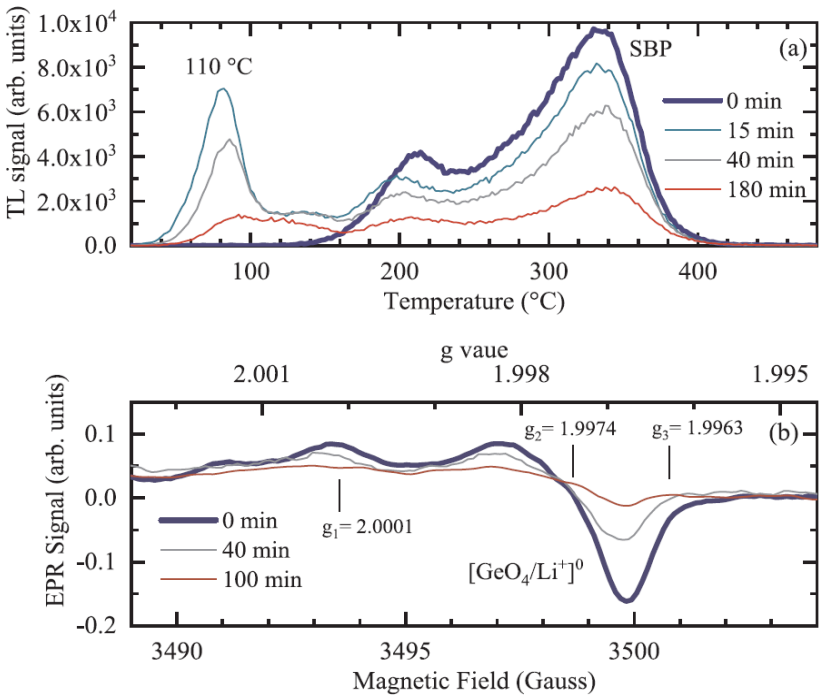

Fig. 6.1: (a) Nat-01 glow curves as a function of UV illumination (365 nm) showing the SBP. The sample has been preheated at 200 °C before each measurement. (b) Nat-01 EPR spectra of $[GeO_4/Li^+]^0$ as a function of UV illumination. The sample has been preheated at 200 °C before the first measurement. Both the SBP and the $[GeO_4/Li^+]^0$ signal are decreasing with increasing illumination time.

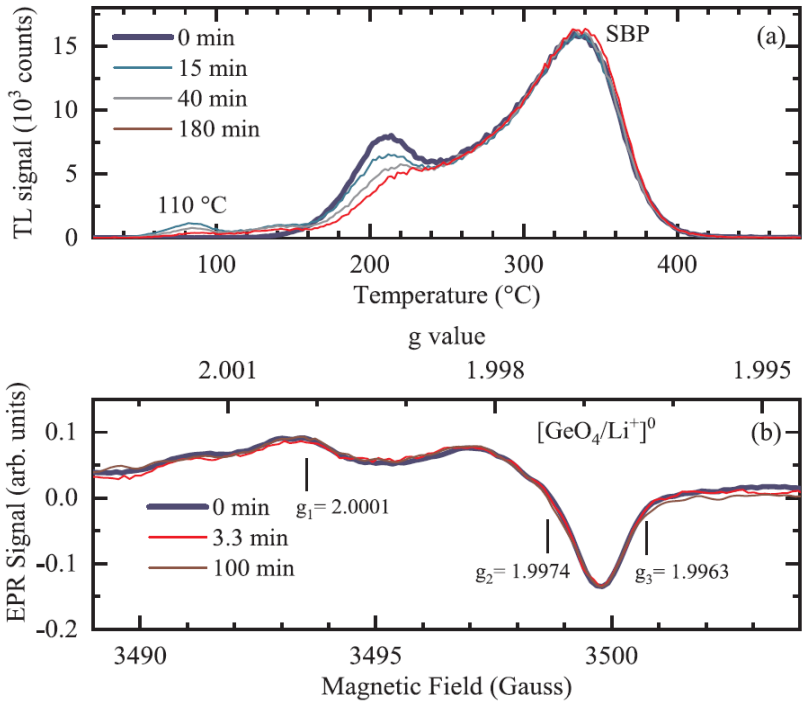

Fig. 6.2: (a) Nat-01 glow curves as a function of blue illumination (470 nm) showing the SBP. The sample has been preheated at 200 °C before each measurement. (b) Nat-01 EPR spectra of $[GeO_4/Li^+]^0$ as a function of blue illumination. The sample has been preheated at 200 °C before the first measurement. Both the SBP and the $[GeO_4/Li^+]^0$ signal are stable with increasing illumination time.

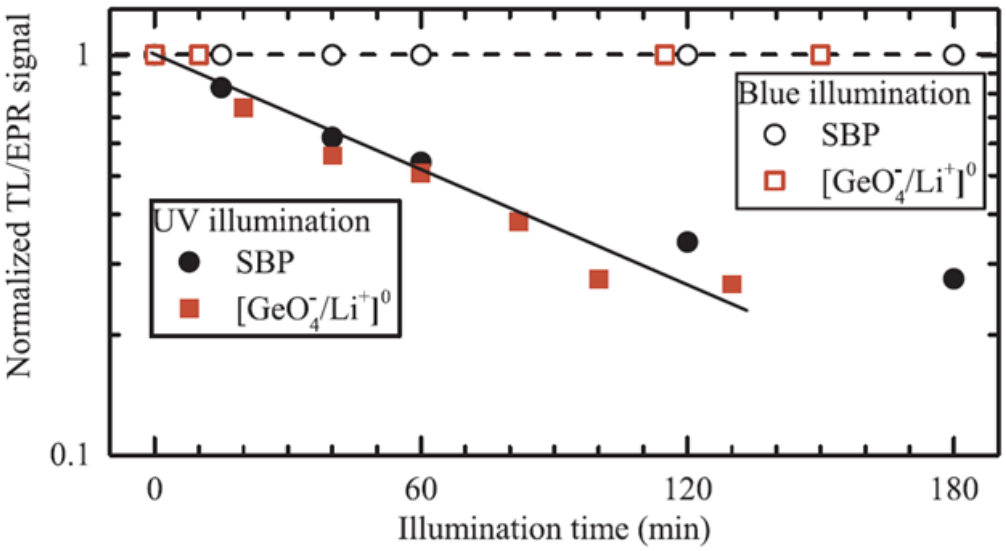

Fig. 6.3: Intensity evaluation of the SBP and $[GeO_4/Li^+]^0$ as a function of illumination time. The straight lines are a guide for the eye. Under blue illumination both signals are stable while they are decreasing under UV illumination.

6.3 Comments

Both EPR and TSL experiments have shown a similar behaviour of the SBP and the $[GeO_4/Li^+]^0$ signal under both UV and blue illumination. In the first case it can be seen a decrease in intensity with increasing illumination time, while in the second both signals are unaffected by illumination.

This seems to validate the hypothesis that the two signals are indeed related to each other. It is also worth mentioning that also the peak observable at around 200 °C is affected by the bleaching, but while the SBP is only affected by UV bleaching, this peak is affected by the blue illumination as well. As a side effect, it can also be seen the appearance of the 110 °C after UV illumination. This is due to a charge transfer that is happening during the illumination due to retrapping, known as Phototransfered Thermoluminescence (PTTL) (Bailiff et al., 1977). Since the illumination process is performed at room temperature, the electrons released from the SBP trap level into the conduction band, can be retrapped by empty trap levels, such as the ones from $[GeO_4]^-$. The fact that from the first illumination time the 110 °C TSL peak is also decreasing, is probably due to a competition between the retrapping process and the release from $[GeO_4]^-$ due to thermal instability, i.e. the level is depleting faster than it is repopulated during illumination. One could ask why it is not observable an increase of the $[GeO_4]^-$ signal in the EPR spectra after illumination. This is because the observed intensity of the 110 °C TSL peak is relatively low, despite seemingly comparable to the SBP. The sample has been annealed at 800 °C, and so the sensitivity of the TSL peaks has been strongly increased. A glow curve acquired without the 200 °C preheating would show a peak with an intensity at least two orders of magnitude larger than the one created by retrapping, so what it is being observed here is a very small effect that indeed does not seem to significantly affect the EPR spectrum. The effect is observed also during blue illumination, but in a much smaller amount, indicating that probably the charge is being transferred from the peak at 200 °C, which is slightly bleaching.

In literature it can found that the $[GeO_4/M^+]^0$ signal is actually due to many contributions, such as $[GeO_4/Li^+]^0_A$, $[GeO_4/Li^+]^0_C$, $[GeO_4/Na^+]^0_A$ and $[GeO_4/Na^+]^0_C$, but in the case of the studied sample it seems that the spectrum is composed by $[GeO_4/Li^+]^0_C$ by at least 70-75%. The g-factors reported in literature for the $[GeO_4/Li^+]_c^0$ signal do not show a full agreement on them, but the values here obtained by fitting with Easyspin, g_1=2.0001, g_2 =1.9974 and g_3 =1.9963, seems to be consistent by the ones published by Weil (1971), g_1 =2.0000, g_2=1.9973 and g_3 =1.9962. Additionally, during illumination there are not any appreciable changes in line shape in the EPR spectra, suggesting that every centre is bleaching at the same rate.

To summarize, the experiment showed a striking correspondence between the SBP and the $[GeO_4/Li^+]^0$ signal under UV illumination. This fact could be extremely important in the field of dating of fired materials (pottery, ceramics, etc.), because of the dosimetric applications of the SBP. It raises also the issue that even partial bleaching of the sample (e.g. under sun light) could lead to errors in the dating experiments.

7. Investigation of the Spectrally resolved TSL peaks of quartz in the 70 °C-220 °C temperature region

In this thesis work, it has been studied the TSL emission in the temperature range of 70 °C-220 °C in different types of quartz, both natural and synthetic. In this temperature region, at least three different TSL peaks could be observed, one of them being the already mentioned 110 °C TSL peak of quartz and the other two observed at around 150 °C and 200 °C. A batch of each sample has also been annealed, in order to study the sensitization of the TSL emission. The interest has also been put on the wavelength of the TSL emission, done by usage of PMT equipped different optical filters (Risø TL/OSL reader setup) and CCD for WR-TSL. The experiment also put to test a theoretical model to describe different wavelength emissions for different TSL peaks proposed by Williams and Spooner (2018).

As shown in section 3 of this work, quartz samples can show sensitization and desensitization of its emission processes. This can affect in different ways different recombination centres. Martini et al. (2014), through RL measurements, were able to characterize a good number of the emission bands of quartz, obtaining the wavelength of emission and the full width at half maximum (FWHM) of them. Their result is reported in Tab. 7.1. This data has been used as a reference for the analysis of the emission bands during TSL.

The results reported in this section have been published in Monti et al. (2019).

Band Name	Wavelength (nm)	Energy (eV)	FWHM (eV)
O	635	1.92	0.39
A	490	2.51	0.46
B	440	2.79	0.46
X	395	3.06	0.89
C	360	3.42	0.58
M	330	3.73	0.45
D	315	3.93	0.49

Table 7.1: *Parameters of the characterized emission bands of quartz. Values from Martini et al., 2014.*

7.1 Experiment procedure

7.1.1 Samples

For this experiments, four different quartz samples have been used. Two of them are of natural hydrothermal growth, Nat-01 and smoky quartz, and two synthetic ones, swept and unswept, already described in the previous sections. The measurements were done on powders of these samples, with

batches of them annealed at 500 °C and 1000 °C for 10 minutes and rapidly cooled at room temperature in air.

Before the experiment, each sample has been irradiated with 80 Gy of beta-rays and then heated from room temperature to 220 °C at 5 °C/s. This procedure was intended to create a common starting point both in natural samples, which had received a natural dose, and in synthetic samples, in order to minimize their differences and better compare their properties.

7.1.2 PMT measurements

This part of the experiment has been realized with the Risø TL/OSL reader setup. Each sample was irradiated with 2 Gy with the beta source incorporated in the instrument, and then the glow curve was recorded at 5 °C/s, with acquisitions every 1 °C. The dose was chosen in order to reduce as much as possible the desensitization of the so-called C-band in the UV emission, expected in annealed samples (Martini et al., 2012a). To discern the two main emissions in quartz, the A-band (blue emission at 2.51 eV) and the C-band (UV emission at 3.42 eV), two different optical filters were used: two interference filters centred at 365 nm and 450 nm, 3CGIX and FB450 (FWHM 15 nm and 40 nm respectively, transmittance spectra reported in Appendix, Fig. A2). It is remarked that these filters have different bandwidth and different physical dimension, and for this reason a direct comparison of the results obtained from their absolute intensities is not possible. In general, considering the filter used, the instrumental sensitivity is larger in the blue region when compared to the UV. This part of the experiment was done because the emission intensities were rather weak and the WR-TSL equipment was not able to detect the TSL emission for every sample.

7.1.3 WR-TSL measurements

With the samples presenting higher emission intensity, the experiment has been realized with the WR-TSL equipment described in section 4, using the 150 lines/mm diffraction grating. The glow curves were acquired with a heating rate of 1 °C/s, with acquisitions made by integrating the recorded signal every 3 °C. The high intensity in the UV region around 360 nm, was enough to create significant second order diffraction signals in the 650-700 nm region and for that reason each experiment was repeated a second time on each aliquot by applying between the sample and the detector a long pass filter that blocks wavelength shorted than 418 nm (KV418 Schott filter produced by ITOS, Appendix, Fig. A3). The two spectra were then combined to obtain the full emission spectrum for each sample. Due to the significantly lower sensitivity of the equipment when compared to a traditional TSL apparatus that uses a PMT, a larger dose had to be delivered to the samples (about 50 Gy of beta rays).

7.2 Results

7.2.1 PMT results

These measurements gave an insight on the effects that the annealing have on the different emissions. The results obtained with the Risø TL/OSL reader are reported in Fig. 7.1 and 7.2, in absolute and

semilog scales, respectively. The semilog scale helps to compare the intensity between different thermal treatments and different samples. The figures also show separately the results obtained with the UV and the blue filter. Previous works have already shown a sensitization of the UV emissions after heating the sample in the 300-1200 °C temperature region (Bøtter-Jensen et al., 1995, Martini et al., 2014). That said, reminding that a direct comparison of the absolute intensity cannot be done, some major and minor observations can be made on the data. Major observations are:
1-In the untreated samples, both natural and synthetic, no signal is detected in the UV region (Fig. 1, first column).

2-In the blue, an emission is detected in all the untreated samples (Fig. 1, second column), either natural or synthetic, both in the 110 °C TSL peak, the main TSL emission, observed in this work at around 85 °C, and for the swept out sample in the higher temperature ones, around 150 °C and 200 °C. Surprisingly the most intense blue emission is observed in the swept out synthetic sample (Fig. 1, d-2).

3-The treatment at 500 °C does not significantly affect the emission intensity of the synthetic samples, neither in the blue nor in the UV. On the contrary, the 500 °C treatment strongly enhances both the blue and the UV emissions in the natural samples (Fig. 1, a and b).

4-The highest emission intensity is observed for samples treated at 1000 °C. Nonetheless, it can be observed that in the natural samples (Fig. 1, a and b) the already intense emissions reached after a 500 °C treatment was only slightly increased as a consequence of the 1000 °C treatment (both UV and blue), as far as the 110 °C TSL peak is considered. Much higher growth is observed in the blue and UV range, for the TSL peaks at higher temperature.

5-For the synthetic samples, a UV emission is detected in the unswept sample after the 1000 °C treatment (Fig. 1, c-1), while a very limited signal increase is observed in the swept sample (Fig.1, d-1). The swept-out sample shows the lowest signal (both UV and blue) among the batches annealed at 1000 °C (Fig. 1, d). Contrary, in the same samples a very intense blue signal is detected after the 1000 °C treatment (Fig. 1, c-2 and d-2). The signal intensity is of the same order of magnitude as the one observed in the natural samples and, similarly to the natural samples (Fig. 1, a-2 and b-2), the intensity increase is more evident in the 150 °C and 200 °C TSL peaks rather than in the 110 °C one.

Analysing in more detail the glow curves obtained one can notice also some minor facts. First of all, in the 1000 °C treated batches at least another peak becomes evident at a temperature lower than the 110 °C peak maximum position. This effect is more evident in the natural samples where a shoulder on the low temperature side of the 110 °C peak is particularly evident. The blue signal of the Nat-01 untreated batch, one can observe a signal shoulder above 125 °C probably due to the natural dose accumulated by quartz over millennia of exposure to natural radiation and only partially erased by

the initial thermal treatment at 220 °C. It must also be pointed out that the blue signal of the untreated swept batch shows a significantly more intense TSL signal compared to all the other untreated samples by more than an order of magnitude.

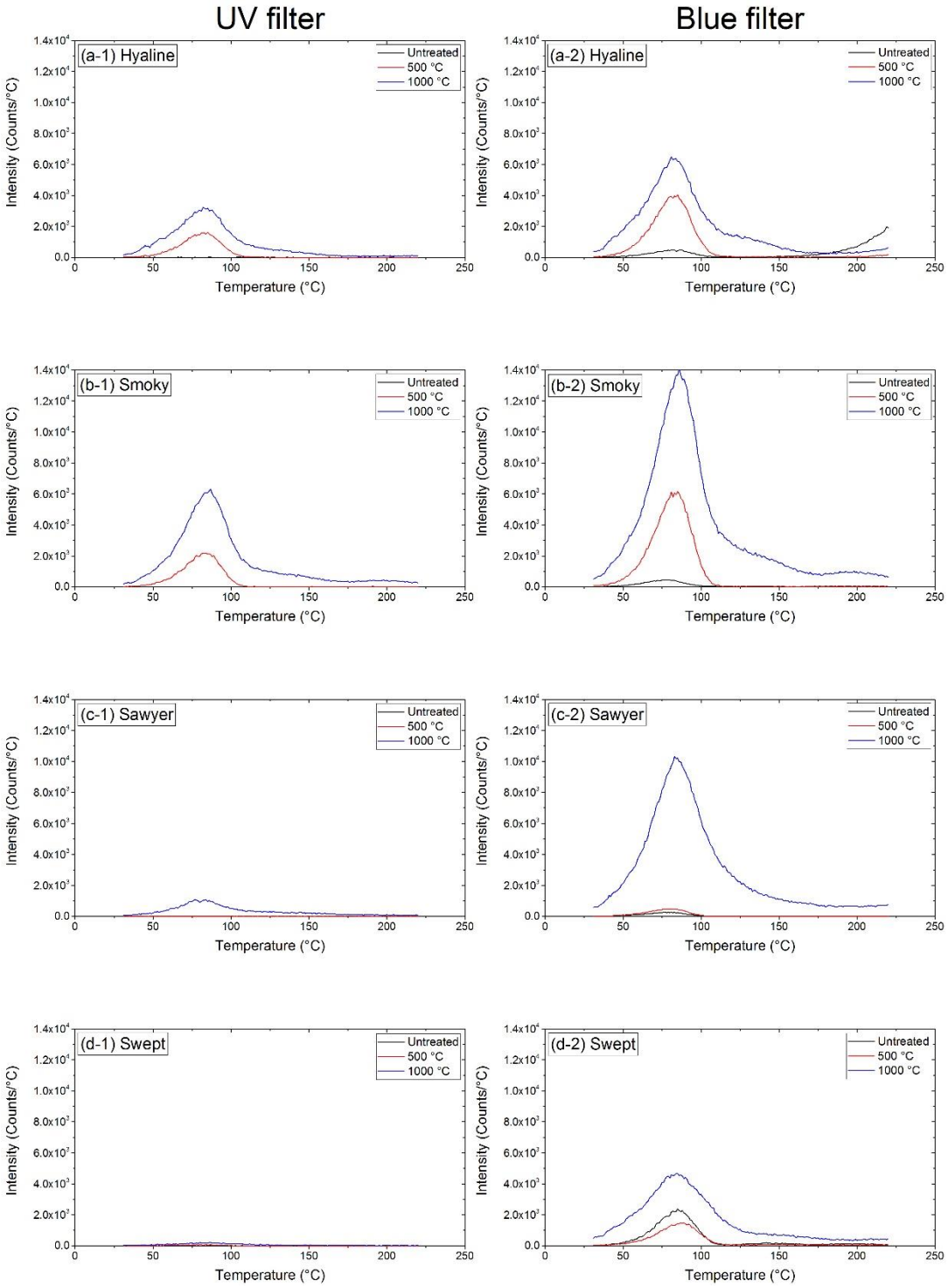

Fig.7.1*: Glow curves of (a) Nat-01, (b) smoky quartz, (c) sawyer quartz and (d) sawyer swept quartz observed with a UV interference filter (365±8 nm), left column, and with a blue interference filter (450±20 nm), right column. Black curves are for untreated batches, red ones for batches treated at 500 °C and blue ones for batches treated at 1000 °C. The samples have been irradiated with 80 Gy, heated to 220 °C, irradiated with 2 Gy and then the TSL was acquired at 5 °C/s.*

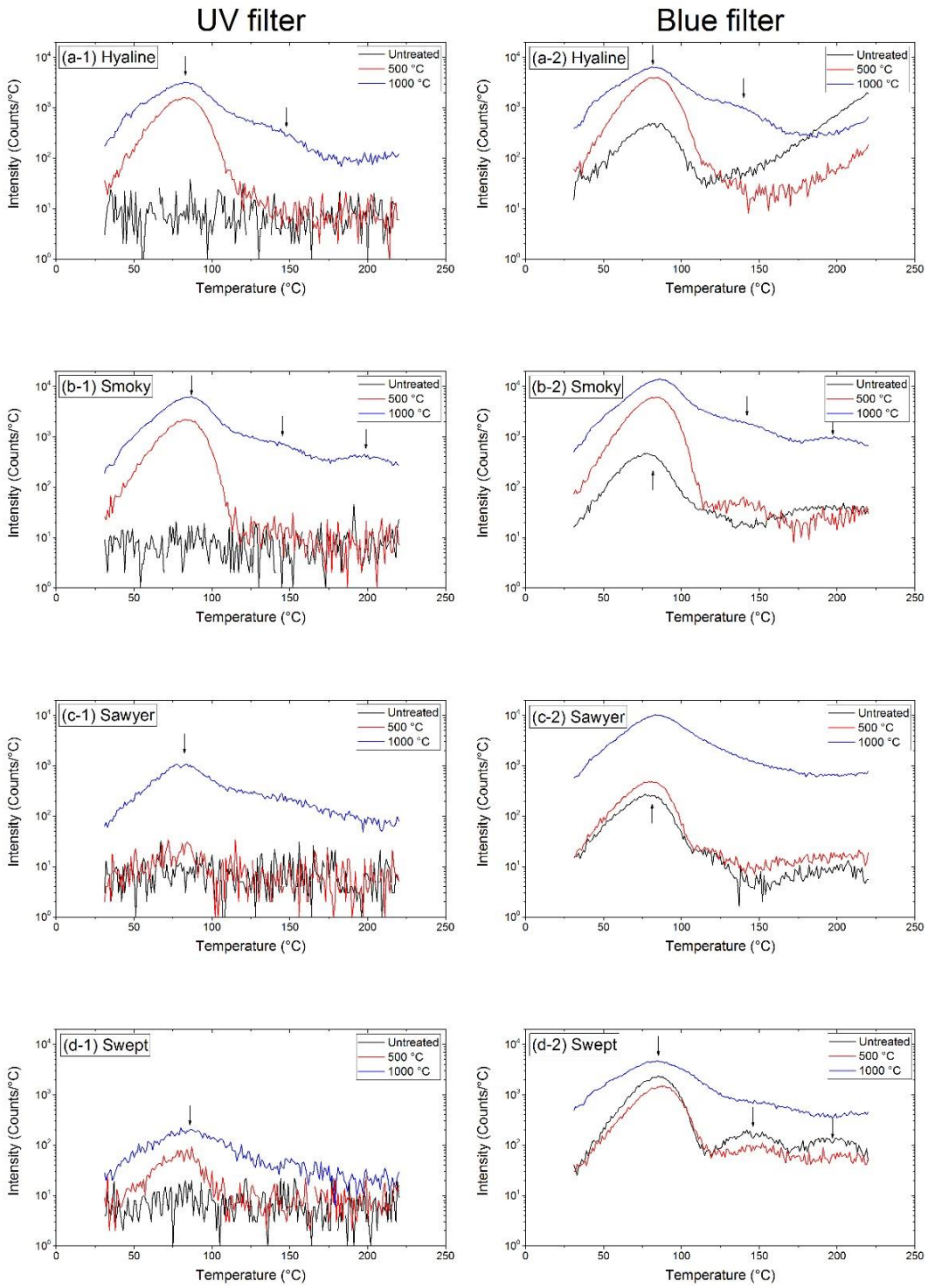

***Fig.7.2**: Glow curves in semilog scale of (a) Nat-01, (b) smoky quartz, (c) sawyer quartz and (d) sawyer swept quartz observed with a UV interference filter (365±8 nm), left column, and with a blue interference filter (450±20 nm), right column. Black curves are for untreated batches, red ones for batches treated at 500 °C and blue ones for batches treated at 1000 °C. The samples have been irradiated with 80 Gy, heated to 220 °C, irradiated with 2 Gy and then the TSL was acquired at 5 °C/s. The peaks referred in text as "at 110 °C, 150 °C and 200 °C" have been highlighted with arrows.*

7.2.2 Wavelength resolved TSL results

Due to the lower sensitivity of the WR-TSL, when compared to common TSL using PMTs, it was

only possible to acquire significant data for the samples annealed at 1000 °C. The contour-plots of the raw TSL measurements are reported in Fig. 7.3-7.6 (without the KV418 filter). In these graphs, one can notice the 110 °C TSL peak, here observed at around 80 °C, and two higher temperature peaks at around 140 °C and 190 °C. The smoky quartz sample, Fig. 7.4, is the one with the higher intensities, which can give more reliable analysis, while the swept sample shows very low intensity and only the 110 °C TSL peak is barely visible and will not be further analysed. It is evident at first glance though, that in the natural samples the main emission is in the UV, while for the synthetic one is in the blue. This is consistent with literature publications about RL measurements such as Martini et al. (2014) for the UV dominance in natural samples and such as Martini et al. (2012b, untreated samples) and Chithambo and Niyonzima (2017, annealed samples). It is also evident that in every sample the 110 °C TSL peak possesses a broader emission when compared to the higher temperature ones.

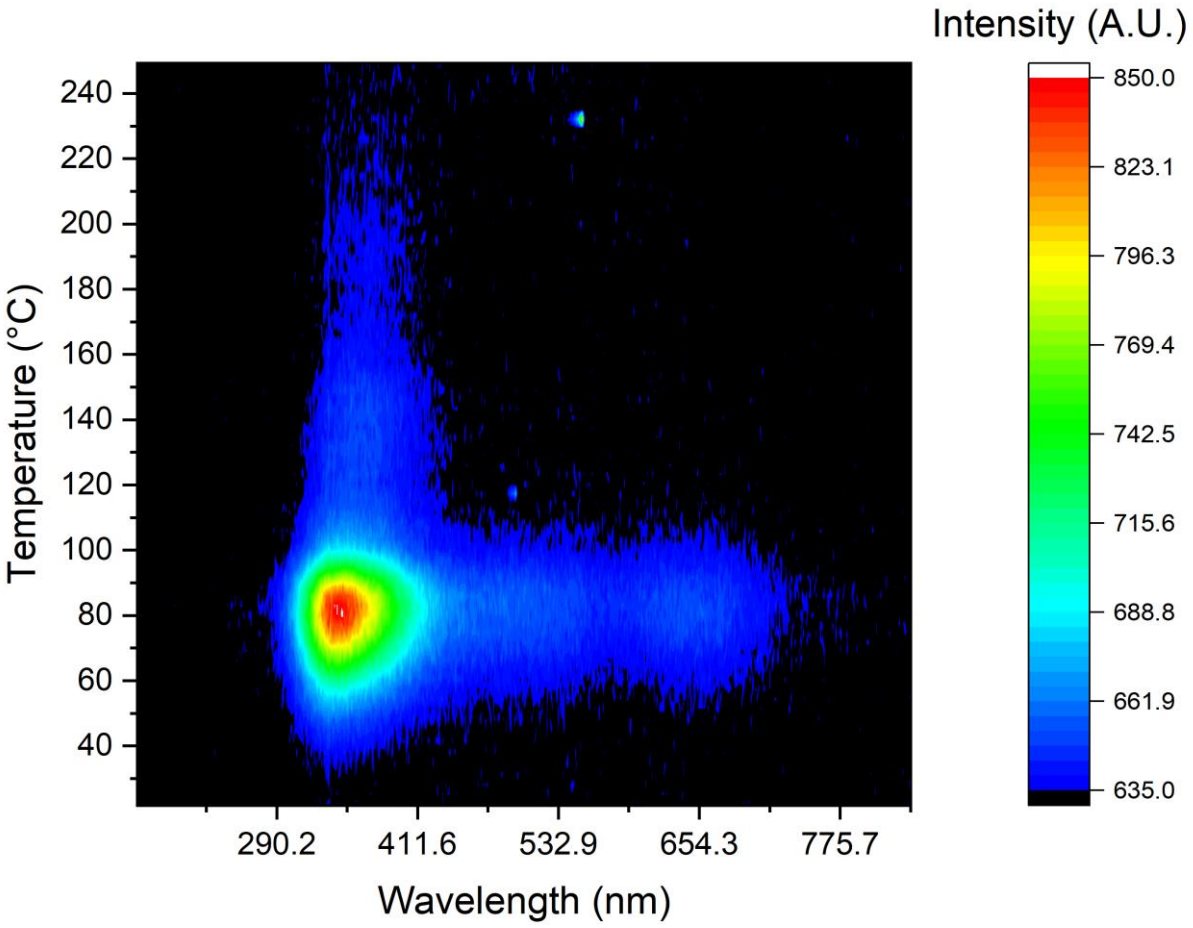

***Fig. 7.3**: Contour-plot of the WR-TSL on Nat-01 annealed at 1000 °C. TSL acquired at 1 °C/s.*

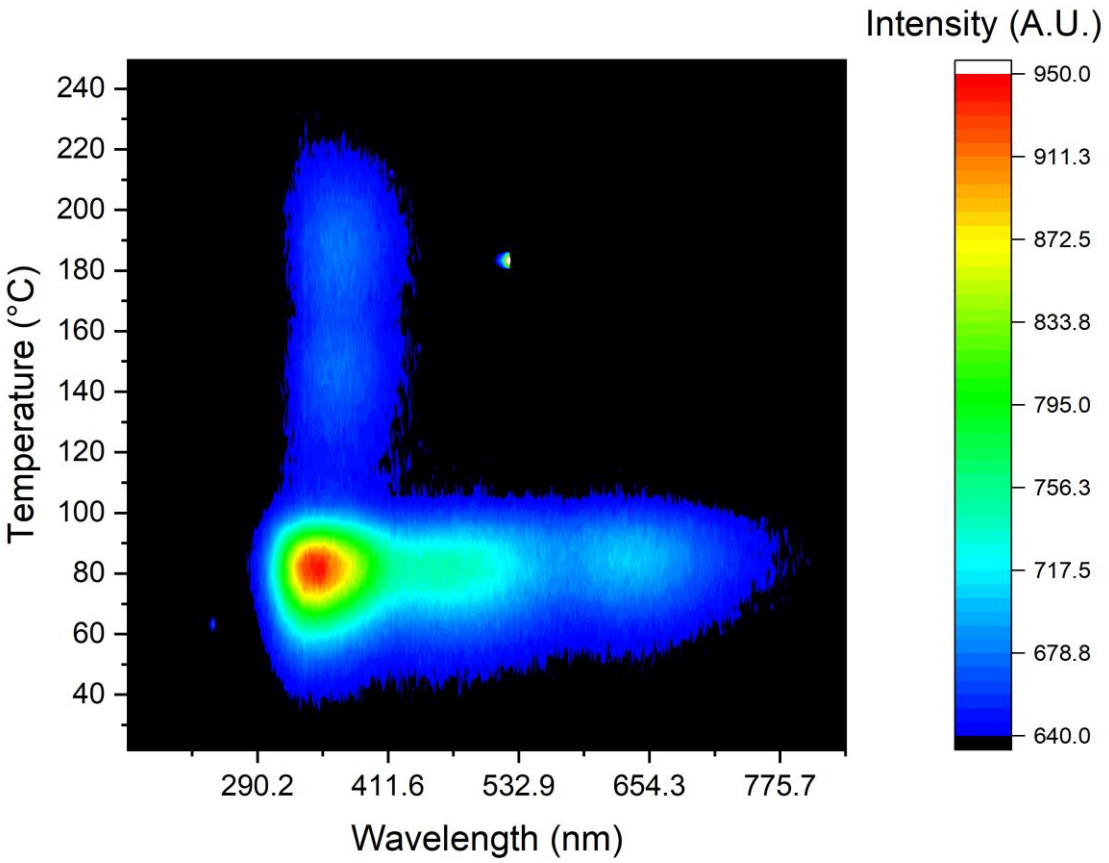

***Fig. 7.4**: Contour-plot of the WR-TSL on smoky quartz annealed at 1000 °C. TSL acquired at 1 °C/s.*

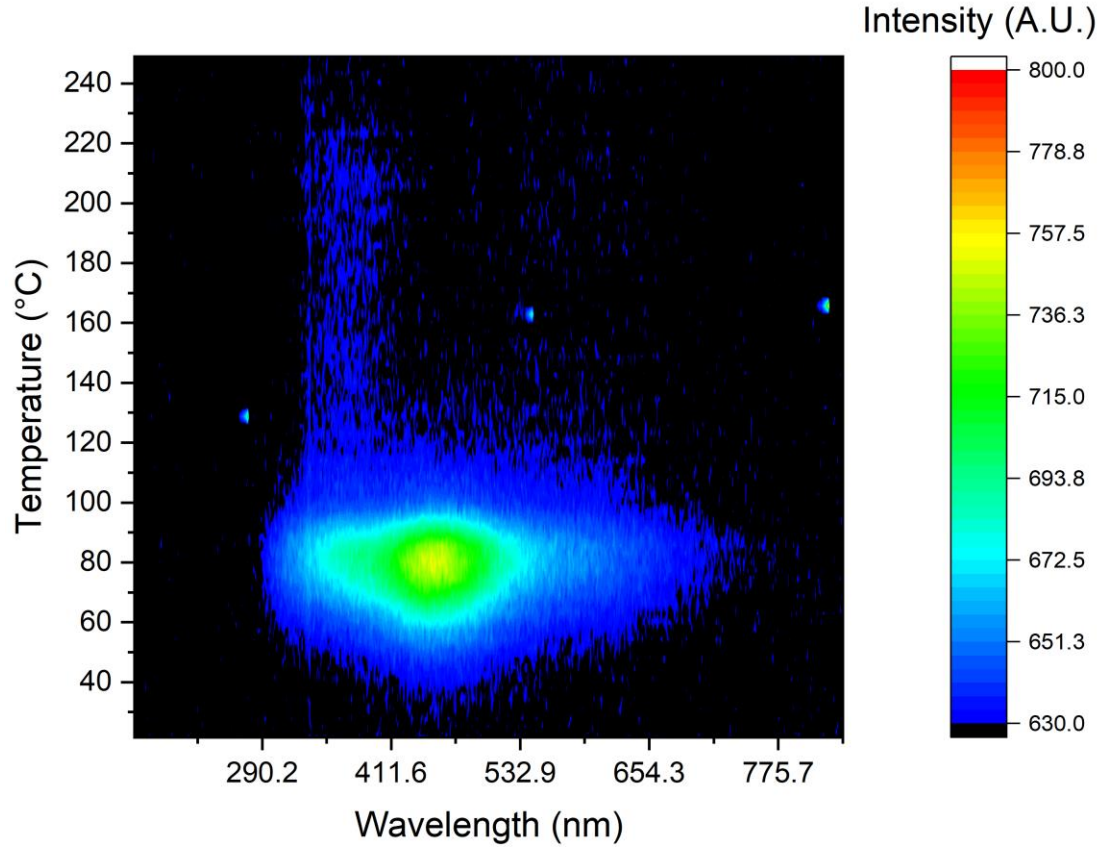

***Fig. 7.5**: Contour-plot of the WR-TSL on sawyer quartz annealed at 1000 °C. TSL acquired at 1 °C/s.*

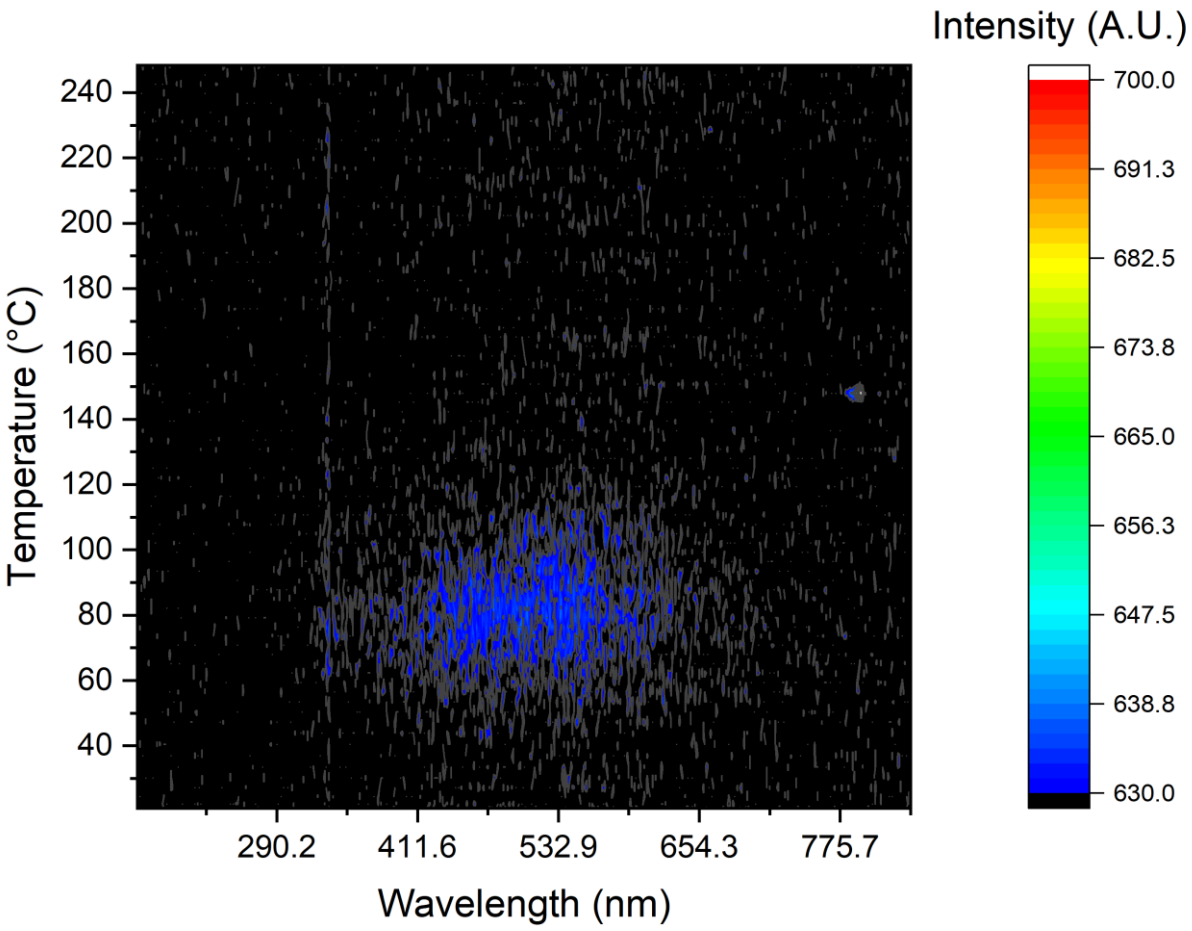

***Fig. 7.6**: Contour-plot of the WR-TSL on swept quartz annealed at 1000 °C. TSL acquired at 1 °C/s.*

To better appreciate the spectral components of each peak, the data has been integrated across three different temperature ranges: 50 °C-110 °C, 130 °C-170 °C and 170 °C-220 °C. The intensities have then been corrected by taking into account the detection system efficiency at different wavelengths, normalized and reported in Fig. 7.7 as a function of energy. For the higher temperature peaks, the spectra have been cut below 2.5 eV, due to the high signal-to-noise ratio which made the picture unreadable. The subtracted background is the average of the flat high energy region of the acquired spectra, beyond 5 eV (not reported in the figures). The spectra have then been decomposed in their basic components by using the parameters reported in Tab. 7.1. The results are reported in Fig. 7.8-7.10. Due to the high number of parameters to optimize, it is indeed reasonable to expect a high error in these decompositions, but nonetheless it is possible to obtain important information from them under a qualitative point of view. In fact, it is evident the difference between the 110 °C TSL peak and the higher temperature peaks. In the first case, the emission is very sample dependant. The 110 °C TSL peaks in the Nat-01 sample there is a broad UV emission involving different components, in the smoky sample it possesses also significant blue and red components, and, in the sawyer sample, the blue component is the dominant one. The higher temperature peaks instead, seems to be composed, in every sample, by a single component, namely the so-called C-band (3.4 eV).

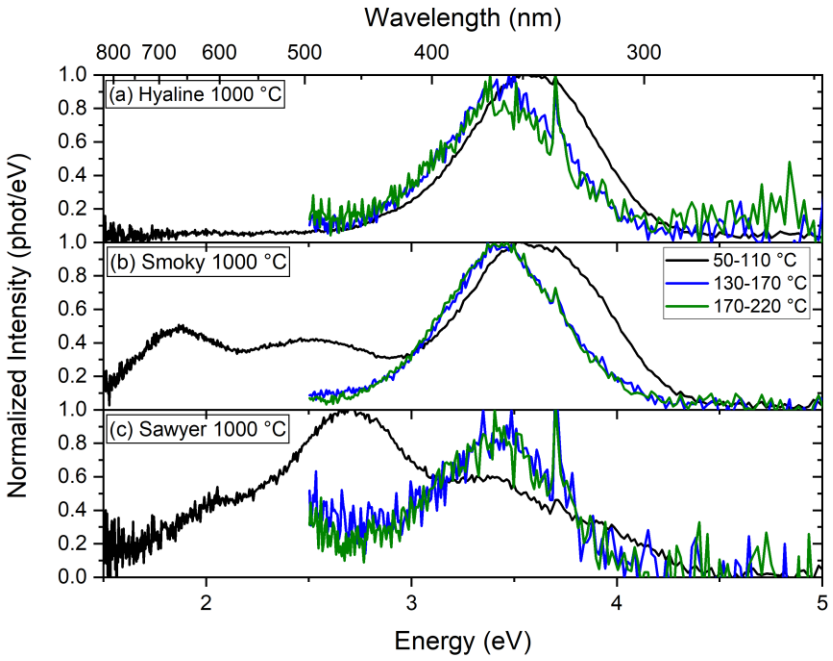

***Fig. 7.7**: Spectra of (a) Nat-01, (b) smoky quartz and (c) sawyer quartz of the 110 °C TSL peak (black line, temperature range between 50 °C and 110 °C), of the peaks at 150 °C (blue line, temperature range between 130 °C and 170 °C) and at 200 °C (green line, temperature range between 170 °C and 220 °C). The graphs present a composed spectrum from two different measurements, one of which realized with a Schott KV418 filter in order to avoid interference from diffraction second order from the UV emission in the visible region intensity.*

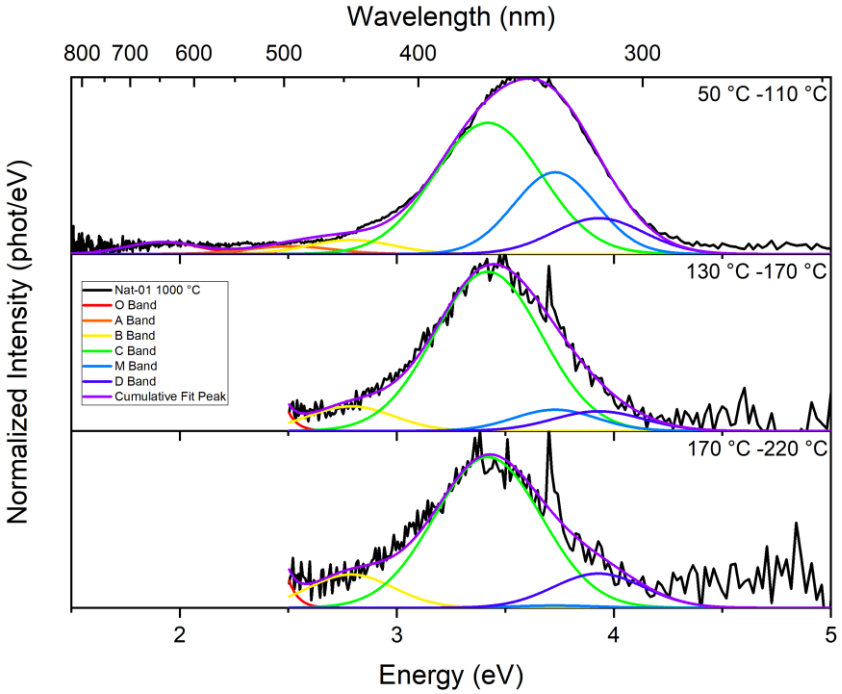

***Fig. 7.8**: Spectral decomposition of the WR-TSL for the Nat-01 sample annealed at 1000 °C. From top to bottom are shown the decomposition of the spectra in the 50 °C-110 °C region, the 130 °C-170 °C region and the 170 °C-220 °C region.*

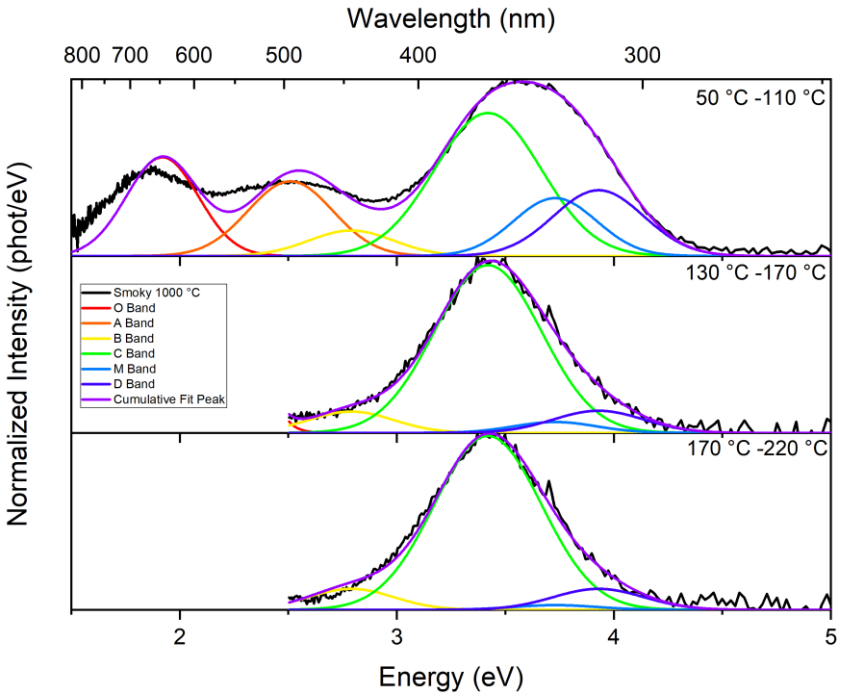

***Fig. 7.9**: Spectral decomposition of the WR-TSL for the smoky quartz sample annealed at 1000 °C. From top to bottom are shown the decomposition of the spectra in the 50 °C-110 °C region, the 130 °C-170 °C region and the 170 °C-220 °C region.*

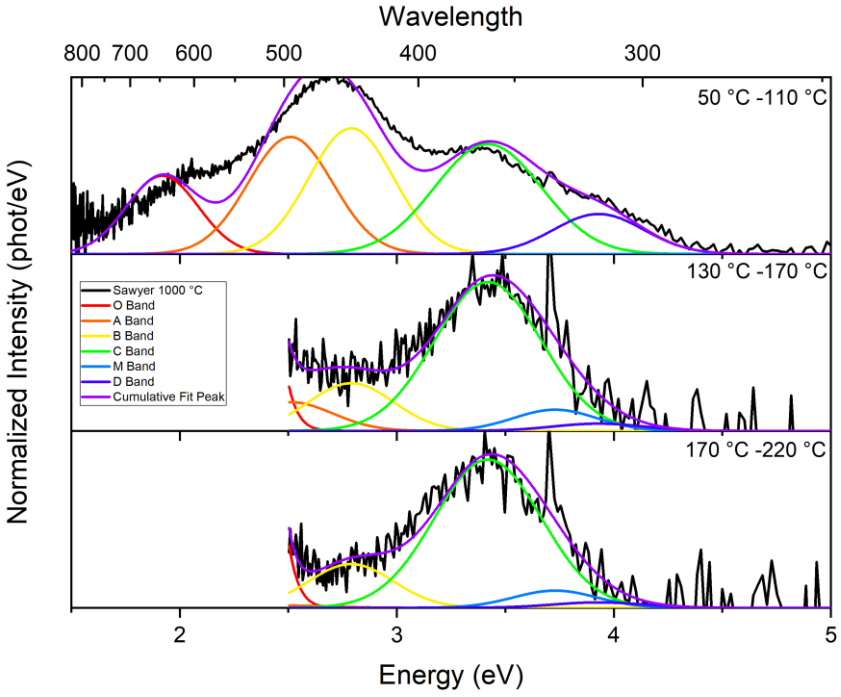

***Fig. 7.10**: Spectral decomposition of the WR-TSL for the sawyer quartz sample annealed at 1000 °C. From top to bottom are shown the decomposition of the spectra in the 50 °C-110 °C region, the 130 °C-170 °C region and the 170 °C-220 °C region.*

7.3 Comments

The effect of thermal treatments on the TSL emission of different quartz samples has been reported. After annealing at 500 °C and 1000 °C, an increase in their TSL sensitivity has been observed, partially confirming the results already reported by several authors (Rendell et al. 1994, Schilles et al., 2001, F de Lima et al., 2002). However, it should be noted that an increase of the TSL sensitivity

is generally reported in the UV emission (Rendell et al. 1994, Schilles et al., 2001, F de Lima et al., 2002) and not frequently in the blue region (Schilles et al., 2001, F de Lima et al., 2002). Moreover, it seems that the 110 °C TSL peak of quartz is likely composite in samples treated at 1000 °C, meaning that its signal is a contribution from different trapping centres generating strong overlapping of TSL peaks. This is more evident looking at Fig. 7.2, where it can be seen that there are deviations from the exponential rise in the first part of the peak in the samples annealed at 1000 °C. This has indeed already been proposed, but it is still under debate (Petrov and Bailiff, 1995, Koul, 2008 and references therein) and given the results shown in section 5 it seems a reasonable conclusion. At lower annealing temperature, however, the 110 °C TSL peak can be easily described by a single trap following first order kinetic, in agreement with the single exponential decay behaviour observed for this peak (Vaccaro et al., 2017).

In the literature, at least two different models have been put forth in order to explain the TSL signal enhancement as an effect of annealing (Zimmerman, 1971, Schilles et al., 2001), suggesting that the thermal treatment either makes more recombination centres available (such as in the pre-dose effect mentioned in section 3) or removes non-radiative recombination centres competing with the luminescent ones. One of such competing centres was proposed to be the E' centre, which is annealed out at about 500 °C (Schilles et al., 2001, Benny et al., 2002). The high intensity of the blue emission in the untreated batch of the swept sample seems, then, to be in agreement with the interpretation of enhanced sensitivity due to the low concentration of competing centres. However, the sensitivity enhancement here observed is generally higher in the UV region, therefore the non-radiative centre should be in competition mostly with the UV recombination centre. More probably, however, is that both the proposed mechanisms for luminescence enhancement occur simultaneously.

The TSL emission spectra reported in Fig. 7.7 show significantly different shapes among the samples. In particular, the natural samples show an emission dominated by UV components. Given the asymmetric shape of the band and the apparent maximum detected at an intermediate energy between the so called C and M bands (3.42 eV and 3.73 eV respectively), it can be assumed that the UV emission is due to the superposition of both C and M bands as previously observed (Fasoli and Martini, 2016). In the case of synthetic unswept crystal, the main TSL emission occurs in the blue region. Even in this case, the emission maximum is observed at intermediate energy between the so-called A and B bands (2.51 eV and 2.79 eV respectively). However, the signal is too weak to allow a reliable deconvolution of the spectrum and it can be seen in Fig. 7.10 that the cumulative fit is not as consistent with the data as other samples UV dominated. It is interesting to remind that despite the B band has been clearly observed in RL emission of quartz (Martini et al., 2014), strong evidence of its contribution also to TSL emission spectra is still missing. Moving to the red region, an emission band, centred on about 1.85 eV is detected in the smoky quartz sample. A red emission has already been reported in the literature at various positions (Hashimoto et al., 1986, 1987, 2007 and 2008, Petrov

and Bailiff, 1995, Spooner and Questiaux, 2000, Schilles et al., 2001, Koul, 2008). Having done the measurement with the KV418 filter, makes it clear that it is a true emission and not an instrumental artefact induced by diffraction, as in the case of the Nat-01 sample, where the red region becomes flat after applying the filter.

Considering now the TSL emissions of the peaks at 150 °C and 200 °C, it is very clear, despite the low signal to noise ratio, that the spectra are very similar in all of the samples. The emission is dominated by a single UV symmetric emission centred at 3.42 eV, which is the characteristic energy of the C band. This is evident already from Fig. 7.7 and confirmed by the decompositions in Fig. 7.8-7.10. Interestingly, no blue emissions are detected for the higher temperature TSL peaks. In the red region, the signal to noise ratio is too low to allow any comment. The fact that the M band is observed only for the 110 °C TSL peak and not for the peaks at higher temperature may be explained by thermal quenching (Curie, 1963). Many works in the literature show that generic UV emission is significantly affected by this phenomenon (Nanjundaswamy et al., 2002). However, thermal quenching is known to not significantly affect the blue emission which was found to be still efficient at much higher temperature, up to 375 °C (Wintle, 1975), therefore it cannot explain why, in Sawyer and Smoky quartz (Fig. 7.5, 7.6 and 7.7), a blue emission is observed in the 110 °C TSL peak emission and not in the higher temperature ones. The quenching energy of the blue emission has been estimated as higher than the one of the UV emission, so it should be expected the vanishing of the UV emission first, and not the blue one as observed. However, it must be specified that the filters used in such studies had rather large spectral windows, unable to separate the contributions of the two different UV bands (M and C) although could discriminate between the blue and the UV emissions (blue and UV emissions: Wintle, 1975, Nanjundaswamy et al., 2002; blue emission: Friedrich et al., 2018).

In order to explain the presented experimental data, it could be considered the presence of spatial correlation between the point defects involved, traps and recombination centres, for some of the observed peaks. In the case of the 110 °C peak it can be assumed that the trapped electrons are released to the conduction band and, once delocalized, they can migrate and easily reach any available recombination centre. Therefore, the UV bands (C and M), the blue and red emissions are all detected. In the case of the peaks at 150 °C and 200 °C, it can be speculated that the traps and recombination centres (specifically those responsible for the C band) are spatially close to each other. Therefore, once the electrons are thermally released from the traps, they directly recombine with the nearby recombination centres with no involvement of the conduction band. This could happen with a thermally assisted tunnel effect, for example, with the result of a TSL spectrum showing only the C band. At the moment there is not though experimental data that could confirm or deny this hypothesis, or even point to a different one. A similar model was proposed by Itoh et al. (2002), which can be referred to as a defect pair recombination model, used to explain the different emissions between the

110 °C and the 325 °C TSL peaks of quartz. The authors proposed that the 110 °C TSL peak would arise from an electron-hole recombination at $[AlO_4]^-$ centres, while the 325 °C one would arise after an ionic migration of an alkali ion M^+.

In a recent work (Williams and Spooner, 2018), a different explanation of the apparent shift of TSL emission spectrum in the temperature range 100 °C-200 °C was proposed, which was previously observed (Krbetschek et al, 1997, and references therein). The authors proposed that the recombination of all the three TSL peaks in that temperature region occurs at the same point defect, specifically the $[AlO_4/h^+]^0$ centre. Once the electron is captured, the emission involves three different excited states of the resulting $[AlO_4]^-$ centre, each one emitting at three different wavelengths progressively increasing with temperature. The results presented in this section, however, seem not to confirm Williams' model. In the presented samples, the emissions of the two TSL peaks at higher temperature (150 °C and 200 °C) are identical, involving a single band (the C one). In contrast, the 110 °C peak's emission is composite and, in the UV, is due to the superposition of the same C band at 3.42 eV and the M one at 3.73 eV as evidenced in a previous work (Fasoli and Martini, 2016).

A possible experiment that could be performed in the future to confirm the spatial correlation could be measuring thermally stimulated conductivity (TSC) in the same kind of sample and comparing the results with the TSL glow curves in this section. The presence, or absence, of TSC peaks could give more insights that could justify or refute the proposed model.

To summarize, the glow curves, in the temperature range from 70 °C to 220 °C, of different types of quartz were investigated. In both natural and synthetic quartz, a blue emission is already present in untreated samples, while UV emissions appear only after thermal treatments. Samples heated up to 1000 °C show the highest emission sensitivity both in the blue and in the UV. The effect of annealing at 500 °C and 1000 °C were considered. The comparison of TSL spectra of three peaks at 85 °C (the "110°C), 150 °C and 200 °C (heating rate 5 °C/s) revealed significant differences. The emission of the 110 °C TSL peak involves several bands, two in the UV region (the C band at 3.42 eV and the M band at 3.73) together with other contributions in the blue region and, for the smoky quartz, also in the red one. By contrast, the emission of the two TSL peaks at higher temperature, 150 °C and 200 °C consist only of a single UV band, the C one at 3.42 eV. These results may be explained by direct recombination from the traps responsible for the higher temperature peaks and the luminescent centre, without involving the conduction band. The data presented, therefore, could not confirm the model by Williams and Spooner (2018), assuming a single point defect with multiple energy levels as the origin for multiple TSL emissions.

8. Sensitivity changes of RL of natural and synthetic quartz

Following the analysis presented in section 7, in this thesis work it was also analysed, on the same samples, how the sensitivity of the different emission bands of quartz (Martini et al., 2014) change during an RL experiment. As already mentioned in the previous sections, each emission band can experience either sensitization or desensitization processes during irradiation.

8.1 Experiment procedure

8.1.1 Samples

The samples used for these measurements are the same described in section 7.1.1.

8.1.2 RL measurements

The RL experiment has been performed with the RL apparatus described in section 4.3. The X-ray tube has been set at a tension between the anode and the cathode of 20 kV and a filament current of 20 mA. In these conditions, the dose rate experienced by the samples is roughly 0.2 Gy/s. The detector has then been set to acquire each spectrum every 30 s, for a total of 50 cycles (6 Gy/cycle, for a total of 300 Gy). The spectra have been then converted to a function of energy, and corrected according to the CCD wavelength sensitivity, previously calibrated. Through a MatLab script, the spectra have been fitted using the parameters reported in Tab. 7.1, in order to obtain the contribution of each component to the overall spectrum of each acquisition. This allowed to obtain the dose dependence of the sensitivity of each component.

8.2 Results

On the top part of Fig. 8.1-8.12 are reported the spectra obtained from the RL measurements after the correction. A colour scale that goes from red, to green, to blue has been used to show the progression of the spectrum during the experiment. A matlab script has been then run to calculate the contribution of each component, by using a Trust-Region algorithm and approximating each component to a gaussian distribution described by the parameters in Tab. 7.1. In the bottom part of Fig. 8.1-8-12 are reported then the respective curves obtained by fitting. In Fig. 8.13-24 the relative intensity of each component as a function of dose are reported. Due to the high number of parameters to optimize in the fitting process, it is to be expected a certain degree of error. Nonetheless, the results may be useful in order to obtain a qualitative view of the sensitivity of each component. Some trends are indeed observable, which lead to believe that the shown information possess a certain degree of reliability. The spikes present on the spectra are very likely originated by electrical interferences of discharge caused by the interaction of the detector with cosmic rays and spurious emissions from air molecules still in the chamber interacting with the X-rays.

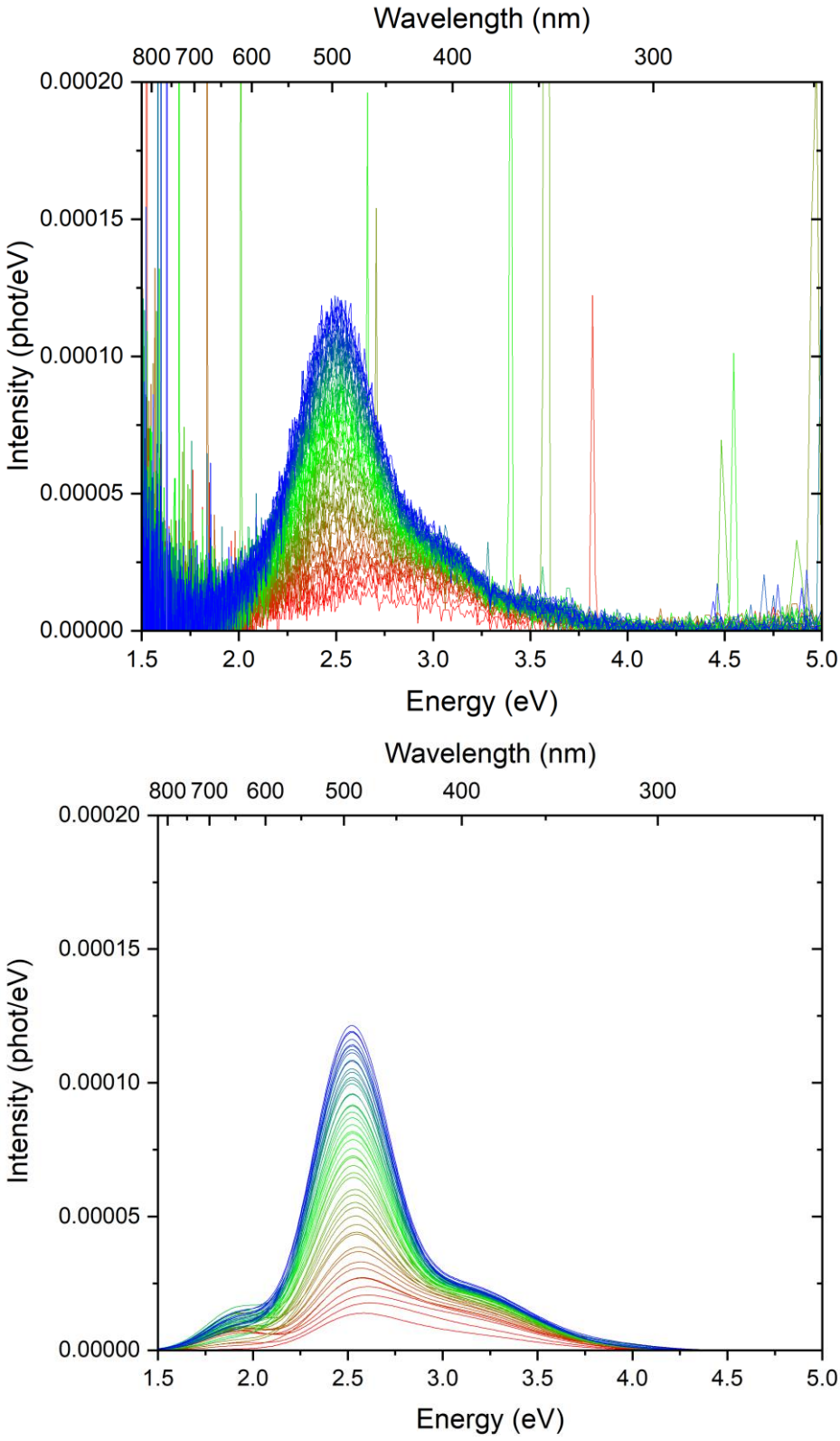

Fig. 8.1*: (top) RL spectra acquired from untreated Nat-01. Each curve represents the total emission acquired during 6 Gy of X-ray irradiation. The colour scale red-green-blue indicates the progression of the total dose absorbed; (bottom) Relative curves obtained by fitting.*

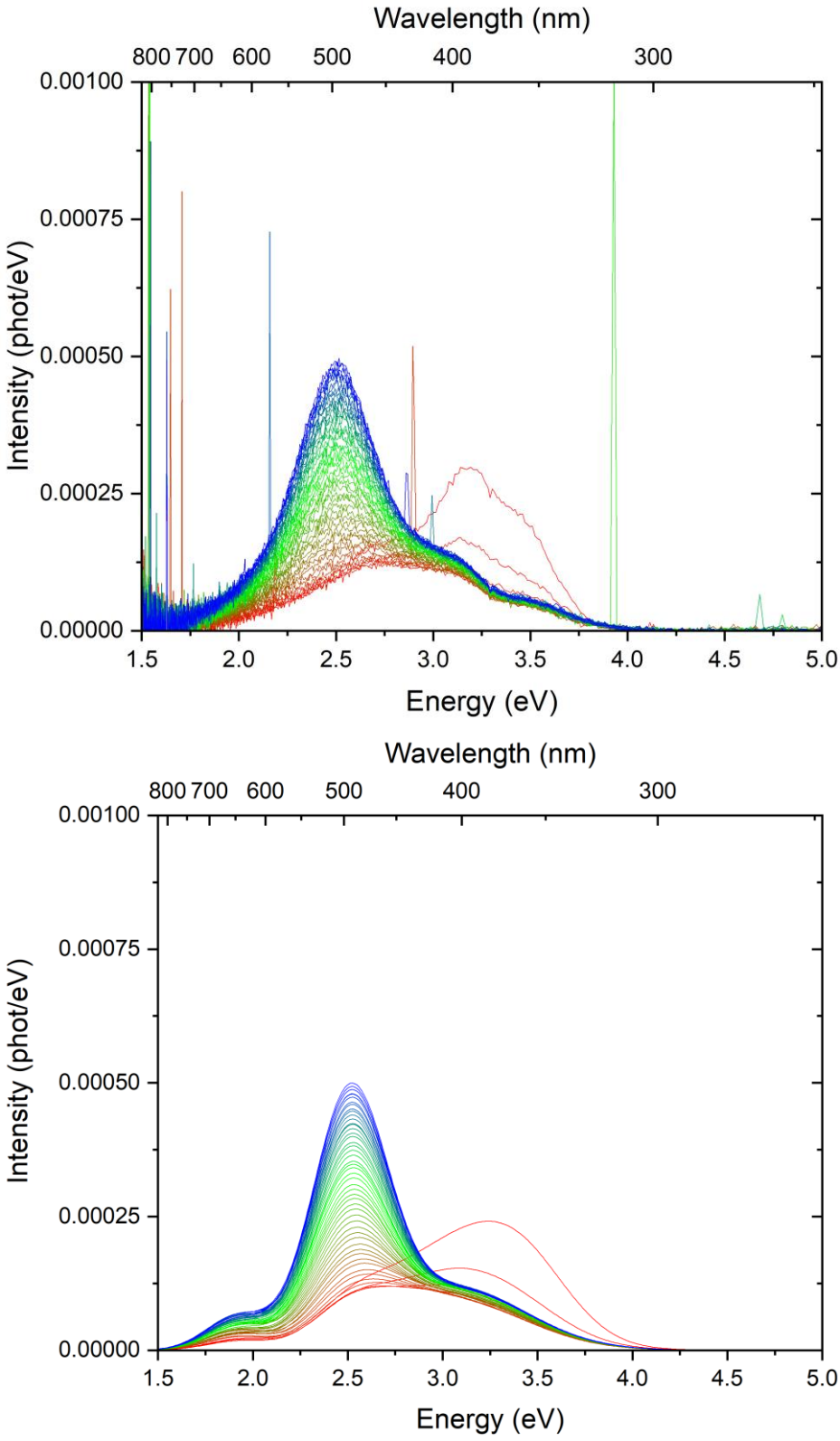

***Fig. 8.2**: (top) RL spectra acquired from Nat-01 treated at 500 °C. Each curve represents the total emission acquired during 6 Gy of X-ray irradiation. The colour scale red-green-blue indicates the progression of the total dose absorbed; (bottom) Relative curves obtained by fitting.*

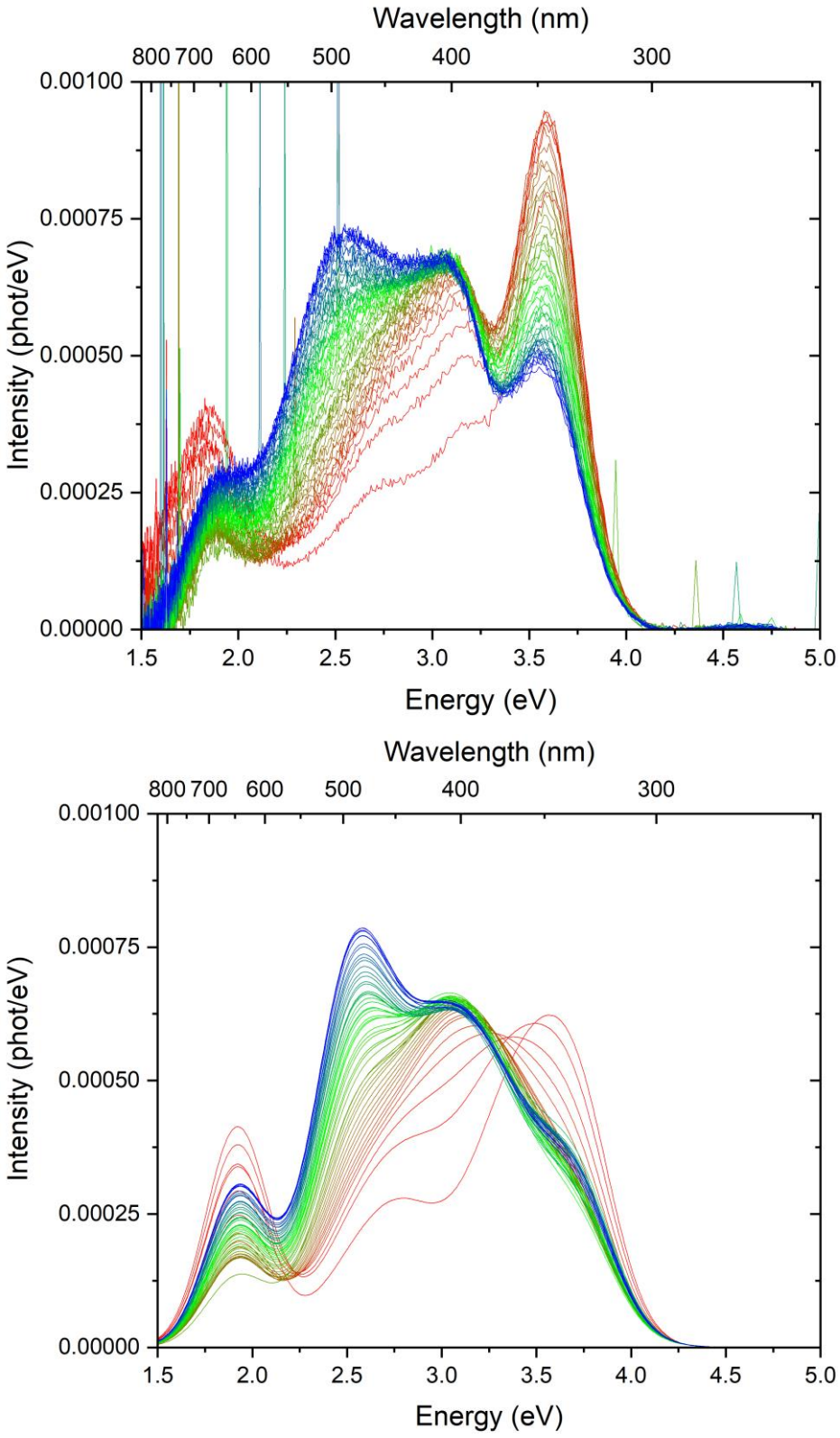

Fig. 8.3*: (top) RL spectra acquired from Nat-01 treated at 1000 °C. Each curve represents the total emission acquired during 6 Gy of X-ray irradiation. The colour scale red-green-blue indicates the progression of the total dose absorbed; (bottom) Relative curves obtained by fitting.*

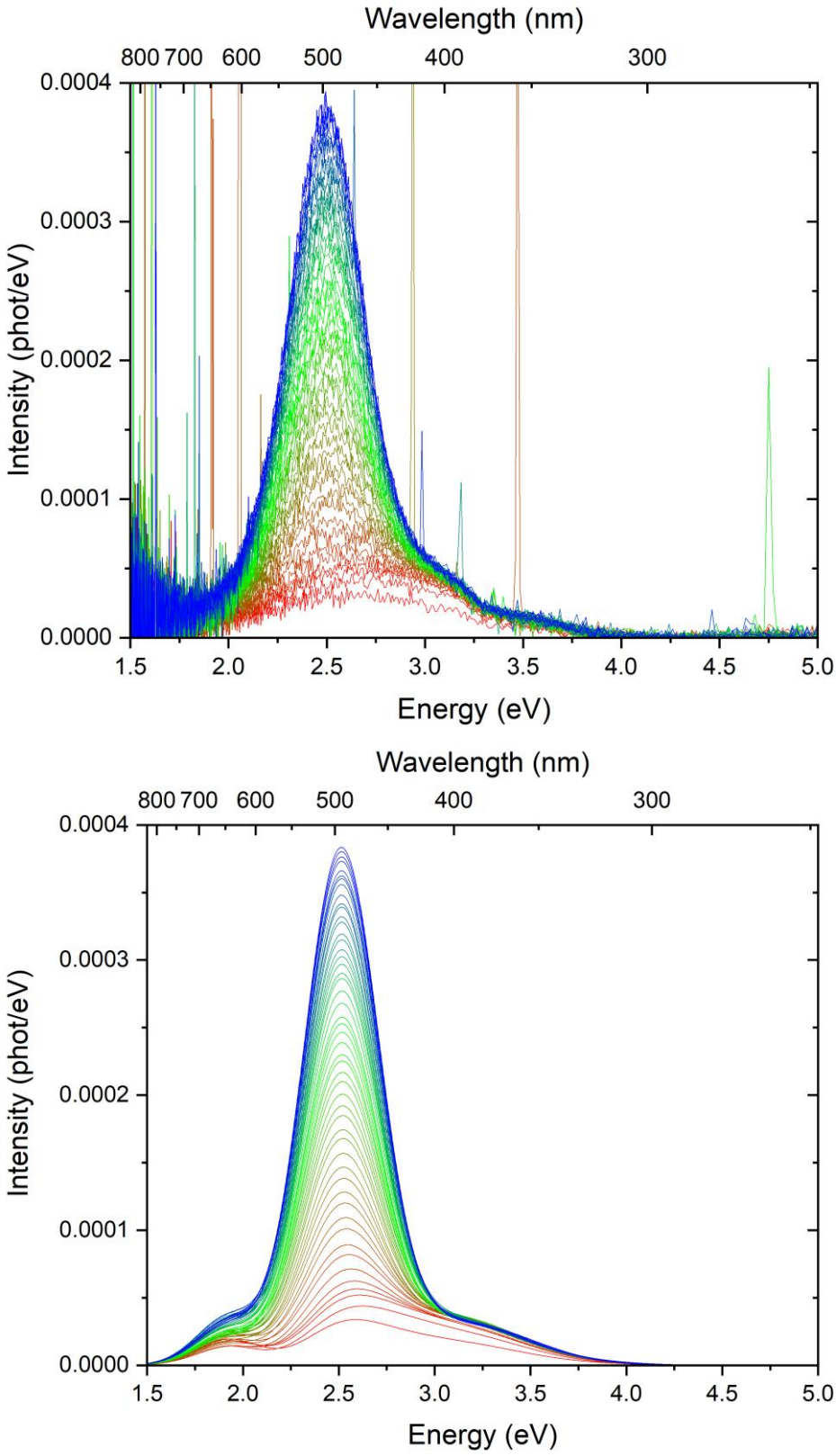

Fig. 8.4*: (top) RL spectra acquired from untreated smoky quartz. Each curve represents the total emission acquired during 6 Gy of X-ray irradiation. The colour scale red-green-blue indicates the progression of the total dose absorbed; (bottom) Relative curves obtained by fitting.*

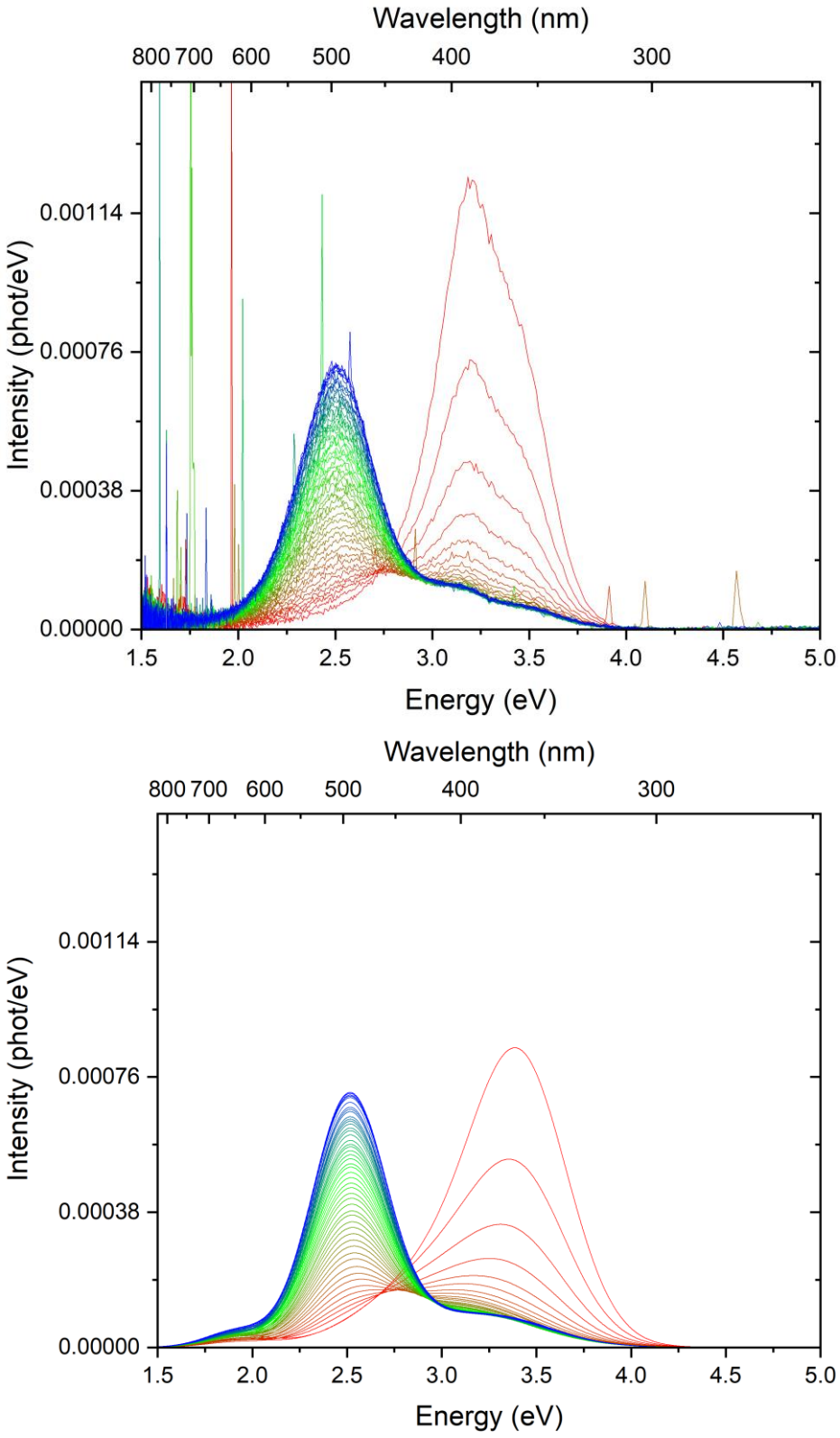

***Fig. 8.5**: (top) RL spectra acquired from smoky quartz treated at 500 °C. Each curve represents the total emission acquired during 6 Gy of X-ray irradiation. The colour scale red-green-blue indicates the progression of the total dose absorbed; (bottom) Relative curves obtained by fitting.*

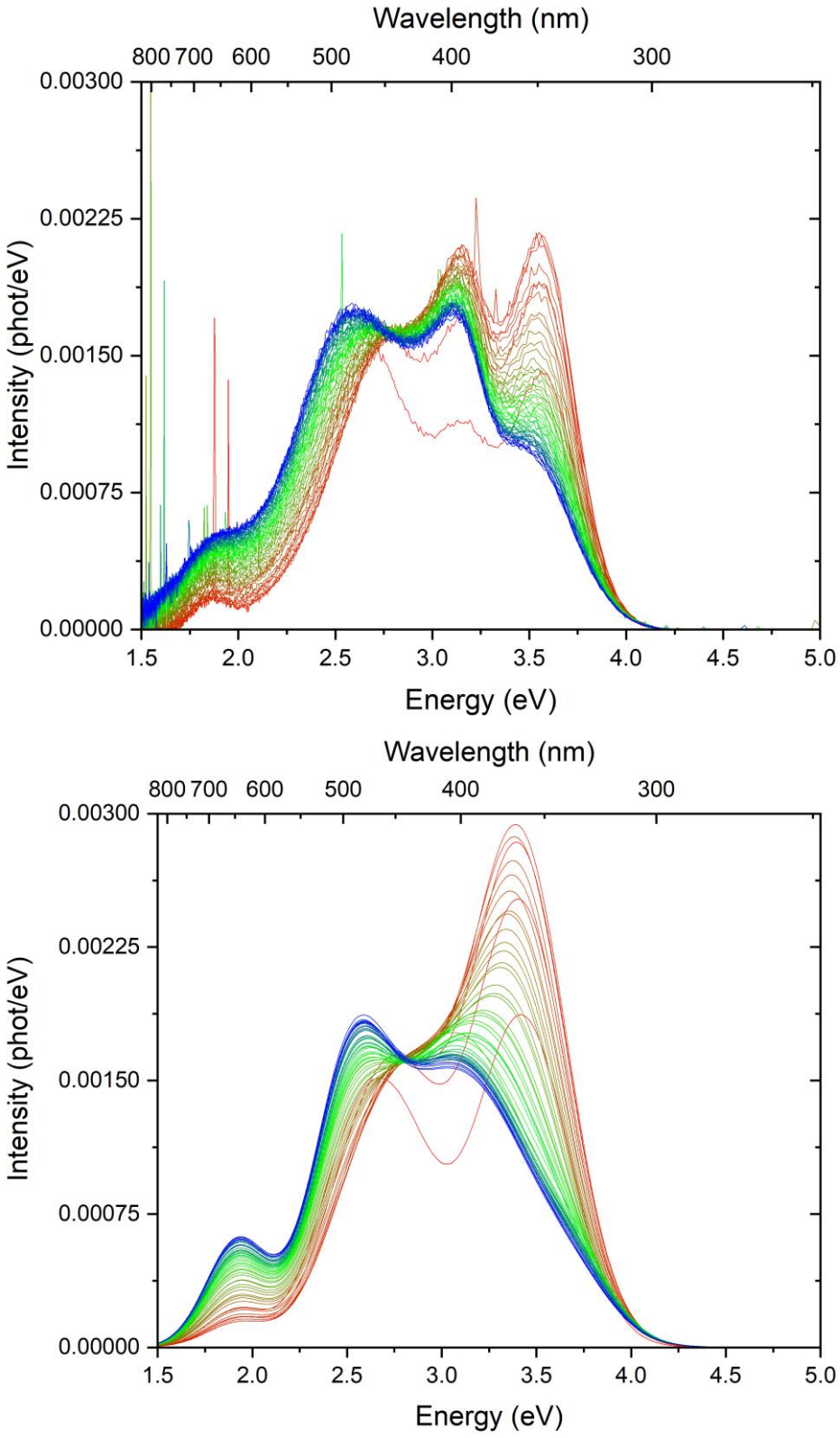

***Fig. 8.6**: (top) RL spectra acquired from smoky quartz treated at 1000 °C. Each curve represents the total emission acquired during 6 Gy of X-ray irradiation. The colour scale red-green-blue indicates the progression of the total dose absorbed; (bottom) Relative curves obtained by fitting.*

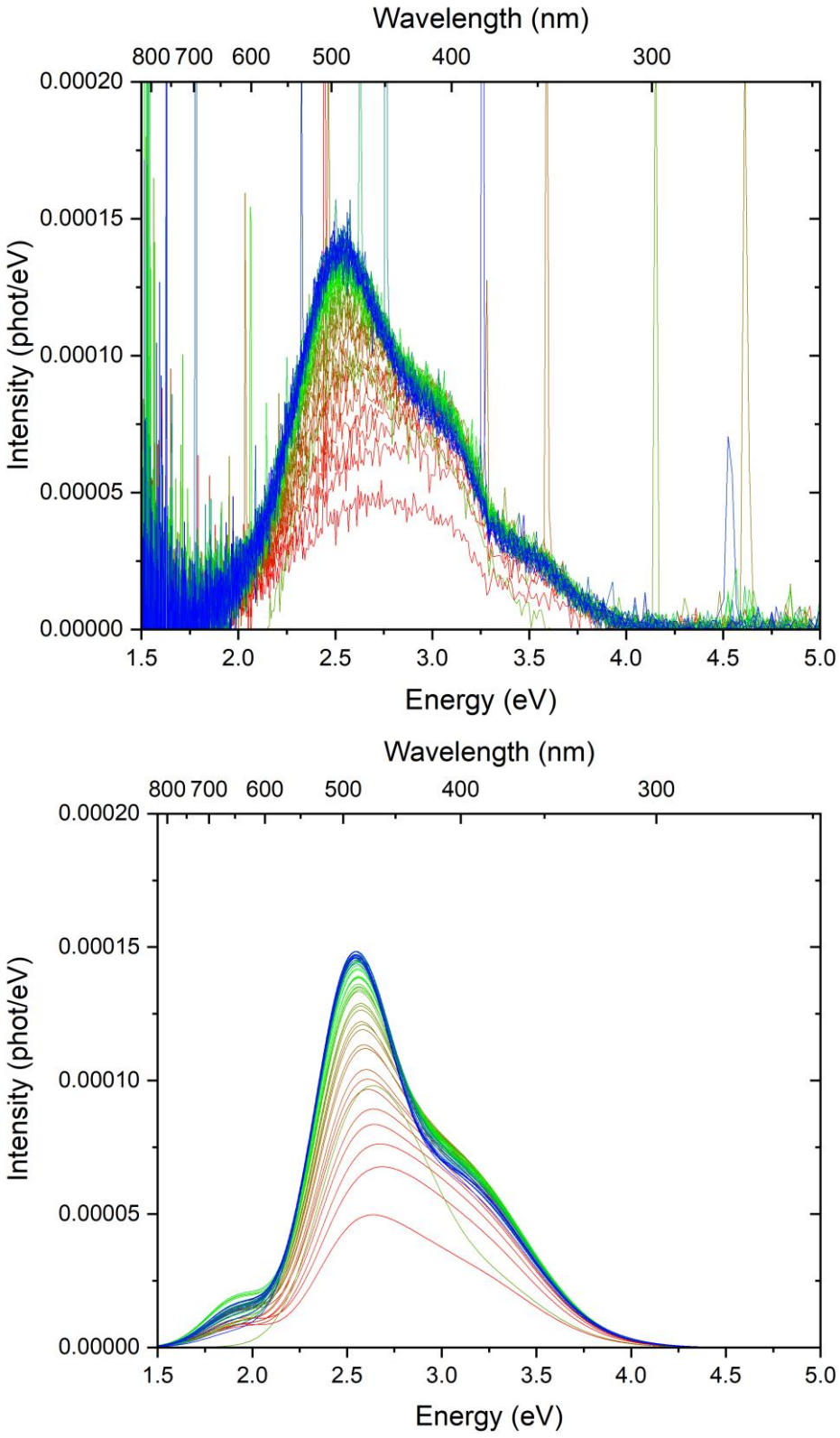

Fig. 8.7*: (top) RL spectra acquired from untreated sawyer quartz. Each curve represents the total emission acquired during 6 Gy of X-ray irradiation. The colour scale red-green-blue indicates the progression of the total dose absorbed; (bottom) Relative curves obtained by fitting.*

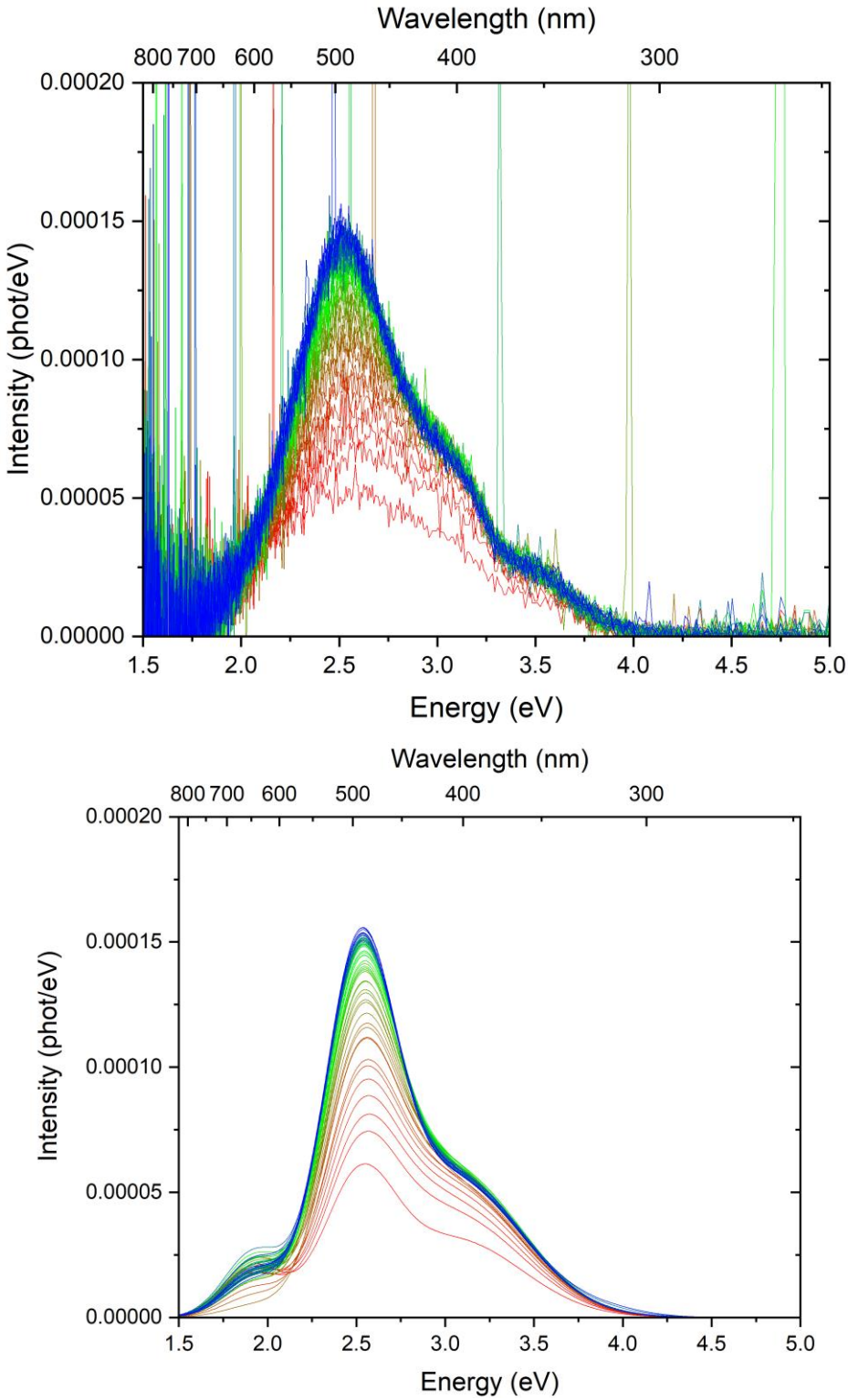

***Fig. 8.8**: (top) RL spectra acquired from sawyer quartz treated at 500 °C. Each curve represents the total emission acquired during 6 Gy of X-ray irradiation. The colour scale red-green-blue indicates the progression of the total dose absorbed; (bottom) Relative curves obtained by fitting.*

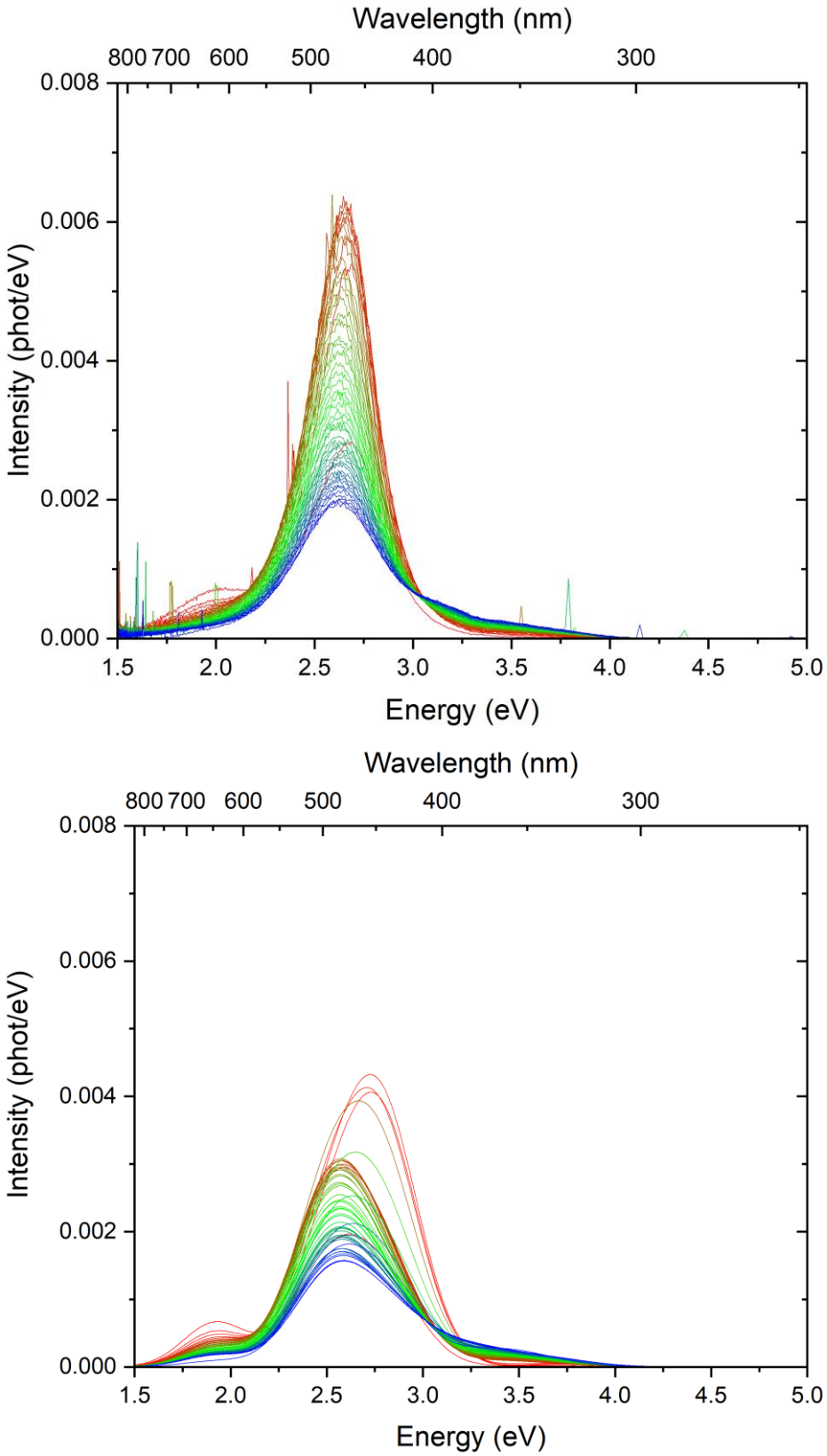

***Fig. 8.9**: (top) RL spectra acquired from sawyer quartz treated at 1000 °C. Each curve represents the total emission acquired during 6 Gy of X-ray irradiation. The colour scale red-green-blue indicates the progression of the total dose absorbed; (bottom) Relative curves obtained by fitting.*

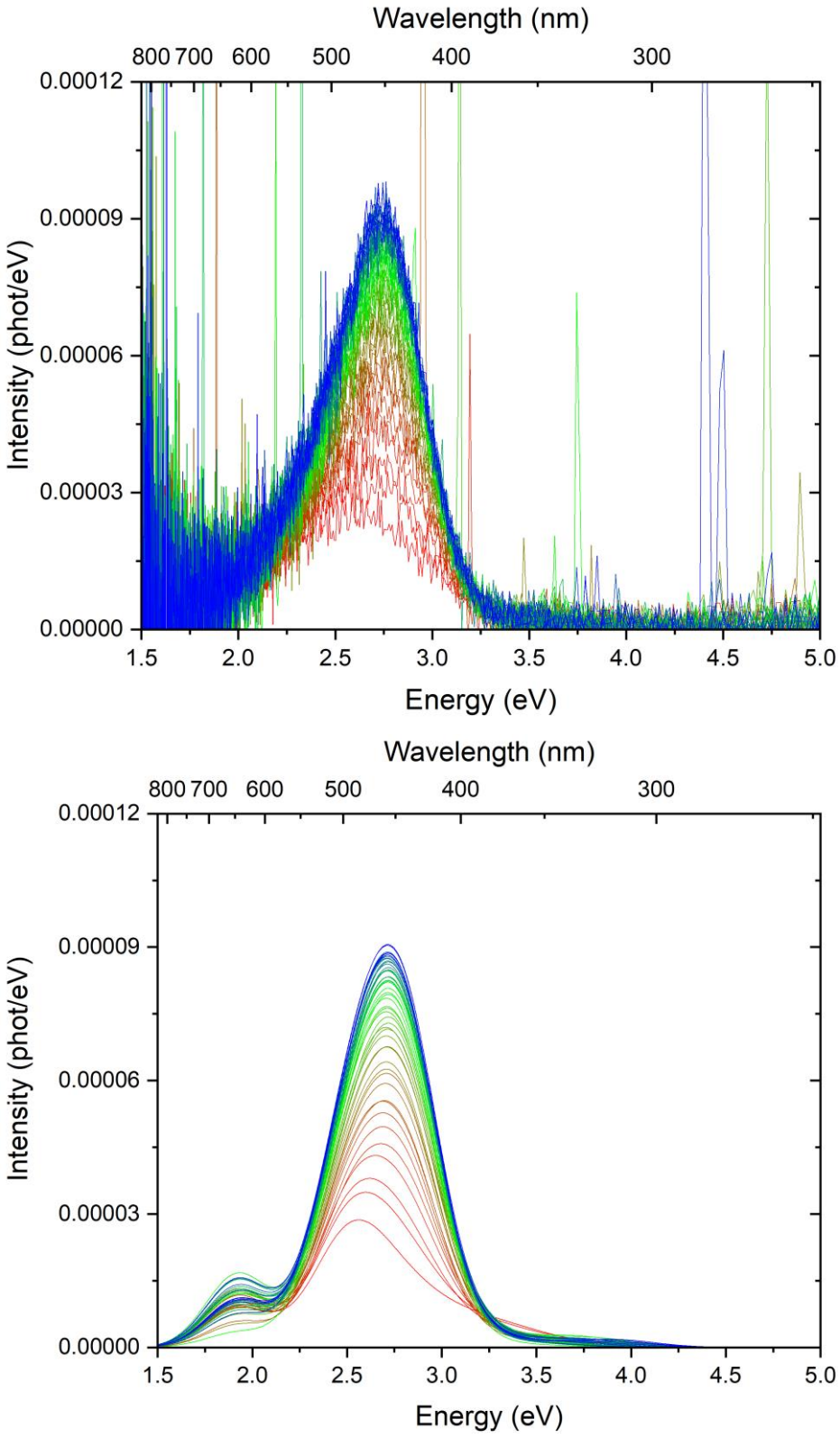

***Fig. 8.10**: (top) RL spectra acquired from untreated swept quartz. Each curve represents the total emission acquired during 6 Gy of X-ray irradiation. The colour scale red-green-blue indicates the progression of the total dose absorbed; (bottom) Relative curves obtained by fitting.*

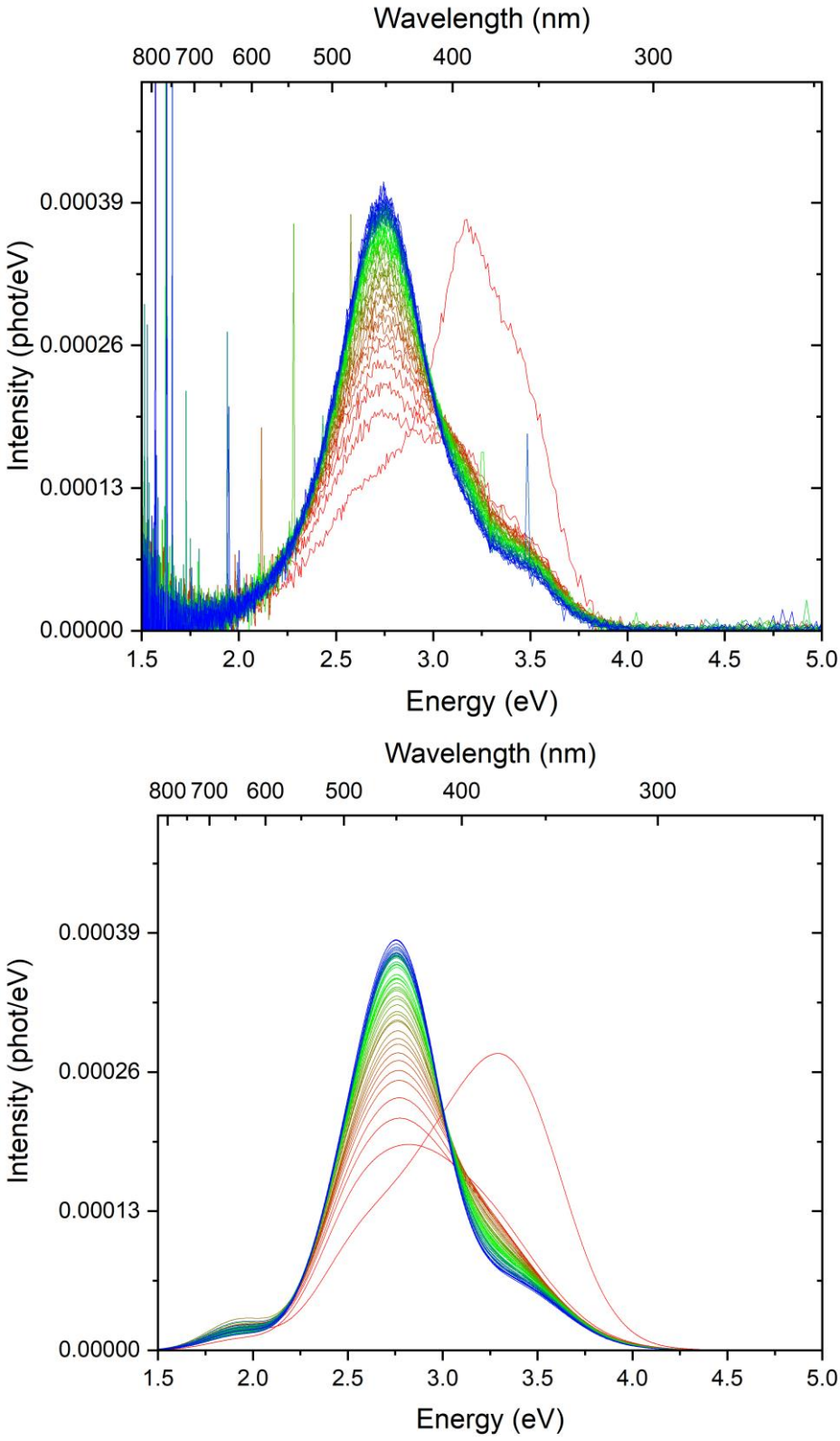

Fig. 8.11*: (top) RL spectra acquired from swept quartz treated at 500 °C. Each curve represents the total emission acquired during 6 Gy of X-ray irradiation. The colour scale red-green-blue indicates the progression of the total dose absorbed; (bottom) Relative curves obtained by fitting.*

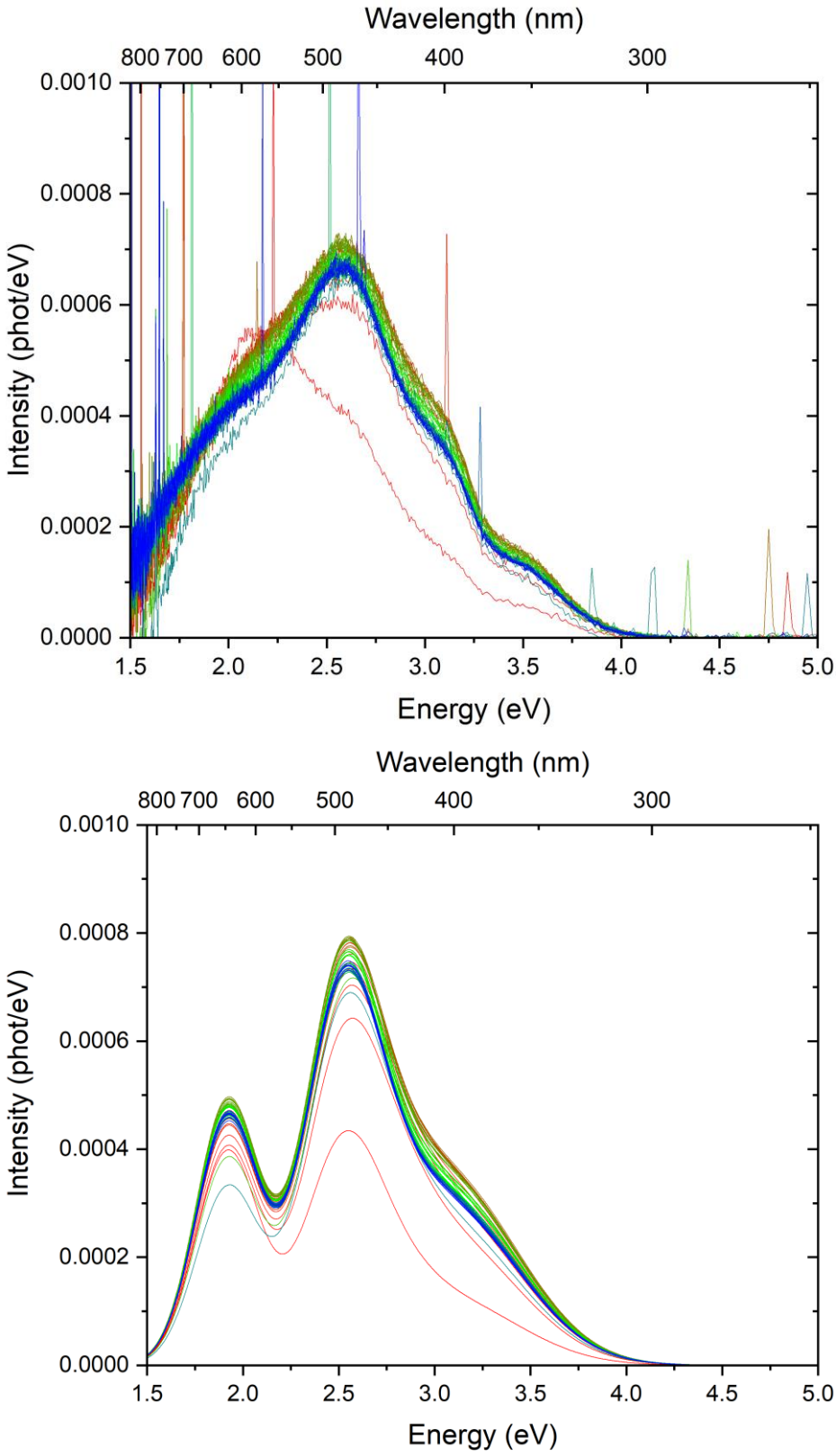

***Fig. 8.12**: (top) RL spectra acquired from swept quartz treated at 1000 °C. Each curve represents the total emission acquired during 6 Gy of X-ray irradiation. The colour scale red-green-blue indicates the progression of the total dose absorbed; (bottom) Relative curves obtained by fitting.*

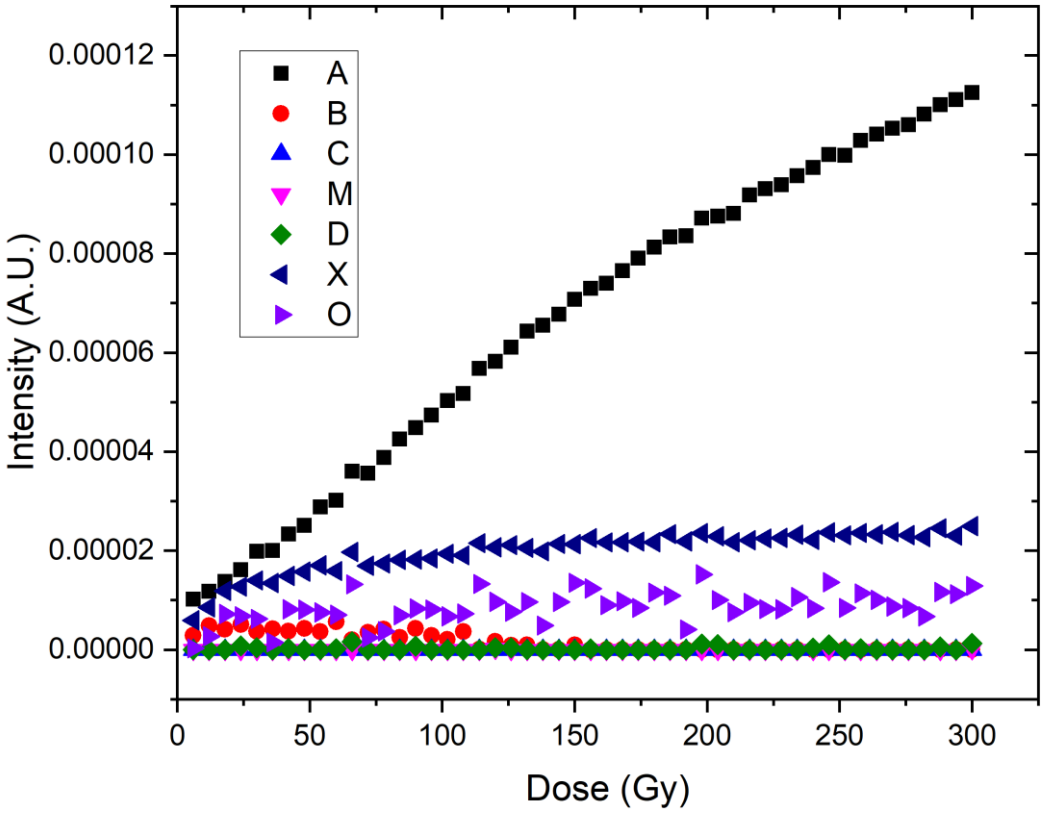

***Fig. 8.13**: Band intensity as a function of dose of untreated Nat-01.*

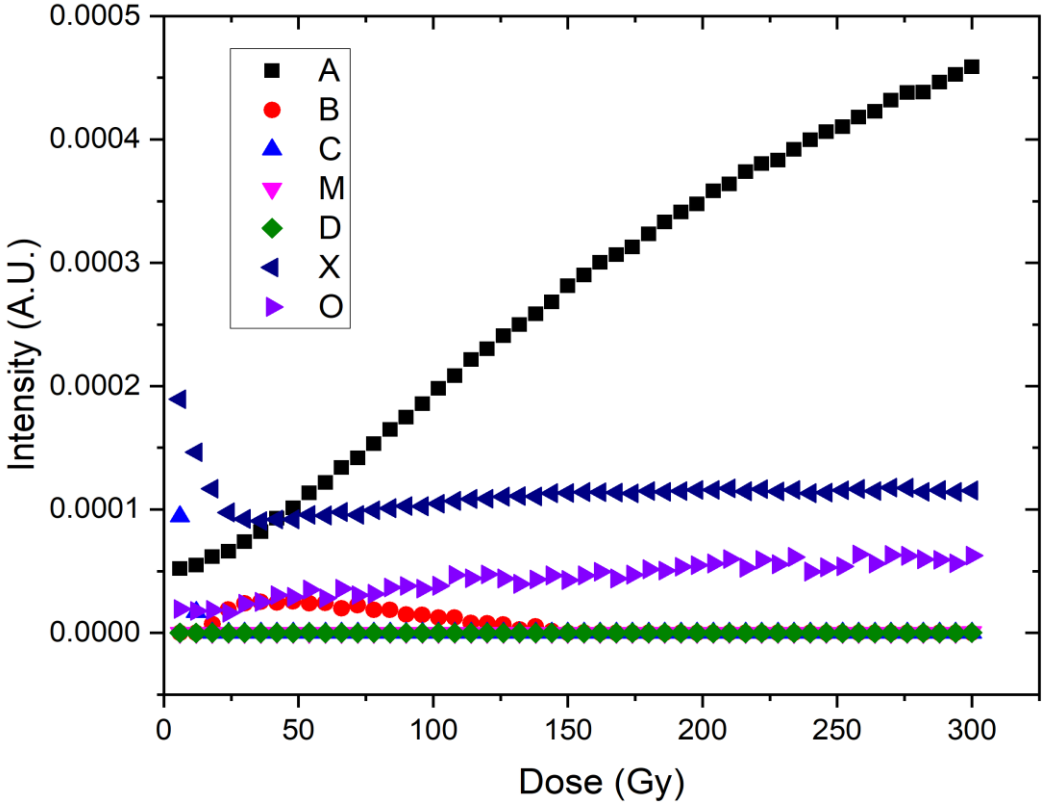

***Fig. 8.14**: Band intensity as a function of dose of Nat-01 treated at 500 °C.*

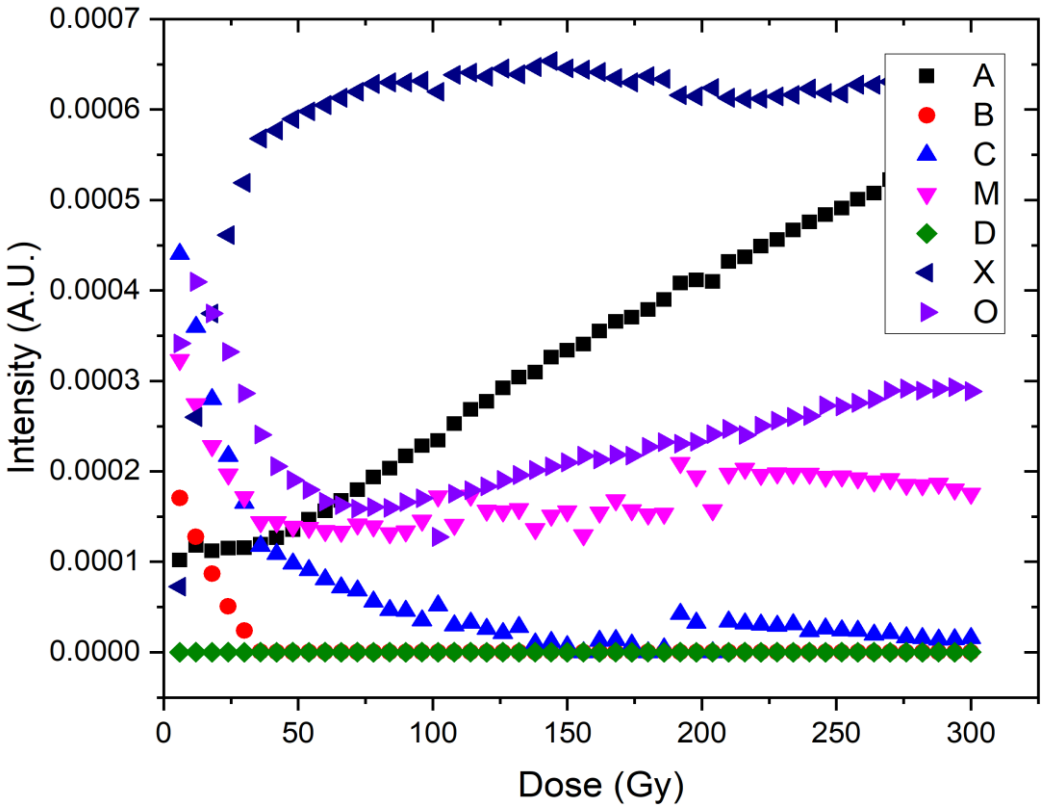

***Fig. 8.15**: Band intensity as a function of dose of Nat-01 treated at 1000 °C.*

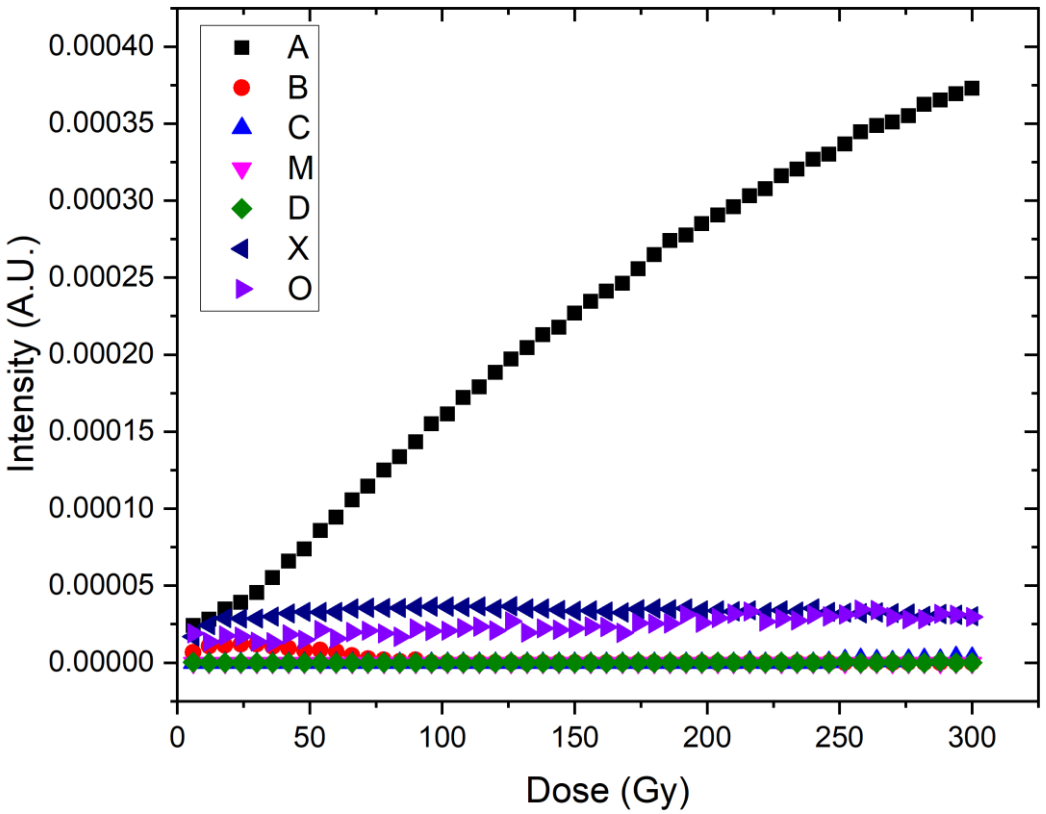

***Fig. 8.16**: Band intensity as a function of dose of untreated smoky quartz.*

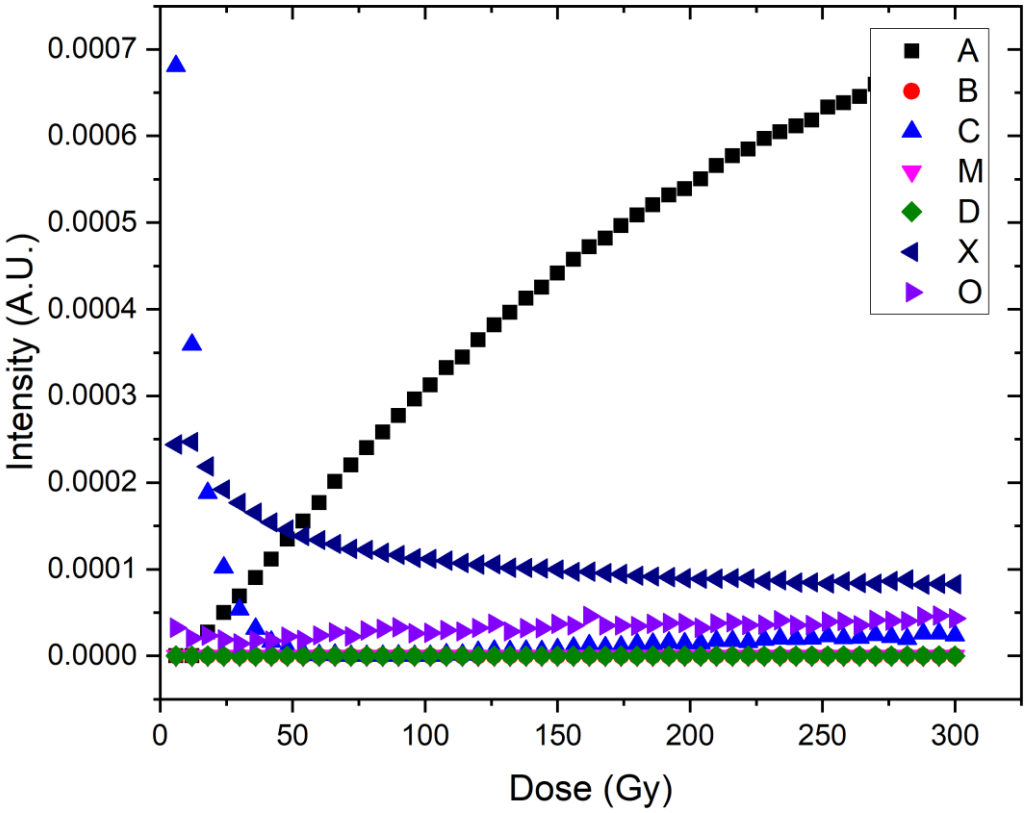

***Fig. 8.17**: Band intensity as a function of dose of smoky quartz treated at 500 °C.*

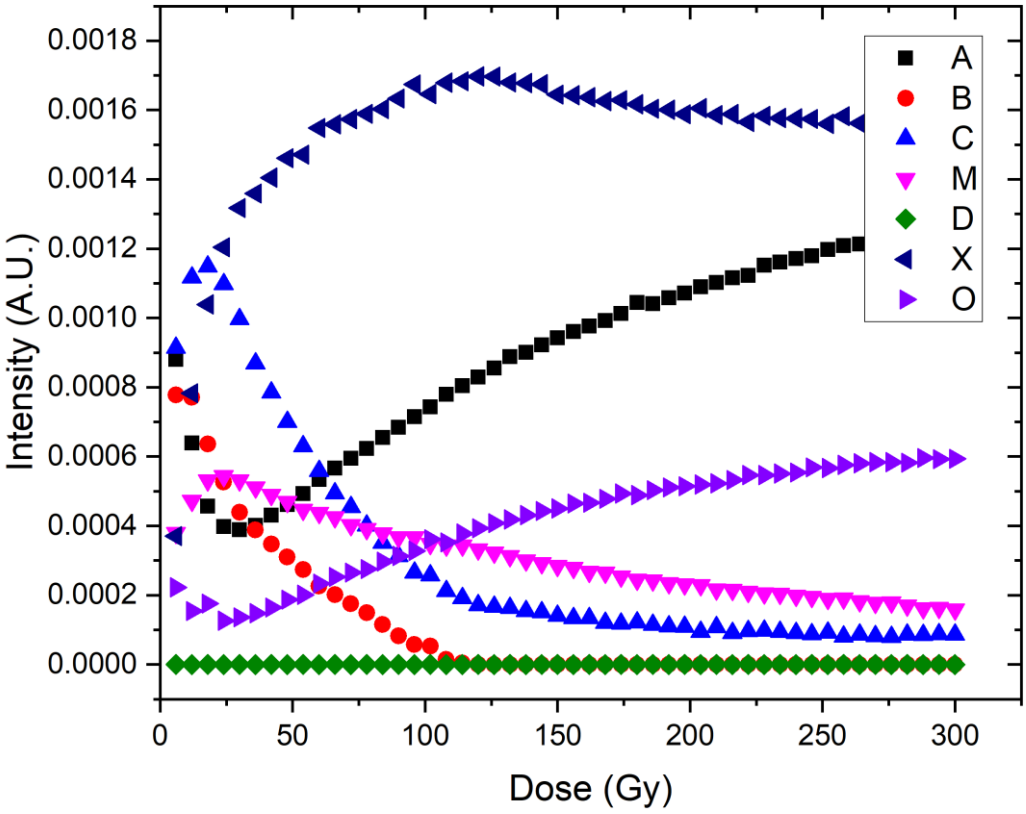

***Fig. 8.18**: Band intensity as a function of dose of smoky quartz treated at 1000 °C.*

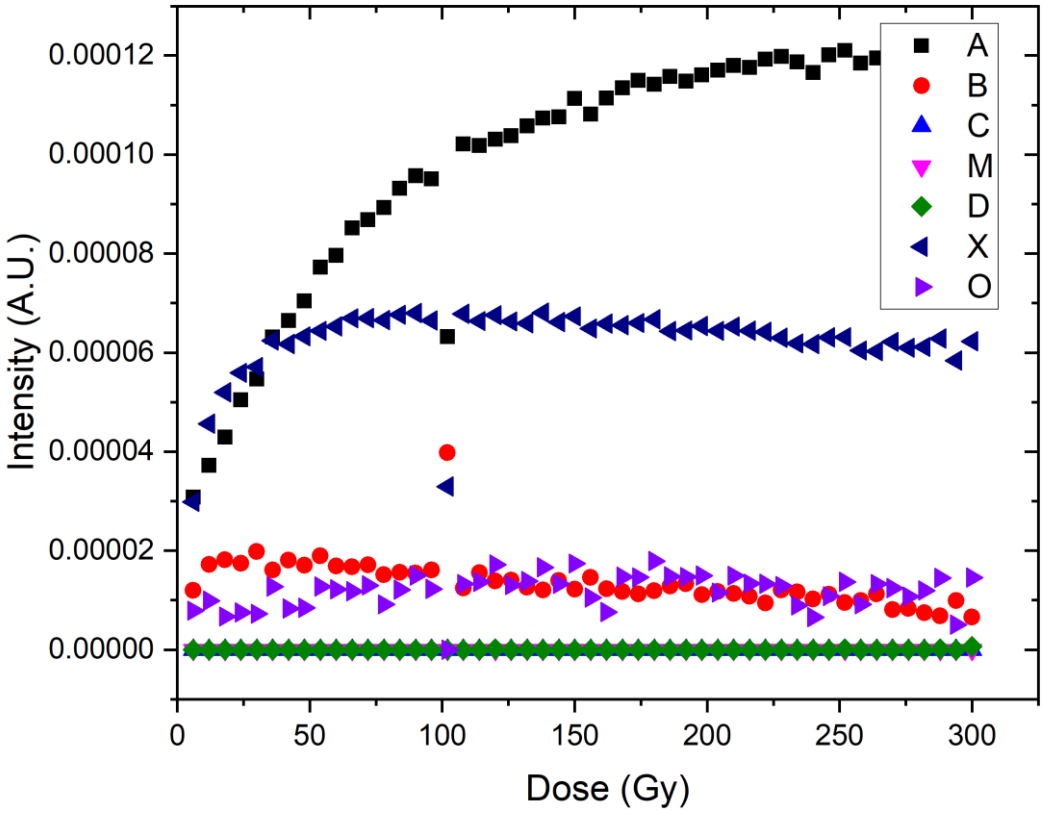

***Fig. 8.19**: Band intensity as a function of dose of untreated sawyer quartz.*

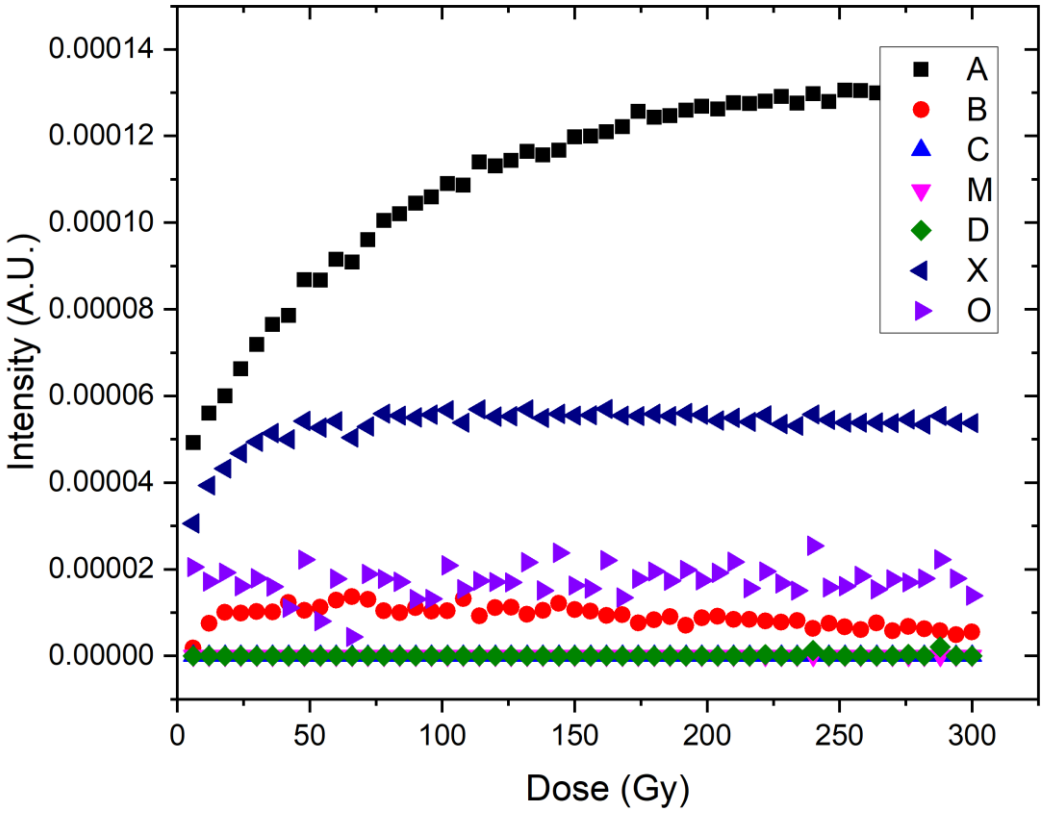

***Fig. 8.20**: Band intensity as a function of dose of sawyer quartz treated at 500 °C.*

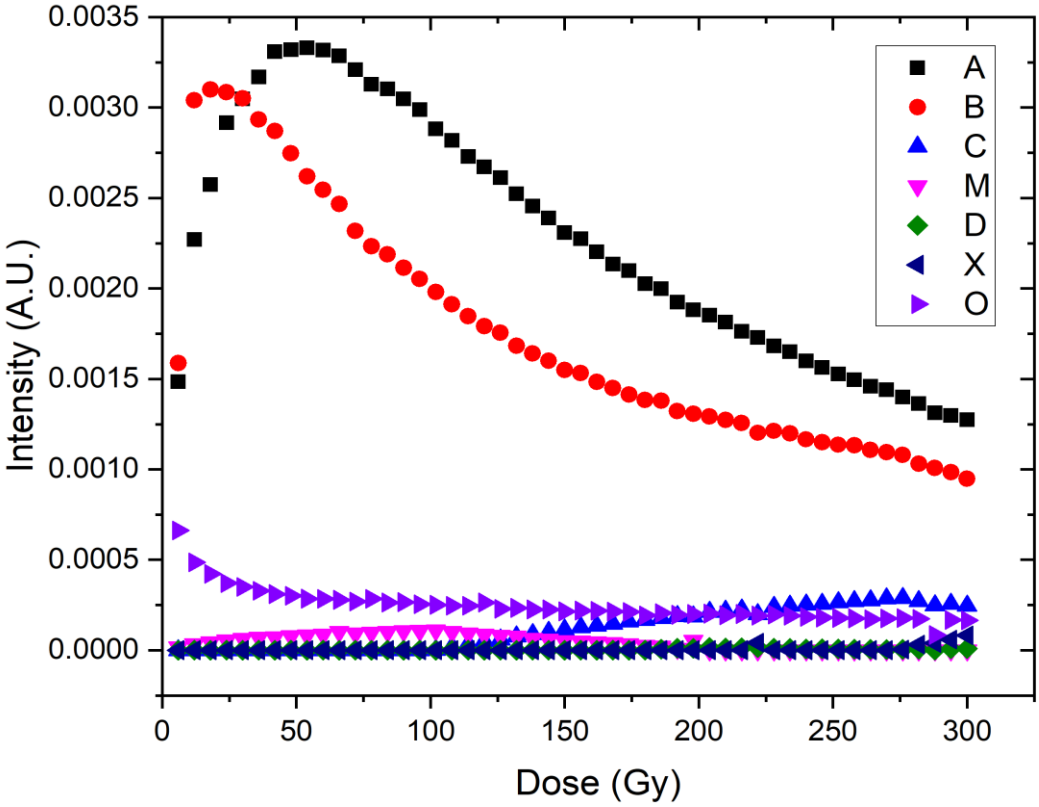

***Fig. 8.21**: Band intensity as a function of dose of sawyer quartz treated at 1000 °C.*

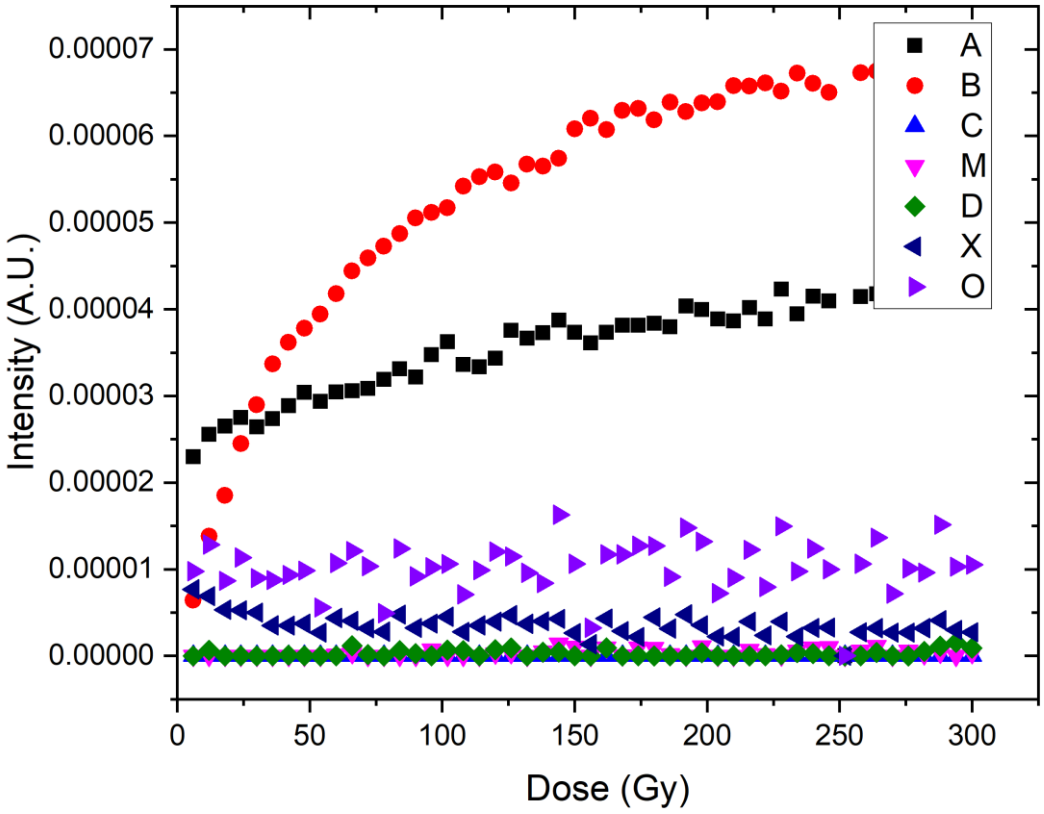

***Fig. 8.22**: Band intensity as a function of dose of untreated swept quartz.*

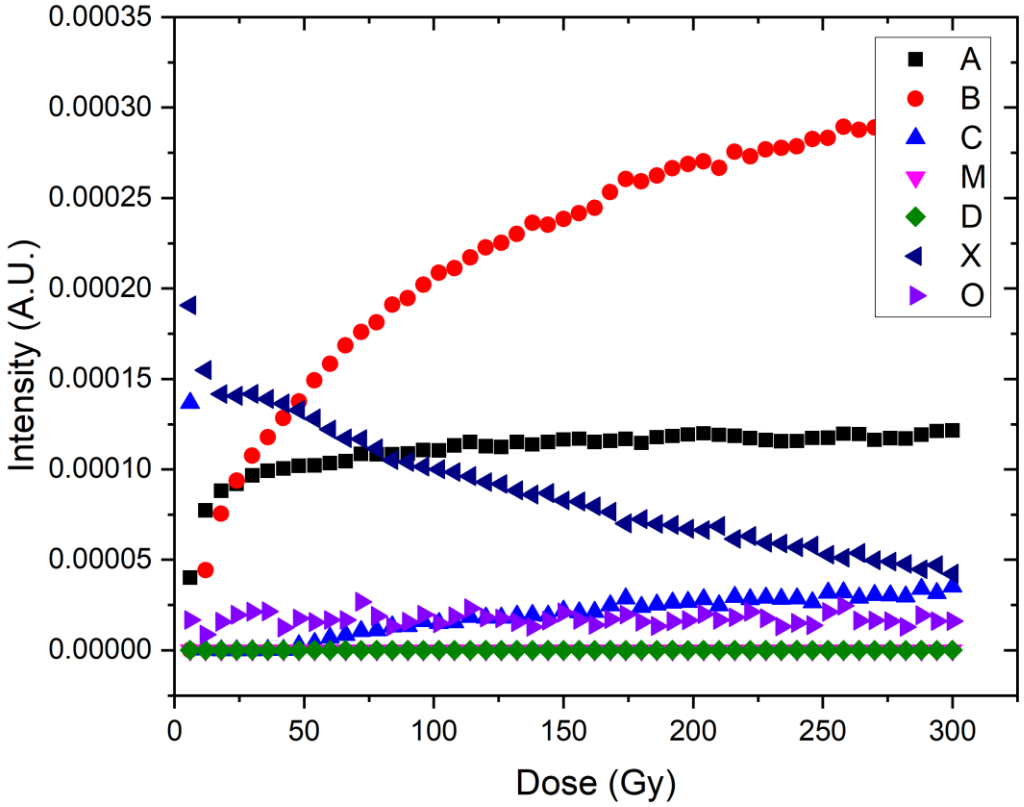

***Fig. 8.23**: Band intensity as a function of dose of swept quartz treated at 500 °C.*

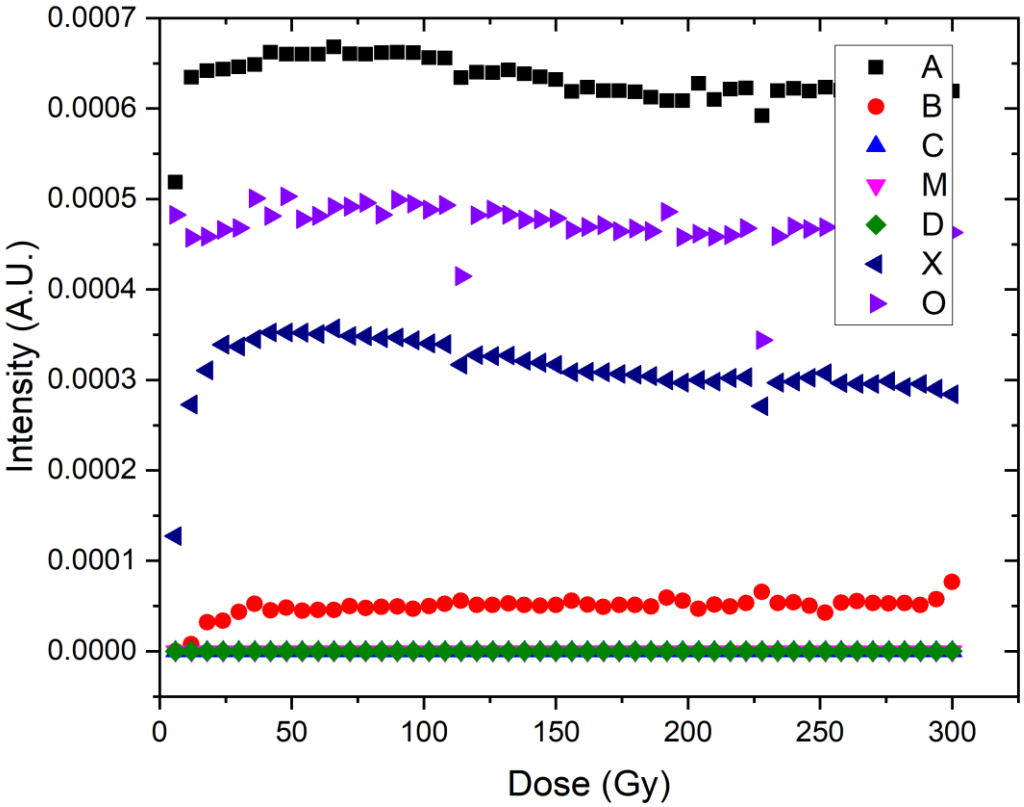

***Fig. 8.24**: Band intensity as a function of dose of swept quartz treated at 1000 °C.*

8.3 Comments

The results reported give an overview on the properties of sensitization and desensitization already briefly discussed in section 3 and reported in section 7, from a TSL point of view. Some of the properties mentioned in section 7.3 and reported in literature can be seen also from the figures 8.1-8.24. Some examples of that are:

1- In most of the samples, it can be appreciated a continuous increase in sensitivity of the blue emission as the total absorbed dose keeps increasing (mainly the A band; Martini et al., 2012b).
2- After annealing, the initial sensitivity of UV emissions (mostly the C band) is greatly increased when compared to the untreated version of the sample, but get desensitized as the irradiation continues (Bøtter-Jensen et al., 1995, Martini et al., 2014)
3- Synthetic samples, generally are dominated by the blue emissions (Martini et al., 2012b, Chithambo and Niyonzima, 2017)

Some comparisons among the presented samples are now in order. For instance, all the unfired samples, except the swept sample, are dominated by the emissions of the blue A band (2.51 eV). In the synthetic samples there are also contributions from the X band (Sawyer unswept sample) and the B band (Sawyer swept sample). For this bands though, a strong proof is still lacking for their involvement in TSL processes. This could suggest that when dealing with unfired samples, one should expect similar emission sensitivities during TSL experiments, and the low UV intensity in Fig. 7.1 and 7.2 seems to be compatible with this hypothesis. For the samples annealed at 500 °C, it is expected for natural samples to show an initial increase of the UV emissions (Martini et al., 2012b) when compared to the unfired samples, followed by a desensitization with the continuous irradiation. It is interesting to note that this happens also for the swept sample, but not for the unswept one. The unswept sample both untreated and annealed at 500 °C present spectra little different. This could be related to the fact that, relatively recently, such sample has already experienced high temperature of the order of hundreds of °C during its growth process (hydrothermal, Hosaka and Taki, 1981) and since the new annealing did not involve any phase transition, unlike the one at 1000 °C, annealing it again did not bring any significant changes in the crystal lattice. Overall, the natural samples show the same properties for the emission bands at each annealing temperature, with some intensity ratio difference between each other. The different intensities could be related to the different concentrations of each impurity responsible for such emissions. The synthetic ones though, show very different spectra when comparing swept and swept samples. The more evident difference is the presence of the B band in the swept sample spectra in the untreated and annealed at 500 °C samples. The untreated swept sample lacks any significant UV emission, while the unswept one shows a significant contribute of the X band. Annealing the swept sample at 500 °C creates the aforementioned C band emission that gets rapidly desensitized, but also the X band makes its appearance, which keeps being significant for the whole acquisition, with a continuous slight desensitization. Even in the unswept sample annealed at 500 °C, the X band has a significant

contribution, but without showing desensitization but rather a sensitization that rapidly reach a saturation value. Finally, the synthetic samples annealed at 1000 °C show a drastically different behaviour. The unswept sample shows a rapid increase in sensitivity of the A and B band (blue emissions) that reaches a maximum, then starting to desensitize. It is also present an emission near 2 eV that could be related to the O band (red emission), which shows a desensitization that seems to saturate at a minimum value. Also the C band can be observed, although not very intense, showing a slight sensitization during the irradiation. Looking at the swept sample, the very first spectra show an emission dominated only by the red O band emission that very rapidly gets matched by the blue emission of the A band and the UV emission of the X band. A slight contribution of the B band (blue) may be present, but an order of magnitude lower than the A band, so it may not be a reliable data. What is really striking, is the very large stability of most of the emissions after roughly 30 Gy. There is indeed a desensitization process going on for the A and X band, but it is very slow (after 250 Gy, less than 10% the A band and less than 20% the X band). Sweeping in fact is a technique developed also to increase the radiation hardness of the material for space applications (Martin, 1988). The large difference in the spectra between the unswept and swept samples, confirms the important role that alkali ions take in the luminescence processes. The fact that the sweeping process was done in air, could also point out the importance of hydrogen, as the lower abundance of alkali ions and higher abundance of hydrogen apparently are the only differences between the two synthetic samples. Hydrogen in quartz has also been deeply studied with infrared measurements, in order to characterize the mechanisms of impurity inclusion in the lattice (Katz, 1962) and it has also been studied in this thesis work with EPR and will be discussed in the following sections. It is also worth mentioning, that similar samples can show different properties, for example by comparing the spectra of the swept sample annealed at 500 °C reported in this section with other published works, such as Martini et al. (2012b), where a similar sample from a different manufacturer shows instead a constant emission as irradiation continues, while the sample presented here shows both sensitization and desensitization processes. Similar experiments were also performed by Chithambo et al. (2017), using synthetic samples produced by Sawyer Technical Materials, where they annealed the samples for 1 hour at different temperatures. Comparing their results on the unswept sample annealed at 1000 °C with the one presented in this section, it appears that the emissions in the blue (A and B bands) and red (O band) follow a similar trend, but they also observe a strong UV emission (C band) which shows a sensitization process with a saturating behaviour. It is worth also mentioning the fact that in some cases (e.g. Fig. 8.15), the drop of intensity of some components corresponds to an increase of others. This fact could point to the hypothesis of a conversion of emitting centres, favoured for example by the ionic transfer of interstitial impurities during irradiation from one centre to the other, activating, or deactivating, the luminescence properties of such centres.

A few words are also due to comment the quality of the fitting curves. As already mentioned in the results section, the large number of parameters to optimize in the fitting process will undoubtedly bring a certain degree of error. Nonetheless, in many cases the curves are in good agreement with the experimental data. The region below 2 eV is the most difficult to fit, also due to the large signal-to-noise ratio. More difficult are the fits on the emission of samples treated at 1000 °C. After such treatment, many emissions are sensitized and gain more weight on the overall spectrum. For example, for the smoky quartz treated at 1000 °C, Fig. 8.6, even the UV region around 3.5 eV is quite different from the experimental data, while this is not so much in the case of the Nat-01 treated at 1000 °C, Fig. 8.3. The comparison between fitting curves and experimental data of the swept sample treated at 1000 °C is striking, Fig. 8.12, as it shows clearly that there are other emissions not included in the well characterized ones reported in Tab. 7.1. Specifically, there is indeed an emission in the region between 2.0 and 2.5 eV and an emission in the 3.5 eV region that does not seem to match the parameters of the M band. In the literature this kind of emission, in the green/yellow region, has already been reported (e.g. Rink et al., 1993, Kuhn et al., 2000). To obtain a good characterization though, it would be needed a sample where such emission is less overlapped with other ones, which unfortunately was not available for this thesis work. It is worth mentioning again how likely is the role of hydrogen and/or alkali ions in the presence of this kind of green/yellow emissions, due to their clear appearance only in the swept sample.

To summarize, the data reported shows an overview of the sensitization properties of different quartz samples. Some of them are already well known in literature, but these data show also how sample dependant they really are. This is indeed a stimulus for further research on quartz properties, as much work is still needed in order to clarify the specific mechanisms involved and the role of the impurities and defects in general in them, while also is still needed a proper characterization of some of the observed emissions.

9. EPR characterization of germanium related centres in natural quartz and the discovery of a new hydrogen related centre

In this thesis work, during the research that lead to the data presented in section 5, a preliminary study was done on pegmatitic quartz samples to calibrate the EPR spectrometer at the Physics Institute of the Czech Academy of Science for the needed experiments. A qualitative study on the dose dependence was done in order to understand the optimal measurements conditions to use and the response of the samples to X-ray radiation. During this study, new lines have been observed that do not belong to the so far observed $[GeO_4]^-$ and $[GeO_4/Li^+]^0$ centres. The characteristics of some of them are a hint of the hyperfine interaction with hydrogen atoms, while the nature of the others is still unclear. A characterization was made of all the signals observed in order to know their thermal stability using pulsed annealing and higher frequency EPR experiments (Q-band) to enhance the spectral resolution. The results shown in this section have been submitted to the Journal Radiation Measurements.

9.1 Experimental procedure

9.1.1 Samples

Most of the measurements were done on the pegmatitic sample labelled K-200 in the previous sections, which was the sample that showed the highest intensity of the studied signals, already known and new ones as well. For the sake of comparison, some measurements in similar conditions were performed on the natural hydrothermal sample previously labelled Nat-01, which was the object of study for Vaccaro et al. (2017 and 2019, section 5). All the samples were studied in their untreated form (as received). The measurements were done on powder with grains of 100-200 μm of diameter and around 50 g per aliquot for the measurements in the X-band. Considering the higher sensitivity of Q-band measurements, and the smaller sample holder size when compared with X-band measurements, a lower amount of sample was necessary and around 5 g of powder was enough. Therefore, in order to maintain a fully random distribution of crystal grains orientation, the powders were crushed to obtain a grain dimension of less than 100 μm in diameter.

9.1.2 EPR measurements

The EPR measurements have been performed with the instrumentation described in section 4.4, located in the Physics institute of the Czech Academy of Science, in Prague. The samples were irradiated while inside a quartz tube that held them in front of the X-ray tube's window and then transferred to a not irradiated tube for measurements. The X-ray tube was set at 50 kV and 30 mA, obtaining a dose rate around 4.2 Gy/s, based on the apparatus technical recommendations and the distance of the sample from the window (1 cm).

The experiments presented can be divided into three parts, based on methodology and objective. In the first part, through X-band experiments, it was qualitatively studied the dose response of the K-200 sample. These measurements showed changes in the spectrum by increasing the irradiation dose

and brought to light new unexpected signals. In the second part, the thermal stability of the observed signals was characterized using pulse annealing. The samples were inserted in an oven that heats quickly to the desired temperature and held there for 7 minutes. The temperature was monitored with a thermocouple attached at the end of the quartz tube holding the quartz powder. In the third part, the samples were studied using the Q-band equipment, in order to obtain a better resolved spectrum. Because the Q-band equipment is in a different location in the city of Prague from the X-band equipment and X-ray tube, the samples were transported after irradiation inside a Dewar filled with liquid nitrogen, in order to preserve the unstable centres until the measurement.

9.2 Results

9.2.1 Dose response

The K-200 sample was progressively irradiated from 100 Gy to 15.7 kGy, approximately, by delivering cumulated doses to the same aliquot. The acquired spectra are reported in Fig. 9.1, along with a provisional labelling for each signal. The main lines observed, "Main Line 1" and "Main Line 2", are due to the overlapping of signals from electrons trapped at different germanium related centres (such as $[GeO_4]^-$ and $[GeO_4/Li^+]^0$, Mackey, 1963, Lutoev, 2006, Toyoda, 2015, Vaccaro et al., 2017, Vaccaro et al., 2019; see also sections 5 and 6).

At the highest doses two secondary lines appeared, one of which, labelled as "Secondary line 1", has already been observed by Kaya-Keleş et al. (2019), although its nature is still unclear, while the other, at the best of the found knowledge, has not been reported in the literature yet.

Additionally, again only at the highest dose, on both sides of the lines shown in Fig. 9.1 and outside the shown range, a couple of symmetrical bands appeared at around 3310 and 3400 Gauss and are reported in Fig. 9.2 for better clarity (they will be referred to as "Sidebands"). The slight apparent asymmetry of the band at higher magnetic field is due to the overlapping of a line originated from the resonator itself. In Fig. 9.2 is also reported a simulated spectrum obtained with EasySpin. The parameters used to draw the curve are g_1=2.0007, g_2=1.9974 and g_3=1.9929, with coupling constants of A_1=233 MHz, A_2=235 MHz and A_3=239 MHz, assuming a hyperfine interaction with hydrogen.

To try to confirm the hydrogen origin of the signal, an annealing in water vapour has been done on the Nat-01 sample, which showed a less intense signal of the sidebands. This was done hoping that some hydrogen from water may migrate inside the lattice. An EPR spectrum was acquired after irradiation with 15 kGy. Then a few drops of deionized water were inserted in the quartz tube holding the powder and then covered with some cotton. The wet sample has been then annealed at 230 °C for 30 minutes, irradiated again with the same dose and then measured with the spectrometer. The two spectra, before and after the annealing in water vapour, are reported in Fig. 9.3. Although there is indeed a slight increase in the sidebands' intensity, it is not remarkable enough to draw any conclusion from it. Due to lack of time, it was not possible to repeat the experiment on the K-200 sample.

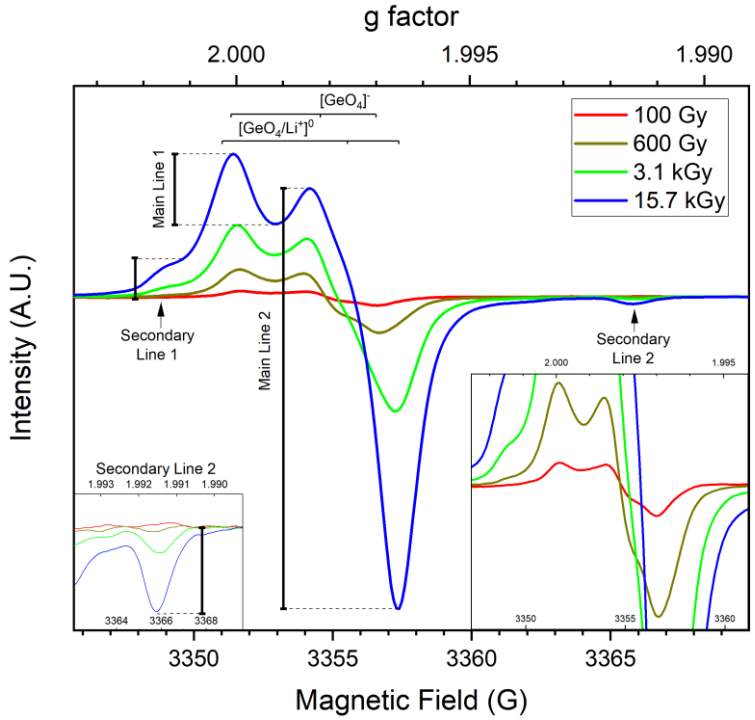

***Fig. 9.1**: Qualitative dose response of the K-200 quartz sample EPR spectrum. A tentative labelling is defined to identify the various lines observed. The vertical lines indicate also the peak-to-peak distance used to evaluate the signal intensity. The insets show a zoomed view on the secondary line 2 (bottom left) and the main lines at the lowest doses (bottom right).*

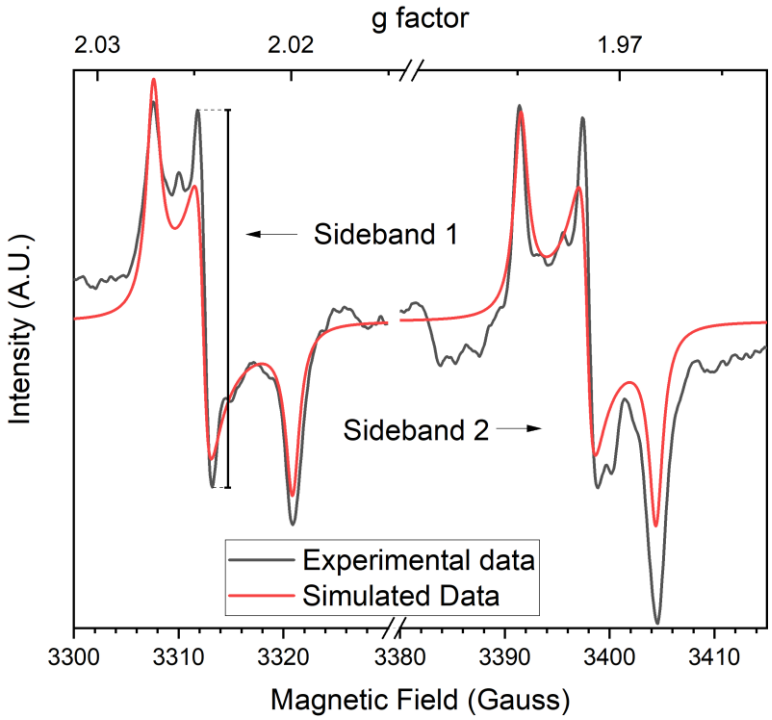

***Fig. 9.2**: Symmetrical lines observed at the sides of the main signal reported in Fig. 9.1. Red curve is a simulated spectrum using the following parameters: g_1=1.9929, g_2=1.9974 and g_3=2.0007, with coupling constants of A_1=233 MHz, A_2=235 MHz and A_3=239 MHz. The vertical line indicates the peak-to-peak distance used to evaluate the signal's intensity.*

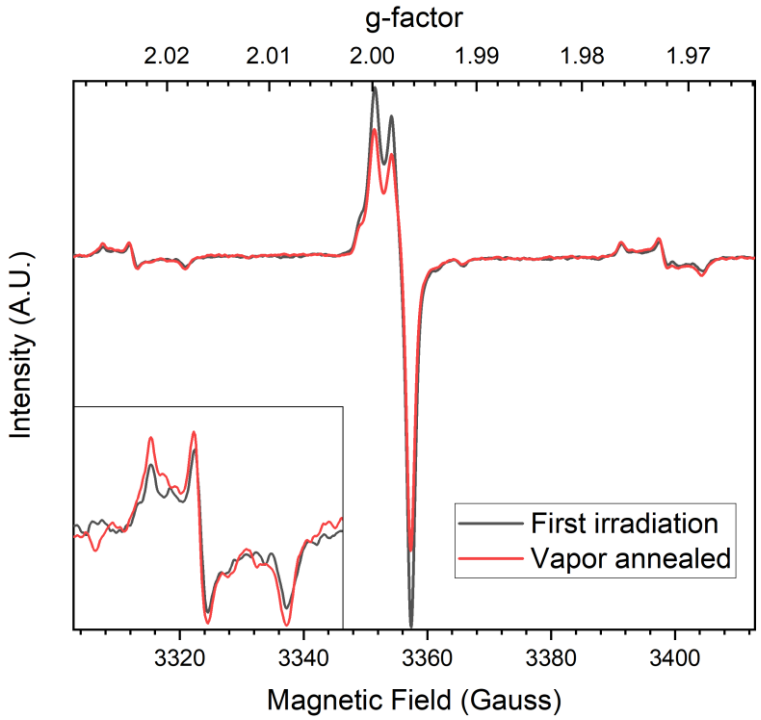

***Fig. 9.3**: Nat-01 EPR spectra before and after annealing in water vapor. Irradiated before each acquisition with 15 kGy. Inset shows a zoom on the low magnetic field sideband.*

9.2.2 Thermal Stability

The thermal stability of the observed signals has been studied by performing pulsed anneals from room temperature up to 270 °C holding the sample at the selected temperature for 7 minutes. The experiment has been repeated at both the lowest dose, 100 Gy, and the highest one, 15.7 kGy, to better appreciate the evolution of both the $[GeO_4]^-$ signal, which is the dominant signal in the spectrum at low dose, and the $[GeO_4/Li^+]^0$, which dominates the spectrum at higher dose. The spectra evolution is reported in Fig. 9.4, while an intensity evaluation as a function of annealing temperature, normalised to the initial intensity, is reported in Fig. 9.5. The intensity of the main lines has been evaluated with the peak-to-peak intensity value, indicated by the vertical lines in Fig. 9.1. The intensity of the secondary lines has been evaluated by the peak-to-baseline intensity, as indicated in Fig. 9.1. Lastly, the intensity of the side bands has been evaluated following the peak-to-peak intensity of the middle line, as indicated in Fig. 9.2.

In Fig. 9.5 are also reported the curves obtained through simulations of the thermal decay, assuming first order kinetics, in order to evaluate the trap depth of the observed paramagnetic centres. The fitted curves were obtained using the following expression:

[19] $$I_{i+1} = I_i \exp\left(-St\, exp\left(-{}^{E_T}/_{k_B T_i}\right)\right)$$

Where I_i is the intensity before the i-th annealing cycle, S the frequency factor, t the annealing time, E_T the trap depth, k_B the Boltzmann constant and T_i the i-th annealing temperature (Buryi et al., 2020). The analysis of $[GeO_4]^-$ lines observed at low dose results in a trap depth of 0.79 eV, with a frequency factor in the order of 10^9 Hz, in agreement with what was calculated for both Thermally Stimulated Luminescence (TSL) and EPR isothermal decay measurements in Vaccaro et al., 2017. Both the

Sidebands decay at the same rate, with a trap depth of 1.14 eV and a frequency factor around 10^{12} Hz. This, together with their symmetry, is an additional clue suggesting that they are originated by the very same centre. Looking closely at the data it is not to be excluded that the decay of these signals could occur with a two-step process, with a first partial decrease around 50 °C. However, the data dispersion for low temperature annealing steps is too high to clarify it. For the other lines, i.e. $[GeO_4/Li^+]^0$ and Secondary Lines 1 and 2, the annealing behaviour requires at least a two-traps model, with trap depths of 1.06 eV and 1.30 eV, respectively, with frequency factor around 10^9 Hz for both traps. The values are the same for both main lines and secondary lines observed at high dose. The value of the deeper trap seems to be compatible with the values reported by Guzzo et al. (2017) and Yazici and Topaksu (2002) on TSL peaks observed above 300 °C which we believe may be the same one studied in Vaccaro et al. (2019) and attributed to $[GeO_4/Li^+]^0$. The values are reported in Tab. 9.1 for comparison. This points to the fact that the centres responsible for the Secondary lines, observable at high dose, are related to some degree to the $[GeO_4/Li^+]^0$ centres, which are responsible for the main lines at high dose.

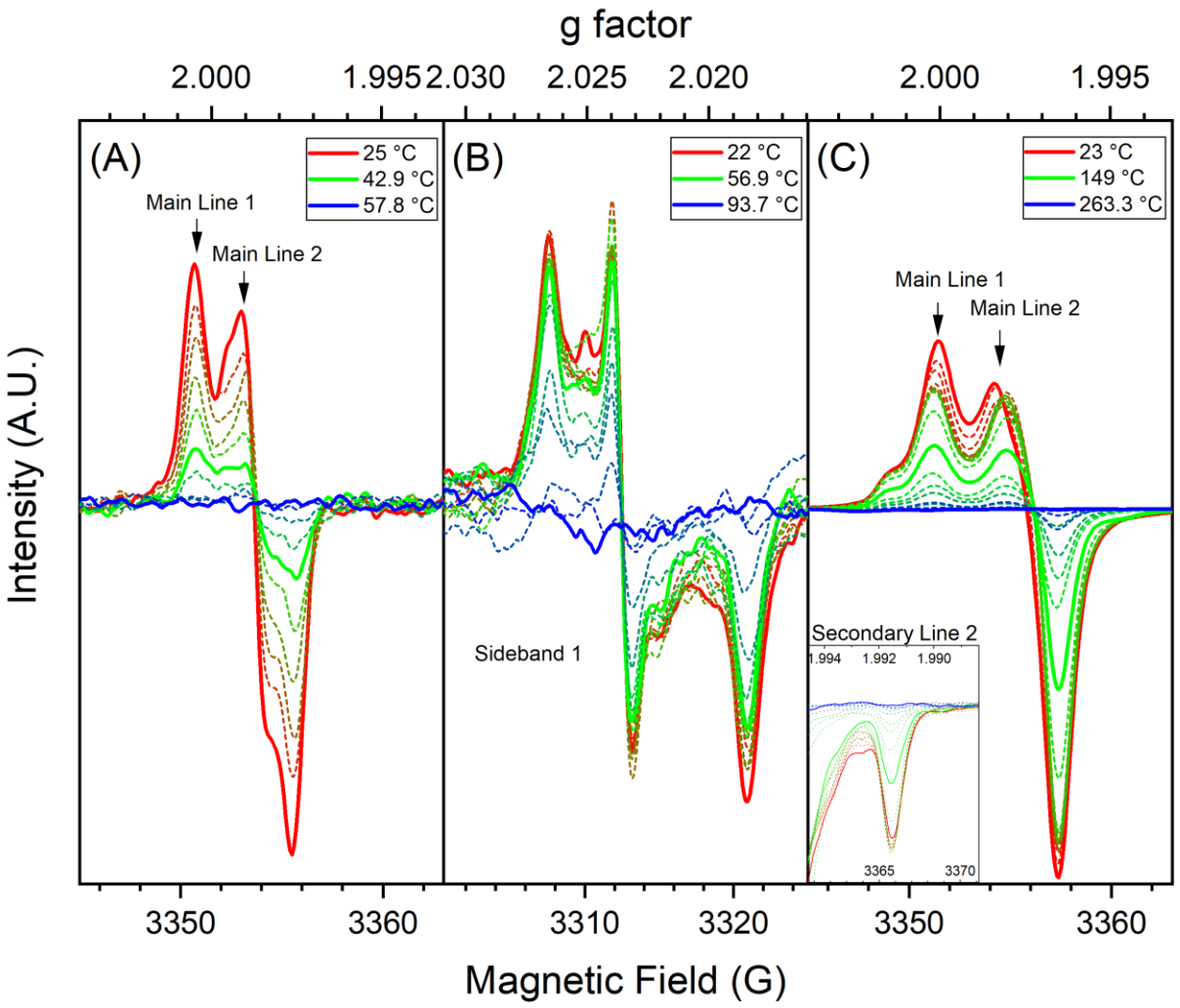

***Fig. 9.4**: EPR spectra acquired from K-200 sample during the pulsed annealing experiment. The colour scale of the curve goes from red, to green, to blue as the anneal temperature grows. In the legend are indicated the first temperature, a middle one and the last one, which corresponding spectra are reported in the graphs with a thicker line than the rest of. (A) Main lines observed at a low dose, 100 Gy; (B) Sideband observed at a high dose, 15.7 kGy, and at a low magnetic field; (C) Main lines observed at a high dose, 15.7 kGy.*

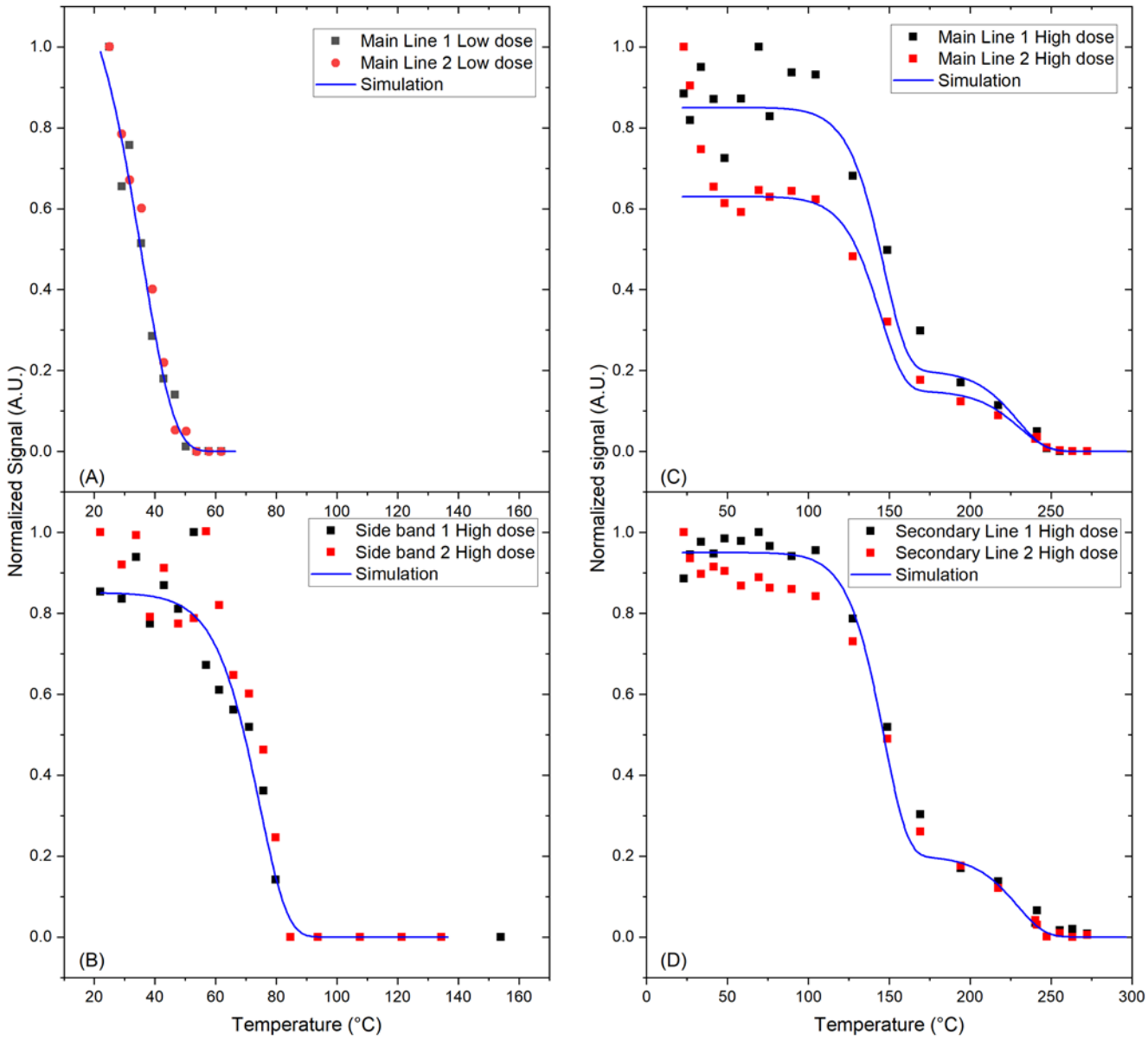

***Fig. 9.5**: Intensities of the signals reported in Fig. 9.4 as a function of annealing temperature during a pulse anneal procedure. Main Lines 1 and 2 refer to the $[GeO_4/Li^+]^0$ centre, while Main Lines 1 and 2 at Low dose refer to the $[GeO_4]^-$ centre. Trap depth evaluation for the main lines observed in K-2-00 quartz, assuming first-order kinetics. (A) Low dose main lines, E_T=0.79 eV, S=1E9 Hz. (B) Side bands at high dose, E_T=1.14 eV, S=5E12 Hz. (C) High dose main line 2, E_{T1}=1.06 eV, E_{T2}=1.30 eV, S_1=5E8 Hz, S_2=9E8 Hz. (D) Secondary lines observed at high dose, E_T and S values as in panel C.*

EPR signals	E_T (eV)	S(Hz)	TSL peak	E_T (eV)	S(Hz)	Ref.
Main lines Low dose	0.79±0.11	1.00E+09	110 °C	0.77±0.07	4.00E+09	Vaccaro et al., 2017
Main and Secondary Lines	1.06±0.27	5.00E+08	325 °C	1.09	/	Guzzo et al. 2017
High Dose	1.3±0.4	9.00E+08				
Sidebands	1.14±0.09	5.00E+12	330 °C	1.07	/	Guzzo et al. 2017
			296 °C	1.22±0.02	2.00E+08	Yazici and Topaksu, 2003
			378 °C	1.28±0.01	2.00E+08	Yazici and Topaksu, 2003

Table 9.1*: Trap parameters obtained from the simulations in Fig. 4 on the thermal stabilities of the observed lines and values found in literature on some TSL peaks.*

9.2.3 Q-band measurements

Finally, the Q-band spectra for both K-200 and Nat-01 samples have been acquired to achieve a less convoluted spectrum and try to obtain the g-factors of the observed signals in a physical way and not just through simulation. The spectra acquired at low dose (100 Gy) are reported in Fig. 9.6, and the ones at high dose (15.7 kGy) in Fig. 9.7. In the same Fig. 9.7, a K-200 spectrum acquired after a 1 h delay from irradiation, holding the sample at room temperature is also reported. This allows to clearly distinguish between the lines from $[GeO_4]^-$ and the ones from $[GeO_4/Li^+]^0$. The delay time was chosen by taking into account the fact that the decay time of the $[GeO_4]^-$ signal at room temperature is known to be around 50 minutes (Vaccaro et al., 2017, and Tab 5.1). For K-200 the decay time, as shown in section 5, is expected to be more, but 50 minutes has been revealed to be enough to spot the desired differences, given also the relatively higher stability of the $[GeO_4/Li^+]^0$ signal (Vaccaro et al., 2019).

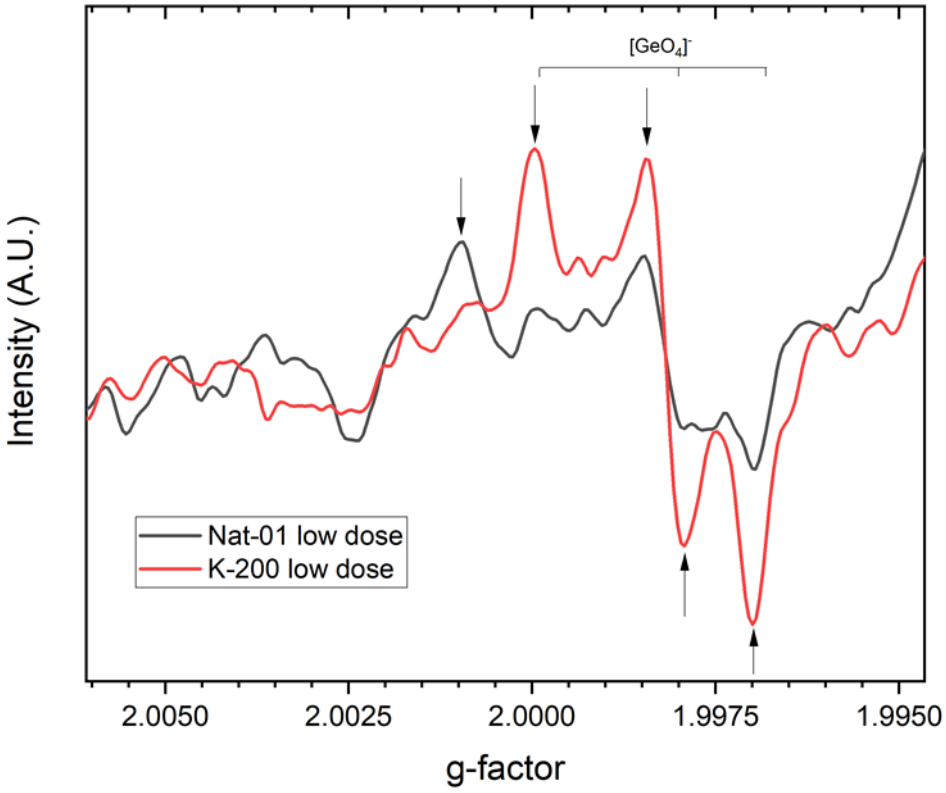

***Fig. 9.6**: Low dose Q-band spectra of K-200 and Nat-01 quartz samples. For better clarity, the intensity is reported as a function of g-factor. The arrows point to the observable lines from $[GeO_4]^-$*

.

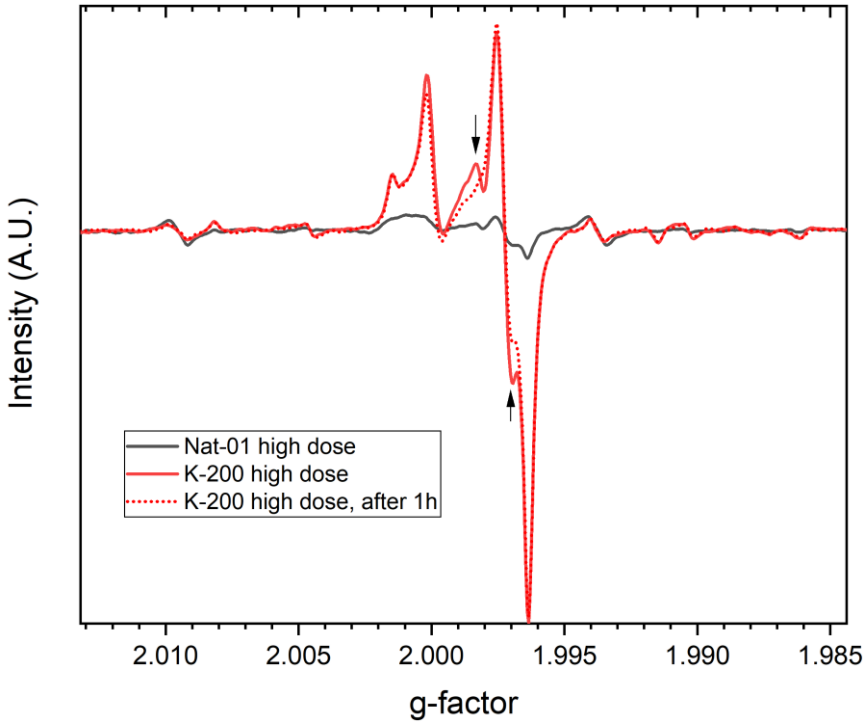

***Fig. 9.7**: High dose Q-band spectra of K-200 and Nat-01 quartz samples. It is also reported the spectrum of K-200 after 1 hour from irradiation at room temperature. For better clarity, the intensity is reported as a function of g-factor. Arrows point at the lines affected by the drop of the intensity of the signal from $[GeO_4]^-$.*

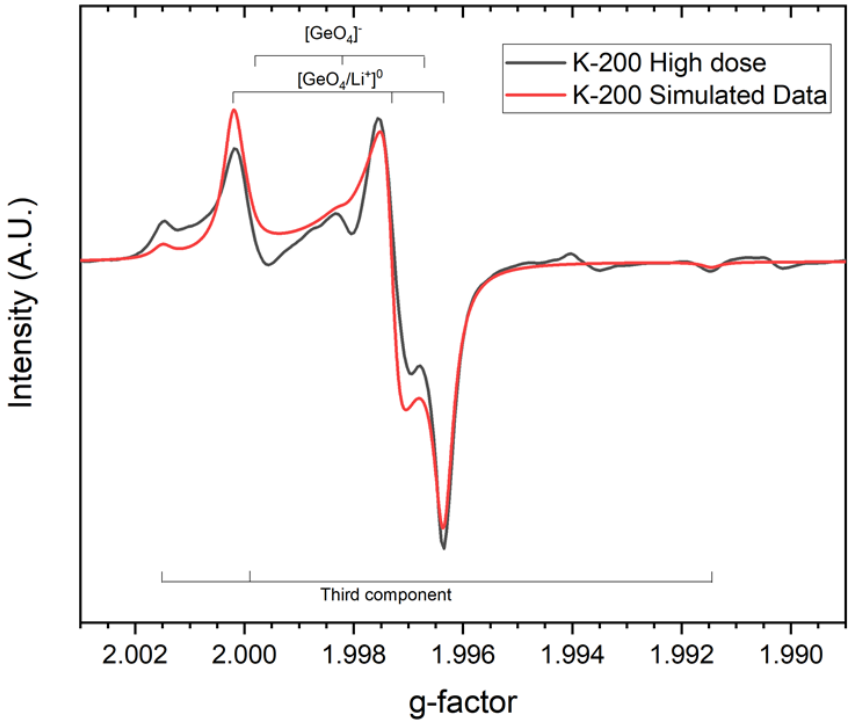

***Fig. 9.8**: Simulation of the EPR spectrum of K-200 at high dose, measured at the Q-band. Intensities are reported as a function of g-factor.*

The spectrum at high dose was further analysed with numerical simulations. The parameters found in the literature on $[GeO_4/Li^+]^0$ allow to perfectly fit the most intense lines, confirming the fact that in this dose range the signal from this centre is the dominant component of the spectrum. In order to improve the quality of the simulation, taking into account also the weaker components, the contribution of the signal from the $[GeO_4]^-$ centre was added. A third signal was required to further improve the simulation, constructed with the g-factor components: g_1=2.0015, g_2=1.9999 and g_3=1.9915. For better clarity, the curve obtained is reported in Fig. 9.8 along with the measured spectrum seen also in Fig. 9.7.

In table 9.2 the EPR parameters used for each signal simulation in this section are summarized.

$[GeO_4]^-$		$[GeO_4/Li^+]^0$		Third component		Sidebands			
g_1	1.9999	g_1	2.0001	g_1	2.0015	g_1	2.0007	A_1 (MHz)	233
g_2	1.9980	g_2	1.9974	g_2	1.9999	g_2	1.9974	A_2 (MHz)	235
g_3	1.9968	g_3	1.9963	g_3	1.9915	g_3	1.9929	A_3 (MHz)	239

***Table 9.2**: EPR parameters of the observed signals used for the simulations in Fig. 2 and 7. $[GeO_4]^-$ and $[GeO_4/Li^+]^0$ are the values reported in Vaccaro et al., 2017 and 2019.*

9.3 Comments

From simulations of the spectra made with Easyspin, using both $[GeO_4]^-$ and $[GeO_4/Li^+]^0$ g-factors reported in Vaccaro et al., 2017, Vaccaro et al., 2019 and references therein, and the measurements made in the X-band in Fig. 9.1, it seems that the $[GeO_4]^-$ signal is initially dominating the spectrum at the lower doses and increasing the irradiation time the $[GeO_4/Li^+]^0$ signal becomes the stronger one. This could be to either a saturation process on the $[GeO_4]^-$ centres or there may be a mechanism

that converts $[GeO_4]^-$ into $[GeO_4/Li^+]^0$ during the irradiation process. Something similar to the latter proposed mechanism has already been considered by McKeever et al (1985), although such process was occurring during an anneal procedure. This results in an apparent shift of the spectrum's main lines, since at low dose the signal is mostly due to $[GeO_4]^-$ centres, which get outnumbered by the more stable $[GeO_4/Li^+]^0$ centres at higher doses. The fact that $[GeO_4]^-$ signal is superimposed to the one from $[GeO_4/Li^+]^0$ is confirmed also from the spectra obtained after pulsed annealing and reported in Fig. 9.5 (panels A and C) and the Q-Band spectra, which will be discussed later in this section.

The results on the simulation reported in Fig. 9.2 and the equivalent thermal stability reported in Fig. 9.5 point to the fact that the sidebands are originated from the same centre, which is showing a hyperfine structure of a paramagnetic centre perturbed by hydrogen. At the best of the found knowledge, this paramagnetic centre has not been reported in the literature, so far. Its precise origin is, though, still not clear, apart from its relationship with hydrogen and the fact that the g values obtained (lower than 2.0023, the free electron value) suggest an half-filled outer shell (Abragam and Bleaney, 2012) and thus that it should be an electron trap. Further investigation would be required in order to clarify its origin, for example using synthetic samples with controlled impurity content or EPR measurements on oriented bulk samples in order to study the angular dependence of the spectrum. What is also interesting about this finding is the fact that paramagnetic hydrogen related centres are usually reported as associated to hole recombination centres in the luminescence properties of quartz rather than to an electron trap (e.g. H_3O_4 or perturbed $[AlO_4]^0$, Jani et al. 1983, Yang and McKeever 1987). Moreover, the few reports of hydrogen related electron traps are from hydrogen compensated centres originated by impurities often not abundant enough in quartz to reach a detectable level for EPR measurement and whose EPR signal, unlike the one observed in the experiments reported in this section, is not usually detectable at room temperature due to fast relaxation times (e.g. $[TiO_4/H^+]^0$, Rinneberg, 1972). Something similar, i.e. an electron centre with hydrogen hyperfine structure observed at room temperature, has been reported by Weil (1971) in the form of $[GeO_4/HLi_2]^0$, but when comparing the g factors, the thermal stability and the absence of Li hyperfine structure, it seems to be a different signal from the one observed in K-200.

On the thermal stability of the other signals, the Main Lines of the spectra at the lowest dose, originated from the $[GeO_4]^-$ centre, decays at around 50 °C. The Main Lines at the highest dose, originated from $[GeO_4/Li^+]^0$, decay at the same rate of the Secondary Lines, suggesting some connection, and showing a two-step process which becomes evident at around 240 °C, with the total signal disappearing at around 260 °C. It is fair to assume that the initial drop in intensity of Main Line 2 at high dose, and the large scattering observed for Main Line 1 at high dose, are due to the interference of the decay of the strongly overlapped $[GeO_4]^-$ signal. This results in an initial drop of Main Line 2 signal followed by a small plateau up to 120 °C, where a further decay then starts. As already briefly mentioned, the centres responsible for the Secondary lines, observable at high dose,

may be related to some degree to the $[GeO_4/Li^+]^0$ centres, which are responsible for the main lines at high dose. One possibility could be a distorted version of the germanium centre which possesses similar thermal stability.

On the two steps decay process it may be speculated that, since an electron trap is being observed, it could be originated either by the depletion of a hole source nearby the electron source (the observed signal) or by the presence of a thermally assisted tunnelling process. In the first case, a hole centre is getting depleted and the positive charges recombine with the electrons of the observed centre, causing the drop of its intensity. In the second case, the first drop of the defect population would be due to the recombination of the trapped electrons with a hole centre nearby through a tunnelling process, then, with the further temperature increase competing with a more classical thermal depletion of the trap levels via conduction band. This could be possible, for example, if there was a recombination centre that during the crystal growth process would originate preferentially in proximity of the defects acting as electron traps, such as the observed one. This way there would be an energy barrier between trap and recombination centre levels, which could be tunnelled with thermal assistance. This could be proven with future thermoluminescence experiments, if there are peaks in the glow curve following the same pattern. This of course would be possible provided that the recombination is radiative.

About the Q-band spectra, it can be underlined how in Fig. 9.6, low dose signal of the $[GeO_4]^-$ centre in Nat-01 is barely distinguishable from the background noise, while in K-200 it is clearly evident. The prominent line, just outside the graph on the far right, is originated from the resonator itself and is, therefore, an artefact. In Fig. 9.7, the high dose K-200 spectrum clearly shows that the main lines observed in the X-band spectra (Fig. 9.1) are composed by at least two different components (i.e. $[GeO_4]^-$ and $[GeO_4/Li^+]^0$). The Nat-01 spectrum, reported for comparison, is not intense enough to draw such conclusions with good reliability. By showing in the same figure a spectrum acquired after keeping the sample at room temperature for 1 hour, it also becomes evident which lines are related to $[GeO_4]^-$, less stable, and which ones to the more stable $[GeO_4/Li^+]$ centre. The two Sidebands reported in Fig. 9.2 could not be observed during the Q-band experiments as clearly as in the X-band ones, despite having used the same irradiation dose, probably because of the lower sample amount, resulting in an intensity below the detection limit. Trying to predict their position in the spectrum using the g-factors reported in the previous sections, one could find some compatible lines in the experimental data, but they are either not prominent enough from the baseline or too much overlapped with the stronger signals to make a reliable evidence as in the X-band spectra.

The simulation shown in Fig. 9.8 is close to the experimental data. As for the third component used to fit the spectrum, its origin is not clear, but at least one of its components, g_1, seems compatible with the value observed by Kaya-Keleş et al. (2019) and with the Secondary line 1. In the Q-band spectra, the "Secondary Line 2" was not detected in a clear way as in the X-band experiments, although g_3 has been set to fit a line with very low intensity when compared with the background that

could be compatible with it. Since the "Secondary line 1" is clearly evident in the Q-band spectra, so it can be assumed that the secondary line either is not originated from the same centre, despite the thermal correlation observed in the X-band, or that it is just not easily detectable in the Q-band experiments. The position of the "Secondary line 1" could suggest that it is originated from an oxygen vacancy related defect, such as one of the family of E' defects. (Usami, 2009, Toyoda, 1993, Arends, 1962).

To summarize, the EPR spectra of two natural samples has been studied, focusing on the new features observed in one of them, specifically the pegmatitic K-200. The qualitative dose response of the spectrum and the thermal stability of its components has been reported. Part of the observed spectrum is composed of already know germanium related signals, which were investigated more in detail in previous studies (Mackey, 1963, Lutoev, 2006, Toyoda, 2015, Vaccaro et al., 2017, 2019, section 5 and 6) and correlated to TSL processes of quartz. Besides these defects, the contribution of at least two more signals, one of which previously unreported, was evidenced. In particular, a new electron trap has been found, which showed a hydrogen hyperfine structure and a thermal stability intermediate between the ones of the two observed germanium centres, disappearing at around 80 °C, while the germanium ones anneal at around 50 °C and 260 °C. The other signal observed is composed of two unassigned lines, which have been labelled Secondary Lines, one of which has recently been reported (Kaya-Keleş et al., 2019). Here it has been found out that both lines have similar thermal stability, so it is possible they are originated from the same centre. An assignment of these lines' origin is still needed in order to confirm this. The Secondary Lines' stability is also comparable to the one of the more stable germanium centres, $[GeO_4/Li^+]^0$, so the responsible defects may be related in some way. Further studies should be aimed at identifying the nature of these unknown centres, both the new ones here presented, and the others already reported in the literature but still unassigned. In addition, it would be interesting to find out if these centres have any correlation with the luminescence properties and dynamics of quartz.

10. Characterization of Titanium and Aluminium related centres with low temperature EPR measurements

Although the works of Vaccaro et al. (2017; summarized in section 3) and Vaccaro et al. (2019; presented in section 5) cleared things up regarding the role of germanium in TSL processes in quartz, there are still other electron traps that may have a role in that. A proposed example has been the titanium related centres (Plötze et al., 2012, Williams and Spooner, 2018). Titanium could have a similar role as germanium, by creating an electron trap in the quartz crystal lattice that can also be compensated by small cations like Li^+ and H^+. Titanium centres have been wildly studied in the past, both to characterize their EPR spectra (Wright et al., 1963, Rinneberg and Weil 1972) and for dating applications by EPR (Ikeya, 1993, Brumby and Yoshida, 1994, Rink, 1997, Toyoda et al.,2000). Williams and Spooner (2018) argued that, while the work presented in Vaccaro et al. (2017) should be taken into account, it was still possible that titanium centres had a role in those TSL processes together with the germanium related ones. Also aluminium centres play an important role in luminescent properties of quartz, as hole traps and recombination centres (McKeever, 1985), although there is still debate on the emission wavelength being either in the blue, 470 nm (McKeever, 1985), or in the UV, 380 nm (Martini et al., 1995). These kinds of centres, though, can only be observed below 120 K (titanium) and below 150 K (aluminium) (Plötze et al., 2012). This is because of the relaxation time of the magnetic moments of the observed spin states, too fast at room temperature to be observed with EPR. This does not mean, though, that they are not stable trap centres at room temperature, and in fact some of them, such as $[TiO_4/Li^+]^0$ and $[AlO_4]^0$, are surely stable at room temperature (Plötze et al., 2012).

In Fig. 10.1 is reported an EPR spectrum (X-band) published by Toyoda and Goff (1996, reproduced in Toyoda, 2015) of a volcanic quartz sample at 77 K, which is representative of the signals expected in the presented samples. As it is shown, the signals of aluminium and titanium centres are more complex than the ones from germanium shown in the previous sections. The natural abundance of ^{27}Al (100%, I=5/2) makes it that the hyperfine interaction splitting is far more influential than the one of ^{73}Ge (7%, I=9/2), and so much more lines are observed and usually, for simplicity, only the most intense ones are used for analysis. The titanium centres' lines show some degree of overlap, but luckily some of them are resolved and that makes it easier to comment on their presence without need to resort to higher frequency measurements or complex simulations to estimate each signals contribution (as is in the case of germanium related centres presented in the previous sections). The hyperfine interaction with compensating ions (Li, Na and H) is much stronger than the case of $[GeO_4/Li^+]^0$ observed at room temperature and so doublets (H, I=1/2) and quartets (Li and Na, I=3/2) of titanium related lines can be appreciated in the spectrum.

In the last section of this thesis work, EPR measurements at 70 K have been conducted on quartz samples with the aim of characterizing the thermal stability of titanium and aluminium related

paramagnetic centres and explore the possibility of correlation with luminescent properties such as the TSL ones. Similar experiments have been conducted in the past, an example of which can be Toyoda et al. (1991), where the authors studied the thermal stability of $[TiO_4/Li^+]^0$, $[AlO_4]^0$ and E' centres. Toyoda et al. experiment has been taken as a guideline to reproduce in the study of the samples presented in this section.

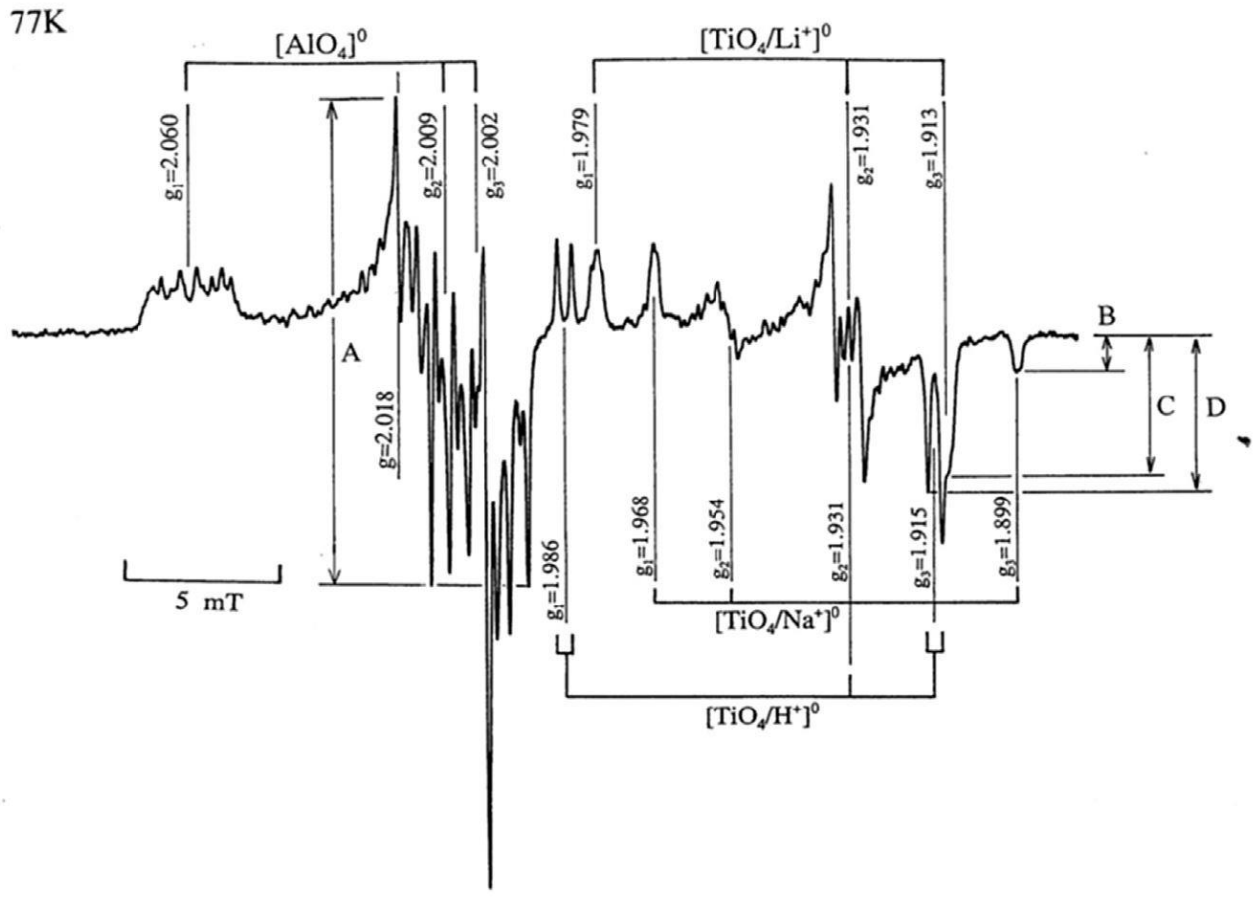

Fig. 10. 1*: An ESR powder spectrum of volcanic quartz at 77 K showing the signals of the Al and the Ti centers (Toyoda and Goff, 1996, Toyoda, 2015)*

10.1 Experimental procedure

10.1.1 Samples

Because of the aim of the study, the samples studied were selected in order to have a quartz crystal with a good abundance of titanium (i.e. enough to be clearly detected through EPR). The samples used were the natural pegmatitic sample previously labelled K-200, which showed enough titanium to be observable with EPR during preliminary studies done during the works for section 5 and 9; a sample of rose quartz, whose colour is believed to be originated by titanium impurities (Goreva et al., 2001); a natural hydrothermal quartz sample which originally had TiO_2 inclusions in the form of rutile needles visible by the naked eye in the bulk crystal. This last sample was chosen with the hope of containing titanium impurities that may have migrated from the rutile phase in the quartz bulk during the crystal growth. This last sample was also first crushed roughly in large grains (diameter in the order of few mm) and then, with the help of an optical microscope, the grains containing rutile needles

were separated from the clear ones, creating two different batches which will be referred to as “with rutile” and “without rutile” for the sake of simplicity. Every sample then has been crushed and sieved to select grains with a diameter between 100 μm and 200 μm. The rose quartz was also divided into three batches, two of which were annealed at 500 °C and 1000 °C, respectively, for 10 minutes and rapidly cooled down to room temperature in air. Due to the low quantity of material available, it was not possible to obtain annealed batches for the other two samples.

10.1.2 EPR measurements

The EPR measurements were performed on the X-band spectrometer located in the Physics Institute of the Czech Academy of Science. The samples were irradiated in the same conditions illustrated in section 9.1.2.

Like for the experiments shown in the previous section, a qualitative dose response study has been done. The samples were irradiated at room temperature, setting the X-ray tube tension and current to 50 kV and 30 mA respectively. The dose range explored is from around 170 Gy up to around 20 kGy, equivalent to irradiation times from 40 s to 1h20’.

A dose was then selected to proceed on the study of the temperature stability of the observed centres. This stability has been studied with pulsed annealings of 15 min each, as in Toyoda et al. (1991). The intensity of the aluminium and titanium lines has been evaluated by the peak-to-peak intensity of the lines with a g-factor of 2.018 (aluminium lines) and 1.913 (titanium lines).

For the experiments, the resonator was cooled down to 70 K with a thermoregulated liquid helium flux. Because of the need of irradiating the sample at room temperature and annealing in an oven, the resonator needed to be cooled down to 70 K for every measurement step. This procedure can take up to 30 minutes in cooling, plus 10 minutes for the measurement. Adding in between the time for irradiation or annealing, a set of measurements was not possible to be done in a single day. To keep into account the thermal decay of the observed signals at room temperature, at the start of each day, a first measurement was taken to compare it with the last one from the previous day and use it to tailor the data together.

Because of the many sharp lines close to each other involved (especially in the aluminium related ones and unlike the germanium related ones observed at room temperature), the EPR spectra in this section will be reported only as a function of the g-factor, and not of the magnetic field, to avoid small shifts due to changes in the microwave frequency between each acquisition that may reduce the readability of the figures.

10.2 Results

10.2.1 Dose response

The first sample to be studied has been the untreated rose quartz, with a cumulative dose on the same aliquot up 20 kGy. In Fig. 10.2 are reported the spectra obtained at each dose step. Between the third and fourth measurement there has been a day, but the differences in the spectrum on the aluminium

and titanium lines are negligible (i.e. they are stable at room temperature). For better clarity, in Fig. 10.3 and 10.4 are reported zoomed versions of the most intense spectrum in Fig. 10.2. Fig. 10.3 highlights the portion of the spectrum containing the aluminium related lines, while 10.4 the titanium ones.

The study has been repeated then on the rest of rose quartz samples and the hydrothermal samples "with rutile" and "without rutile". It was not possible to do it also on the K-200 sample because of the limited time available at the Physics Institute of the Czech Academy of Science. Due to the similar dose responsivity observed, and to save up time, the annealed rose quartz samples were studied only up to 5 kGy. In fact, the two most intense spectra in Fig. 10.2 (5 kGy and 20 kGy) do not show any significant difference, beside the intensity. Fig. 10.5 reports the spectra from the rose quartz annealed at 500 °C, Fig. 10.6 the ones from the rose quartz annealed at 1000 °C, Fig. 10.7 the ones from the hydrothermal quartz "with rutile" and Fig. 10.8 the ones from the hydrothermal quartz "without rutile". These last two ones do not seem to possess any titanium related lines.

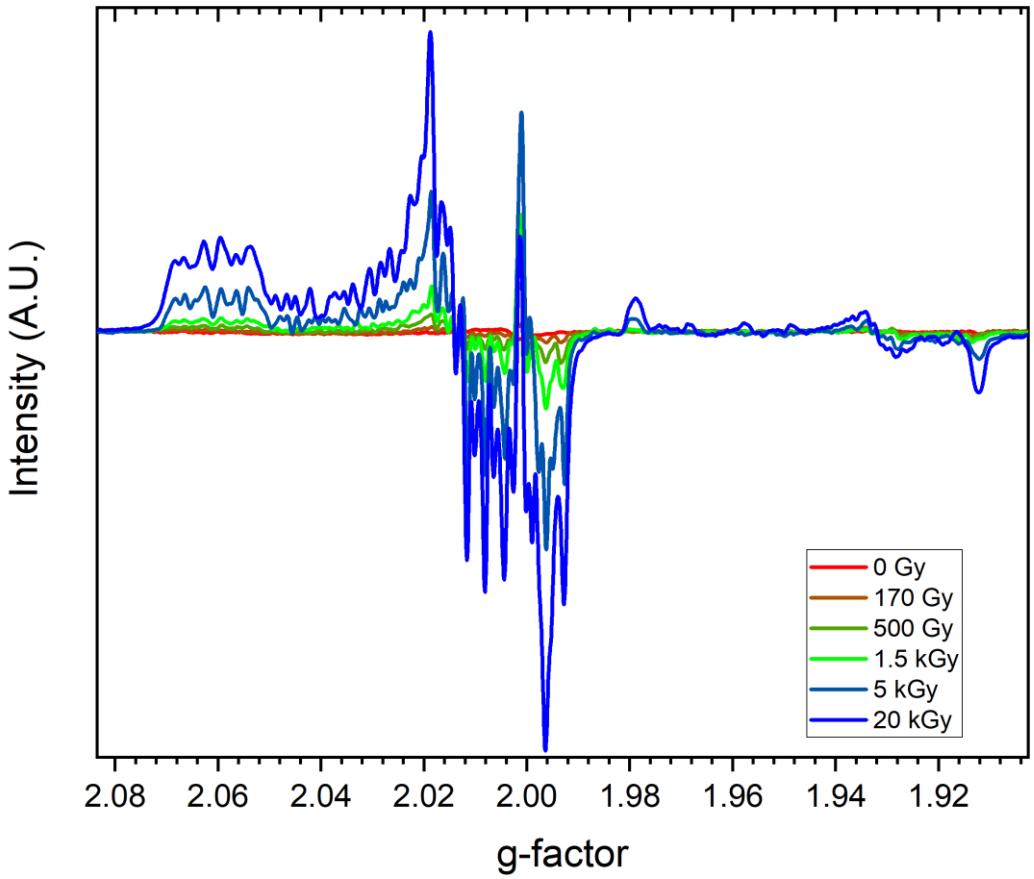

***Fig. 10.2**: EPR spectra dose response in untreated rose quartz at 70 K.*

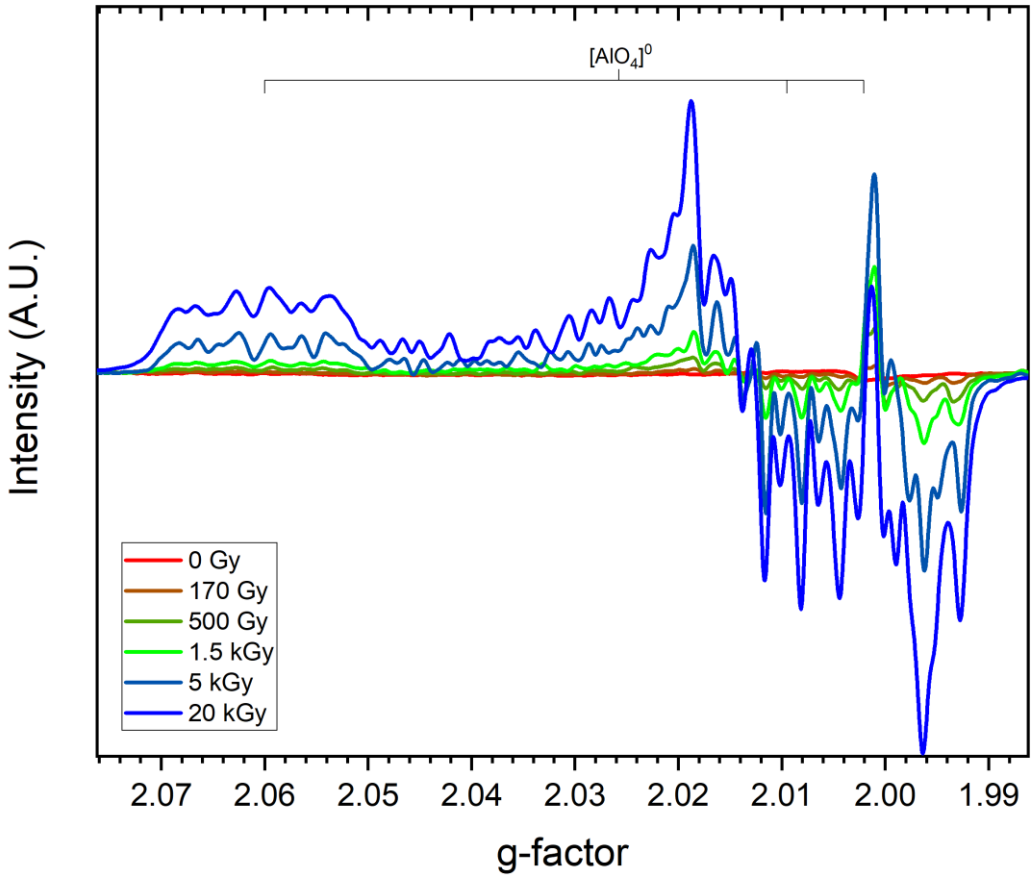

***Fig. 10.3**: Aluminium related EPR lines dose response in untreated rose quartz at 70 K.*

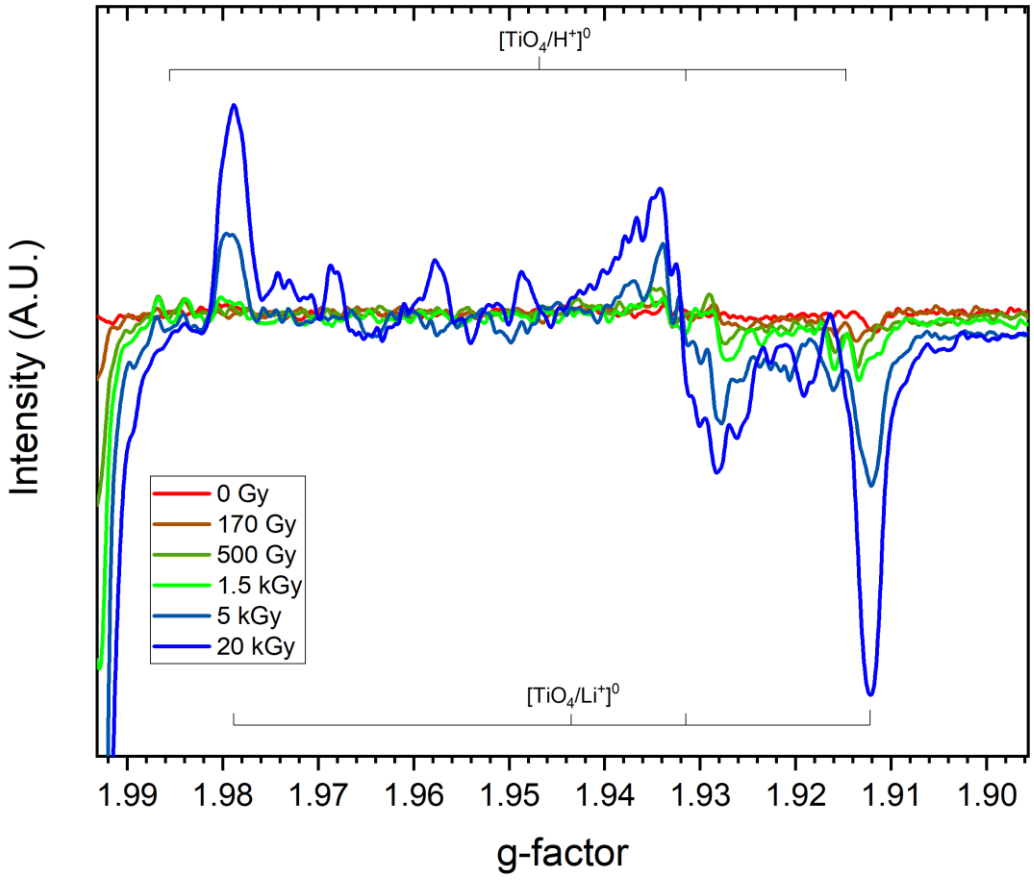

***Fig. 10.4**: Titanium related EPR lines dose response in untreated rose quartz at 70 K.*

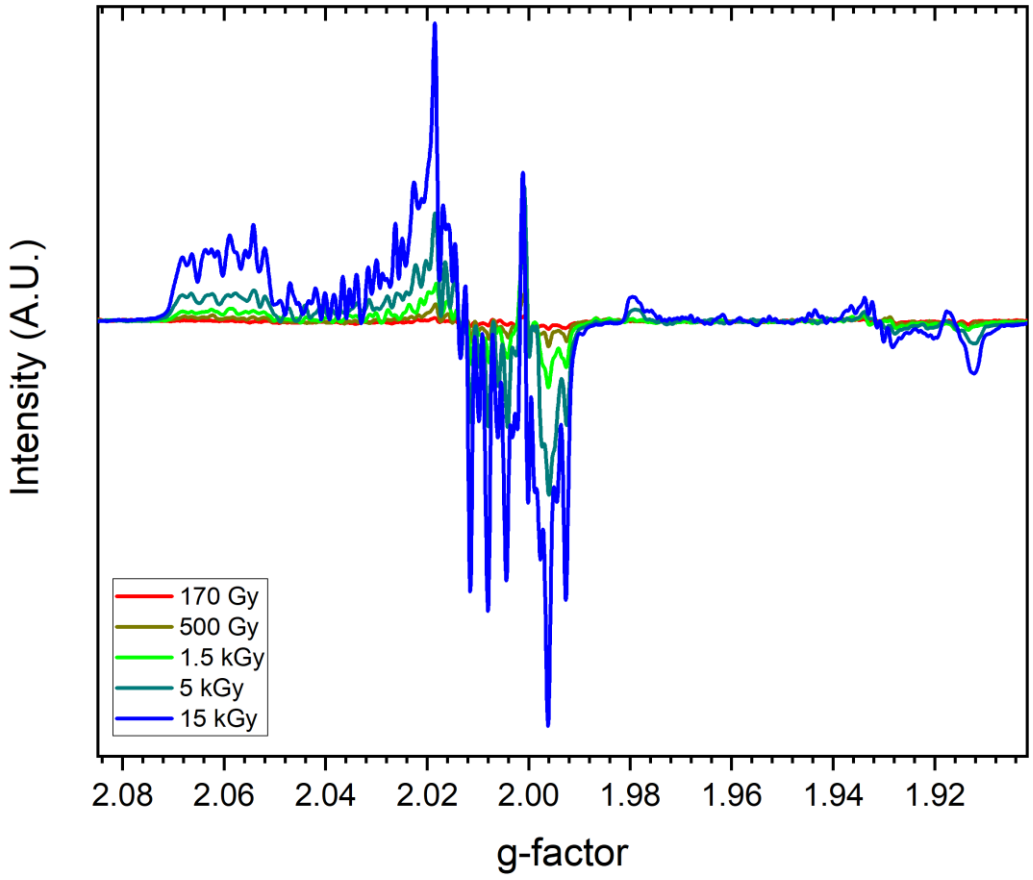

***Fig. 10.5**: EPR spectra dose response in rose quartz (annealed at 500 °C) at 70 K.*

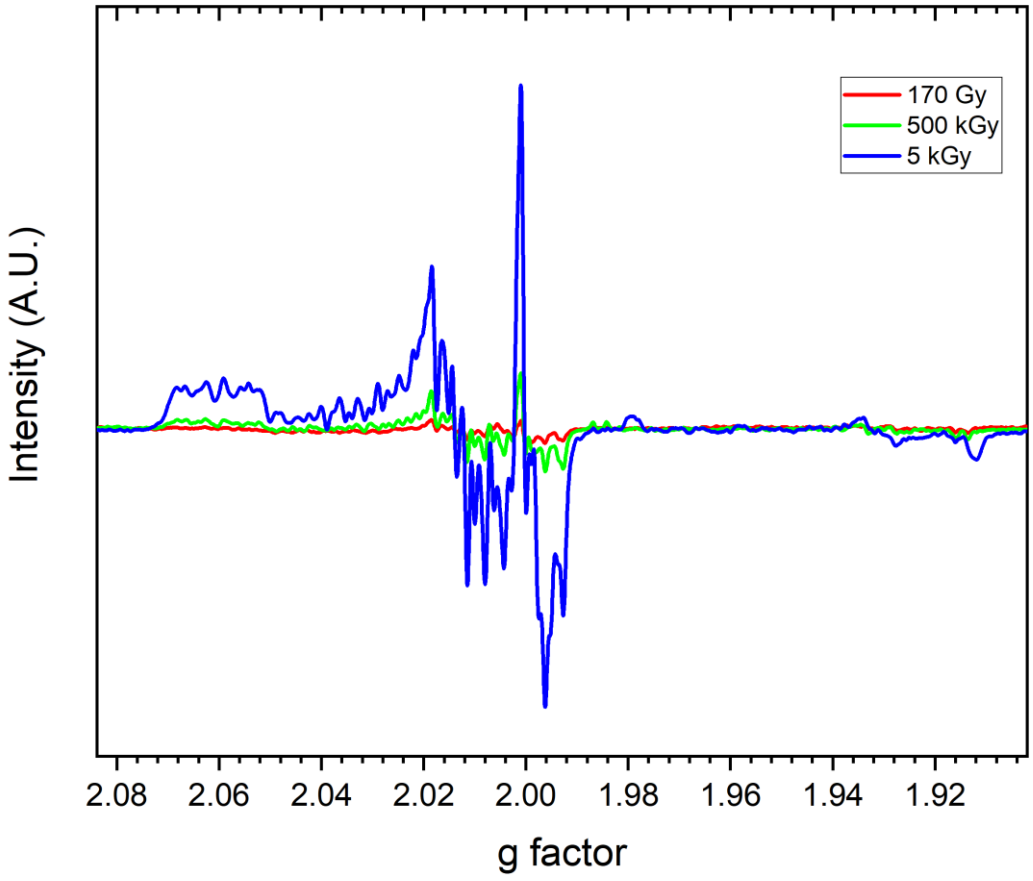

***Fig. 10.6**: EPR spectra dose response in rose quartz (annealed at 1000 °C) at 70 K.*

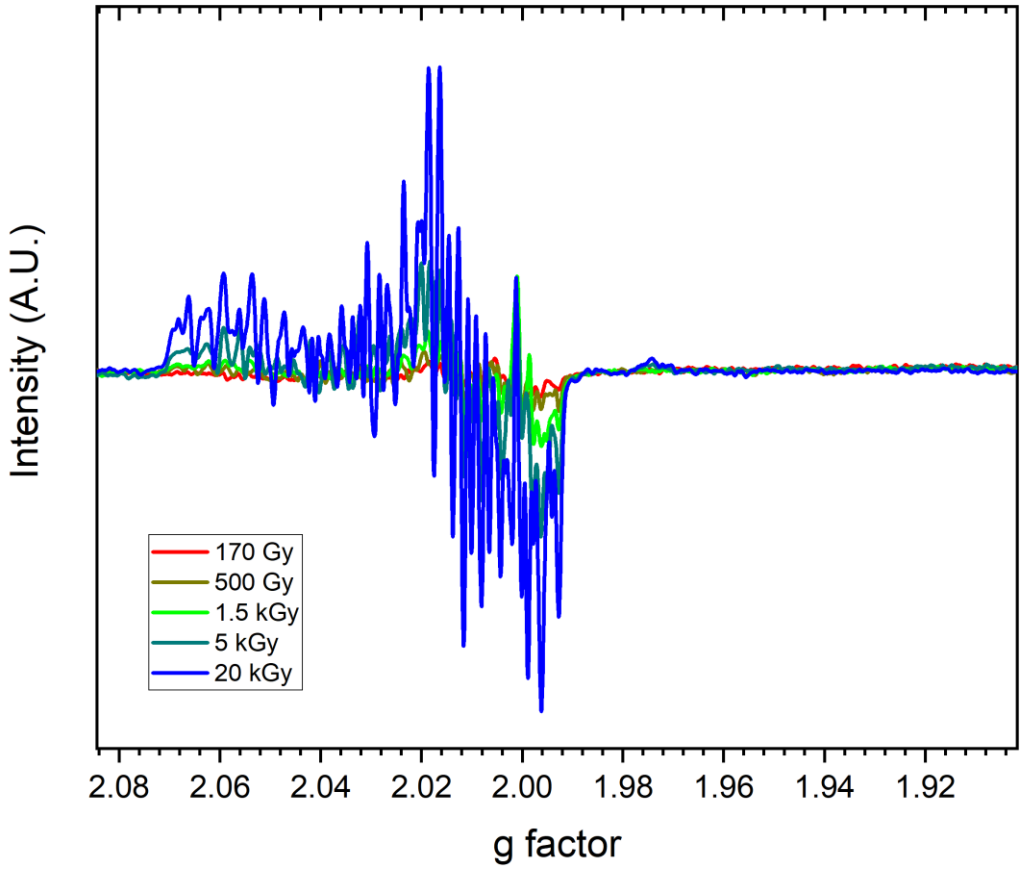

***Fig. 10.7**: EPR spectra dose response in hydrothermal quartz "with rutile" at 70 K.*

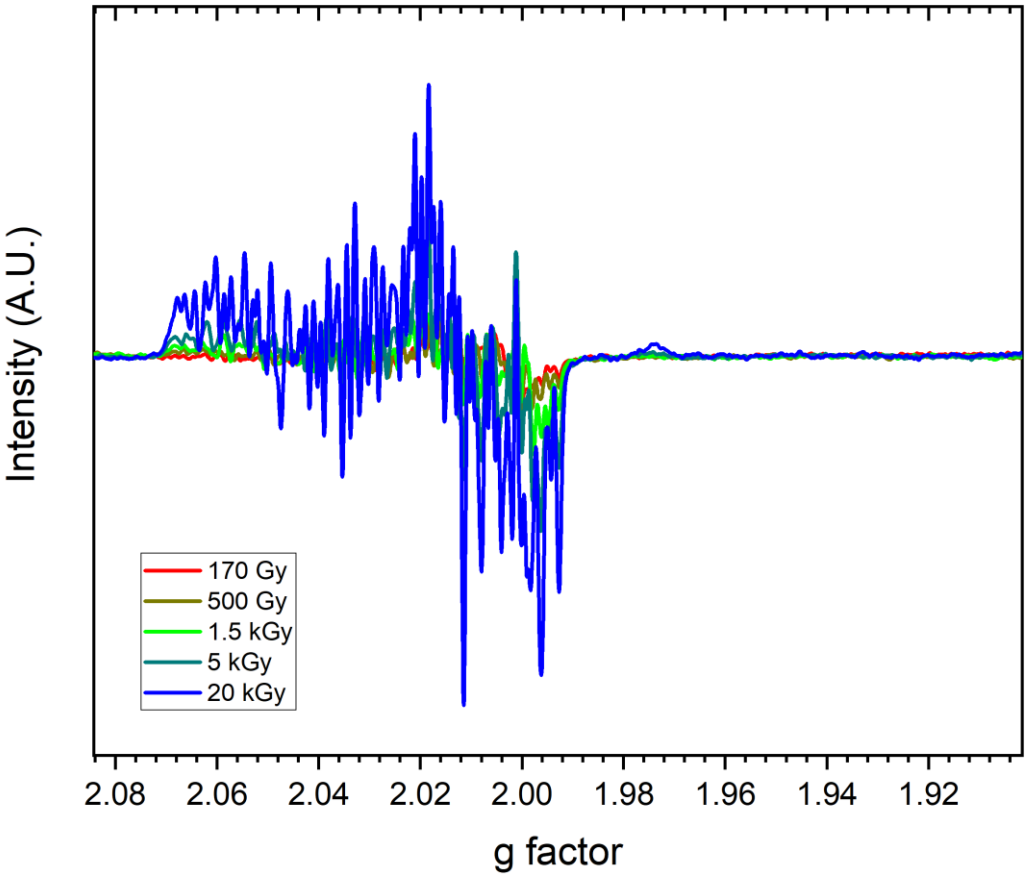

***Fig. 10.8**: EPR spectra dose response in hydrothermal quartz "without rutile" at 70 K.*

10.2.2 Thermal stability

Again, the first studied sample was the untreated rose quartz. After an initial irradiation of 20 kGy, the EPR spectrum at 70 K was acquired to be used as initial intensity of the studied centres. Then the sample has been annealed at a certain temperature for 15 minutes and then measured again (like in Toyoda et al., 1991). As explained in the previous subsection, this kind of measurements are very long, and with a temperature step of 20/25 °C from room temperature up to 450 °C, three days were needed to complete the study on the first sample. In Fig. 10.9 are reported the EPR spectra obtained, showing the evolution of the intensity of the observed lines after each annealing step. For better clarity, in Fig. 10.10 are reported the same spectra from Fig. 10.9 with a focus on the aluminium related lines and in Fig. 10.11 with a focus on the titanium related lines. At around 325 °C the spectrum becomes flat in the aluminium and titanium lines region, but there is the appearance of a new line appears, increasing in intensity with further annealing, with a g-factor around 2.003. The position of this line could suggest that it is originated from a centre of the E' family. The intensity of each signal has been evaluated comparing it to the initial intensity, except the line at a g factor of 2.003 which was normalized to the highest intensity obtained at the highest annealing temperature. The results are reported in Fig. 10.17. The experiment has then been repeated on the other samples with fewer steps of annealing. The spectra obtained are reported from Fig. 10.12 to Fig. 10.16 and the intensity evaluations from Fig. 10.18 to 10.23.

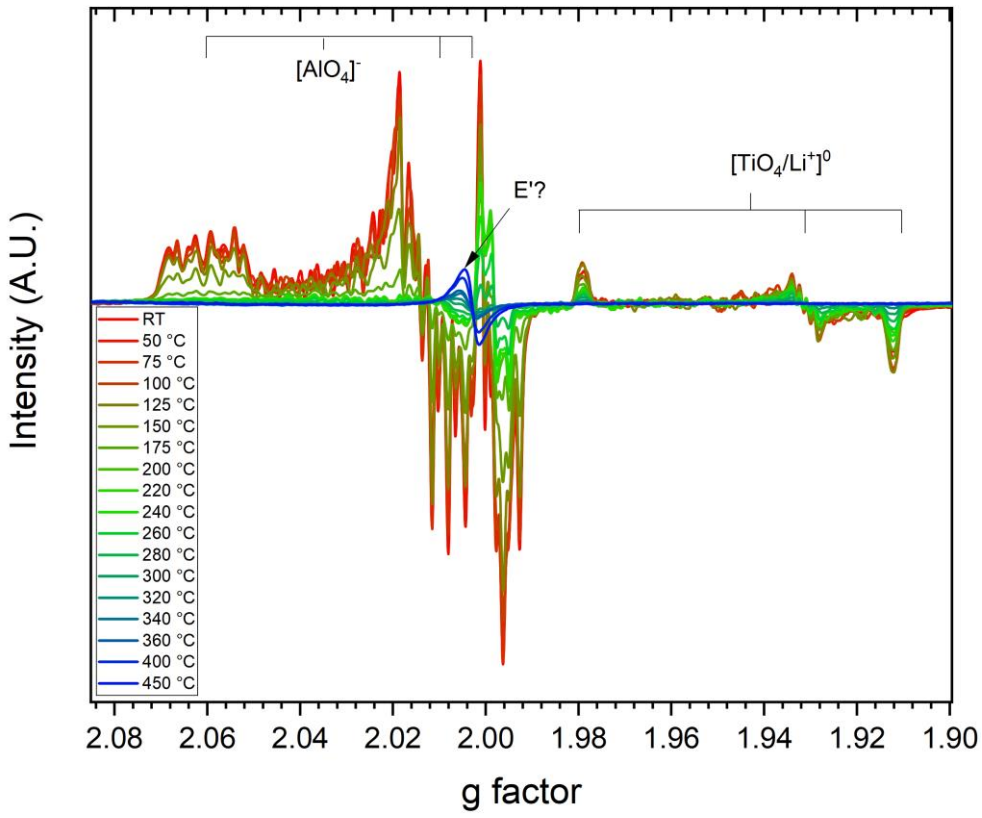

***Fig. 10.9**: Temperature dependence of the EPR spectrum of untreated rose quartz at 70 K. The colour scale red-green-blue shows the progression of the spectrum intensity after each annealing step.*

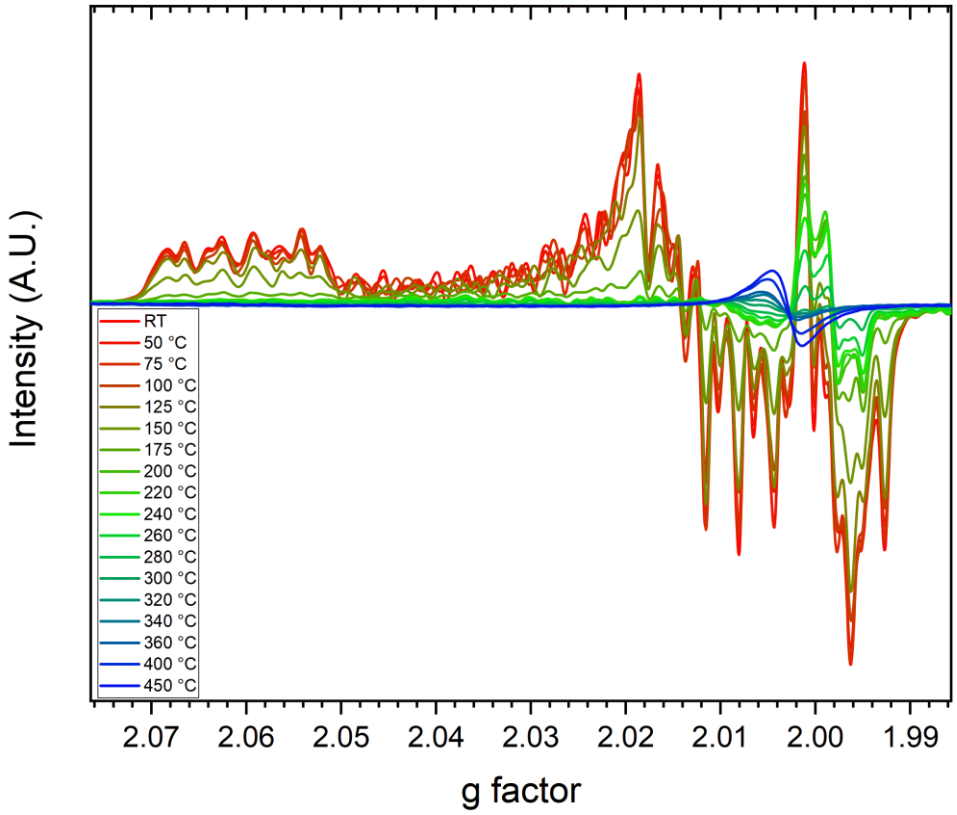

***Fig. 10.10**: Temperature dependence of the EPR spectrum of untreated rose quartz at 70 K (zoom on Al lines). The colour scale red-green-blue shows the progression of the spectrum intensity after each annealing step.*

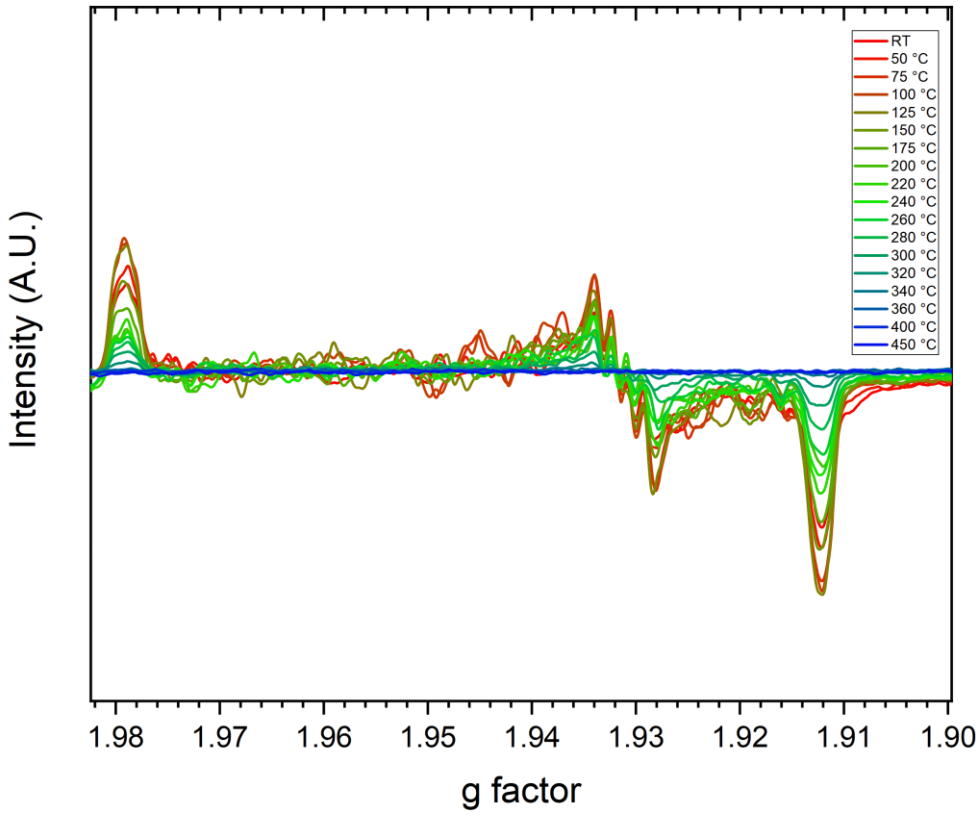

***Fig. 10.11**: Temperature dependence of the EPR spectrum of untreated rose quartz at 70 K (zoom on Ti lines). The colour scale red-green-blue shows the progression of the spectrum intensity after each annealing step.*

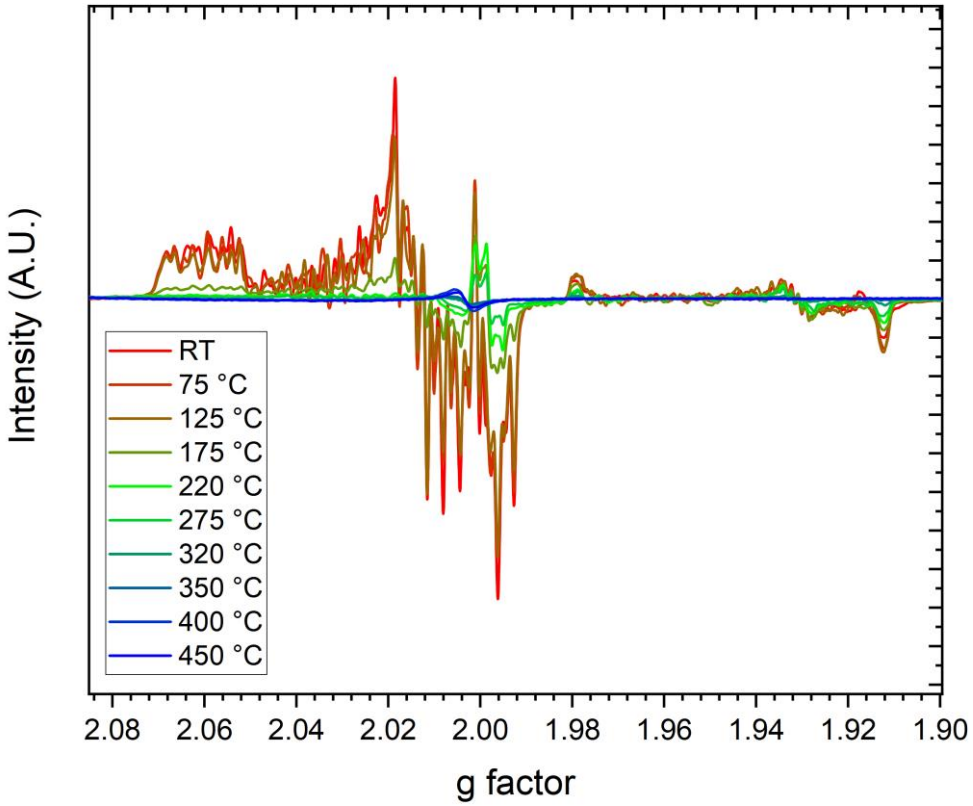

***Fig. 10.12**: Temperature dependence of the EPR spectrum of rose quartz (annealed at 500 °C) at 70 K. The colour scale red-green-blue shows the progression of the spectrum intensity after each annealing step.*

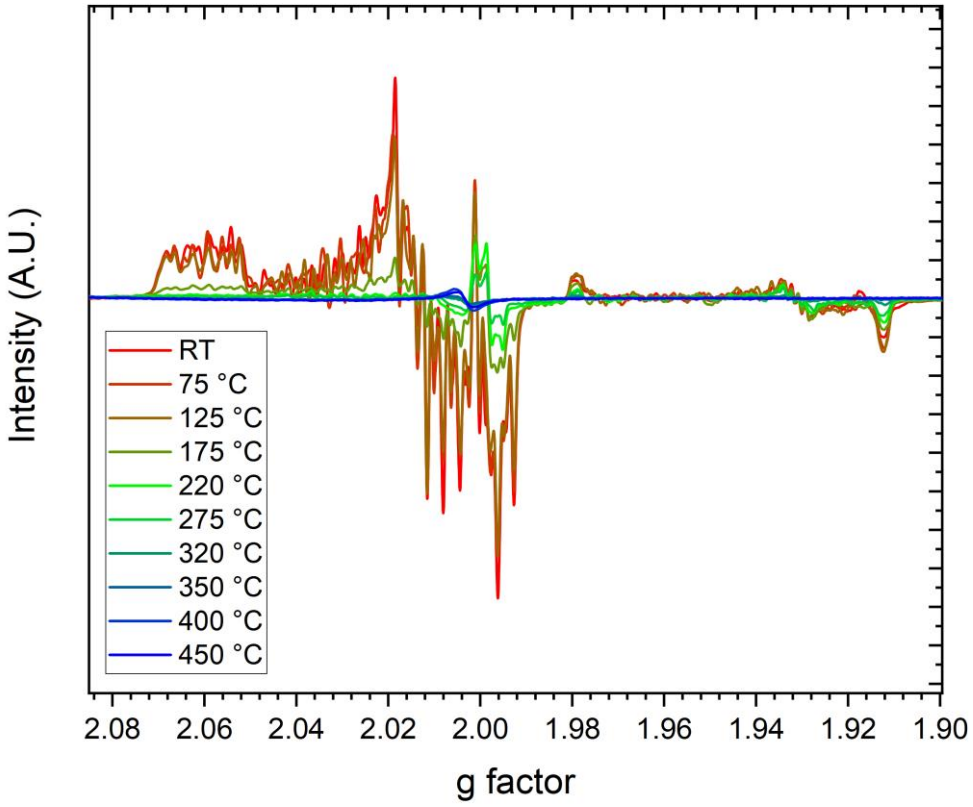

***Fig. 10.13**: Temperature dependence of the EPR spectrum of rose quartz (annealed at 1000 °C) at 70 K. The colour scale red-green-blue shows the progression of the spectrum intensity after each annealing step.*

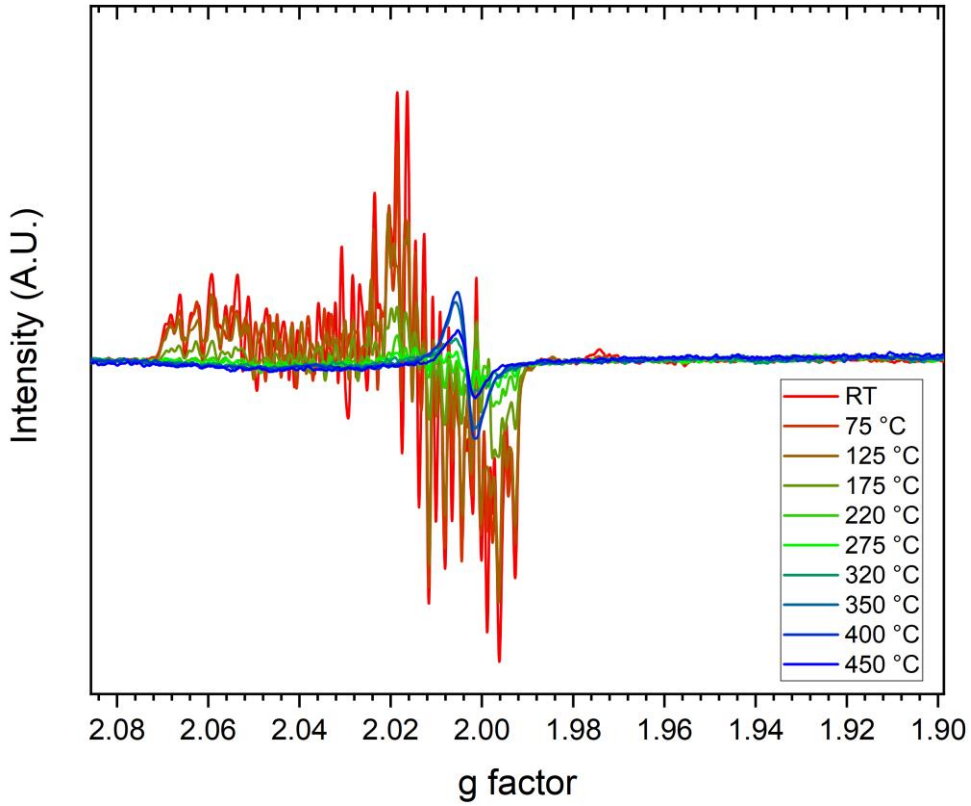

***Fig. 10.14**: Temperature dependence of the EPR spectrum of hydrothermal quartz "with rutile" at 70 K. The colour scale red-green-blue shows the progression of the spectrum intensity after each annealing step.*

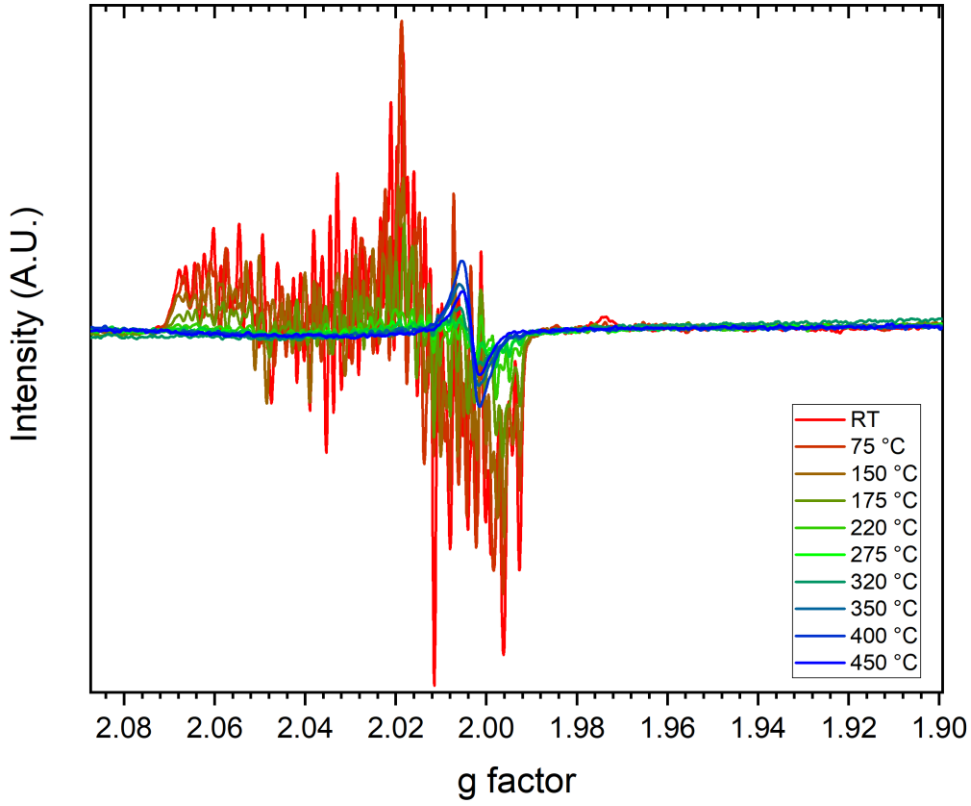

***Fig. 10.15**: Temperature dependence of the EPR spectrum of hydrothermal quartz "without rutile" at 70 K. The colour scale red-green-blue shows the progression of the spectrum intensity after each annealing step.*

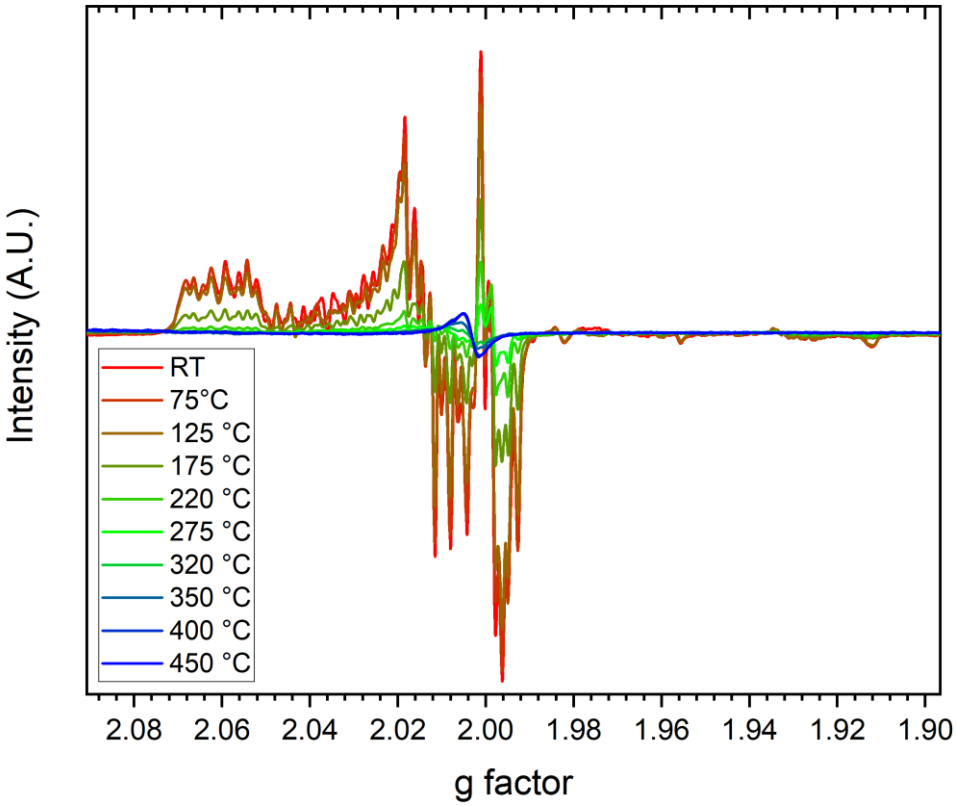

***Fig. 10.16**: Temperature dependence of the EPR spectrum of K-200 at 70 K. The colour scale red-green-blue shows the progression of the spectrum intensity after each annealing step.*

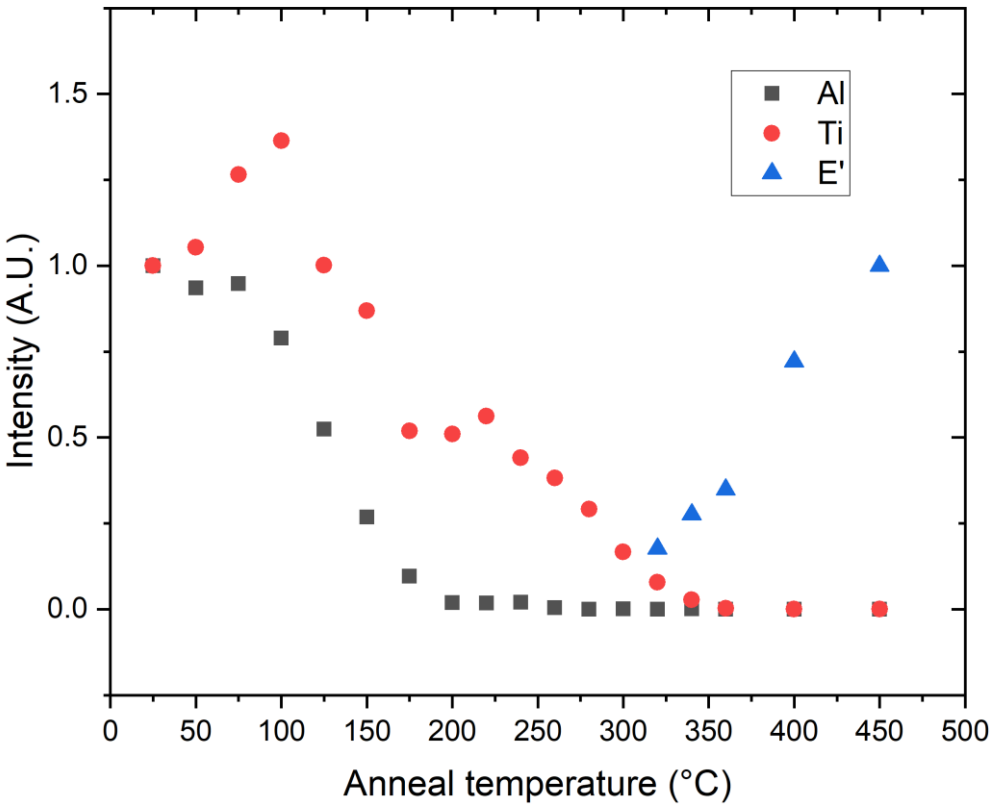

***Fig. 10.17**: Temperature dependence of the EPR lines of untreated rose quartz at 70 K from Al, Ti and possibly E' centres.*

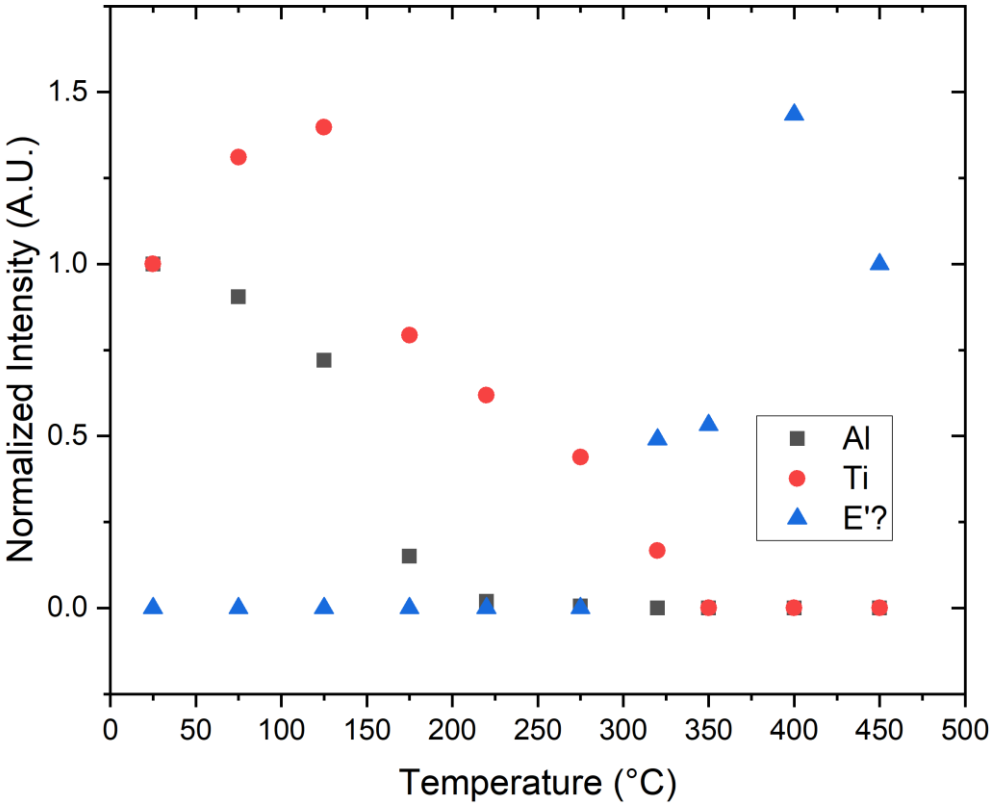

***Fig. 10.18**: Temperature dependence of the EPR lines of rose quartz (annealed at 500 °C) at 70 K from Al, Ti and possibly E' centres.*

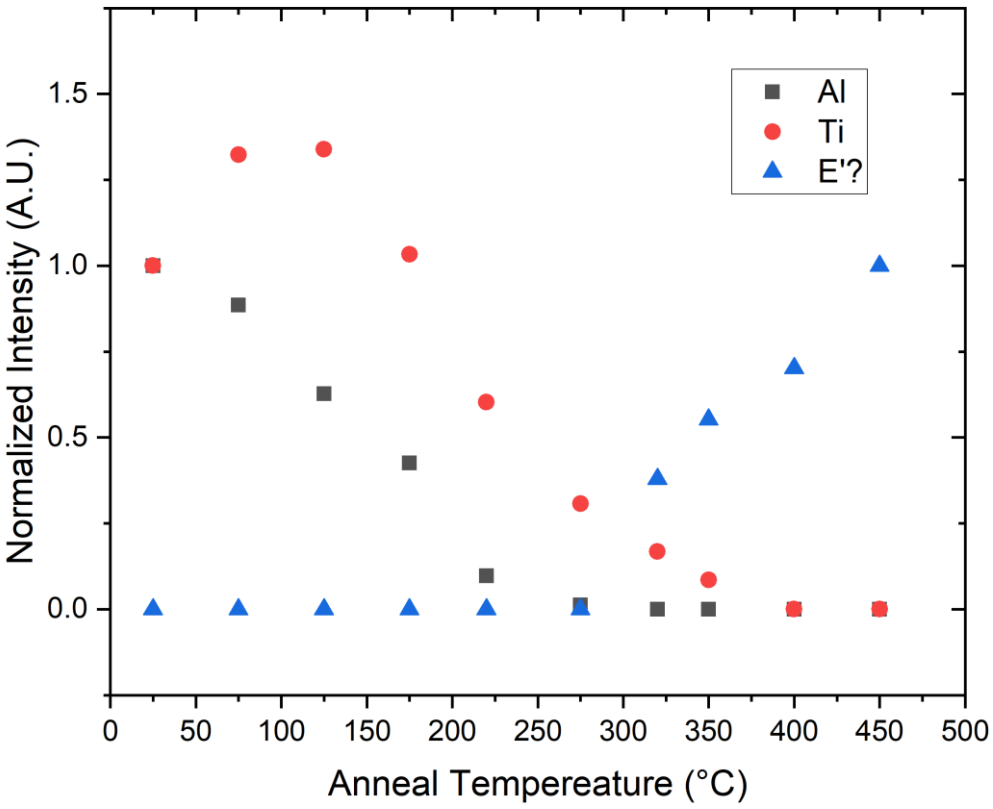

***Fig. 10.19**: Temperature dependence of the EPR lines of rose quartz (annealed at 1000 °C) at 70 K from Al, Ti and possibly E' centres.*

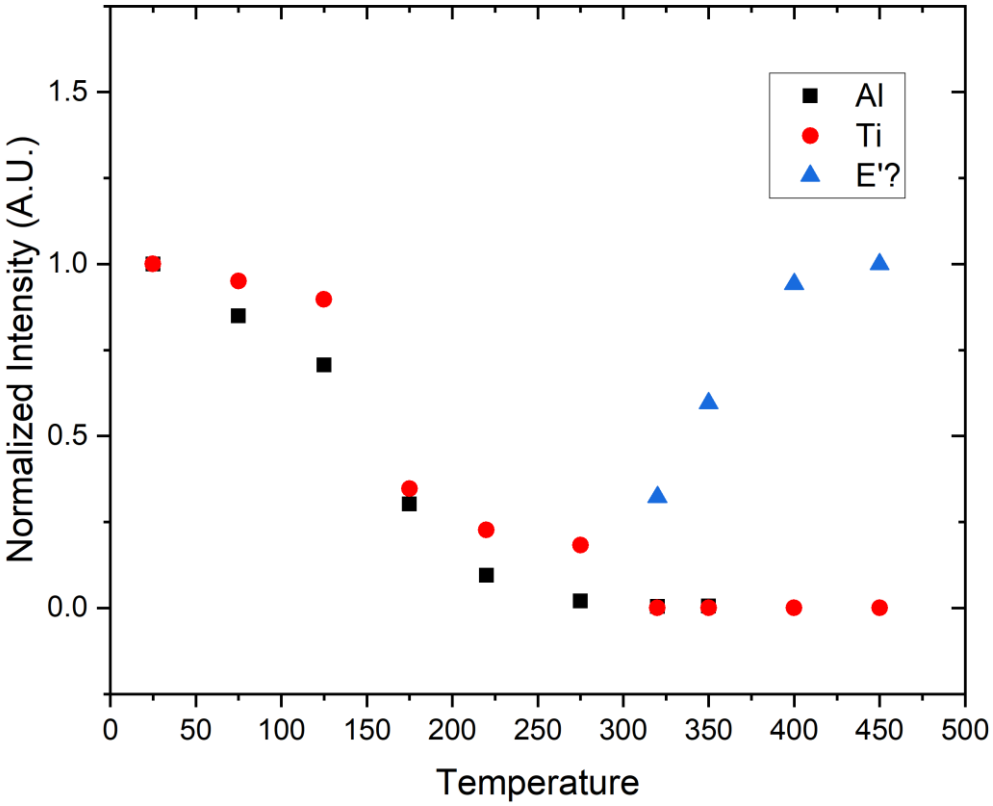

***Fig. 10.20**: Temperature dependence of the EPR lines of K-200 at 70 K from Al, Ti and possibly E' centres.*

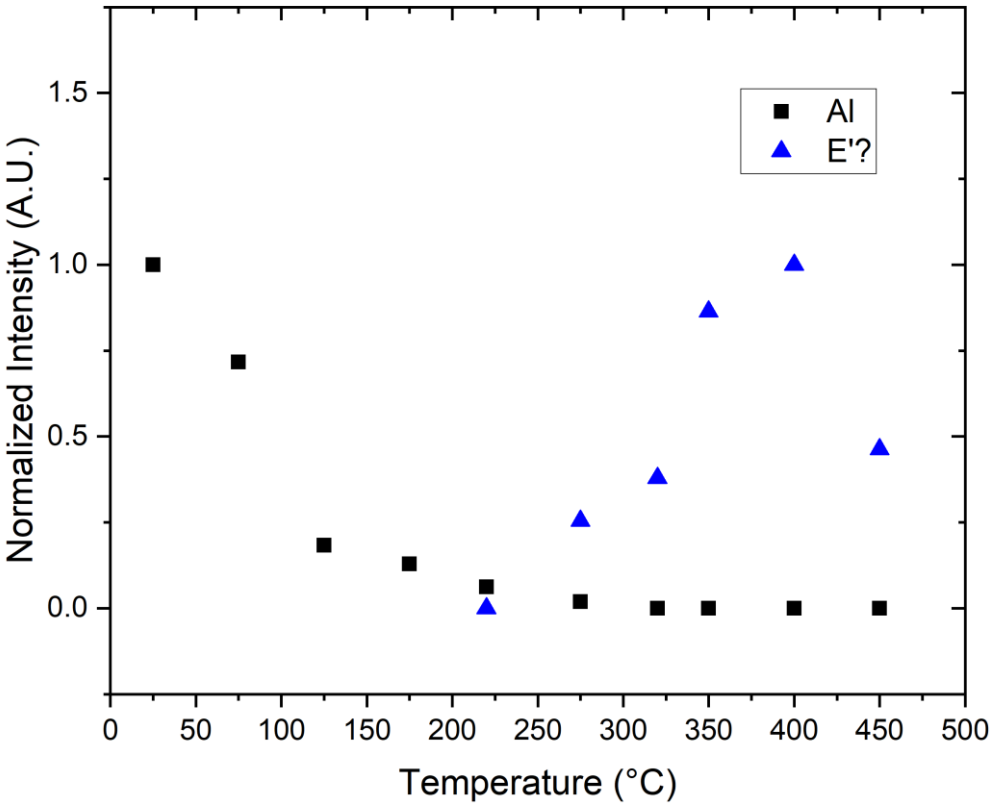

***Fig. 10.21**: Temperature dependence of the EPR lines of hydrothermal quartz "with rutile" at 70 K from Al, Ti and possibly E' centres.*

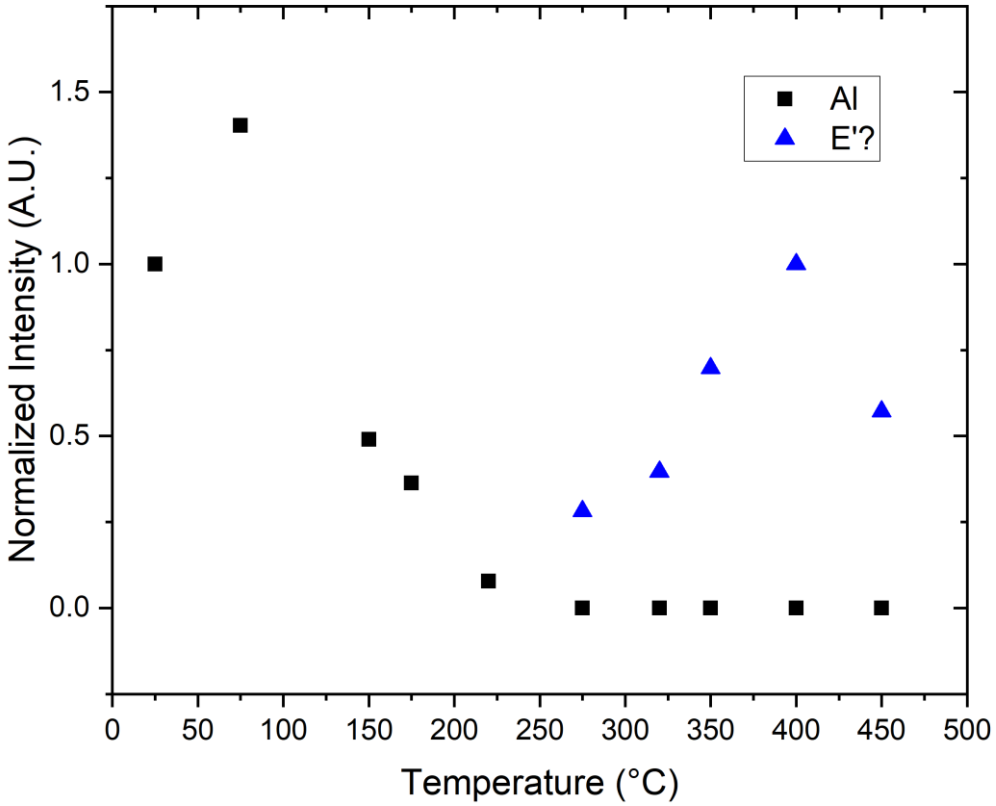

***Fig. 10.22**: Temperature dependence of the EPR lines of hydrothermal quartz "without rutile" at 70 K from Al, Ti and possibly E' centres.*

10.3 Comments

The qualitative dose response and thermal stability of aluminium and titanium lines has been studied. The $[AlO_4]^0$ lines do not seem to show any particular change in their shape, beside the overall intensity, in the dose range studied, while some comments are needed for the titanium ones. Like in the case of $[GeO_4]^-$ and $[GeO_4/Li^+]^0$, $[TiO_4/H^+]^0$ and $[TiO_4/Li^+]^0$ seem to possess a different dose sensitivity. Below 1.5 kGy, the former is the one more intense in the spectrum, while above 1.5 kGy, the latter becomes the dominant one. The possible explanations of this may be the same ones proposed in the previous section for the germanium centres (i.e. either a saturation of one of them or a process of conversion of one centre into the other). On the thermal stabilities, the rose quartz samples seem to show the same general behaviour (i.e. independent from previous annealing). There is an initial increase of the titanium line intensity around 100 °C. This could be related to an increase of the $[TiO_4/H^+]^0$ centres, whose lines overlap with the one from the $[TiO_4/Li^+]^0$ centres. This increase in this temperature range has already been described in the past, for example by McKeever (1985). The titanium lines then show at least a two-step decay process, with the first step starting at around 125 °C and the second at around 225 °C. The aluminium lines instead show a single step decay, which seems to be correlated with the first step of the titanium lines. The observed behaviour of aluminium and titanium signals appear to be the opposite of what reported by Toyoda and Ikeya (1991), which is reproduced in Fig. 10.23. In their work, the authors observed a single step decay of the titanium lines and a two steps decay of the aluminium ones. The same authors, in 1994, published work where

they instead observe a trend similar to the one reported in this thesis work, where the aluminium centre appears to be much less stable than the titanium one. This could just trivially be related to a different abundance of such impurities in the different samples, where the decay of the aluminium signal and the first step of the titanium decay may be related to a process allowed by the presence of both traps, while the second titanium decay step is process purely thermal. This is worth to be further clarified in future studies. The aluminium and titanium centres showed a lower thermal stability than previous studies (e.g. Toyoda and Ikeya, 1991) and this could have major implications in EPR dating, since is one of the centres used in this method (Timar-Gabor et al. 2020). Recently it has also been observed that such centres possess a thermal stability that depends on the dose, being lower in the high dose range of the kGy like in this thesis work (Benzid and Timar-Gabor, 2020). The K-200 sample showed a similar aluminium intensity as the rose quartz samples, but a much lower intensity of the titanium lines. Moreover, it did not show the initial increase in intensity of the titanium lines, believed to be related to the hydrogen compensated centres. Other than that, the trend seems to be similar. The two hydrothermal samples, "with" and "without rutile", against the initial hypothesis did not show any titanium related signals. At the highest doses there is the slight appearance of a line that may be related to $[TiO_4/Na^+]^0$ centres, but the signal-to-noise ratio is too low to allow more comment. The aluminium lines are also much less intense than in the other samples, which made their intensity difficult to be evaluated. The data on Fig. 10.21 and Fig. 10.22 are expected to show a high degree of error, due to the low signal-to noise ratio, but they seem to be comparable to the other samples.

As briefly mentioned in the results section, a new line appears during the annealing at around 300 °C. The line has a g-factor around 2.003, and it could be related to the E' family of centres. Its intensity as a function of annealing temperature does not agree with what reported by Toyoda and Ikeya (Fig. 10.23), where they observed the E' signal rise at around 200 °C and disappear at around 450 °C. Here instead the signal is increasing up to 450 °C in some of the reported samples. In the rose quartz annealed at 500 °C and the two hydrothermal samples the signals show a maximum intensity after annealing at 400 °C, then starting to decrease. It is possible that due to the large temperature step in the last measurements (50 °C) the maximum was just missed and what appears as a constant increase may contain a sharp spike. The shape of the signal, a single peak-to-peak line, seems not to be compatible with reported EPR spectra of E'_1, like the ones by Toyoda and Ikeya in their work. It is possible that the centre may be related to the so-called "Counterfeit E'_1 signal" reported by Toyoda and Schwarcz (1997). The authors observed that at high doses a new signal would overlap with the real E'_1 centre, causing a change in the spectral shape of its lines into something similar to what has been observed in this thesis work. The thermal stability reported, though, is completely different, being erased after an annealing at 170 °C. At the current state, no other hypothesis on its nature have been made and it should be explored more in future studies.

On the possibility of the involvement of these centres in luminescence properties, it is useful to remind that aluminium centres are already believed to be radiative recombination centres, although there is still debate on the emission wavelength (e.g. McKeever, 1985, and Martini et al., 1995). Titanium centres act as electron traps, and they could be related to TSL glow peaks, as suggested by Williams and Spooner (2018). The two steps process here observed could be originated by the two different titanium centres, $[TiO_4/H^+]^0$ and $[TiO_4/Li^+]^0$. Due to the overlapping of the two signals and other lines it is not easy to quantitively estimate the contribution of each type of centre. In the past, two TSL peaks decays have been observed in a very similar experiment (15 min annealing at different temperatures), although using different instrumentation, where one of the peaks being observed around 220 °C and the other at around 330 °C (5 °C/s). The observed trend is reported in Fig. 10.24 (Monti, 2017), where it can be seen how the two peaks disappear at around the same temperature as the titanium and aluminium lines reported in this section. Later, the peak at 330 °C has been associated with the SBP (375 °C) and $[GeO_4/Li^+]^0$ with other experiments (section 6, Vaccaro et al., 2019), but a further contribution from $[TiO_4/Li^+]^0$ cannot be excluded. Future studies could explore this possibility of correlation between EPR and TSL signals using the same experimental conditions. Additional information could be also obtained using samples with known impurity concentrations (unknown in the presented samples), either obtained from controlled synthetic growth or by concentration measurement through techniques such as Laser Ablation Inductively Coupled Plasma Mass Spectrometry (LA-ICP-MS, Monnier et al., 2018).

To summarize, the EPR lines of titanium and aluminium related centres has been studied. The qualitative dose response has been studied, revealing a different dose sensitivity of $[TiO_4/H^+]^0$ and $[TiO_4/Li^+]^0$. The thermal stability of the observed lines has been studied as a function of annealing temperature, revealing a two steps process of decay for titanium lines. A tentative suggestion of correlation with luminescence properties has been proposed in the form of the TSL peak at 220 °C and a contribution to the TSL peak at 330 °C (possibly the SBP). During the study an EPR line that could be related to the E' family of centres has been observed. It is not excluded that it may be instead the so-called "Counterfeit E'_1" line reported by Toyoda and Schwarcz (1997).

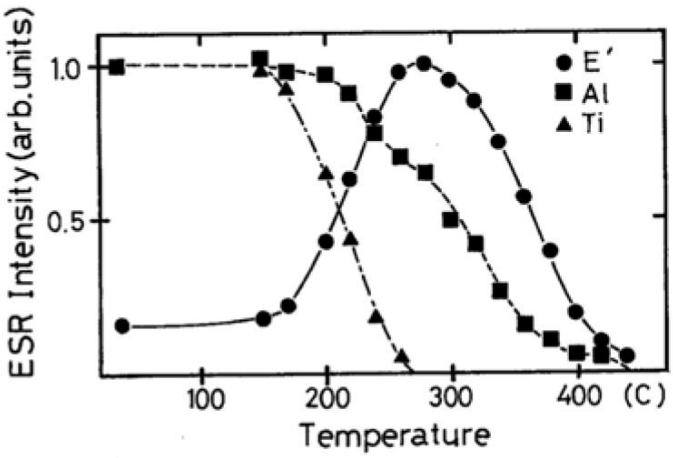

***Fig. 10.23**: Plot of ESR intensity versus temperature showing the results of isochronal annealing experiments. The ESR intensities of Al and Ti centers decrease at 220 °C and 170 °C, respectively, while the intensity of E' centers increases between 170 °C and 280 °C, and the decreases above 300 °C. The heating duration is 15 min. for each temperature step. (Toyoda and Ikeya, 1991)*

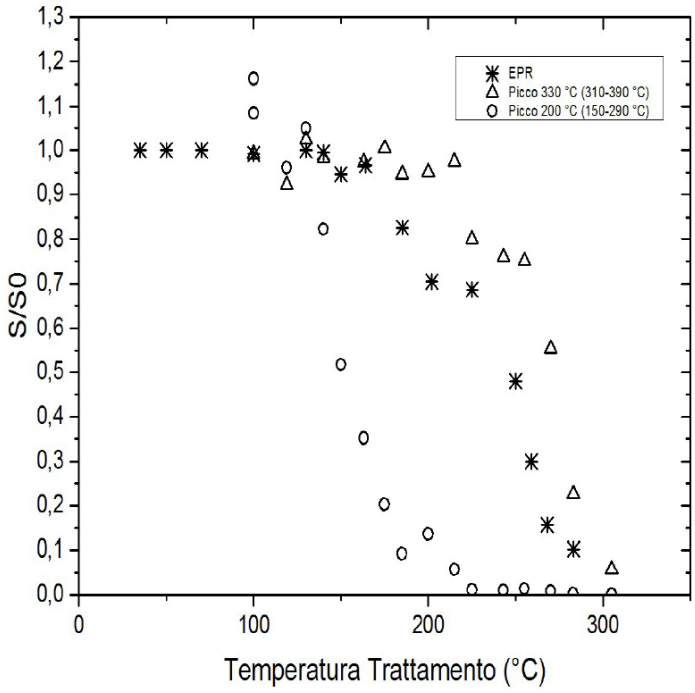

***Fig. 10.24**: Thermal stability of $[GeO_4/Li^+]^0$ (stars), the TSL peak at 220 °C (circles) and the TSL peak at 330 °C (triangles) in K-200 as a function of annealing temperature. Each annealing was 15 min long.*

11. Conclusions and final remarks

In this thesis work, many studies on luminescence and paramagnetic properties of quartz have been reported. Following the groundwork on Vaccaro et al. (2017), new answers on the role of germanium related centres have been found by connecting a TSL glow-peak, the so-called Slowly Bleachable Peak (SBP), also known as the TSL peak of quartz at "375 °C") to the $[GeO_4/Li^+]^0$ centre. The conclusion has been obtained by taking advantage of both signals' bleaching properties under UV illumination. With the new answers found about the role of germanium related centres in quartz luminescence properties, also new questions rose. In fact, the unstable $[GeO_4]^-$ centre has been found to show an anomalous decay time that strongly depends on the sample studied. Being that the effect is observable through both EPR and TSL experiments, thanks to the relation to the 110 °C TSL peak of quartz, it is an additional confirmation of the correlation reported by Vaccaro et al. (2017). Nonetheless, this anomaly is still without a clear explanation on why it is observed only on certain samples. Some possible ideas have been proposed, for example the possibility to be observing slightly different versions of the same centre, but experimental data to confirm them is still needed. While this specific result has no direct impact in dosimetric applications of the 110 °C TSL peak of quartz, one should wonder if the effect may be observable in higher temperature peaks, such as the SBP, used in direct dosimetric measurements.

The emission properties of quartz in both RL and TSL experiments have been studied, showing a strong sample dependence on the emission wavelengths. TSL experiments showed the evidence of different recombination processes depending on the peak's temperature, proving the inapplicability of a theoretical model on the reported samples. This clearly shows the fact that a complete model to describe quartz properties still needs to be formulated as well as the strong sample dependencies of them. The RL ones showed how composition, annealing and sample origin have an influence on the overall emission spectrum, confirming already known information about it, but also providing a wide overview on the subject and also pointing at possible different emissions between samples apparently very similar.

The paramagnetic properties of different kinds of impurity centres have been characterized. The EPR experiments showed that there are still unreported signals to discover in quartz samples. Germanium related centres have shown to possess a more complex behaviour than what is known so far about their thermal stability. Titanium and aluminium centres in quartz have shown that the observed phenomena are strongly sample dependent as well. Further studies on the newly reported hydrogen related centre could bring more insights into the role of this ion in quartz luminescence properties.

The results of this thesis do not reach a final point even after decades of research on quartz, but they definitely lay out new starting points for future investigations on the subject. The newly found EPR signals still lack an assignment on the possible centres that originate them. Known centres such as the titanium related ones may be related to TSL properties as already reported in the literature, but a

strong correlation is still missing. The studies here presented may lead to believe that there are just a few TSL peaks in quartz glow curves, but it is already known that most glow peaks are composed by many overlapping peaks. The groundwork of Vaccaro et al. (2017) on the $[GeO_4]^-$ centre and the presented study on the $[GeO_4/Li^+]^0$ centre have just barely scratched the surface of the topic aimed, together with other works in the literature, to the identification of all the centres responsible for the TSL peaks observed in quartz samples. These kinds of studies may also be used to better understand other quartz properties that have not been explored in this thesis work, like OSL properties and non-conventional luminescence experiments, such as Linearly Modulated-OSL or Photo-transferred-TSL. Other techniques could be explored using the same approach of this thesis work, by comparing their data with luminescent ones. An example could be thermally stimulated conductivity (TSC), which was already used in studies on quartz (e.g. Martini et al., 2000). New studies could be made on samples similar to the ones reported here, having the newly found knowledge. New studies could also use synthetic samples with tailored properties, such as impurity content and growth conditions. In fact, the works presented in this thesis work were all done only on natural samples and commercial synthetic samples, where the impurity composition can show little homogeneity. Precise knowledge of the composition of the samples could help to interpret even the data reported in this thesis work. A special attention should be placed on the link between Al and Ti and the stabilities of their related paramagnetic centres, which showed sample dependant thermal stabilities (Toyoda, 1991, 1994 and 2015 and chapter 10). The information could be obtained also through composition analysis techniques, such as LA-ICP-MS (Monnier et al., 2018). Of course there are several possibilities to follow, some hints to follow have been proposed in this thesis work, but indeed the research on quartz's luminescence properties and their relation to point defects is far from over.

12. References

In the digital version of this thesis work, each reference is provided by a hyperlink, where possible.

Abragam A. and Bleany B., *Electron Paramagnetic Resonance of Transition Ions*, Oxford University Press, 2012

Arends J., Dekker A.J. and Perdok W.G., *Color Centers in Quartz Produced by Crushing*, Physica Status Solidi, 1963, vol. 3, p. 2275-2279

Akhavan, A.C., *The Quartz Page* (http://www.quartzpage.de), 2005

Bailey, P., and Weil, J.A., EPR Study of the $[SiO_4/Li]^0$ Centre in α-Quartz, Journal of the Chemical Society Faraday Transactions, 1991, vol. 87(19), p. 3143-3146

Bailiff., I.K., Bowman, S.G.E., Mobbs, S.F., and Aitken, M.J., *The phototransfer technique and its use in thermoluminescence dating*, Journal of Electrostatics, 1977, vol. 3, p.269-280

Bailiff, I.K., *Pre-dose dating*, Scientific Dating Methods, 1991. Göksu, H.Y., Oberhofer, M. & Regulia, D. Kluwer Academic Publishers. 1: 155-174

Benny, P.G., Gundu Rao, T.K., and Bhatt, B.C., *The E1'-centre and its role in TL sensitization in quartz*. Radiation Measurements, 2002. **35**(4): p. 369-373.

Benzid, K., and Timar-Gabor, A., *The compensation effect (Meyer-Neldel rule) on $[AlO_4/h^+]^0$ and $[TiO_4/M^+]^0$ paramagnetic centers in irradiated sedimentary quartz*, AIP Advances, 2020, vol. 10, 075114

Bloch, M., Mancini, O., and McClelland, T., *Effects of radiation on performance of space-borne quartz crystal oscillators*, 2009 IEEE International Frequency Control Symposium Joint with the 22nd European Frequency and Time forum

Bos, A.J.J., *Theory of thermoluminescence*, Radiation Measurements, 1994, vol.41, p. 45-56

Bøtter-Jensen, L., Agersnap Larsen, N., Mejdahkm, V., Poolton, N.R.J., Morris, M.F. and McKeever, S.W.S., *Luminescence sensitivity changes in quartz as a result of annealing*, Radiation Measurements, 1994. **24**(4): p. 535-541.

Brumby, S., Yoshida, H., An investigation of the effect of sunlight on the ESR spectra of quartz centres: implications for dating, Quaternary Science Reviews, 1994, vol. 13, p. 615-618

Chen R., McKeever S.W.S., *Theory of Thermoluminescence and Related Phenomena*, 1997, World Scientific

Chen, R., Pagonis, V., and Lawless, J.L., *Evaluated thermoluminescence trapping parameters-What do they really mean?*, Radiation Measurements, 2016, vol.91, p.21-27

Chithambo, M.L. and Niyonzima, P., *Radioluminescence of annealed synthetic quartz.* Radiation

Measurements, 2017. **106**: p. 35-39.

Curie, D., Luminescence in Crystals, New York, John Wiley & Sons, 1963.

De Lima, J.F., Navarro, M.S., and Valerio, M., *Effects of thermal treatment on the TL emission of natural quartz*. Radiation Measurements, 2002. **35**: p. 155-159.

Fasoli, M. and Martini, M., *The composite nature of the thermoluminescence UV emission of quartz.* Journal of Luminescence, 2016. **173**: p. 120-126.

Feigl, F.J., Fowler, W.B., Yip, K.L., *Oxygen vacancy model for E'$_1$ center in SiO$_2$*, Solid State Communications, 1974, vol. 14, p. 225-229

Fleming, S.J., *The pre-dose technique: a new thermo-luminescent dating method.* Archaeometry, 1973. **15**(1): p. 13-30.

Franklin, A.D., *On the interaction between the rapidly and slowly bleaching peaks in the TL glow curves of quartz*, Journal of Luminescence, 1997, vol.75, p.71-76

Friedrich, J., Kreutzer, S., and Schmidt, C., *Radiofluorescence as a detection tool for quartz luminescence quenching process*. Radiation Measurements, 2018. **120**: p. 33-40.

Garlick, G.F.J., and Gibson, A.F., *The Electron Trap Mechanism of Luminescence in Sulphide and Silicate Phosphors*, Proceedings of the Physical Society, 1948, vol. 60(6), p. 574

Goreva, J.S., Ma, C., Rossman, R., *Fibrous nanoinclusions in massive rose quartz: The origin of rose coloration*, American Mineralogist, 2001, vol. 86, p. 466-472

Götze, J., Plötze, M., Habermann, D., *Origin, spectral characteristics and pratical applications of the cathodoluminescence (CL) of quartz – a review*, Mineralogy and Petrology, 2001, vol. 71, p. 225-250

Guzzo, P.L., Barros, V.S.M., Khoury, H.J., Lumin, J., *Spectroscopic account of the point defects related to the sensitization of TL peaks beyond 220 °C in natural quartz*, Journal of Luminescencee, 2017, vol.188, p. 118-128

Halperin, A., *Single irradiation excitation of the thermoluminescence (TSL) related to the [SiO$_4$Li]^0 center in quartz*, Journal of Physics and Chemistry of Solids, 1990, vol. 51, p. 303-306.

Halperin, A., Sucov, E.W., T*emperature dependence of the X-ray induced luminescence of Al-Na-containing quartz crystals*, Journal of Physics and Chemistry of Solids, 1993, vol. 54, p. 43-50.

Hansen, V., Murray, A.S., Buylaert, J.P., Yeo, E.Y. and Thomsen, K., *A new irradiated quartz for beta source calibration*. Radiation Measurements, 2015. **81**: p. 123-127.

Hashimoto, T., Hayashi, Y., Koyanagi, A., Yokosaka, K., *Red and blue colouration of thermoluminescence from natural quartz sands,* Nuclear Tracks and Radiation Measurements, 1986, vol. 11, p. 229-235

Hashimoto, T., Yokosaka, K., Habuki, H., *Emission properties of theremoluminescence from natural quartz-Blue and red TL response to absorbed dose*, Nuclear Tracks and Radiation Measurements, 1987, vol. 13, p. 57-66

Hashimoto, T., Yanagawa, Y., Yawata, T., *Blue and red thermoluminescence of natural quartz in the temperature region from -196 to 400 °C*, Radiation Measurements, 2007, vol. 42, p. 341-346

Hashimoto, T., *An overview of red-thermoluminescence (RTL) studies on heated quartz and RTL application to dosimetry and dating*, Geochronometria, 2008, vol. 30, p. 9-16

Hoogenstraaten, W., Philips Res. Rept., 1958, vol. 13, p.515

Hosaka, M., Taki, S., *Hydrothermal growth of quartz crystals in NaCl solution*, Journal of Crystal Growth, 1981, vol.52, p.837-842

Hunter, P.G., Spooner, N.A. and Smith B.W., *Thermoluminescence emission from quartz at 480 nm as a high-dose radiation marker*, Radiation Measurements, 2018. **120**: p. 143-147.

Huntley, C., Krueger, K., *Phase Diagram of Silicon Dioxide*, presentation available at prezi.com, 2015

Isoya, J., Weil, J.A., and Claridge, R.F.C., *The dynamic interchange and relationship between germanium centers in α-quartz*, The Journal of Chemical Physics, 1978, vol. 69, p. 4876-4884

Itoh, N.D., Stoneham, D., and Stoneham, A.M., *The predose effect in thermoluminescent dosimetry*, Journal of Physics: Condended Matter, 2001, vol.13(10), p.2201

Itoh, N.D., Stoneham, D., and Stoneham, A.M., *Ionic and electronic processes in quartz: Mechanisms of thermoluminescence and optically stimulated luminescence*, Journal of Applied Physics, vol. 92, p. 5036-5044, 2002

Ikeya, M., *New applications of electrion spin resonance*, World Scientific, 1993

Jani M.G., Bossoli R.B. and Halliburton L.E., *Further characterization of the E'1 center in crystalline SiO2*, Physical Review B, 1983, vol. 27, issue 4, p. 2285-2293

Kats, A., *Hydrogen in alpha-quartz*, Philips Research Reports, 1962, vol. 17, p. 133-279.

Kaya-Keleş S., Polymeris G.S. and Meriç N., *A component resolved study on the stable signal of Merck α-quartz: Tentative correlation among TL peaks, OSL components and EPR signals*, Nuclear Instruments and Methods in Physics Research Section B: Beam Interactions with Materials and Atoms, 2019, vol. 458, p. 44-56

Koul, D.K., *110 °C thermoluminescence glow peak of quartz — A brief review*. Pramana, 2008. **71**(6): p. 1209-1229.

Krbetschek, M.R., Götze, J., Dietrich, A. and Trautmann, T., *Spectral informations from minerals relevant for luminescence dating*, Radiation Measurements, 1997. **27**: p. 695-748.

Kuhn, R., Trautmann, T., Singhvi, A.K., Krbetschek, M.R., Wagner, G.A., Stolz, W., *A study of*

thermoluminescence emission spectra and optical stimulation spectra of quartz from different provenances, Radiation Measurements, 2000, vol. 32, p. 653-657

Lutoev, V.P., *Deconvolution of Powder ESR Spectra: Ge Centers in Natural Quartz*, Applied Magnetic Resonance, 2008, vol. 33, p.19-35

Mackey, J.H., *EPR Study of Impurity-Related Color Centers in Germanium-Doped Quartz*, Journal of Chemical Physics, 1963, vol.39(74), p.74-83

C. F. Macrae, C.F., Sovago, I., Cottrell, S. J., Galek, P. T. A., McCabe, P., Pidcock, E., Platings, M., Shields, G. P., Stevens, J. S. , Towler, M., and Wood, P. A., *Mercury 4.0: from visualization to analysis, design and prediction*, Journal of Applied Crystallography, 2020, vol. 53, p. 226-235

Malik, D.M., Kohnke, E.E., Sibley, W.A., *Low-temperature thermally stimulated luminescence of high-quality quartz*, Journal of Applied Physics, 1981, vol. 52, p. 3600-3605

Marfunin, A.S., *Spectroscopy, luminescence and radiation centres in minerals*, Springer-Verlag, 1979, Berlin.

Martin, J.J., *Electrodiffusion (Sweeping) of Ions in Quartz – A Review*, IEEE Transactions on ultrasonics, ferroelectrics and frequency control, 1988, vol. 35, p. 288-296

Martini, M., Paleari, A., Spinolo, G., Vedda, A., *Role of $[AlO_4]^0$ centres in the 380-nm thermoluminescence of quartz*, Physical Review B, 1995, vol. 52 (1), p. 138-142

Martini, M., Meinardi, F., Vedda, A., *The role of alkali ions in the 190 K TSL peak in quartz*, Radiation Measurements, 2000, vol. 32, p. 673-677

Martini, M., Fasoli, M., Villa, I. and Guibert, P., *Radioluminescence of synthetic and natural quartz.* Radiation Measurements, 2012a. **47**(9): p. 846-850.

Martini, M., Fasoli, M., Galli, A., Villa, I. and Guibert, P., *Radioluminescence of synthetic quartz related to alkali ions.* Journal of Luminescence, 2012b. **132**(4): p. 1030-1036.

Martini, M., Fasoli, M., and Villa, I., *Defect studies in quartz: Composite nature of the blue and UV emissions.* Nuclear Instruments & Methods in Physics Research Section B-Beam Interactions with Materials and Atoms, 2014. **327**: p. 15-21.

May, C.E. and Partridge, J.A., *Thermoluminescent Kinetics of Alpha-Irradiated Alkali Halides*, The Journal of Chemical Physics, 1964, vol. 40(5): p. 1401-1409

McKeever, S.W.S., *Thermoluminescence of Solids*, Cambridge: Cambridge University Press, 1985, Cambridge Solid State Science Series

McKeever, S.W.S., Chen, C.Y., and Halliburton, L.E., *Point defects and the pre-dose effect in natural quartz.* Nuclear Tracks and Radiation Measurements (1982), 1985. **10**(4): p. 489-495.

McKeever, S.W.S., *Thermoluminescence in Quartz and Silica.* Radiation Protection Dosimetry,

1984. **8**(1-2): p. 81-98.

McKeever, S.W.S., *Mechanisms of thermoluminescence production: Some problems and a few answers?* International Journal of Radiation Applications and Instrumentation. Part D. Nuclear Tracks and Radiation Measurements, 1991. **18**(1): p. 5-12.

McMorris, D.W., *Impurity color centers in quartz and trapped electron dating: Electron spin resonance, thermoluminescence studies*, Journal of Geophysical Research, 1971, vol.76(32), p.7875-7887

Monnier, L., Lach, P., Salvi, S., and Melleton, J., *Quartz trace-element composition by LA-ICP-MS as proxy fro granite differentiation, hydrothermal episodes, and related mineralization: The Beauvoir Granite (Echassieères district), France*, Lithos, 2018, vol. 320-321, p. 355-377

Monti, A.M., *Ruolo dei difetti di punto in quarzo nell'intrappolamento e nella luminescenza*, Università degli Studi di Milano-Bicocca, 2017

Monti, A.M., Fasoli, M., Panzeri, L., Martini, M., *Investigation of the spectrally resolved TL peaks of quartz in the 70°C-220°C temperature region*, Radiation Measurements, 2019, vol.127

Nanjundaswamy, R., Lepper, K., and McKeever, S.W.S., *Thermal Quenching of Thermoluminescence in Natural Quartz.* Radiation Protection Dosimetry, 2002. **100**(1-4): p. 305-308.

Nuttall, R.H.D., Weil, J.A., *Two hydrogenic trapped-hole species in α-quartz*, Solid State Communications, 1980, vol. 33, p. 99-102

Pagonis, V., Chithambo, M.L., Chen, R., Chruścińska, A., Fasoli, M., Li, S.H., Martini, M., and Ramseyer, K., *Thermal dependence of luminescence lifetimes and radioluminescence in quartz.* Journal of Luminescence, 2014. **145**: p. 38-48.

Petrov, S.A. and Bailiff, I.K., *The '110°C' TL peak in synthetic quartz.* Radiation Measurements, 1995. **24**(4): p. 519-523.

Plötze, M., Wolf, D., Krbetschek, M.R., Chap. 8 "*Gamma-irradiation dependency of EPR and TL spectra of quartz*". In: Göetz, J., Möckel, R. (Eds.), *Quartz: Deposits, Mineralogy and Analytics. Springer-Verlag*, Heidelberg, 2012

Preusser, F., Chithambo, M.L., Götte, T., Martini, M., Ramseyer, K., Sendezera, E.J., Susino, G.J. and Wintle, A.G., *Quartz as a natural luminescence dosimeter.* Earth-Science Reviews, 2009. **97**(1): p. 184-214.

Randall, J.T., and Wilkins, M.H.F., *Phosphorescence and electron traps I. The study of trap distributions*, Proceedings of the Royal Society A, 1945a, vol. 184(999)

Randall, J.T., and Wilkins, M.H.F., *Phosphorescence and electron traps II. The Interpretation of long-period phosphorescence*, Proceedings of the Royal Society A, 1945b, vol. 184(999)

Rendell, H.M., Townsend, P.D. and Wood, R.A., *Thermal Treatments and Emission-Spectra of Tl from Quartz.* Radiation Measurements, 1994. **23**(2-3): p. 441-449.

Rink, W.J., Rendell, H., Marseglia, E.A., Luff, B.J., Townsend, P.D., *Thermoluminescence spectra of igneous quartz and hydrothermal vein quartz*, Physics and Chemistry of Minerals, 1993, vol. 20, p. 353-361

Rink, W.J., *Electron spin resonance (ESR) dating and ESR applications in quaternary science and archaeometry*, Radiation Measurements, 1997, vol. 27, p. 975-1025

Rinneberg H and Weil J.A., *EPR Studies of Ti_3^+-H^+ Centers in X-irradiated α-Quartz*, The Journal of Chemical Physics, vol. 56, p. 2019-2028, 1972

Rudra, J.K., Fowler, W.B., Feigl, F.J., *Model for the E'2 center in alpha quartz*, Physical Review Letters, 1985, vol. 55, p. 8223-8230

Schilles, T., Poolton, N.R.J., Bulur, E., Bøtter-Jensen, L., Murray, A.S., Smith, G.M., Riedi, P.C. and Wagner, G.A., *A multi-spectroscopic study of luminescence sensitivity changes in natural quartz induced by high-temperature annealing.* Journal of Physics D: Applied Physics, 2001. **34**(5): p. 722.

Skuja, L., *Optical properties of defects in silica*. In Pacchioni, G., Skuja, L., Griscom, D.L. (Eds.), *Defects in SiO_2 and Related Dielectrics*: Academic Publishers, Amsterdam, 2000, p. 73-116

Skuja, L., Ollier, N., Kajihara, K., *Luminescence of non-bridging oxygen hole centers as a marker of particle irradiation of -quartz*, Radiation Measurements, 2020, vol. 125, 106373

Spooner, N.A., Prescott, J.R., Hutton, J.T., *The effect of illumination wavelength on the bleaching of the thermoluminescence (TL) of quartz*, Quaternary Science Reviews, 1988, vol.7(3-4), p. 325-329

Spooner, N.A. and Questiaux, D.G., *Kinetics of red, blue and UV thermoluminescence and optically-stimulated luminescence from quartz.* Radiation Measurements, 2000. **32**(5): p. 659-666.

Stoll, S., and Schweiger, A., *EasySpin, a comprehensive software package for spectral simulation and analysis in EPR*, Journal of Magnetic Resonance, 2006. Vol. 178(1), p.42-55

Timar-Gabor, A., Chruścińskac, A., Benzid, K., Fitzsimmonsd, K.E., Begy, R., Bailey, M., *Bleaching studies on Al-hole ($[AlO_4/h]^0$) electron spin resonance (ESR) signal in sedimentary quartz*, Radiation Measurements, 2020, vol. 130, 106221

Toyoda, S., Ikeya, M., *Thermal stabilities of paramagnetic defect and impurity centers in quartz: Basis for ESR dating in thermal history*, Geochemical Journal, 1991, Vol. 25, p. 437

Toyoda S., Kohno H. and Ikeya M., *Distorted E'1 Centers in Crystalline Quartz: An Application to ESR Dating of Fault Movements*, Applied Radiation and Isotopes, 1993, vol. 44, issues 1-2,

p. 215-220

Toyoda, S., Goff, F., *Quartz in Post-caldera Volcanic Rocks of Valles Caldera, New Mexico: ESR Finger Printing and Discussion in ESR Ages*, New Mexico Geological Society Guidebook, 1996, 47th Field Conference, p. 303-309

Toyoda, S., Schwarcz, P., *Counterfeit E'_1 signal in quartz*, Radiation Measurements, 1997, vol. 1, p. 59-66

Toyoda, S., Voinchet, P., Falguères, C., Dolo, J.M., Laurent, M., *Bleaching of ESR signals by the sunlight: a laboratory experiment for establishing the ESR dating of sediments*, Applied Radiation and Isotopes, 2000, vol. 52(5), p. 1357-1362

Toyoda, S., *Paramagnetic Lattice defects in quartz for applications to ESR dating*, Quaternary Geochronology, 2015, vol. 30, p. 498-505

Usami T., Toyoda S., Bahadur H., Srivastava A.K. and Nishido H., *Characterization of the E'1 center in quartz: Role of aluminium hole centers in oxygen vacancies*, Physica B, 2009, vol 404, p. 3819-3823

Vaccaro, G., Panzeri, L., Paleari, S., Martini, M. and Fasoli, M., *EPR investigation of the role of germanium centers in the production of the 110°C thermoluminescence peak in quartz.* Quaternary Geochronology, 2017. **39**: p. 99-104.

Vaccaro, G., Panzeri, L., Monti, A.M., Martini, M., Fasoli, M., *Optical bleaching of the 375 °C TL peak, $[GeO_4/Li^+]^0$ EPR center and OSL signal in irradiated natural quartz*, Journal of Luminescence, 2019, vol.205, p.61-65

Weil, J.A., *Germanium-Hydrogen-Lithium Center in α-Quartz*, Journal of Chemical Physics, 1971, vol.55, p.4685-4698

Weil, J.A., *A review of electron-spin spectroscopy and its application to the study of paramagnetic defects in crystalline quartz*. Physics and Chemistry of Minerals, 1984, vol. 10, p. 149-165

Williams, O.M. and Spooner, N.A., *Defect pair mechanism for quartz intermediate temperature thermoluminescence bands.* Radiation Measurements, 2018. **108**: p. 41-44.

Wintle, A.G., *Thermal Quenching of Thermoluminescence in Quartz.* Geophysical Journal of the Royal Astronomical Society, 1975. **41**: p. 107-113.

Woda, C., Schilles, T., Rieser, U., Mangini, A. and Wagner, G.A., *Point defects and the blue emission in fired quartz at high doses: a comparative luminescence and EPR study.* Radiation Protection Dosimetry, 2002. **100**, Nos 1-4, p. 261-264.

Wright, P.M., Weil, J.A., Buch, T., Anderson, J.H., *Titanium Colour Centres in Rose Quartz*, Nature, 1963, vol. 197, p. 246-248

Yang X.H. and McKeever S.W.S., *Characterization of the pre-dose effect using ESR and TL*, Nuclear Tracks and Radiation Measurements, 1987, vol. 14, nos 1-2, p. 75-79

Yang X.H. and McKeever S.W.S., *The pre-dose effect in crystalline quartz*, Journal of Physics D: Applied Physics, 1990, vol. 23, p.237-244

Yazici, A.N., and Topaksu, M., *The analysis of thermoluminescence glow peaks of unannealed synthetic quartz*, Journal of Physics D: Applied Physics, 2003, vol. 36, p. 620-627

Zimmerman, J., *The radiation-induced increase of the 100 C thermoluminescence sensitivity of fired quartz.* Journal of Physics C: Solid State Physics, 1971.

Thanks to the respective journals for granting permission to reproduce figures from their publications.

Appendix

Following the transmittance spectra of optical filters used in this thesis work are reported.

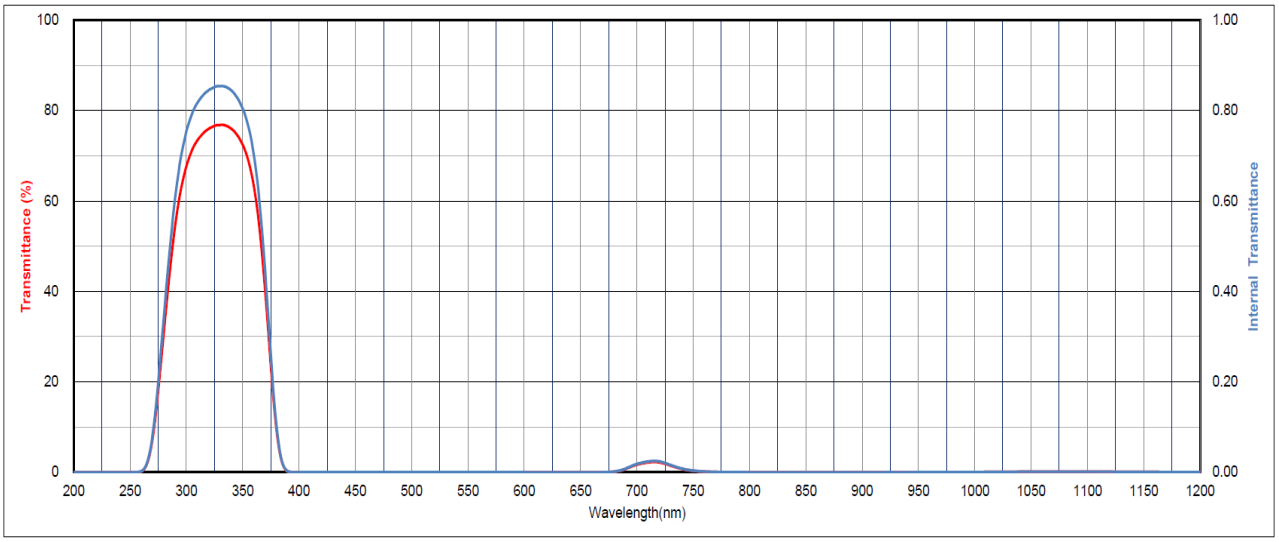

Fig. A1: Transmittance spectrum of the Hoya U-340 optical filter as provided by the manufacturer.

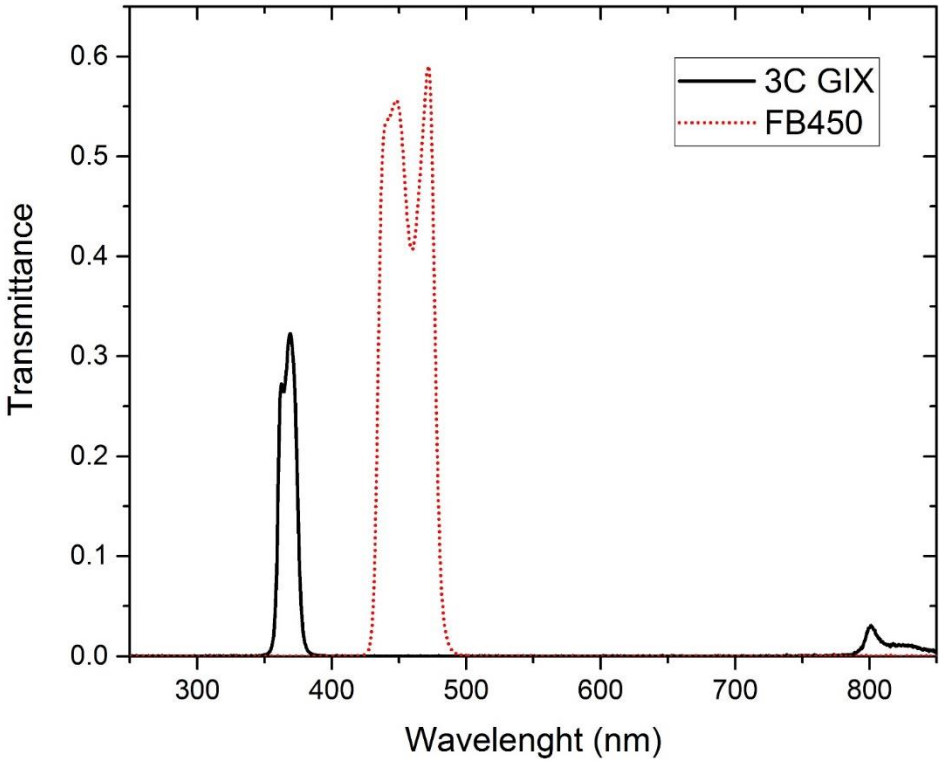

Fig. A2: Transmittance spectrum of the interferential filters 3C GIX (UV, 365 nm, FWHM 10 nm) and FB450 (Blue, 450 nm, FWHM 40 nm). Spectra acquired with a Cary

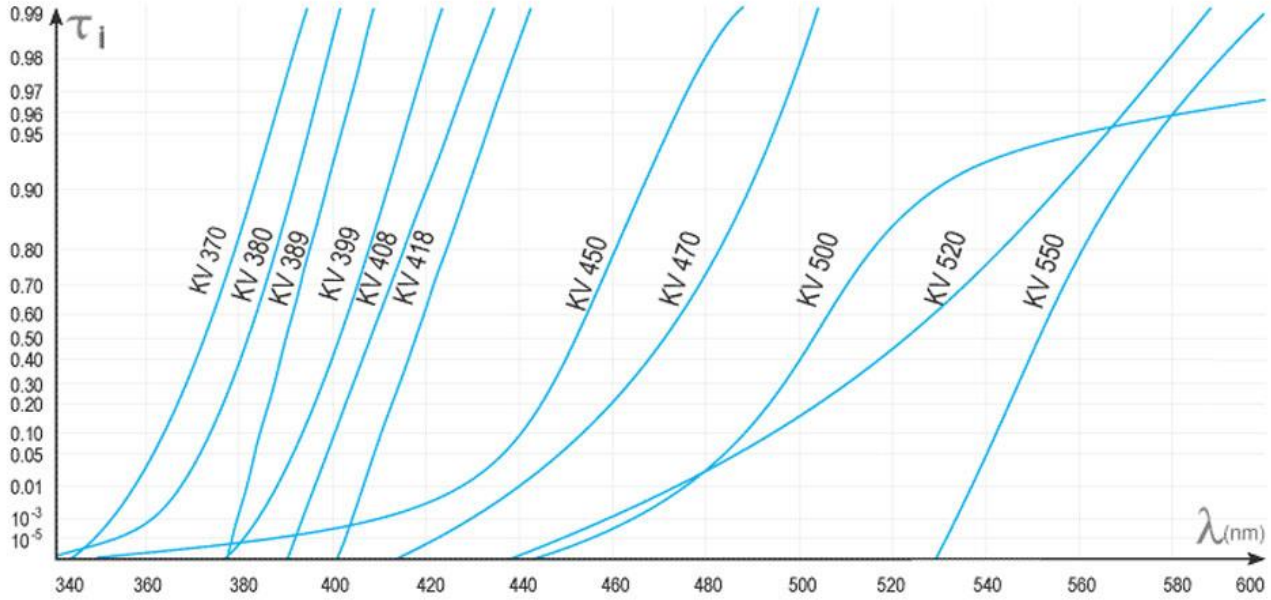

Fig. A3: Transmittance spectrum of the KV418 shortpass filter as provided by the manufacturer.

Following is reported the approximated Randall-Wilkins equation used to obtain the glow curve fits:

[A1] $$I(T) = n_0 s \exp\left(-\frac{E_T}{kT}\right) \exp\left[-\frac{s}{\beta} \mathrm{T} \exp\left(-\frac{E_T}{kT}\right)\right](1+$$

$$-\frac{\left(0.2677737343 + 8.6347608925\,\frac{E_T}{kT}\right) + 18.0590169730\left(\frac{E_T}{kT}\right)^2 + 8.5733287401\left(\frac{E_T}{kT}\right)^3 + \left(\frac{E_T}{kT}\right)^4)}{\left(3.9584969228 + 21.0996530827\,\frac{E_T}{kT}\right) + 25.6329561486\left(\frac{E_T}{kT}\right)^2 + 9.5733223454\left(\frac{E_T}{kT}\right)^3 + \left(\frac{E_T}{kT}\right)^4}$$

Acknowledgments

This last section will be more personal, and so I will drop the impersonal style I used so far in my thesis work (which I personally like more when discussing data). I want to thank everyone that helped me during my PhD program. I'm not very good with words, so I'll just keep it simple, although I guarantee that my thanks come from the depth of my heart. I'll start with thanking Prof. Marco Martini, for being my PhD tutor and having introduced me to this subject and its complexity since my master's thesis. I want also to thank Prof. Mauro Fasoli for all the help he gave me while using the instrumentation and all his useful comments on the work I've been doing. I thank Prof. Martin Nikl, from the Physics Institute of the Czech Academy of Science in Prague, for hosting me during my abroad period and Dr. Maksym Buryi for teaching me about EPR, how to properly operate a spectrometer and process the data obtained.

Finally, I thank my family, my friends and all the colleagues I spent these three years with for encouraging me during my PhD project and helping me in too many ways to be able to list all of them.